12-2023

Fourier Analysis and Optimization of Inductive Wireless Power Transfer for Electric Vehicle Charging

Andrew P. Foote
University of Tennessee, Knoxville, afoote5@vols.utk.edu

To the Graduate Council:

I am submitting herewith a dissertation written by Andrew P. Foote entitled "Fourier Analysis and Optimization of Inductive Wireless Power Transfer for Electric Vehicle Charging." I have examined the final electronic copy of this dissertation for form and content and recommend that it be accepted in partial fulfillment of the requirements for the degree of Doctor of Philosophy, with a major in Electrical Engineering.

Daniel J. Costinett, Major Professor

We have read this dissertation and recommend its acceptance:

Hua Bai, Han Cui, Omer C. Onar

Accepted for the Council:

Dixie L. Thompson

Vice Provost and Dean of the Graduate School

(Original signatures are on file with official student records.)

Fourier Analysis and Optimization of Inductive Wireless Power Transfer for Electric Vehicle Charging

A Dissertation Presented for the

Doctor of Philosophy

Degree

The University of Tennessee, Knoxville

Andrew Paul Foote

December 2023

For my loving wife Rachel and all our family

Acknowledgments

This project was funded by Volkswagen Group of America (VWGoA) under Volkswagen Group Innovation. I thank my colleagues at Innovation Hub Knoxville, William Henken, Marton Kardos, Nathan Strain, Cecile Grubb, Joey Michaud, Chuhee Lee, and Hendrik Mainka for their support, direction, and encouragement, and Dr. Nikolai Ardey of Volkswagen Group Innovation for his enthusiasm and support of the wireless power transfer PhD topic.

My graduate research and education have been funded from many different sources since the beginning of my time in Knoxville in June 2016. I thank the Bredesen Center for Interdisciplinary Research, the Department of Energy Wide-Bandgap Traineeship, Oak Ridge National Laboratory, the University of Tennessee, and Volkswagen Group Innovation for funding my PhD research.

I express my appreciation and thanks to my advisor, Daniel Costinett, for his patience, guidance, and support throughout most of my PhD studies at the University of Tennessee, Knoxville (UTK). I also thank Burak Ozpineci for advising and co-advising me at Oak Ridge National Laboratory (ORNL), Ruediger Kusch as my mentor from Volkswagen Group, and Lee Riedinger, Leon Tolbert and Fred Wang of UTK. I would also like to especially thank my committee members: Kevin Bai, Helen Cui, and Omer Onar.

I was helped and encouraged by a wonderful group of friends and colleagues at CURENT and UTK and I especially thank Kamal Sabi, Saeed Anwar, Jared Baxter, Quillen Blalock, Spencer Cochran, Stephen Fatokun, Jie Li, Ling Jiang, Taher Naderi, Peter Pham, Ruiyang Qin, Joseph Setelin, Jingjing Sun, Yu Yan, Chongwen Zhao, and many others for their feedback, comradery, and encouragement.

During my work and collaboration with ORNL, I was also surrounded by many colleagues and friends. I especially thank Omer Onar for his mentorship and collaboration in the high-power tests of my demonstrators at ORNL. I further thank Jason Pries and Suman Debnath for their mentorship and Mostak Mohammad, Devendra Patil, Emre Gurpinar, Jon Wilkins, Christian Boone, Subhajyoti Mukherjee, Erdem Asa, Shajjad Chowdhury, Rafal Wodja, Branndon Chen, and Utkarsh Kavimandan.

I would like to express my gratitude and thanks for my family and their unwavering support, encouragement, and inspiration – my loving and wonderful wife Rachel, my parents John and Liz Foote, my wife's parents Alan and Catherine Buchanan, my siblings Daniel and Laura, and all my family.

Above all, I would like to thank God for giving me a mind to think and love, and hands to work and create. With God, all things are possible.

Abstract

With the growth of electric vehicle (EV) popularity, different charging options to increase user convenience and reduce charging time such as high power wireless charging are increasingly being developed and researched. Inductive wireless power transfer (WPT) systems for EVs must meet specifications such as stray field, battery power and voltage operating range, efficiency, and ground clearance. The coil geometry and design have a large impact in meeting these constraints. Typical design approaches include iterative analysis of predetermined coil geometries to identify candidates that meet these constraints.

This work instead directly generates WPT coil shapes and magnetic fields to meet specifications and constraints through the optimization of Fourier basis function coefficients and that can be used to predict system efficiency and performance.

The proposed Fourier Analysis Method (FAM) applies to arbitrary planar coil geometries and does not rely on iterative finite-element analysis (FEA) simulations. This flexibility allows for rapid design evaluation across a larger range of coil geometries and specifications. The method is used to consider the trade-off of coil current and stray field for given power levels to illustrate the flexibility and generality of the method. A 6.6 kW proof-of-concept demonstrator WPT system is built from the optimization result to compare model efficiency, stray fields, and performance to experimental measurements. The methodology is then used in the optimization, design, analysis, and testing of two 120 kW demonstrators, including thermal modeling and integration.

Table of Contents

List of Tables

List of Figures

Chapter 1

Introduction

Climate change, the health effects of exhaust pollutants in populated areas, technology improvements, and energy security have led to massive efforts in many countries to quickly transition to battery electric vehicles (EVs) from traditional internal combustion engine (ICE) vehicles. Many governments have provided subsidies or fuel-economy standards to encourage the purchase and manufacture of EVs [1]. As of the beginning of 2021, there are 31 national and local governments that plan to ban internal combustion engine (ICE) vehicles in some manner in the upcoming years [2]. These regulatory tailwinds and advantages in vehicle acceleration, energy costs, and efficiency have increased the sale and production of EVs. Including plug-in hybrid electric vehicles (PHEVs), the sale of electric vehicles exceeded 2.1 million globally in 2019, a 40% year-over-year increase in the total number of EVs in the world from 2018 [1]. A chart of the sales of EVs world-wide is shown in Figure 1.1. The electrification of city buses has also been increasing rapidly due to the suitability of electric drive trains to route lengths and urban driving cycles, and the desire to improve air-quality in cities. Currently, there are about half a million electric buses in circulation, mostly in China, but there have been notable increases in Europe, India, and North America in recent years [1].

Lithium-ion battery technology has rapidly improved in recent years in both cost and performance. Battery pack prices have fallen to around $156/kWh in 2019 compared to $1,100/kWh in 2010 [1]. Significant technical improvements of the energy density, cycle lifetime, and power density have been made and are expected to continue as new battery

technologies, such as solid-state, lithium-air, and lithium-sulfur batteries, reach maturity. In the next few years, batteries could have cell-level energy densities of 325 Wh/kg, compared to 100-260 Wh/kg today [1]. Technological improvements in preventing lithium plating and thermal design have also improved battery charging rates and cycle life. Many contemporary battery packs can charge at C-rates of 1.5 C to 2 C and the Porsche Taycan can charge up to 3 C [3, 4].

1.1 Electric Vehicle Fast-Charging

In surveys on passenger electric vehicles, "range anxiety" and charging concerns dominated most of the responses [5]. To react to this pain point, EV battery pack sizes have been increasing. The average battery back is 55 kWh in 2021, compared to 37 kWh in 2018, and many EVs have pack sizes of 70-80 kWh, corresponding with 215-250 mile (346-402 km) ranges [1]. For 6.6 kW Level 2 charging, the charging times of these large battery packs can take hours, much longer than the typical 10 minutes it takes to refuel an ICE vehicle. If a trip exceeds the range of the battery pack and charging is needed enroute, long charging times can greatly hinder long-distance trips with EVs.

To combat this and encourage public charging, DC fast-charging stations have been implemented on many major highways and routes to reduce charging times [4]. These stations have increasingly high power levels and are being standardized worldwide, such as with the Combined Charging System (CCS) standard in the United States and the European Union and the GB/T standard in China [6]. For example, Electrify America stations (CCS) can supply up to 350 kW for compatible vehicles [7]. The combination of fast-charging and large battery packs enables EVs to take long-distance trips comparable to ICE vehicles as illustrated in Figure 1.2 [4]. However, even higher charging power levels may be required for heavier electrified vehicles, such as delivery trucks or tractor trailers, which often require over 150 kW or even 350 kW to maintain normal highway speeds [8]. Due to this, the adoption of EVs for medium and heavy-duty freight in regional or long-haul applications has been very low [1] although standardization efforts such as the Megawatt Charging System (MCS) are moving forward [9].

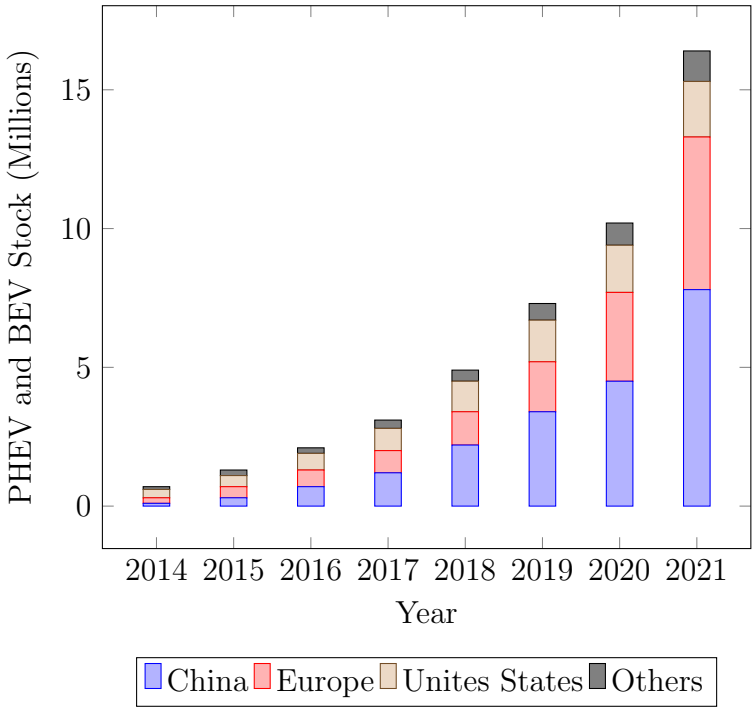

Figure 1.1: Light-duty BEVs and PHEVs stock worldwide since 2014 [1].

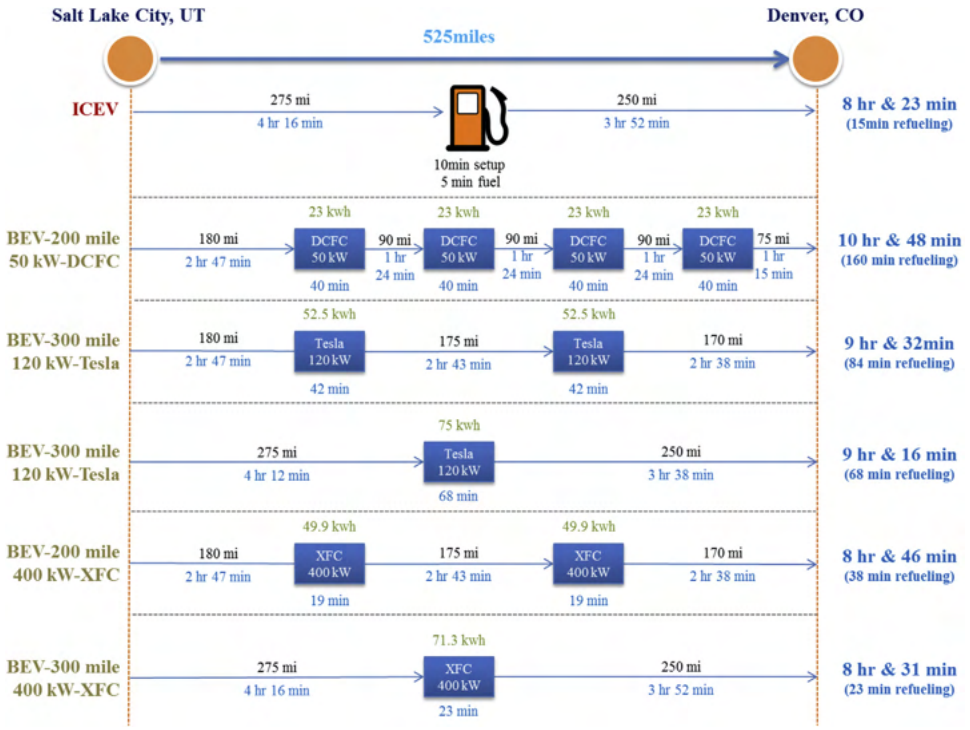

Figure 1.2: Travel time for an example trip from Salt Lake City, Utah to Denver, Colorado with different charging methods [4].

Another related trend is the rise in EV battery voltages to 800 V and beyond from current 400 V levels. Higher voltages allow less current at a given power level, reducing the size and weight of charging cables, motors, and interconnects. For example, to charge at 350 kW at 400 V, 875 A is needed whereas only 437.5 A is needed at 800 V. Without the use of liquid-cooled wires, the gauge of the wire required to carry these high currents can easily exceed the Occupational Safety and Health Administration (OSHA) 50 lbs lifting limit for one person for a standard 6 foot long charging cable [4]. Due to this, liquid-cooled cables have been introduced to limit the weight of the cable at many public charging stations [7]. In the future, even higher voltages such as 1000 V to 1500 V may be used to further integrate charging stations with solar and other power sources. Voltage levels like these are well beyond the standard household voltages used by the general public. Therefore, DC fast chargers have several safety features to make them compatible for public use such as isolation transformers [10, 11].

1.2 Wireless Charging for EVs and Electric Buses

Wireless power transfer (WPT) for Electric Vehicles (EVs) has several advantages over conductive charging, including improvements in convenience, safety, automation, and resistance to vandalism. In WPT systems, there can be no moving parts or connectors exposed to the elements and there is no need for users to handle or plug in the charger. With these benefits, WPT systems have been implemented in consumer homes, bus stops, docks, and warehouses with power levels from 3 kW to 300 kW [12]. There is also interest in future applications for automated vehicles and electrified highways [8]. A simple illustration of a WPT system compared to a conductive DC-fast charger is shown in Figure 1.3. The general flow of power for the WPT system is as follows: on the primary or ground-side, a front-end PFC rectifier converts the grid voltage to high-voltage DC. This is inverted with a high-frequency inverter to excite the primary or ground side coil. The induced voltage on the secondary or vehicle side is rectified and used to charge the EV battery pack. The different parts of the WPT system that are separated by a physical airgap are usually discussed as two separate parts: the ground assembly (GA) and the vehicle assembly (VA). In this

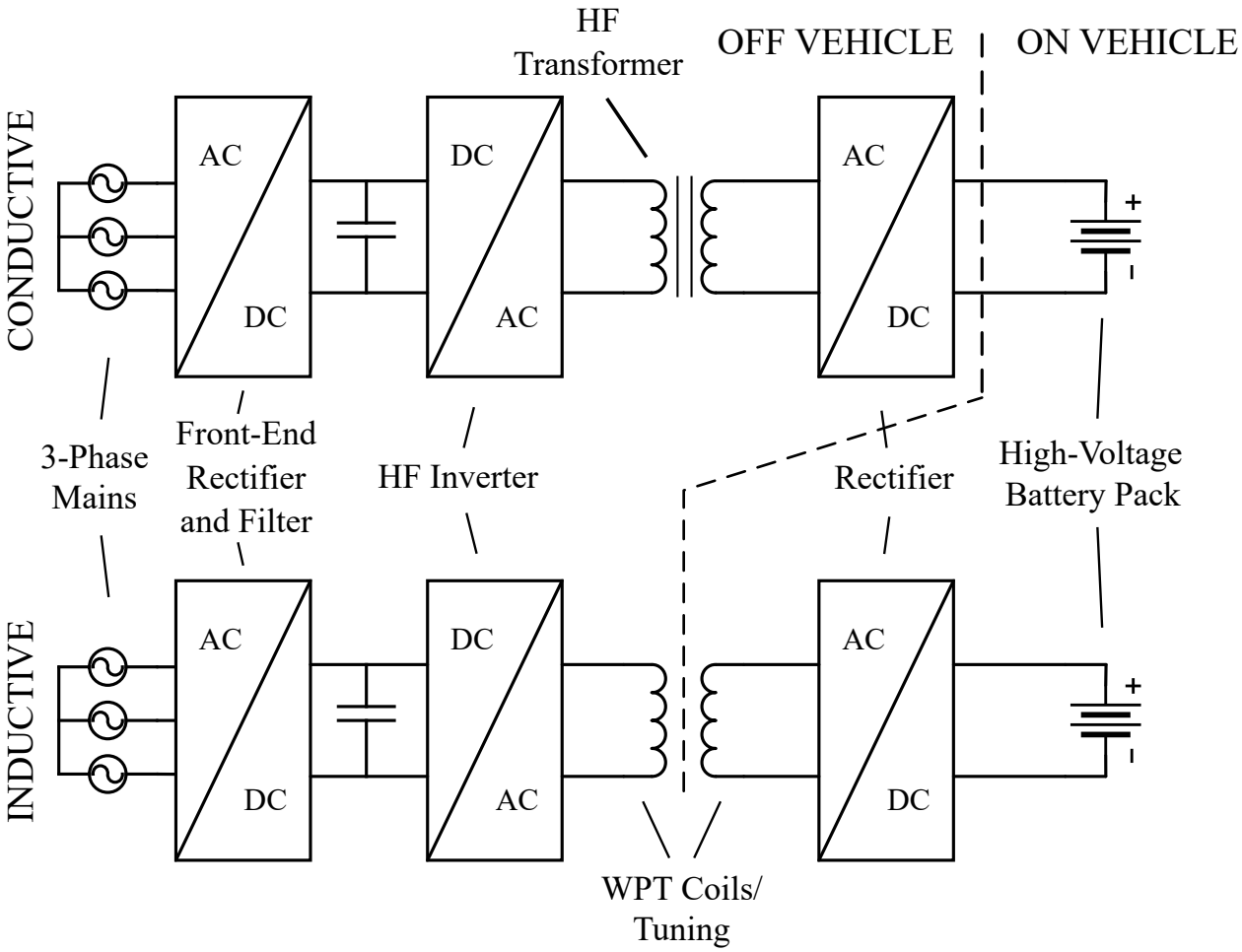

Figure 1.3: Block diagram of a typical conductive DC-fast charging system vs. a high-power inductive WPT system. As seen, the inductive WPT stage replaces the isolated DC/DC converter used in the conductive charger.

terminology, each GA typically contains ferrite, a primary coil, compensation elements, and possibly an inverter, and each VA contains ferrite, a secondary coil, compensation elements, and a rectifier as in Figure 1.3. Typically, the grid-connected front-end rectifier is located within a separate enclosure from the GA close to the grid transformer. In some systems, the GA high-frequency inverter may also be in this separate enclosure.

Many of the current real-world implementations of high-power wireless systems are for electric buses, which use WPT for opportunity-charging at stops. Frequent opportunity-charging allows buses to have smaller, less-costly batteries compared to electric buses that have to have enough range for an entire shift or day without charging. These WPT systems often use many VAs on the underside of the buses paired with multiple GAs in parallel to achieve high power levels, each limited to a power of around 50 kW to 75 kW [13, 14]. In total, the paralleling of these modules can charge the buses up to 200 kW or higher. Examples of implemented systems of this kind are given in Figure 1.4.

For passenger vehicles, WPT must fit within smaller wheelbases and tracks and operate with larger airgaps than electric buses. With the smaller space on the underside of passenger vehicles, the number of VAs of the WPT system will be limited. The ground clearance of passenger vehicles may also be larger than buses. Buses often kneel at stops, reducing ground clearance to 100 mm to 175 mm. In passenger EVs, the airgaps for flush mounted GAs may be equal to normal vehicle ground clearances, which often range from 125 mm to 250 mm depending on the vehicle type. To meet applicable regulatory requirements, such as stray field safety limits, thermal limits, and other restrictions at an attractive cost, most commercial WPT systems for passenger vehicles have been limited to 22 kW or lower, with the highest-power commercial system reaching 75 kW for a taxi opportunity-charging demonstration [15]. For fast-charging applications, higher power levels than these are needed in order to make wireless charging competitive with DC fast charging. This area of research has led to many projects on increasing the power density of inductive WPT systems and research demonstrations of up to 120 kW have been performed in single VA and GA systems [16, 17].

(a)

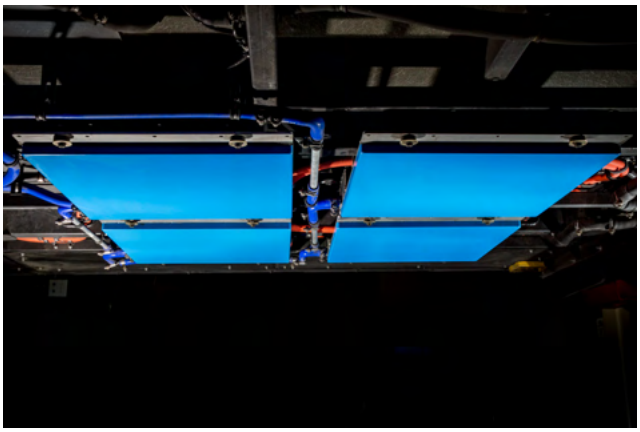

(b)

(c)

(d)

(e)

Figure 1.4: Examples of current implementations of inductive wireless charging. (a) Momentum Dynamics Bus (now InductEV) 200 kW system in Wenatchee, Washington and (b) Underside of Momentum Dynamics System. (c) Momentum 75 kW taxi charging system [15, 18]. (c) WAVE Bus 200 kW System near Los Angeles, California [19]. (d) Bombadier Primove Bus 150-200 kW System [20].

1.3 Requirements and Challenges for WPT Systems

There are several challenges and barriers to further developing and implementing wireless charging at high power levels. These are related, as they have been with other developments in charging technology, to the need for standardization and interoperability of the infrastructure with different vehicles and regulatory and safety requirements.

1.3.1 Infrastructure Interoperability

Currently, most commercial automotive WPT solutions feature individualized systems for use with electric buses and home charging for passenger vehicles. However, in parking lots, traffic lights, and highways, many classifications of vehicles may be present, from passenger vehicles to larger trucks or delivery vehicles. Therefore, it is essential that public WPT systems are standardized to be interoperable with different WPT equipment, vehicle manufacturers, and power levels. This is apparent in the philosophy of current public fast charging stations with Combined Charging System (CCS) or CHAdeMO standard plugs that adapt to charge at different levels [7, 21]. In the same way, WPT systems must be interoperable and able to charge different types and classes of vehicles. This call is also present in reviews of WPT [12, 13, 22, 23].

Recently, the Society of Automotive Engineers (SAE) published the J2954 standard for light-duty passenger vehicles WPT [24]. J2954 is limited to light-duty vehicles in stationary charging applications. In this standard, four power levels are defined for WPT: 3.7 kVA, 7.7 kVA, 11.1 kVA, and 22 kVA. A primary focus of the standard is the interoperability of differing vehicle ground clearances and airgaps, power levels, and coil geometries with all applicable safety standards. Standardization and interoperability for higher power classes of WPT systems beyond 22 kVA is not currently included in the J2954 standard, but is being addressed in the SAE J2954/2 Technical Information Report at power levels up to 500 kW [25]. The compatibility requirements within the J2954 standard are already illustrative of the need for interoperability. For example, the ranges of airgaps and power levels in the J2954 standard are defined to set expectations for the compatibility of different ground assemblies (GAs) and vehicle assemblies (VAs). The standard requires that all GAs

rated for a large airgap be compatible with VAs with equal or less airgap or "Z-class" rating. Likewise, GAs and VAs of different power levels should be downward compatible with all lower power units, the power level being constrained by the lowest power GA or VA in each instance. The three classes of airgap, airgap compatibility matrix, and the power class compatibility matrix are given in Table 1.1. The standard also contains a specified misalignment tolerance of +/- 7.5 cm in the driving direction and +/- 10 cm in the transverse direction and the position of the GA within a parking space [24].

The standard also addresses compatibility among different types of coil geometries. The coil geometries overviewed in J2954 are reproduced in Figure 1.5, the main two being the Double-D (DD) and rectangular coil type [24]. Even at low power levels, the interoperability and alignment of these different coil shapes can be difficult. For example, the standard implements an offset for the case of a GA with a DD coil and a VA with a rectangular coil such that the rectangular VA is aligned over one half of the DD coil. This compatibility has been validated up to 11 kW [26], but with challenges of heating and stray field stemming from the lack of compatibility between DD and rectangular coil types. These issues will only worsen at high power levels. The advantages and disadvantages of these different types of coil shapes will be reviewed in Chapter 2.

1.3.2 Stray Magnetic Fields

To achieve higher power levels in wireless systems, the total amp-turns passing through the coils increase and stronger electromagnetic fields are created. However, to be automotive-compliant in the US and European markets, these fields cannot exceed regulatory limits. The public exposure magnetic field limit set by the International Commission on Non-Ionizing Radiation Protection (ICNIRP) 2010 standard is 27 µT(rms) in the frequency range of 3 kHz – 10 MHz as illustrated in Figure 1.6a [27]. These field limits are well below what would be required to significantly heat flesh or metallic objects. Instead, the limits are intended to reduce phenomena such as nerve stimulation and retinal disturbances such as phosphenes and long-term exposure [27]. In SAE J2954 this equates to a 27 µT(rms) field limit outside the vehicle extents and within the vehicle in the 85 kHz frequency range of 79-90 kHz as in Figure 1.6b. The same limit also applies to the operating frequencies of most WPT systems

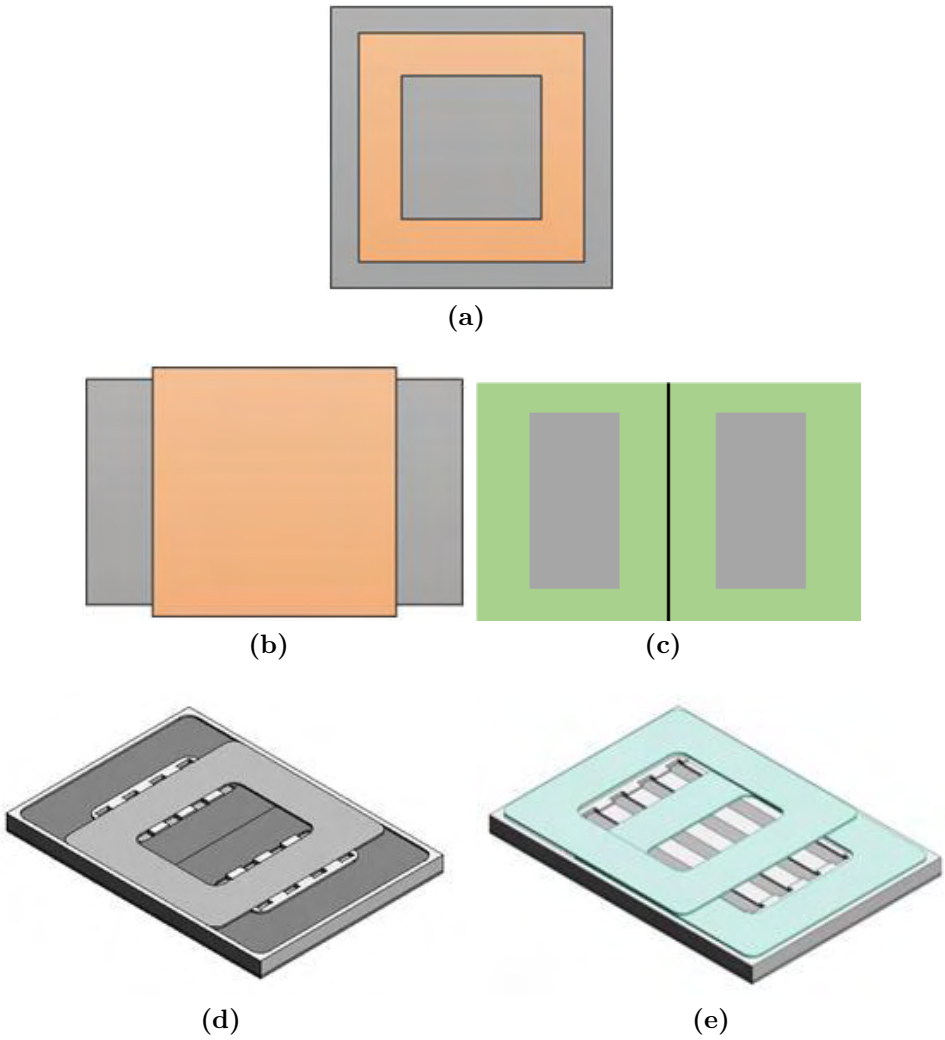

Figure 1.5: Types of coil geometries given in SAE J2954: (a) Circular/square non-polarized, (b) Solenoid polarized, (c) Double-D (DD) polarized, (d) multi-coil Double-D Quadrature (DDQ), (e) multi-coil Bipolar Pad (BPP) [24].

in the literature: 22 kHz-150 kHz. Lower limits than this do exist in some standards. For example, the American Association of Medical Instrumentation (AAMI) suggests an even lower limit of 15 µT(rms) for pacemaker compatibility and the ICNIRP 1998 magnetic field limit of 6.25 µT(rms) is still referenced in some standards in the 85 kHz frequency range [24]. However, the 27 µT(rms) limit is used as the stray field limit in most publications and will be used as the reference value in this work.

1.3.3 Foreign Object Detection

Within the limits of the GA, large alternating magnetic fields may be present. These fields will induce eddy currents on any conductive object that is present in the extents of the GA. Small objects such as coins, paper clips, foil wrappers, and others can all be heated to high temperatures if exposed to these fields. Objects that are magnetic and conductive, such as steel screws with magnetic alloys, are especially poor in this regard, as illustrated in Figure 1.7. Likewise, any nonmetallic object or living creature under the EV during system operation may be exposed to fields beyond the stray field limits detailed previously. Because of this, foreign and living object detection under the vehicle is essential.

These factors have led to a variety of detection technologies with sensing algorithms based on changes in resonant tanks, sensing coil arrays, thermal image processing, and motion detection [28]. If a foreign or living object is detected, shut down of the WPT system is required. Tests for this functionality usually include placing several test objects around the area of the GA [24]. For many WPT systems, adding additional hardware such as thermal cameras and motion detectors has proven effective in detection of both metal and living objects. These solutions are likely required in higher power systems as many passive-based approaches based on system parameter estimation may have trouble detecting small changes in loss in higher power systems. For example, it takes under a watt of power to heat the foil or copper coin in Figure 1.7a to 44°C, the minimum burn temperature.

Table 1.1: SAE J2954 Compatibility Requirements

Z-class	VA Ground Clearance Range (mm)			
Z1	100-150			
Z2	140-210			
Z3	170-250			
Ground Clearance Compatibility Matrix				
	Z1 VA	Z2 VA	Z3 VA	
Z1 GA	O	X	X	
Z2 GA	O	O	X	
Z3 GA	O	O	O	
Power Class Compatibility Matrix				
	3.7 kVA VA	7.7 kVA VA	11 kVA VA	22 kVA VA
3.7 kVA GA	O	O	O	O
7.7 kVA GA	O	O	O	O
11 kVA GA	O	O	O	O
22 kVA GA	O	O	O	O

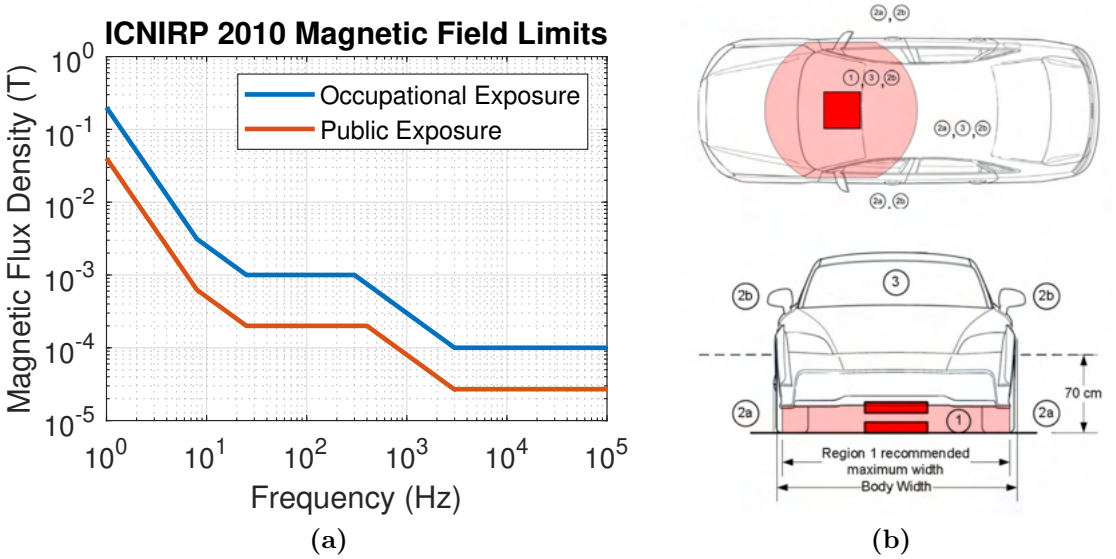

(a) (b)

Figure 1.6: Examples of field limit standards: (a) ICNIRP 2010 magnetic field limits [27]. (b) Top and front view of field regions in SAE J2954 [24].

1.3.4 Electromagnetic Interference

As with all electronic devices and chargers, WPT systems must comply with all electromagnetic interference (EMI) and electromagnetic compatibility (EMC) regulations and directives for both radiated and conducted forms of noise. These apply at the nominal power transfer frequency, but are especially important at higher frequencies. For example, the harmonics of a 85 kHz inverter square wave in a WPT system can interfere with radio communications and not comply with Federal Communications Commission (FCC) regulations within the United States. This non-compliance would prevent the production and sale of the WPT system. Many of these regulations refer to several international standards such as CISPR 11, from the International Special Committee on Radio Interference, that provide specific limits and testing methods to ensure that electronics do not interfere with radio communication through radiated EMI or cause interference with other connected electronic devices through conducted EMI [29, 30]. In CISPR 11, high-power public wireless charging systems with an AC mains connection greater than 22 kW are considered Group 2, Class A devices. The lower-power systems for residential use are considered as Group 2, Class B devices [31]. The magnetic field limits for the radiated magnetic field at a distance of 10 m for these two groups are plotted in Figure 1.8.

There are also grid-related power factor and EMI requirements, especially for systems at high power levels. These standards commonly require less than 5% total harmonic distortion (THD) in the grid input current and high power factors (PF) [32]. Meeting these standards often requires power factor correction (PFC) rectifiers and grid-side filters. These stages are commonly present in conventional fast-charging stations connected to the grid and are largely decoupled from the WPT system by the DC-link capacitor before the HF inverter as in Figure 1.3. Therefore, in this work, the design of the high-frequency inverter, compensation components, inductive coils, and vehicle-side power electronics is considered independently from the EMI requirements of the grid and the PFC rectifier design. Instead, the type of PFC rectifier and grid voltage inform the design specifications at the system level, such as the range of DC link input voltages of the high frequency inverter of the WPT system [32].

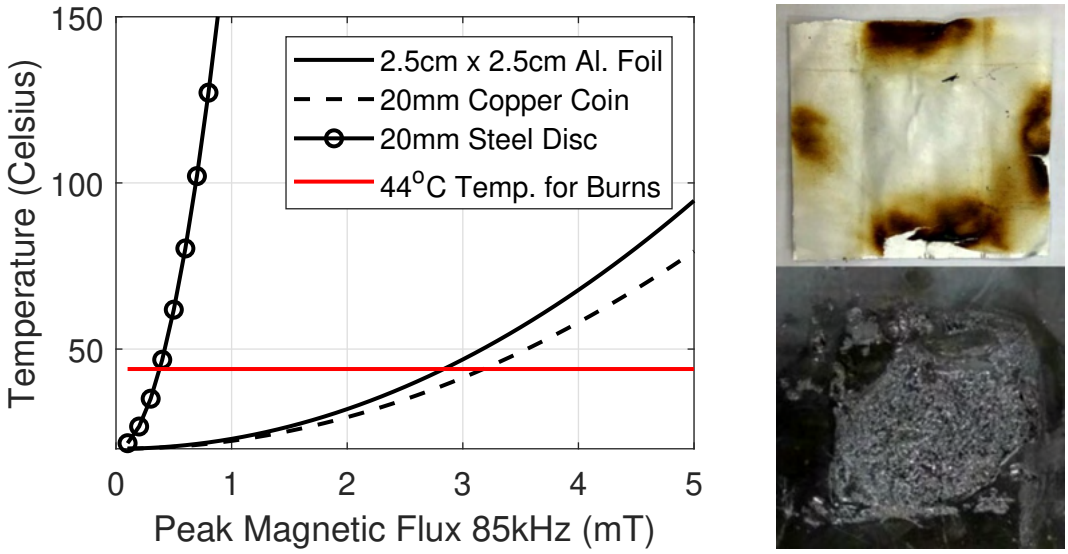

(a) (b)

Figure 1.7: The inductive heating of objects: (a) Steady-state temperatures of objects exposed to orthogonal 85 kHz magnetic field under room temperature ambient conditions with a heat transfer coefficient of 10 W/°K m^2. (b) Burned foil-backed paper and melted plastic on surface of a GA [28].

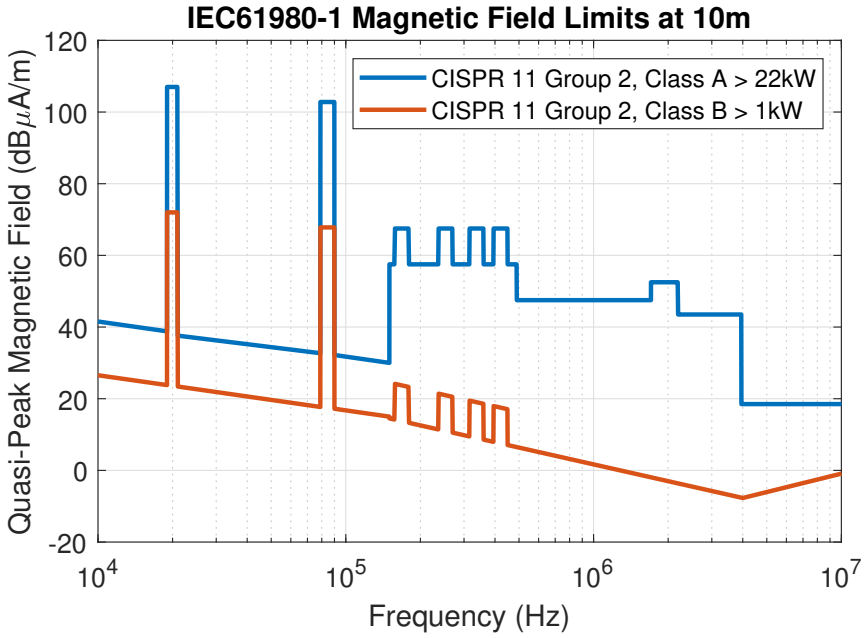

Figure 1.8: Quasi-peak radiated magnetic field limits at 10 m for WPT Systems using the CISPR 11, Group 2 Equipment Classifications [30]. As in the IEC61980-1 standard, an allowance of 10 dB is added for the range of the second through fifth harmonics of WPT systems using the nominal 79 kHz to 90 kHz operating frequency. At 85 kHz, the limits are 67.8 dBμA/m and 102.8 dBμA/m, respectively, for Class B and Class A, Group 2 devices.

Summary

To enable high-power inductive wireless charging, additional research must be done to meet the efficiency, stray field, and performance requirements. Although WPT presents a compelling user experience and greater flexibility for opportunity-charging, several compatibility, compliance, and standardization challenges must be overcome to achieve power levels similar to DC conductive fast charging. Many of these concerns are present in other charging installations, but many are specific to WPT. Coil geometry compatibility, misalignment, foreign object detection, stray field, and EMI magnetic field limits are all considerations for WPT that are more difficult than in conductive systems. The cost and weight of WPT relative to conductive charging must also be considered. These barriers have motivated many works in the literature, as will be reviewed next.

Chapter 2

Literature Review

Inductive WPT research has grown greatly in recent years, with higher-power systems being demonstrated every year and a growing multitude of subtopics. Inductive wireless power transfer is useful for a variety of applications, but this review will mainly cover inductive WPT systems designed for the automotive and transportation industries. These systems have been proposed as a solution to meet the requirements and overcome the technological barriers detailed previously. Capacitive WPT systems have also been proposed, but are limited by the need for high frequencies and voltages compared to inductive WPT [33].

In inductive WPT systems, the fields generated by the coils decay rapidly across the airgap at a rate inversely proportional to the coil area. This decay relates to the coupling coefficient of the coils, or the ratio of how much flux passes through the coil across the airgap versus the self-flux passing through the driving coil. In general, coils with larger areas have fields that decay more gradually than fields with smaller areas. Because of this, the coils must be sized such that their diameter or geometric mean length (GML) is large compared to the airgap. Therefore, comparing the efficiency and coil sizes of systems with varying airgaps must be given in the context of their airgaps to provide a fair comparison as proposed in [34, 35].

In Table 2.1, the systems in the literature are compared with the 6.6 kW and 120 kW proof-of-concept demonstrators of this work. Likewise, as stray fields are a function of the total amp-turns of the coil structure, the stray field and power level are compared by dividing the square root of power level by the stray field at 80 cm. The power density of systems is

also compared in terms of coupler-area and gravimetric power density, where the gravimetric power density includes weight of the VA coil conductors, ferrite, enclosure, and capacitor bank without the rectifier or onboard DC/DC as given in most publications. As the GML of coils is fixed with respect to the airgap to achieve high efficiency, the area-related power density of low-power systems is often lower than high-power systems.

The power density of the inductive systems in Table 2.1 includes components that perform the function of less than half of a conventional isolated DC/DC converter, making direct comparisons to On-Board Chargers (OBCs), conductive DC fast chargers, and others more difficult. In conductive DC fast charging systems, power is transferred directly to the battery without the need for additional onboard components and weight. Therefore, the weight or size of the isolated DC/DC converter is not critical as the isolated DC/DC converter or isolation transformer is located within the DC fast charger enclosure or interface [10]. On-board chargers (OBCs) are optimized for cost, size, and weight, but also typically contain a front-end rectifier and an isolated DC/DC converter and are at lower power. Nevertheless, the Department of Energy 2025 target power density for on-board chargers, including the front-end rectifier and complete isolated DC/DC stage, is 4 kW/kg and 4.6 kW/L with isolated DC/DC stage efficiency above 98% [36]. Inductive charger VAs are also located onboard the vehicle, making similar cost, size, and weight targets necessary. Similar power density targets for WPT VAs, which perform a function similar to the rectifier and transformer secondary of an isolated DC/DC converter, or around half of an isolated DC/DC converter, would easily be 8 kW/kg and 9.2 kW/L or more. The power densities of the state of the art systems in Table 2.1 are much lower than this 8 kW/kg figure, under 4 kW/kg and 250 kW/m^2.

2.1 Coil Geometry Design

There has been significant research and experimentation on the geometry of WPT coils. The geometry affects virtually every performance metric of the WPT system, such as efficiency, stray field, and misalignment performance. For high-power systems, such as those in Table 2.1, these main coil geometries can be divided into two primary categories: unipolar

coils, such as circular and rectangular coils; and bipolar coils, such as the Double-D (DD) coil, and recently the three-phase bipolar coil. Images of these coils are shown in Figure 2.1.

The bipolar coil shape was introduced in the literature as an alternative to the unipolar or circular shape in [37]. This shape is the planar layout of the solenoidal polarized coupler or flux-pipe of Figure 1.5b. In [22, 37], the unipolar coil flux path is compared to an E-type core shape and the bipolar is compared to a C or I-core. In general, comparisons between the two shapes have claimed that a lower amount of stray field per unit power is possible for the bipolar coil shape than the unipolar coil shape, but higher efficiency and power density is possible for the unipolar shape [38, 39, 40].

In [38], an iterative FEA comparison of the two coil structures is performed over given geometric variables such as the width and length of the coils and the inner width of the bipolar windings. It is concluded from the results that the Double-D (bipolar) coil has lower coupling, area, and weight-related power density, but the stray field at a fixed reference point was a factor of two lower for the Double-D (bipolar) compared to the rectangular (unipolar) design. However, the location of this measurement point is quite important.

As detailed in [41, 40], the stray field is only minimized on the short axis of the DD while it increases on the long axis of the coil in the direction of the poles. This knowledge is convenient for designers in instances where the field must be reduced on specific axes, such as preventing fields on the sides of vehicles. The DD geometry cannot prevent fields in the orthogonal direction, such as towards the front bumper of the vehicle in a DD WPT system placed near the front axle of a vehicle with the long axis of the coil oriented in the direction of travel. Furthermore, the stray fields of DD or bipolar coils are mainly oriented in the X-Y plane horizontal to the ground, reducing the effectiveness of aluminum shielding [40, 42].

In [41], an polyphase version of the bipolar coil geometry was proposed, producing the three-phase bipolar coil as shown in Figure 2.1d. In this study, FEA simulations were performed to compare coil shapes such as circular, bipolar, and three-phase bipolar coils with the same circular extent in terms of the stray field, ferrite thickness, ferrite flux density, and others. The stray fields from the three-phase bipolar coils are similar to the fields of the bipolar coils, but revolve each period such that the field at any radial point resembles the peak field from a bipolar structure when excited by three-phase currents. This allows the

Table 2.1: State of the Art WPT Systems in Literature and Demonstrators of this Work

Institute/ Company	Power Level	Airgap (mm)	Coil Dimensions (Airgap/GML)	Stray Field at 0.8m - X, Y ($kW^{0.5}/\mu T$)	Efficiency	Freq. (kHz)	Coil Shape	Power Density
ETH Zurich [22, 38]	50kW	160	0.760m x 0.410m (0.286)	N/A, 22.5µT (N/A, 0.31)	95.8% DC/DC	85	Rect.	160kW/m^2 2.0kW/kg
ETH Zurich [22, 38]	50kW	160	0.760m x 0.410m (0.286)	N/A, 12.5µT (N/A, 0.57)	95.3% DC/DC	85	DD	160kW/m^2 2.0kW/kg
Fraunhofer [43]	22kW	135	0.60m x 0.60m (0.225)	N/A	91% System	105	Circular	61kW/m^2 2.0kW/kg*
Warwick [44]	50kW	200	0.75m x 0.3m (0.422)	N/A	89% System	85	DD	222kW/m^2
Auckland [45]	50kW	210	0.620m x 0.605m (0.343)	At (7.5cm, 10cm) N/A, 28.6µT (N/A, 0.25)	At (7.5cm, 10cm) 93.7% DC/DC	85	Rect.	133kW/m^2
ORNL (DD) [16, 42]	120kW	125	0.876m x 0.673m (0.163)	At 11kW 19.1µT, 12.3µT (0.17, 0.27)	97.1% DC/DC	25	DD	203kW/m^2 2.28kW/kg*
ORNL (3Φ) [41]	50kW	150	0.544m x 0.471m (0.296)	N/A, 34.7µT (N/A, 0.20)	95.1% DC/DC	85	3Φ-DD	195kW/m^2 3.65kW/kg*
6.6kW Demonstrator	6.6kW	125 210 250	0.71m x 0.536m (0.203) (0.340) (0.405)	1.8µT, 1.4µT (1.43, 1.84) 4.4µT, 3.6µT (0.58, 0.71) 6.5µT, 4.5µT (0.40, 0.57)	97.6% 95.6% 93.1% DC/DC	86.5	Shielded Rect.	17.4kW/m^2 0.81kW/kg
Gen. 2 120kW Demonstrator	120kW	125	0.42m x 0.54m (0.262)	3.4µT, 3.5µT (3.26, 3.14)	97.2% DC/DC	89	Shielded DD	530kW/m^2 4.1kW/kg

*These works do not include the weight of their resonant components in their reported weights.

peak flux magnitudes in the coil ferrites to be more-uniformly distributed than the bipolar shape, potentially reducing the thickness of the ferrite. This dramatically increases the power density of the shape relative to other shapes but requires a three-phase inverter and rectifier. Given the reduction of peak current per phase, the stray field of the system is reduced, but each phase still demonstrates similar behavior as other bipolar coils.

2.2 Shielding Design for Stray Field Reduction

Several papers have proposed adding additional conductors, winding turns, and materials to reduce the stray field of the WPT system. An overview of these methods is shown in Figure 2.2. In general, the methods can be practically divided into two categories: additional shielding turns that are either actively driven or shorted, and the addition of magnetic or conducting materials to redirect or block fields. In [46], the arrangements of driven and shorted litz wire shielding turns are reproduced in Figure 2.2a. In the driven configuration, the shielding turns are connected in series with the coil windings so that the shielding current is the same as the coil current. In the shorted arrangement, the wire turns are shorted such that current is induced in the wire loop to oppose the change of flux through the loop, making the shielding current independent from the coil current. These loops can be split into separate structures on either side of the coil as proposed in [47]. The ring shields of [46, 48] are a special case of the shorted shield, where the number of turns in the coil is equal to one. The relative losses of these methods have been shown to depend on the conductivity of the conductor. In [46, 49], the use of litz wire was found to be more efficient than solid copper or aluminum ring shields. As in Figure 2.3, at 85 kHz and the 22-150 kHz frequency range of interest for most EV WPT systems, litz wire has reduced resistance compared to solid wire with similar cross sections due to reduced skin effect loss. Therefore, for a given shielding current at WPT, the use of litz wire for shielding turns will likely yield lower losses than other shielding methods for EV WPT chargers.

The other class of shielding methods involves the study of placing magnetic and conductive material around the coil. The conductive materials produce eddy currents opposing changing magnetic fields, similar to the shorted-turn shielding method. Magnetic

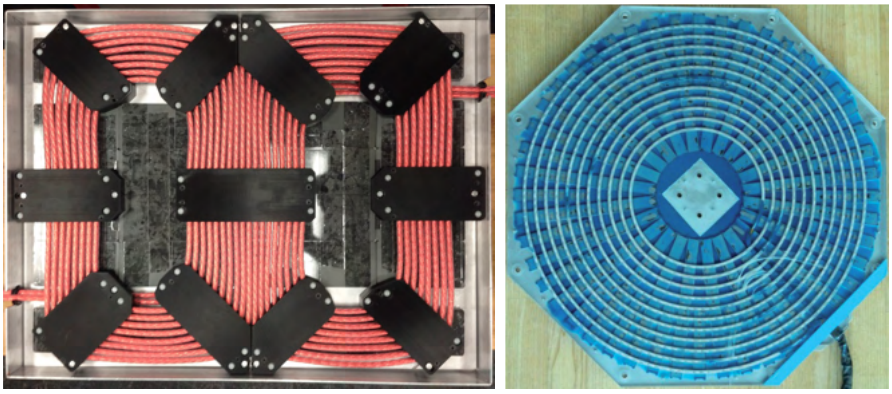

(a) (b)

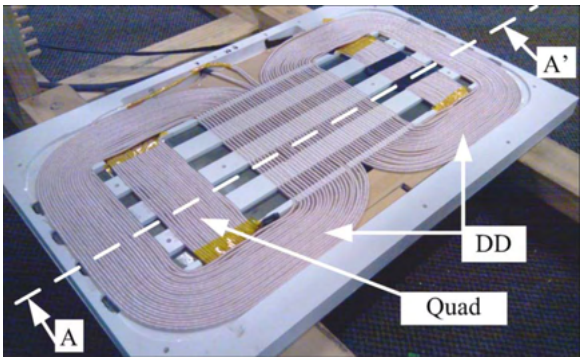

(c)

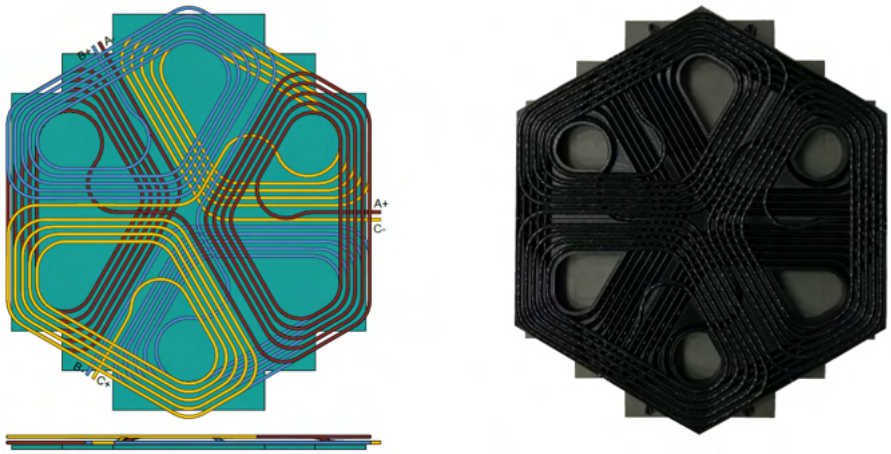

(d)

Figure 2.1: Examples of coil geometries within the literature: (a) ORNL Double-D (DD) type coil [16, 42]. (b) Circular coil [43]. (c) Photo of DDQ coil [37]. (d) Layout and photo of a 50 kW three-phase bipolar coil designed by ORNL [41].

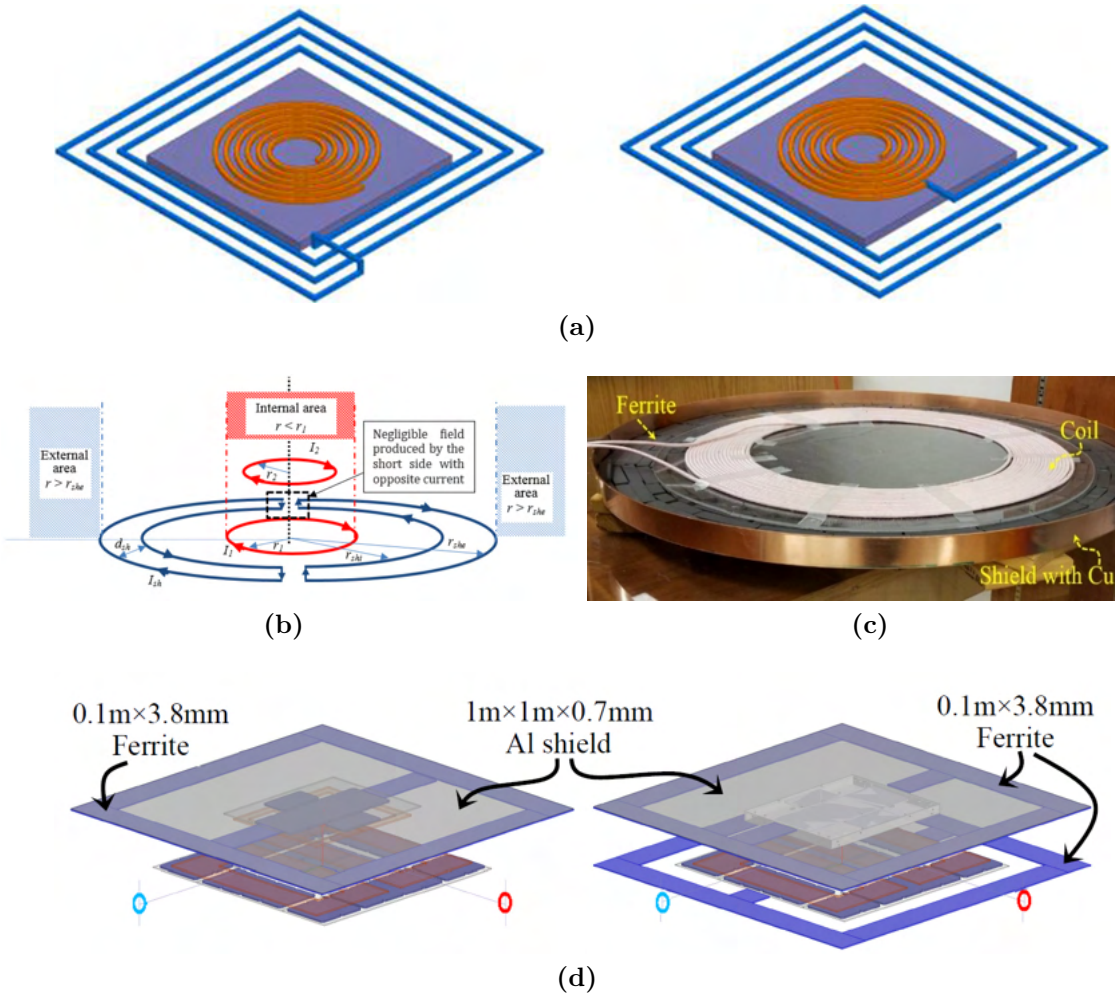

Figure 2.2: Examples of shielding methods in the literature: (a) Driven and shorted litz Wire [46]. (b) Split driven shield [47]. (c) Coil with copper ring [48]. (d) Ferrite and aluminum shield of DD coil [42].

materials modify the equivalent permeability of magnetic paths in the wireless links, ideally attracting the fields away from the exterior of the system. For the EV application, conductive materials will be present in the region around the WPT system, such as the steel frame or aluminum underbody of the EV. In SAE J2954, a 1 m $\times$ 1 m $\times$ 0.7 mm aluminum sheet is given as the model for a EV aluminum underbody for benchtop field testing [24]. Although this reduces the field for unipolar structures such as circular or rectangular coils, the presence of aluminum has been shown to increase the stray field of a DD or bipolar coil [42]. This is resolved by adding ferrites around the coil structure in VA and GA as in Figure 2.2d. In [50], adding vertical walls of ferrite "teeth" to the WPT coils was somewhat effective in reducing the stray field, but it reduces the effective airgap of the system.

Although these shielding methods have proven effective in reducing the stray field of WPT systems, the effect on the power density or weight of the system must be considered. Shielding turns will increase the effective area of a GA or VA, reducing the area-related power density. Likewise, adding additional metal or ferrite sheets past the normal coil extents can greatly increase the weight and cost of the coils and reduce the gravimetric power density. Ultimately, the VA is placed on an EV including the weight and area of all shielding materials used in the VA. Therefore, shielding should be considered inherently as part of the coil geometry, cost, area, and weight and not optimized separately.

2.3 Conductor Selection

Low-resistance conductors are critical for high-efficiency WPT, especially as the airgap increases and the coupling coefficient of the system decreases. As detailed later, the high operating frequencies of WPT systems cause current to crowd the edges of the conductors and increase the AC resistance of the conductors above the DC resistance of the conductors [51]. To avoid this effect, most of the systems rely on conductor strand diameters sized to be less than the skin depth at the operating frequency with the use of litz wire, such as in all the systems in Table 2.1. A comparison of the AC resistance of litz wire compared to solid wire is shown in Figure 2.3.

Commercially available litz wire can be obtained with strand diameters of 30 µm or 50 AWG, but with increases in cost and manufacturing difficulty. As the strand size decreases, the ratio of insulation material to conductor and the overall cost of the wire becomes greater. Strand breakage can also become an issue in very small strand diameters. A tradeoff of the cost and loss of litz wire in [52] found that the optimal increase in AC resistance over DC resistance considering cost ranged from 1.045 to 1.737 for strand sizes of 32 AWG to 50 AWG, respectively. The proximity effect increase in AC resistance is sensitive to both the internal and external fields on the litz wire conductors. The internal fields can be found as functions of the current, but external fields vary depending on the coil geometry in WPT systems. Implementation of this sort of conductor optimization in the context of WPT coil design is essential to reduce both cost and loss.

2.4 Magnetic Material Design

Magnetic material can constitute a large part of the total weight of coil assemblies. The desired thickness and loss of the magnetic material are a function of the coil geometry and the flux density in the material. For a given thickness of magnetic material, the flux density must be less than the saturation flux of the material and low enough to limit hysteresis loss and heating. In [38], the number of ferrites backing the coil was parameterized in an optimization to show the effect on efficiency and gravimetric power density for rectangular and Double-D shapes. In [53], the thickness of the core was varied and optimized depending upon the coil geometry to reduce ferrite volume relative to a constant-thickness ferrite sheet. This was accomplished by introducing a linearly increasing thickness of ferrite such that the ferrite thickness underneath the densest area of the coil geometry was maximized. In [54], a ferrite-less Double-D pad with a reflecting coil was investigated for roadway application GAs for reduced weight and cost. However, lower coupling and efficiency was found compared to those of the full-ferrite solution, making the solution less practical for high-power systems.

Currently, MnZn ferrite is used as the magnetic material in most WPT systems, such as in all of the systems in Table 2.1 where the ferrite material is listed [16, 22, 38, 41, 42, 44]. There also are examples in the literature of implementing nanocrystalline core material in

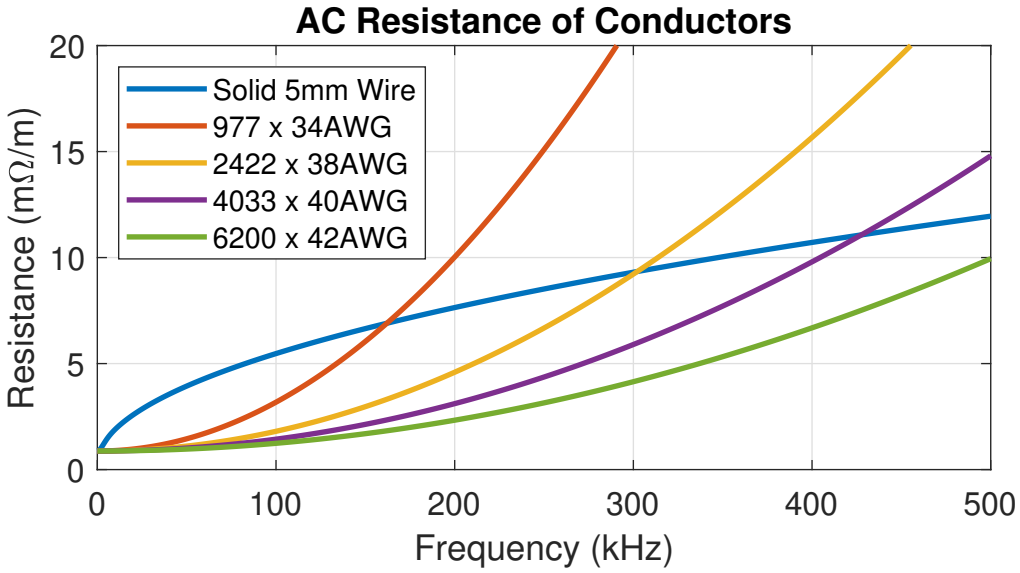

Figure 2.3: Ideal AC resistance of different conductors of the same copper area over frequency considering skin and litz wire internal proximity effects.

Table 2.2: Overview of Common Magnetic Materials [51].

Material Name	Initial Relative Permeability	Saturation Flux (T)	Resistivity (Ω-cm) at 20°C	Curie Temperature (°C)
MnZn Ferrite	1000-4000	0.4-0.8	0.5-10^3	150-220
NiZn Ferrite	150	0.3	10^3-10^7	300
Fe-Based Nanocrystalline	15000-150000	1.2-1.5	1.2× 10^{-6}	600
80% Ni - 15% Fe Permalloy	12000-100000	1.5	50× 10^{-6}	460
50% Co - 50% Fe Supermender	10000	2.3	35× 10^{-6}	950

bipolar-type coils [55, 56]. This would be attractive given the high saturation flux density and permeability of the material. However, the high conductivity of the nanocrystalline material creates large losses and eddy currents when the flux is orthogonal to the lamination layers of the material, which is often unavoidable in planar coils, especially when considering misalignment conditions. These additional losses may negate any possible improvements in coupling or weight relative to ferrite. In general, any high-conductivity magnetic material may face this sort of problem in WPT, such as in Table 2.2. This and high costs have precluded the use of several novel magnetic materials with higher saturation flux or permeability.

2.5 Thermal Modeling and Cooling of WPT Systems

As the power level of the WPT systems increase, so do the losses in the power electronics, conductors, and magnetic materials. If these losses are not dissipated through cooling, the temperatures of components of the WPT system will increase. If temperatures exceed the limits of the materials, such as the temperature ratings of semiconductor switches, wire insulation, or enclosure materials, the system can be compromised. Below these ultimate limits, other thermal effects such as thermal cycling stress and increases in conductor resistance must be considered for their impact on reliability and efficiency.

For many low-power WPT systems, passive cooling or forced air cooling is enough to effectively cool the system. In [22, 38, 44], the systems are cooled either by passive or forced air cooling. However, forced or passive air-cooling may not be possible or attractive for automotive applications. In [57], burying a coil in sand significantly reduced passive cooling, leading to high operating temperatures. In the context of roadway WPT systems under asphalt, similar thermal issues were seen in the design of a 200 kW dynamic WPT system, leading to very high asphalt surface temperatures [58]. Further modeling and validation of the temperature distribution for a 6.6 kW system was considered in [59], but did not discuss active cooling options for high-power systems. The enclosure of WPT coils in thermally conductive epoxy is proposed as a possible route to improve the thermal characteristics of

the WPT system [58, 60], but will also be limited by the low heat transfer coefficient of passive air cooling if no other cooling is implemented.

In [16, 41], liquid cooling is used for the inverter and rectifier, but not for the coil. Liquid cooling loops are already present in DC fast charging stations and in most EVs as the preferred cooling solution for the battery, drive inverter, and on-board power electronics due to its high thermal conductivity and heat capacity compared with air-cooled systems [4]. Research into the integration of liquid cooling the coil conductors and ferrite seek to capitalize on this for inductive coil assemblies, but requires detailed modeling of the thermal conductivity of litz wire, ferrite, and thermal interface materials. The placement of coolant loops within the GA and VA must be done carefully: metal tubing exposed to alternating magnetic field will induce eddy current losses and additional heat. Additionally, automotive liquid cooling systems typically use a mixture of glycol and water as a coolant circulated through the vehicle to cool the battery pack, onboard chargers, drive inverter, and motors. In many electric vehicles, the cooling loop is actively cooled by the compressor and refrigerant loop to regulate the temperature of the coolant. However, the inhibited glycol-water coolant used in electric vehicles often contains and accumulates impurities through corrosion and is too conductive for direct contact with electrical parts [61]. This issue is also present in the design and maintenance of induction heating systems where low conductivity water is circulated through copper tubing [62]. In electric vehicles, this need has lead to the use of a heat exchanger interfacing the glycol coolant loop with an oil or another dielectric fluid if direct, non-insulated cooling is required as in [63] with additional costs, part count, and complexity.

Therefore, in automotive wireless power transfer, insulating the coolant loop from the power electronics and resonant tank is attractive from a design standpoint. This sort of indirect cooling places potting materials, ferrite, or litz wire in the primary heat transfer path. Heat transfer of a similar path is analyzed in [64], where the transverse thermal conductivity of the litz wire is shown to vary according to the bundling and number of strands, and is on the order of 1-2 W/(m-K)– much lower than the thermal conductivity of copper. Several other elements such as insulation requirements, coolant type, costs, and others must be included for successful automotive design.

2.6 Electromagnetic Interference Reduction

The need to comply with EMI/EMC standards worldwide has brought about several approaches to reduce the conducted and radiated EMI of WPT systems. These approaches include coil geometry design, multiphase operation, filter design, and inverter modulation. A summary of these methods is given in Figure 2.4.

Coil geometry optimization for reduced radiated EMI has been similar in nature to shielding research to reduce the stray fields to meet ICNIRP and other safety standards. In particular, the use of adjacent rectangular coils driven with opposite phase has been shown to reduce both radiated and conducted EMI. In [65, 66], measurement of an electric bus WPT system with two transmitters driven in opposite phase reduced the radiated EMI by around 30 dB [26]. The same authors also found that this arrangement reduced the third-harmonic conducted EMI around 20 dB compared to the in-phase power transmission of the same system [67]. This result was also found in [18] for a 260 kW modular bus system.

The impact of coil design has also been considered. In [26], as in Figures 2.4b, 2.4c, the SAE J2954 reference designs for DD coils and rectangular coils were tested for stray field and radiated EMI compliance. Here the DD coils and interoperability tests of rectangular and DD coils operating at 11 kW and 210 mm and 250 mm airgap actually fail to meet the 10 m CISPR 11 Class B residential limit in Figure 1.8 of 67.8 dBµA/m within 79 kHz to 90 kHz at optimal alignment. Only the tests of rectangular coils at 11 kW met the CISPR 11 Class B limit with approximately 5 dBµA/m at maximum misalignment. However, all coil types met the extended 82.8 dBµA/m for 11.1 kVA systems suggested in SAE J2954. Multiphase coils have also been proposed to reduce EMI. In [68, 69] a three-phase system for drone charging was shown to eliminate integer multiples of the third-harmonic radiated and conducted EMI. This reduction is also expected in other three-phase systems [41].

Filter design within the system has also been shown to be effective. Instead of using a single capacitor in series and parallel, researchers have proposed filter networks with additional stages. These form low-pass filters that reduce high-frequency noise faster than compensation with a single capacitor. In [70], an LCL T-network was added as a third-order filter to the resonant tank. In general, a large number of filters are possible, each with

varying effects on changing loads and misalignments [71], but additional losses, cost, and weight will limit the number of components. In particular, the LCC compensation type has been extensively studied due to its constant-current characteristics [72] and has been shown to reduce conducted EMI [73].

Finally, a variety of inverter modulation methods have been proposed to modify the spectral components of the WPT system. Spread-spectrum operation, where the inverter frequency is increased and decreased within the allowed frequency band, can be used to reduce the quasi-peak or average noise of the fundamental and its harmonics. However, it will not reduce the peak measurement value. In [76], different probability density functions for spread spectrum modulation were implemented on a 3 kW system at the cost of reduced efficiency. Spread spectrum has also been explored on 44 kW and 100 kW systems to reduced radiated and conducted EMI [67, 70, 74]. Selected harmonic elimination using inverter modulation has also been explored for wireless power transfer [69] as it has been for other applications [75]. Here, the inverter firing angles are optimized to reduce selected harmonics at the cost of additional switching actions. However, these additional switching actions will cause more loss for the higher-frequency inverters used in WPT than for lower frequency drive inverters. Similarly, frequency modulation during operation may also be unattractive to manufacturers compared to fixed-frequency operation due to regulatory requirements.

2.7 Research Gaps

In the preceding literature review, the sensitivity of several performance metrics have been linked to the coil geometry design. To achieve high power levels for public fast-charging applications, interoperability and efficient operation for different vehicle platforms' airgaps over standardized misalignment are essential. Here, the coil design has a direct impact on the coupling and power transfer efficiency. Additionally, there are several magnetic field safety and EMI regulatory standards relevant to WPT systems. Varying coil geometries, shielding methodologies, and multiphase systems have been proposed and shown to reduce both the fields at the edge of the EV and the radiated EMI. In particular, the radiated EMI requirements highlight the need to reduce the stray fields of WPT systems in all directions,

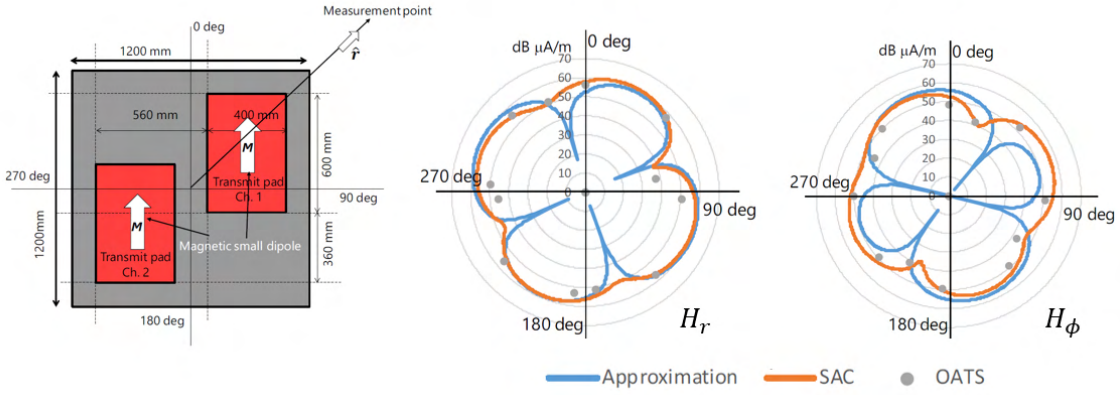

(a)

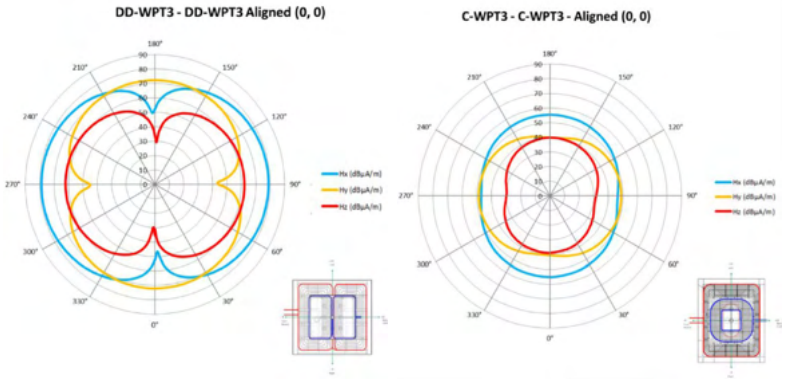

(b) **(c)**

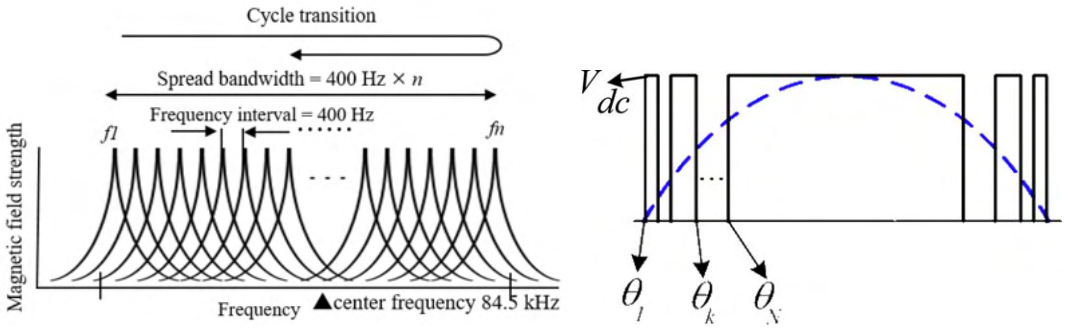

(d) **(e)**

Figure 2.4: Examples of EMI reduction methods in the literature: (a) Field patterns at 10m from a pair of pads with opposite phase [65], (b) field patterns at 10 m from DD and (c) rectangular coils [26], (d) spread-spectrum modulation [74], and (e) switching angles for selective harmonic elimination [75].

not just in the closest direction from the wireless system to the edge of the vehicle. This must be taken into account in the comparison of bipolar or DD, rectangular, and other coil geometries. However, given the large design space of possible coil geometries and design variables and the time-consuming nature of the evaluation of losses, coupling, stray field, and magnetic material flux density, the co-optimization of WPT coil design in terms of efficiency, cost, weight, and stray field has been limited.

Therefore, the following research gaps are identified to motivate the work contained in this dissertation:

- Coil geometry, magnetic material, and conductor sizing optimization to produce systems with reduced stray field, cost, weight and loss over a wide design range of coil geometries
- Flexible evaluation of fields, currents, losses and coupling for generalized coil shapes
- Fair comparison of WPT coil geometries for interoperable, standardized high-power systems
- Thermal modeling and automotive-compliant cooling implementation for high-power WPT coils

Chapter 3

Multiobjective Coil Design Using the Fourier Analysis Method

The design of WPT systems to meet specifications such as power level, coupling, airgap, misalignment tolerance, stray field, and efficiency requires the computation of the fields and inductances of various coil geometries. This is often accomplished with finite element analysis (FEA) approaches [38, 77] or analytical methods [47]. In either case, a parameterized square or circular coil geometry is defined before the design process begins, limiting the scope of coil geometries considered in the design. As reviewed, complex coil geometries such as bipolar coils and coils with shielding turns have been shown to enable higher power levels under stray field limits. However, attempting to consider all possible coil geometries, as well as other design parameters such as operating frequency, number of turns, and conductor types, results in a nearly intractable design space. With an increasing number of iterations needed, optimization with FEA-based methods that rely on brute-force iterations with full or partial 3D modeling becomes increasingly computationally expensive. Likewise, many analytical methods are pertinent only to circular or rectangular coils and are not general enough to model a wide variety of possible geometries and coil aspect ratios. This work develops a coil design methodology which is not constrained by predefined geometric templates, broadening the scope of design optimization in WPT systems.

The Fourier Analysis Method (FAM) is a promising candidate to meet this challenge. In the Fourier Analysis Method (FAM), the coil fields are designed to optimize performance

through the variation of Fourier basis function coefficients. The computed fields are then discretized into winding geometries. This allows for the rapid computation of coil conductor geometry, inductance, current, and fields. The FAM is used to develop a convenient and fast method to optimize coil geometry for given stray field and power level specifications.

3.1 Review of Fourier Basis Function Optimization for Coil Design

In general, the coil design problem is ill-poised because there are infinitely many possible current distributions on a plane that can create a given field at a distance. However, the problem can be regularized to have one unique solution when objectives such as minimum power dissipation or stored energy are considered. In general, several types of basis functions in coil geometry optimizations are possible such as triangular basis functions and Fourier basis functions [78]. However, most coil designs exhibit symmetry such that the number of sinusoidal or Fourier basis functions needed are lower, reducing matrix sizes, the number of iterations, and overall computational time.

The design of magnetic components using Fourier basis functions is already well known in the design of MRI gradient coils [78, 79], fusion devices [80], and electric machines [81, 82]. In the field of wireless power transfer, it has been used to analytically predict the fields and mutual inductance of coils. In [83], it has been used to decompose and analyze circular and rectangular filament coils bounded by magnetic or conductive media to predict their mutual inductance. Similar modeling was used to model closely spaced rectangular coils in [84, 85]. However, this work considers the application of this methodology to solve the coil design optimization problem for WPT when constrained by stray field as published in [86].

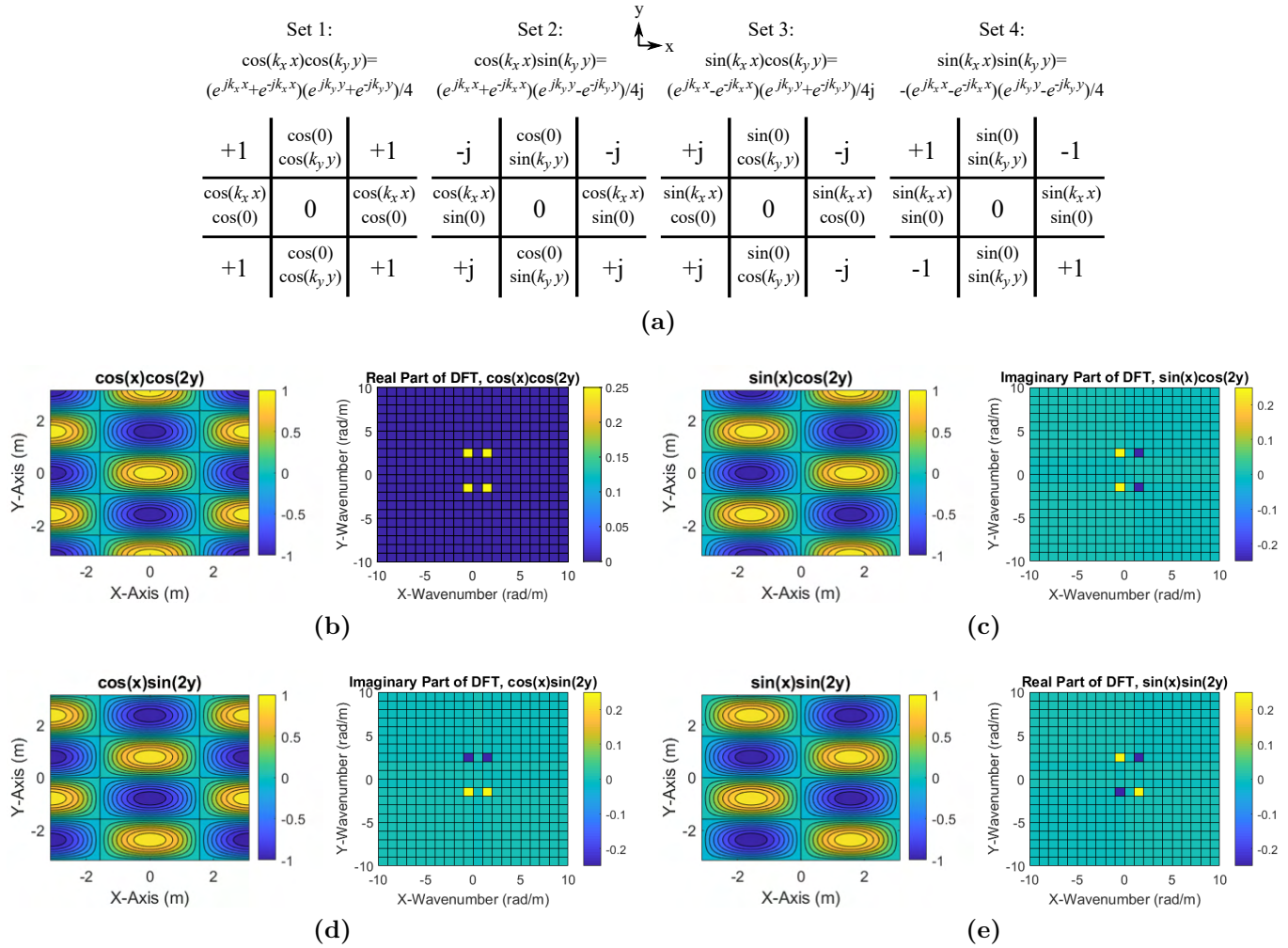

Figure 3.1: Diagrams of the 4 Basis Functions sets considered in the Fourier Analysis Method. (a) The symmetry conditions for each basis function set comprised of real and complex conjugate relationships. With these relationships, each basis function can be represented by one value in the first quadrant, limiting the number of variables and constraints needed in the optimization function. (b) Example of a $\cos k_x x \cos k_y y$ basis function. (c) Example of the $\sin k_x x \cos k_y y$ basis function. (d) Example of the $\cos k_x x \sin k_y y$ basis function. (e) Example of the $\sin k_x x \sin k_y y$ basis function.

3.2 The Fourier Analysis Method

The FAM models the scalar magnetic potential of the coil as a function of the coefficients of Fourier basis functions. These functions are two-dimensional sinusoidal functions of different spatial wavelengths in the Cartesian x-y plane. As illustrated in Figure 3.2, each basis function is defined by spatial wavenumbers k_x and k_y in the x and y-directions, in units of radians per meter. As later shown, the wavenumber in the z-direction, k_z, is a function of k_x and k_y. These wavenumbers are defined by $k = 2\pi/\lambda$ where λ is the wavelength of the sinusoidal function. The four basis function sets considered in the FAM shown in Figure 3.1 are combinations of the sine and cosine functions. In the FAM, an $N \times N \times 4$ matrix of coefficients is used as the optimization variable, where N is a positive integer representing the number of rows and columns of the variable matrix. Each $N \times N \times 1$ matrix represents the first quadrant of a basis function set. Each basis function set can be used with or independently of the others. To compute the full Fourier-domain matrix of the coil shape, each $N \times N \times 1$ matrix is multiplied and reflected according to the symmetry conditions of Figure 3.1a to create a $(2N-1) \times (2N-1)$ matrix. The summation of these matrices yields the Fourier-domain coefficients $\psi(k_x, k_y)$ of the coil shape. The scalar magnetic potential in the spatial domain, $\Psi(x, y, z)$, is the Inverse Discrete Fourier Transform (IDFT) of this matrix,

$$\Psi(x, y, z) = \sum_{m=1}^{2N-1} \sum_{n=1}^{2N-1} \psi(k_x, k_y) e^{j(k_x x + k_y y + k_z z)}/4. \tag{3.1}$$

The potentials in the x-y plane are calculated with a discretization in the x and y dimensions of dx and dy respectively.

3.2.1 Field and Current Computation

In the Fourier domain, the basis functions can be directly differentiated or integrated to obtain algebraic relationships between the potential Ψ and the field $\boldsymbol{B}$ by the relationship $\boldsymbol{B} = \mu_0 \boldsymbol{H} = -\mu_0 \nabla \Psi$. Neglecting displacement current in quasi-magnetostatic conditions, the wavenumber k_z is derived by observing that $\nabla \times \boldsymbol{B} = 0$ in the absence of airgap currents.

Combined with $\nabla \cdot \boldsymbol{B} = 0$, the fields and potentials satisfy

$$\nabla^2 \Psi = \nabla^2 \boldsymbol{B} = 0. \tag{3.2}$$

Therefore, when real non-zero wavenumbers exist in the x and y-directions, k_z is imaginary and is

$$k_z = \pm\sqrt{-k_x^2 - k_y^2} = \pm j\gamma. \tag{3.3}$$

The magnetic potential in the airgap must satisfy

$$\frac{\partial^2 \Psi}{\partial z^2} - k_z^2 \Psi = 0 \tag{3.4}$$

which has a solution

$$\Psi(z) = c_1 e^{-\gamma z} + c_2 e^{\gamma z}. \tag{3.5}$$

The constants c_1 and c_2 are found using the boundary conditions at $\Psi(0)$ and $\Psi(z_{gap})$, yielding the relationship derived in [81]

$$\Psi(z) = \frac{\sinh \gamma z}{\sinh \gamma z_{gap}} \Psi(z_{gap}) - \frac{\sinh \gamma (z - z_{gap})}{\sinh \gamma z_{gap}} \Psi(0). \tag{3.6}$$

By differentiating this with $\boldsymbol{B} = \mu_0 \boldsymbol{H} = -\mu_0 \nabla \Psi$, the B_z field at $z = 0$ and $z = z_{gap}$ are

$$\begin{bmatrix} B_z(z_{gap}) \\ B_z(0) \end{bmatrix} = -\mu_0 \gamma \begin{bmatrix} \coth \gamma z_{gap} & -\frac{1}{\sinh \gamma z_{gap}} \\ \frac{1}{\sinh \gamma z_{gap}} & -\coth \gamma z_{gap} \end{bmatrix} \begin{bmatrix} \Psi(z_{gap}) \\ \Psi(0) \end{bmatrix} \tag{3.7}$$

For a discrete set of spatial frequencies, the fields at a distance z where $z \leq z_{gap}$ due to the potential of the primary coil varying in the x and y plane at $z = 0$, are a function of z_{gap} and $\gamma = \sqrt{k_x^2 + k_y^2}$ for ferrite backed coils as in (3.8)-(3.10). As this calculation determines the fields from the primary coil only, it is assumed that no currents are present in the secondary coil such that $\Psi(z_{gap}) = 0$ in (3.7) and the tangential fields are zero at the surface of the ferrite.

$$B_x(x,y,z) = \sum_{m=1}^{2N-1}\sum_{n=1}^{2N-1} \frac{-\mu_0 j k_x \psi(k_x,k_y) e^{j(k_x x + k_y y)}}{4} \frac{\sinh\gamma(z-z_{gap})}{\sinh\gamma z_{gap}} \tag{3.8}$$

$$B_y(x,y,z) = \sum_{m=1}^{2N-1}\sum_{n=1}^{2N-1} \frac{-\mu_0 j k_y \psi(k_x,k_y) e^{j(k_x x + k_y y)}}{4} \frac{\sinh\gamma(z-z_{gap})}{\sinh\gamma z_{gap}} \tag{3.9}$$

$$B_z(x,y,z) = \sum_{m=1}^{2N-1}\sum_{n=1}^{2N-1} \frac{-\mu_0 \gamma \psi(k_x,k_y) e^{j(k_x x + k_y y)}}{4} \frac{\cosh\gamma(z-z_{gap})}{\sinh\gamma z_{gap}} \tag{3.10}$$

For air-core coils, the fields will be half or less as the magnetic path lengths are double or more than in ferrite backed coils. Here, the boundary condition $\Psi(z) = 0$ occurs at infinity.

$$\begin{bmatrix} B_z(z_{gap}) \\ B_z(0) \end{bmatrix} = -\mu_0\gamma \begin{bmatrix} 1/2 & -e^{-\gamma z_{gap}} \\ e^{-\gamma z_{gap}} & -1/2 \end{bmatrix} \begin{bmatrix} \Psi(z_{gap}) \\ \Psi(0) \end{bmatrix} \tag{3.11}$$

By (3.6)-(3.11), fields with higher k_x and k_y, i.e. with shorter wavelengths, will decrease in magnitude faster in the z-direction than those with smaller k_x and k_y. In short, the near-field scattering phenomenon describes how coils with larger diameters have fields that decay more slowly away from the coil surface than those of smaller coils.

The potentials of the coils are determined by currents flowing in the plane of the coil. The continuous surface currents in the x and y-direction are K_x and K_y

$$\boldsymbol{K} = \nabla \times \hat{\boldsymbol{k}}\Psi = \frac{\partial \Psi}{\partial y}\hat{\boldsymbol{i}} - \frac{\partial \Psi}{\partial x}\hat{\boldsymbol{j}} \tag{3.12}$$

$$K_x(x,y,0) = \sum_{m=1}^{2N-1}\sum_{n=1}^{2N-1} j k_y \psi(k_x,k_y) e^{j(k_x x + k_y y)}/4 \tag{3.13}$$

$$K_y(x,y,0) = \sum_{m=1}^{2N-1}\sum_{n=1}^{2N-1} -j k_x \psi(k_x,k_y) e^{j(k_x x + k_y y)}/4. \tag{3.14}$$

3.2.2 Computation of Coil Inductance, Current, and Power

With these fields and potentials, the mutual and self magnetic energies of the surface Ω, E_m and E_s respectively, are

$$E_m(\psi) = \int_\Omega \Psi(x, y, 0) B_z(x, y, z_{gap}) d\Omega \tag{3.15}$$

$$E_s(\psi) = \frac{1}{2} \int_\Omega \Psi(x, y, 0) B_z(x, y, 0) d\Omega. \tag{3.16}$$

These energy values are related to the total magnetic energy of the system,

$$W = E_{s1}(\psi) + E_{s2}(\psi) + E_m(\psi) = \frac{1}{2} L_1 I_1^2 + \frac{1}{2} L_2 I_2^2 + M I_1 I_2. \tag{3.17}$$

Assuming matched coils with $L_1 = L_2$ operating with coil RMS currents of $I_1 = I_2$, the equivalent coupling coefficient k of the system is

$$k = \frac{E_m(\psi)}{2E_s(\psi)} = \frac{\int_\Omega \Psi(x, y, 0) B_z(x, y, z_{gap}) d\Omega}{\int_\Omega \Psi(x, y, 0) B_z(x, y, 0) d\Omega}. \tag{3.18}$$

By choosing the number of turns of the coil, N_T, the conductor paths, currents, and coil shape are determined by the contours C of the continuous magnetic potential

$$I_1 = (\max \Psi(x, y, 0) - \min \Psi(x, y, 0))/N_T \tag{3.19}$$

$$C = \min \Psi(x, y, 0) + \left(0 : (N_T - 1) + \frac{1}{2}\right) I_1. \tag{3.20}$$

Equation (3.17) is used to calculate L_1 and L_2 and the mutual inductance of the system, M, once I_1 and I_2 are determined. The coil-to-coil power transfer of the system, P, is then

$$P = 2\pi f E_m(\psi) = 2\pi f M I_1 I_2. \tag{3.21}$$

3.3 Validation of Inductance and Field Models

To validate the modeling of the fields and inductance of coils with FAM, a pair of coils with extents of $x_{ext} = 0.3$ m and $y_{ext} = 0.5$ m and airgap of $z_{gap} = 0.2$ m were designed as in Figure 3.3. The potentials and fields are shown with a coil-coil power transfer of 20 kW at 85 kHz. The geometry is a three-pole field shape centered on the origin that consists of only $\cos x \cos y$ basis functions.

The contours of the magnetic potential of Figure 3.3b with $N_T = 14$ at values of C are derived and used to build the air-core coils in Figure 3.4a with 10 AWG litz wire. Inductance measurements of the coils were taken on a Keysight E4990A impedance analyzer. The inductance values from the FAM, FEA simulations, and experimental measurements are given in Table 3.1. As seen, the inductance values derived from the FAM method are within 5% of the FEA results and 7% of the measurements. The FEA simulation result of the fields is shown in Figure 3.4b. Field measurements of B_z on the surface of the coil were taken with a sensing coil 31 mm in diameter with 45 turns of 24 AWG magnet wire and are plotted in Figure 3.4c. Comparison of the model fields and inductance with the measured values demonstrates that the FAM can accurately predict the inductance, coupling, and field distribution for the complex coil shape.

3.4 Optimization of Stray Field and Current

Using the FAM, a multi-objective optimization is formulated and solved to design coil geometries with objectives and constraints based on minimizing the total current in the coil while limiting the stray field maximum outside the coil extent. Each objective and constraint are normalized to scale derivatives to similar values to assist the convergence of gradient-based solvers.

The optimization is formulated as the minimization of the surface integral of the total squared current in the coil structure, $\int_\Omega K(x,y,0)^2 d\Omega$. The surface integral

$$\int_\Omega K(x,y,0)^2 d\Omega = (||K_x(\psi)||_2^2 + ||K_y(\psi)||_2^2)/16 \tag{3.22}$$

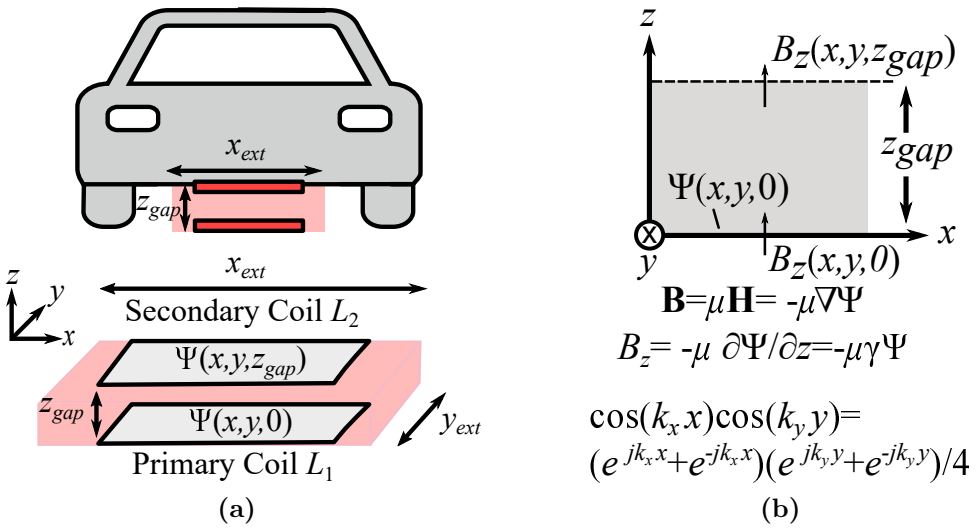

Figure 3.2: Illustrations of the Fourier Analysis Method (FAM): (a) Illustration of the EV WPT field boundaries given by x_{ext} and y_{ext}, system airgap z_{gap}, and magnetic scalar potential $\Psi(x, y, z)$ used in the Fourier Analysis Method (FAM). (b) FAM axes layout and key equations.

Table 3.1: Comparison of FAM, FEA, and Experimental Measurements with N_T =14

	Ferrite-Backed Coil		
Parameter	FAM (Continuous)	FEA (Windings)	
Self Inductance L_1, L_2	30.64 µH	31.01 µH	
Mutual Inductance M	1.31 µH	1.27 µH	
	Air-Core Coil		
Parameter	FAM (Continuous)	FEA (Windings)	Measurements
Self Inductance L_1,L_2	15.32 µH	16.15 µH	16.56 µH, 16.20 µH
Mutual Inductance M	0.32 µH	0.31 µH	0.31 µH

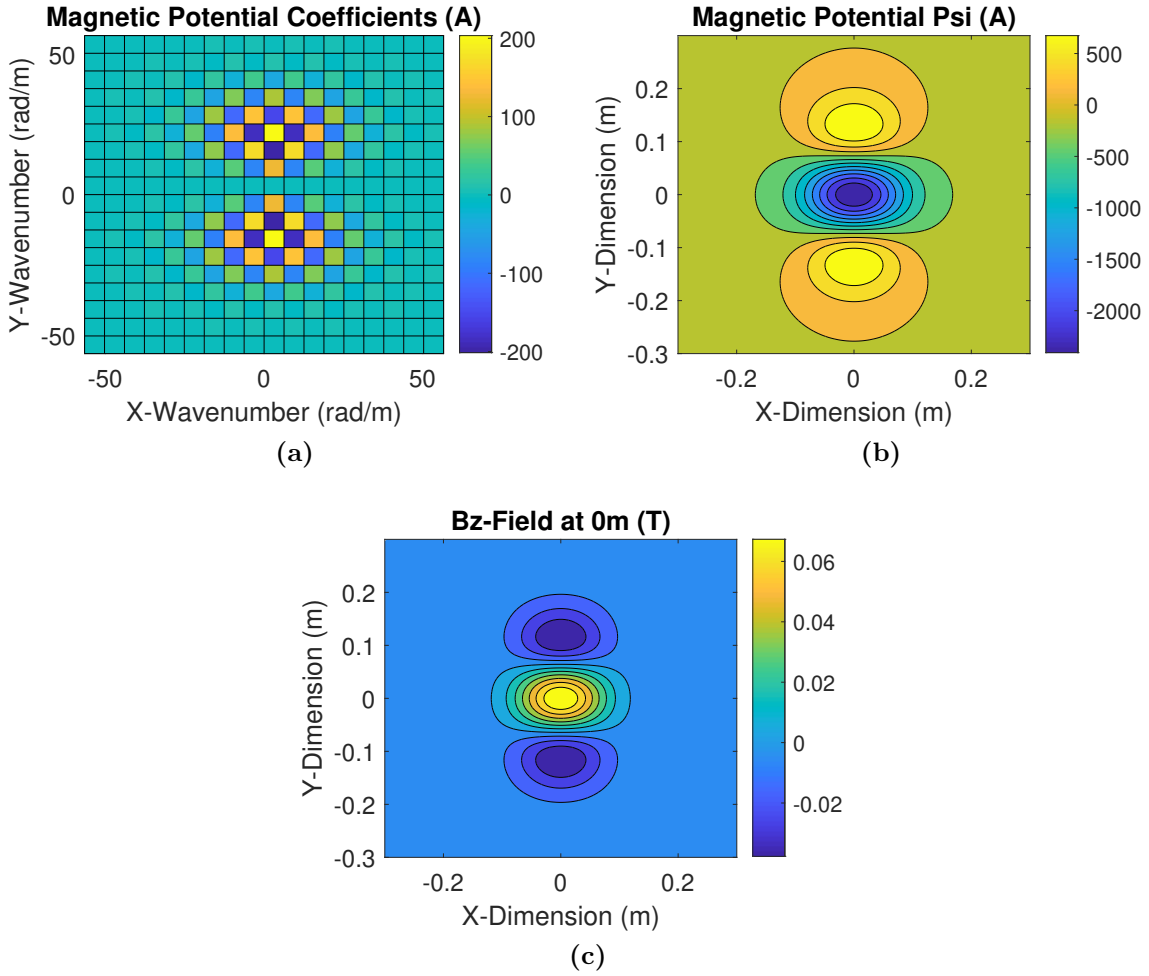

Figure 3.3: Three-pole coil shape derived from the FAM: (a) Basis function coefficients $\psi(k_x, k_y)$, (b) magnetic scalar potential, and (c) surface B_z field of one ferrite coil from the FAM with an airgap of z_{gap} =0.2 m and a coil to coil power transfer of 20 kW at 85 kHz.

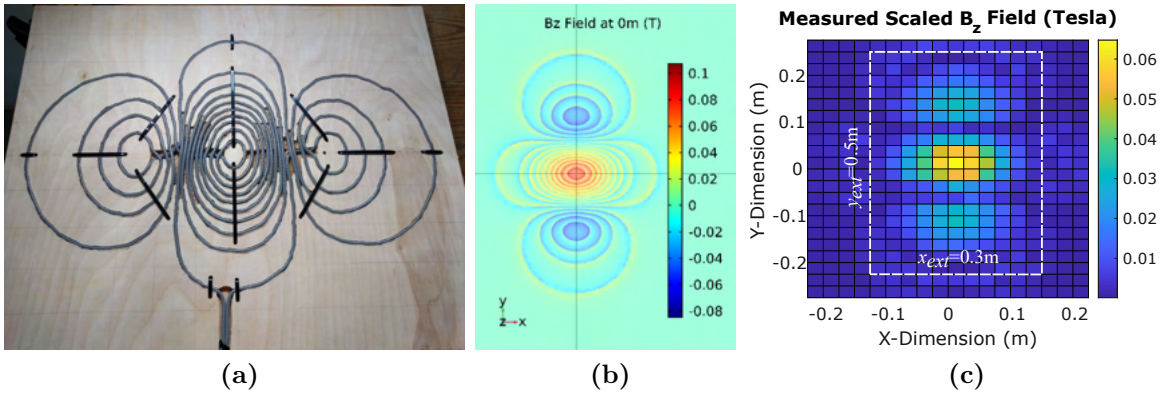

Figure 3.4: Construction and measurement of the three-pole coil: (a) Constructed air-core coil and (b) FEA simulation of the coil. (c) Scaled measured magnitude of the B_z field.

is calculated by noting that the Fourier transform is unitary. This avoids the computation of $K(x, y, 0)$ in each objective function evaluation step. The 1-norm of the magnitude of the basis function coefficient ψ is multiplied by a small value β included to eliminate small values of unused basis function sets such as $\sin 0 \cos y$ as given in Figure 3.1. In this implementation, $\beta = 0.1$. This yields the objective function

$$\frac{||K_x(\psi)||_2^2 + ||K_y(\psi)||_2^2}{16P} + \beta \frac{||\psi||_1}{P} \tag{3.23}$$

The first constraint is the coil-coil power transfer computed using (3.21),

$$(P - 2\pi f E_m(\psi))/P \leq 0. \tag{3.24}$$

The next constraint is the maximum average stray field magnitude $B_{str,lim}$ in the airgap outside the measurement extents x_{meas} and y_{meas},

$$(||B_{str,avg}(x, y)||_{50} - B_{str,lim})/B_{str,lim} \leq 0. \tag{3.25}$$

The inclusion of the stray field as a constraint ensures the compliance of the system with safety standards on public magnetic field exposure. This is computed as the 50-norm of the spatial stray-field matrix which approximates the infinity norm or the maximum magnitude of the matrix. $B_{str,avg}$ is the average field magnitude outside the measurement extents x_{meas} and y_{meas} and is calculated similar to B_{avg} in (3.29). The average of the fields in the airgap is derived by integrating the contribution from each basis function from $z = 0$ to $z = z_{gap}$ and dividing by z_{gap} to obtain the average field in the airgap,

$$B_{x,avg}(x, y) = \sum_{m=1}^{2N-1} \sum_{n=1}^{2N-1} \frac{-\mu_0 j k_x \psi(m, n) e^{j(k_x x + k_y y)}}{\gamma z_{gap} \sinh \gamma z_{gap}} (\cosh \gamma z_{gap} - 1) \tag{3.26}$$

$$B_{y,avg}(x, y) = \sum_{m=1}^{2N-1} \sum_{n=1}^{2N-1} \frac{-\mu_0 j k_y \psi(m, n) e^{j(k_x x + k_y y)}}{\gamma z_{gap} \sinh \gamma z_{gap}} (\cosh \gamma z_{gap} - 1) \tag{3.27}$$

$$B_{z,avg}(x, y) = \sum_{m=1}^{2N-1} \sum_{n=1}^{2N-1} \frac{-\mu_0 \gamma \psi(m, n) e^{j(k_x x + k_y y)}}{\gamma z_{gap}}. \tag{3.28}$$

The average field magnitude $B_{avg}(x,y)$, is then

$$B_{avg}(x,y) = \sqrt{B_{x,avg}(x,y)^2 + B_{y,avg}(x,y)^2 + B_{z,avg}(x,y)^2}. \tag{3.29}$$

The third constraint limits the continuous current density to the desired coil extents x_{ext} and y_{ext} such that the surface integral of the stray current squared, $\int_\Omega K_{str}(x,y,0)^2 d\Omega$, is a small percentage, α = 1e-4, of the surface integral of the total current $\int_\Omega K(x,y,0)^2 d\Omega$,

$$\frac{\int_\Omega K_{str}(x,y,0)^2 d\Omega - \alpha \int_\Omega K(x,y,0)^2 d\Omega}{\int_\Omega K(x,y,0)^2 d\Omega} \leq 0. \tag{3.30}$$

In summary, the objective function and constraints form the optimization

$$\begin{gathered}
\min \left(\frac{||K_x(\psi)||_2^2 + ||K_y(\psi)||_2^2}{16P} + 0.1\frac{||\psi||_1}{P} \right) \\
\text{s.t.} \\
(P - 2\pi f E_m(\psi))/P \leq 0, \\
(||B_{str,avg}(x,y)||_{50} - B_{str,lim})/B_{str,lim} \leq 0, \\
\frac{\int_\Omega K_{str}(x,y,0)^2 d\Omega - \alpha \int_\Omega K(x,y,0)^2 d\Omega}{\int_\Omega K(x,y,0)^2 d\Omega} \leq 0.
\end{gathered} \tag{3.31}$$

3.4.1 Optimization Outputs, Tradeoff of Current and Stray Field

For $B_{str,lim}$ of 5 µT to 1 mT the optimization of (3.31) was solved using x_{ext} = 0.7 m and y_{ext} = 0.5 m with an airgap of z_{gap} = 0.2 m, coil-coil power of P = 6.6 kW, and frequency of f = 85 kHz. The measurement extents were x_{meas} = 0.8 m and y_{meas} = 0.6 m such that the stray fields are measured at a distance of 5 cm from the coil extent. The design space dimensions are $D_x = D_y$ = 1.4 m with discretization $dx = dy$ = 0.02 m. The spatial wavenumbers k_x and k_y of the basis functions are chosen so that $k_x = m(2\pi/D_x)$ and $k_y = n(2\pi/D_y)$. N = 15 was chosen so the optimization variable is a $15 \times 15 \times 4$ matrix of weights when all basis functions are used. With these parameters, each evaluation of (3.31) took 18.1 ms when using all basis functions. The processor is an Intel Xeon C5-1620 with 80 GB of RAM.

The solutions for $B_{str,lim}$ of 5 µT to 1 mT are plotted in Figure 3.6. The current magnitude integral is computed as the square root of (3.22). As seen in Figure 3.6, some basis functions do not converge when constrained by field $B_{str,lim}$ values: below $B_{str,lim} = 7$ µT for the $\cos x \cos y$ basis function, below $B_{str,lim} = 6$ µT for $\sin x \cos y$, and below $B_{str,lim} = 20$ µT for $\cos x \sin y$ and $\sin x \sin y$. In these cases, convergence requires basis functions with higher frequencies. With higher numbers of basis functions N, and more iterations, solutions for these points could likely be found. However, these outputs require a relatively high current magnitude and may not result in efficient geometries. Likewise, with higher stray field limits than 200 µT, the stray field limit did not constrain the output compared to the stray current constraint.

As $B_{str,lim}$ is reduced, there is an improvement in the outputs of the $\sin x \cos y$ set over the $\cos x \cos y$ set. Outputs representing combinations of the $\cos x \cos y$ and $\sin x \cos y$ basis functions were possible at this crossover point. It is expected that additional crossover points with other basis function sets will occur as $B_{str,lim}$ is further reduced. It was observed that the optimality of the basis function sets is sensitive to the aspect ratio of the coil used. For example, if x_{ext} is chosen to be smaller than y_{ext}, the $\cos x \sin y$ basis function set required less current overall than the $\sin x \cos y$ basis function set.

The $\cos x \cos y$ basis functions result in rectangular, circular, or other unipolar coil shapes or shapes with odd numbers of poles. The $\sin x \cos y$ and $\cos x \sin y$ basis functions result in bipolar shapes or shapes with even numbers of poles oriented in the x-direction or y-direction, respectively. The $\sin x \sin y$ basis function results in coil structures with multiples of four poles. Examples of each of these for the highest stray field bound for $B_{str,lim} = 1$ mT are shown in Figure 3.5 on the top row for a number of turns of $N_T = 20$.

The solutions for $B_{str,lim} = 1$ mT in Figures 3.5 are dominated by lower frequency wavenumbers with longer spatial wavelengths that have smaller decay in the z-direction. The solutions for $B_{str,lim} = 20$ µT have higher frequency wavenumbers with smaller main poles and have small side-pole structures similar to shielding turns. All solutions for $B_{str,lim} = 20$ µT have total amp-turn values greater than their respective counterparts with $B_{str,lim} = 1$ mT which result in larger total current magnitudes in the coil for the same power transfer level.

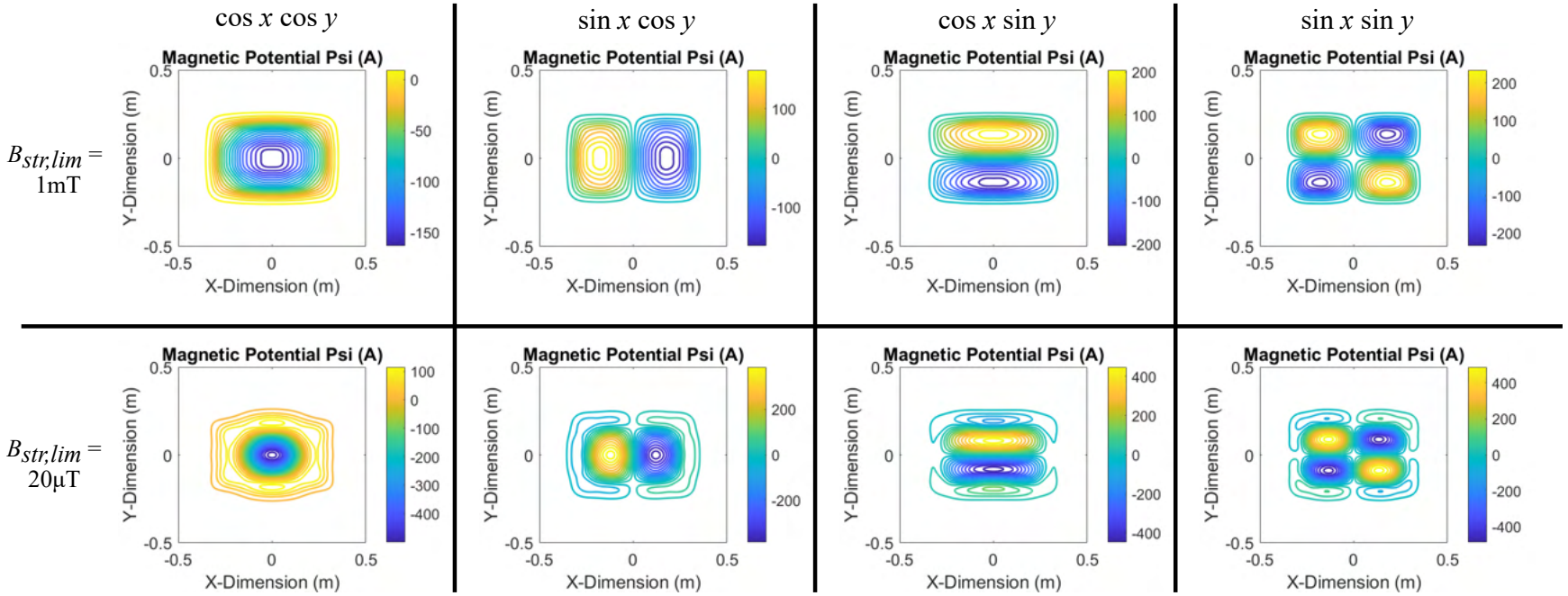

Figure 3.5: Various coil geometries derived from the FAM optimization. Top: Plots of coil contours from each basis function for $x_{ext} = 0.7$ m and $y_{ext} = 0.5$ m when constrained by $B_{str,lim} = 1$ mT with a number of turns $N_T = 20$. From left to right, a rectangular coil from the $\cos x \cos y$ set, a bipolar coil in the x-direction from the $\sin x \cos y$ set, a bipolar coil in the y-direction from the $\cos x \sin y$ set, and a 4-pole coil from the $\sin x \sin y$ set. Bottom: Plots when constrained by $B_{str,lim} = 20$ μT with a number of turns $N_T = 24$. From left to right, a shielded rectangular coil from the $\cos x \cos y$ set, a shielded bipolar coil in the x-direction from the $\sin x \cos y$ set, a shielded bipolar coil in the y-direction from the $\cos x \sin y$ set, a shielded 4-pole coil from the $\sin x \sin y$ set.

3.4.2 Analysis of Coil Geometries

Based on the optimization results, the two coil geometries in Figure 3.7 were selected for further analysis. These points are from the optimization where $B_{str,lim} = 100$ µT for the $\cos x \cos y$ basis function and the $\sin x \cos y$ basis function. For a coil-coil power transfer of 6.6 kW, the $\cos x \cos y$ coil has $V_1 = 382.3$ V and $I_1 = 17.3$ A and the $\sin x \cos y$ coil has $V_1 = 305.4$ V and $I_1 = 21.6$ A. An FEA solver was used to derive the inductance and fields for the 85 kHz operating frequency for comparison with the values derived in FAM. The fields at mid-airgap from the two coils geometries from FAM and FEA simulations are shown in Figure 3.8. The inductance values derived from the FAM versus FEA simulations are given in Table 3.2.

3.4.3 Misalignment Model

The FAM can predict system performance over both translational and rotational misalignments. This is done by calculating the mutual inductance of the system in misaligned conditions. In the Fourier domain, translational misalignment is done by adding a phase shift to the Fourier components, where x_{sft} and y_{sft} are the translational misalignment of the coil in the x-direction and y-direction respectively as in (3.32). An example of this operation is shown in Figures 3.9a and 3.9b.

$$\psi_{sft}(k_x, k_y) = \psi(k_x, k_y) e^{j(-k_x x_{sft} - k_y y_{sft})} \tag{3.32}$$

Rotation in the spatial domain produces the same rotation in the Fourier domain as in (3.33), where θ_{sft} is the rotational misalignment. An example of this is shown in Figure 3.9c.

$$\begin{bmatrix} k'_x \\ k'_y \end{bmatrix} = \begin{bmatrix} \cos\theta_{sft} & -\sin\theta_{sft} \\ \sin\theta_{sft} & \cos\theta_{sft} \end{bmatrix} \begin{bmatrix} k_x \\ k_y \end{bmatrix} \tag{3.33}$$

Due to the limited number of basis functions used in the optimization, this operation is done by taking the spatial domain potential, which has a finer discretization, rotating it,

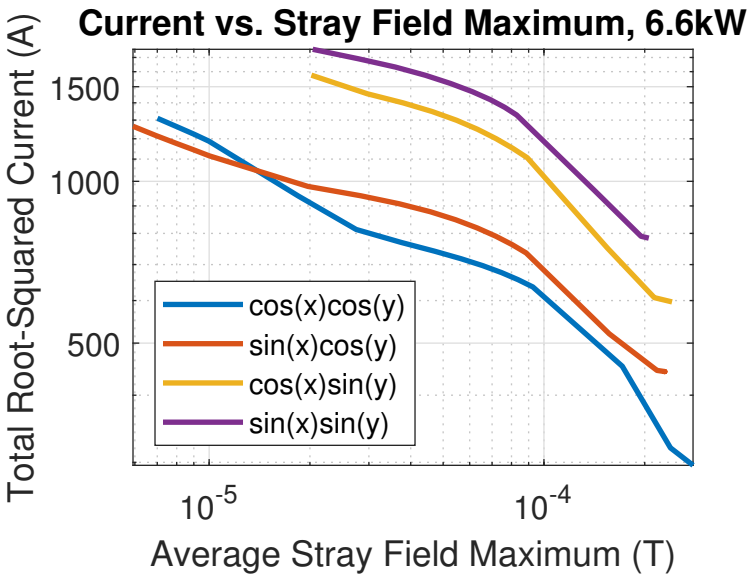

Figure 3.6: The maximum average stray field magnitude for the optimized coils vs. the square root of the integral of the current magnitude squared over a range of $B_{str,lim}$ of 5 µT to 1 mT.

Table 3.2: Calculated Inductance Values, FAM vs. FEA

Parameter	FAM	FEA (Windings)	Error FAM/FEA
$\cos x \cos y$ Coil			
Self Inductance	229.6 µH	236.8 µH	-3.0%
Mutual Inductance	40.9 µH	37.7 µH	8.5%
$\sin x \cos y$ Coil			
Self Inductance	185.5 µH	199.2 µH	-6.9%
Mutual Inductance	25.8 µH	26.6 µH	-3.0%

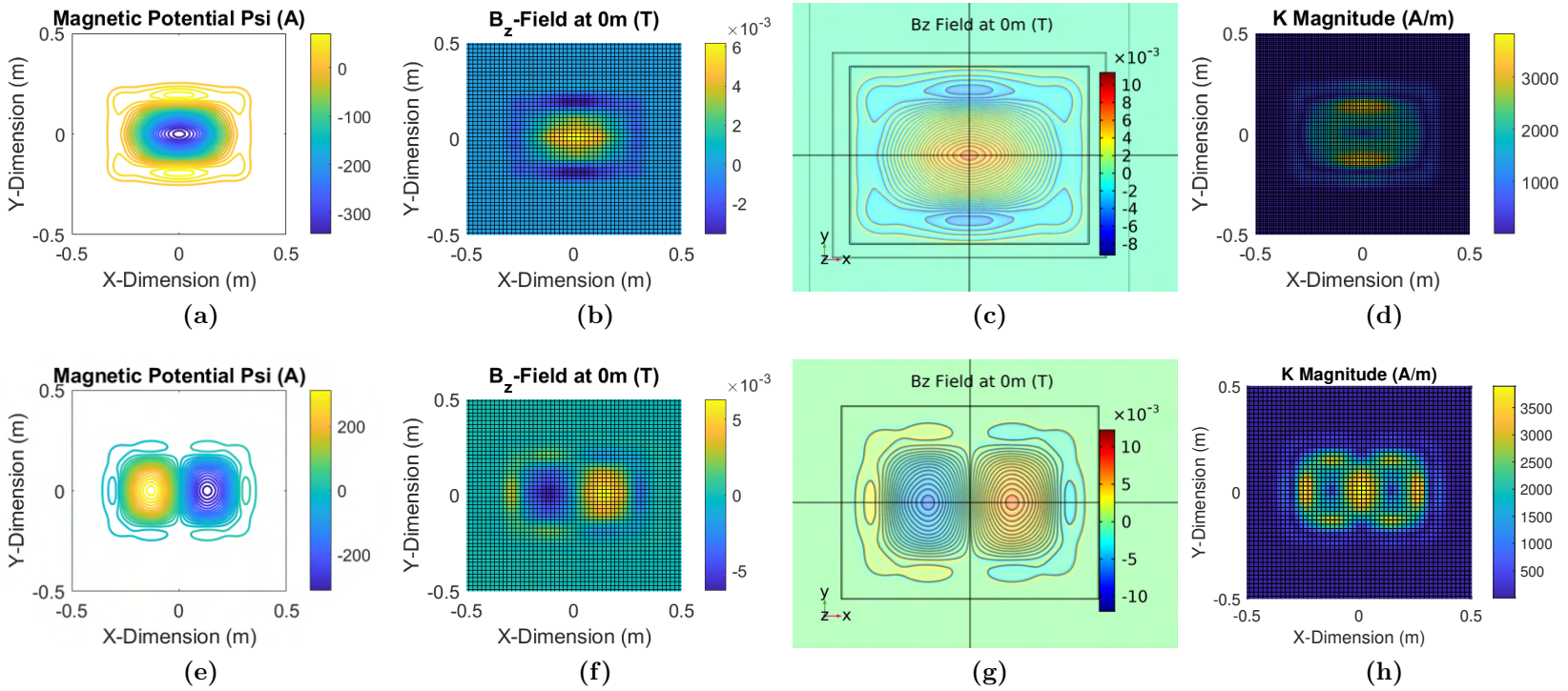

Figure 3.7: Points from the optimization where $B_{str,max} = 100$ µT shown when $f = 85$ kHz and $P = 6.6$ kW. (a) Coil structure from the $\cos x \cos y$ set with $N_T = 25$. (b) Discretized surface field of the $\cos x \cos y$ coil shape. (c) FEA output of the $\cos x \cos y$ coil. (d) Surface current magnitude of the $\cos x \cos y$ coil. (e) Coil structure from the $\sin x \cos y$ set with $N_T = 30$. (f) Discretized surface field from the $\sin x \cos y$ coil. (g) FEA output of the $\sin x \cos y$ coil. (h) Surface current magnitude of the $\sin x \cos y$ coil.

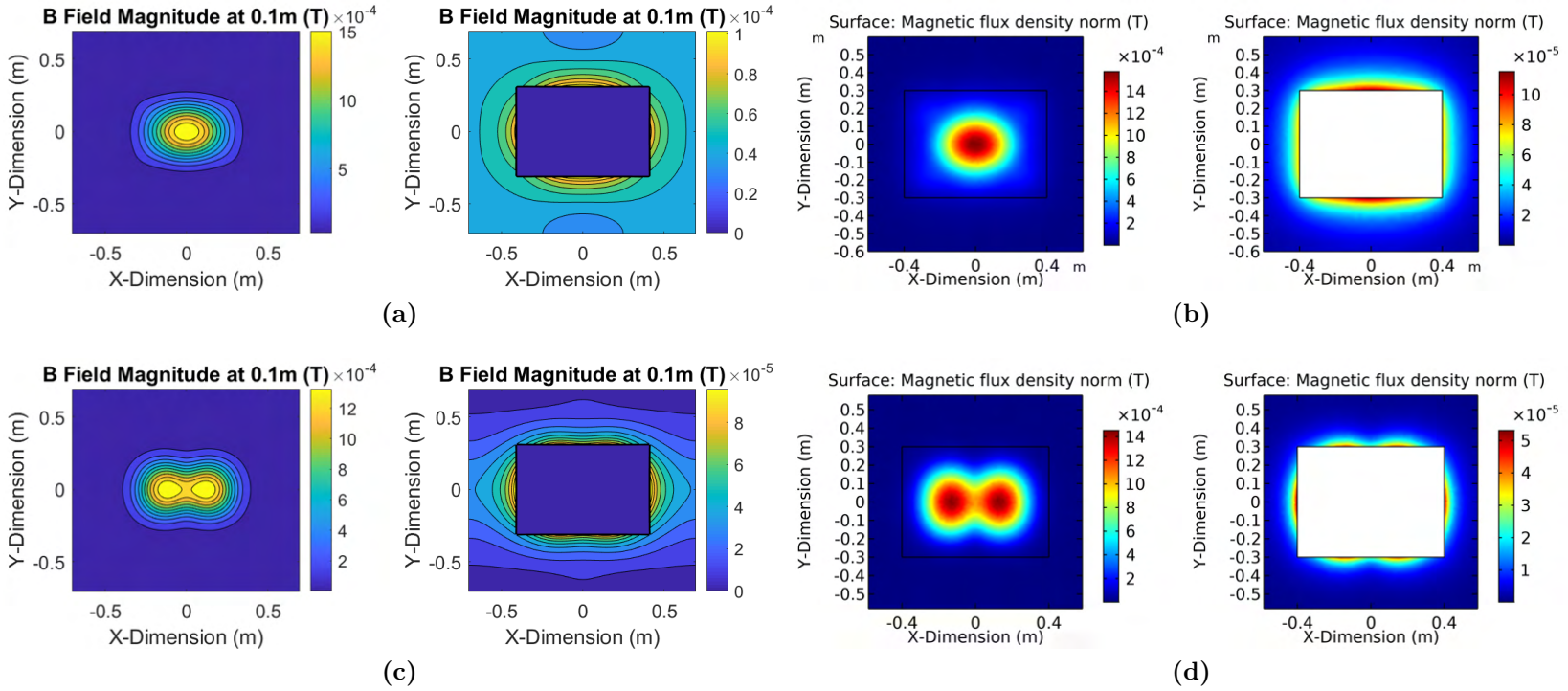

Figure 3.8: Fields calculated in FAM and simulated in FEA for the $\cos x \cos y$ coil: (a) Calculated field magnitude at $z = 0.1$ m for the $\cos x \cos y$ coil. (b) Fields from FEA simulation with one coil energized for the $\cos x \cos y$ coil. (c) Calculated stray field at $z = 0.1$ m for the $\sin x \cos y$ coil. (d) Fields from FEA simulation with one coil energized for the $\sin x \cos y$ coil.

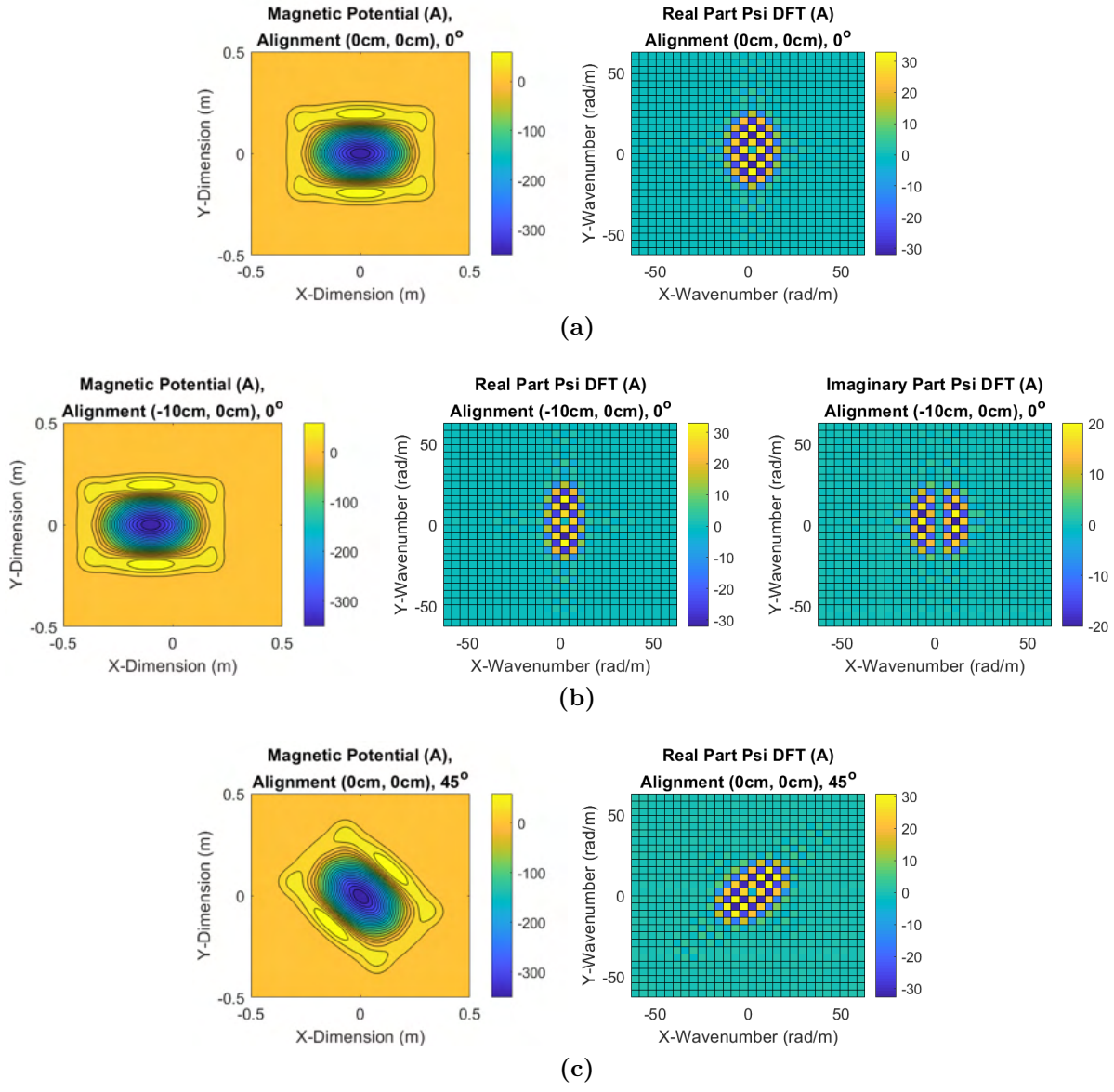

Figure 3.9: Magnetic scalar potential under different misalignment cases. (a) Magnetic potential and DFT when aligned. (b) Magnetic potential and DFT with translational misalignment of -10 cm in the x-direction. (c) Magnetic potential and DFT with rotational misalignment of 45°.

which includes interpolation, and then taking the discrete Fourier transform to determine the Fourier components.

3.5 Circuit and Loss Modeling

3.5.1 Coil Conduction Losses

As alternating current flows through coupled transformer windings, the losses in the wire can be calculated by

$$P_w = \frac{1}{2}\begin{bmatrix}\mathbf{I}_1 & \mathbf{I}_2\end{bmatrix}\begin{bmatrix}R_{11} & R_{12}\\ R_{21} & R_{22}\end{bmatrix}\begin{bmatrix}\mathbf{I}_1^*\\ \mathbf{I}_2^*\end{bmatrix}, \tag{3.34}$$

where $\mathbf{I}_1$ and $\mathbf{I}_2$ are the current phasors of the primary and secondary coils respectively [87]. However, in inductive power transfer, the relative phase shift between the winding will be near 90° such that the mutual resistance terms, R_{12} and R_{21} can be neglected. This leaves only the self-resistance of the coils R_{11} and R_{22}.

The increase in self-resistance of a coil due to alternating current is comprised of two orthogonal and linear effects, the skin effect and the proximity effect. The skin effect is caused by the change in the magnetic field within the conductor due to the change in current within that wire as in Ampere's Law. This creates a voltage in the conductor volume, per Faraday's Law, that creates eddy currents. In the interior of the conductor, the eddy currents oppose the direction of the original current, whereas they add around the edges of the conductor. The combination of these effects causes a phenomenon known as the skin effect, where the current in the conductor crowds around the exterior of the conductor. This is often characterized by the skin depth δ of the conductor as defined in

$$\delta_s = \sqrt{\frac{\rho}{\pi\mu f}} = \sqrt{\frac{2\rho}{\omega\mu}}, \tag{3.35}$$

which is defined as the depth in which the field and current density in the conductor falls to e^{-1} of its initial value at the surface of a conductor with resistivity ρ. For example, at room temperature the resistivity of copper is $\rho_{Cu,0} = 1.68\text{e-}8$ Ω-m for copper. Given the magnetic permeability of copper is $\mu_{Cu} \approx \mu_0$, $\delta_s = 0.224$ mm at 85 kHz.

The resistivity of copper increases with temperature by a factor of $C_{Cu,T} = 0.393\%/^{\circ}\text{C}$, making the resistivity of copper a function of the temperature of the conductor in

$$\rho_{Cu} = \rho_{Cu,0}(1 + (T_{Cu} - 20^{\circ}C)C_{Cu,T}). \tag{3.36}$$

Given the crowding of the current and the associated increase in current density, the skin depth can be used in the calculation of the total AC resistance of WPT coil conductors due to the skin effect R_s. For an individual circular conductor, the ratio $F_R(\zeta) = R_s/R_{DC}$ is a function of the ratio ζ of strand diameter d_{str} and the skin depth δ_s,

$$\zeta = \frac{d_{str}}{\sqrt{2}\delta_s}. \tag{3.37}$$

$$F_R = \frac{\zeta}{2\sqrt{2}}\left(\frac{\text{ber}_0(\zeta)\text{bei}_1(\zeta) - \text{ber}_0(\zeta)\text{ber}_1(\zeta)}{\text{ber}_1(\zeta)^2 + \text{bei}_1(\zeta)^2} - \frac{\text{bei}_0(\zeta)\text{ber}_1(\zeta) + \text{bei}_0(\zeta)\text{bei}_1(\zeta)}{\text{ber}_1(\zeta)^2 + \text{bei}_1(\zeta)^2}\right) \tag{3.38}$$

As derived in [51, 88], formula (3.38) is comprised of Kelvin functions that separate the real and imaginary parts of the value of Bessel functions of the first kind $\text{J}_v(\cdot)$ of order v with argument complex argument $\text{j}^{3/2}x$ as in

$$\text{J}_v(\text{j}^{3/2}x) = \text{ber}_v(x) + \text{j}\,\text{bei}_v(x). \tag{3.39}$$

Within a circular litz wire cable, there are n conductors of diameter d_{str}. Once F_R is computed, the total resistance of the wire including skin effect and DC-resistance, R_s, is

$$R_s = \frac{r_{DC}F_R(\zeta)L_T}{n} \cdot 1.015^{N_b} \cdot 1.025^{N_c}. \tag{3.40}$$

$$r_{DC} = \frac{4\rho_{Cu}}{\pi d_{str}^2} \tag{3.41}$$

where I_{RMS} is the total RMS-current through the litz wire and r_{DC} is the resistance of one strand in the litz wire per unit length. Here, L_T is the total length of wire in the coil multiplied by additional factors to account for the additional length of each conductor due to the number of bundling operations N_b and number of cabling operations N_c as given in the manufacturer datasheet.

Besides the skin effect within the individual conductors, losses can occur from the effect of external fields from conductors near each other, known as the proximity effect. For litz wire, this is subdivided into two primary categories: internal proximity effect loss and external proximity effect loss. These two effects are governed by the coefficient G_R as defined in (3.42) which is a function of ζ derived in a similar fashion to F_R [51, 88],

$$G_R = -\frac{\zeta\pi^2 d_{str}^2}{\sqrt{2}}\left(\frac{\mathrm{ber}_2(\zeta)\mathrm{ber}_1(\zeta)+\mathrm{ber}_2(\zeta)\mathrm{ber}_1(\zeta)}{\mathrm{ber}_0(\zeta)^2+\mathrm{bei}_0(\zeta)^2}+\frac{\mathrm{bei}_2(\zeta)\mathrm{bei}_1(\zeta)-\mathrm{bei}_2(\zeta)\mathrm{bei}_1(\zeta)}{\mathrm{ber}_0(\zeta)^2+\mathrm{bei}_0(\zeta)^2}\right). \tag{3.42}$$

Internal proximity effect losses occur within a single litz wire cable because of the magnetic field generated from the current enclosed in the cable. The external proximity effect is due to the effect of the total field of the coil on each section of a conductor. For ferrite-backed coils with a nonzero gap between the ferrite and windings, the external field, $\hat{H}_e$, is the total field on each section of the wire. The cross-product of this and the wire direction yields the field orthogonal to the direction of current in the winding section. This includes all H_z components, as the coils are assumed to be in the x-y plane, and can include H_x and H_y components depending on the direction of the section of wire [89]. The result of this line integration of the field along the coil contours of the wire for a given current can be taken and then normalized by the current in the wire I_{RMS} to yield the external proximity effect resistance. The summation of these two terms yields the total increase in resistance due to the proximity effect,

$$R_{prox} = n \cdot r_{DC} \cdot G_R(\zeta) \cdot \left(\oint |\vec{H}_e \times \hat{dr}|^2 / I_{RMS}^2 + \frac{1}{2\pi^2 d_o^2} L_T\right) \cdot 1.015^{N_b} \cdot 1.025^{N_c}. \tag{3.43}$$

An example of the coil contours and fields used to compute (3.43) for $I_{RMS} = 17.3$ A is given in Figure 3.7d. The external fields and the direction of each section of the wire are calculated with an interpolation of the discrete points for each field component. Once the resistance increases due to the skin effect and proximity effect are calculated, the total

AC resistance of each coil R_{11} and R_{22} at a given frequency is found by the addition of R_s and R_{prox}.

3.5.2 Ferrite Losses

Magnetic materials are often used in WPT systems to increase the airgap field strength and coupling of the system. This occurs primarily because of the high permeability of the materials which effectively creates a low reluctance path within the system where the H-field is effectively zero. For example, when a high-permeability material is placed directly behind the coil conductor in a planar coil, the effective magnetic path length is halved. Losses occur in interactions between the field and magnetic materials. Losses in soft magnetic materials are primarily broken down into hysteresis loss and conduction losses. However, the resistivity of ferrite materials is high, on the order of 5 Ω-m, such that the eddy currents in the material are neglected. The Steinmetz equation,

$$P_{fe} = C_m f^{\alpha} B_p^{\beta} (T_{fer}^2 C_{t2} - T_{fer} C_{t1} + C_{t0}), \tag{3.44}$$

is an empirical formula of ferrite hysteresis losses within certain ranges where C_m, α, and β are curve-fit coefficients, P_{fe} is the specific hysteresis loss of the material, and B_p is the peak flux density in the material.

The losses are also a function of ferrite temperature, T_{fer}. Many ferrite materials have lower losses when operating at temperatures well above room temperature. For the Ferroxcube 3C95 material, an operating temperature of 25°C increases the loss by 16% relative to the nominal level given by the Steinmetz parameters at 85°C. Mechanical stresses in the ferrite can also increase the loss as detailed later in Section 5.4.

To evaluate (3.44), the spatial flux density in the ferrites must be calculated. In the Fourier Analysis Method, this is conveniently done by taking the integral of each Fourier component in free space in the z-direction to the distance of $\mu_{fer} t_{fer}$ to yield the average flux density in the ferrite of a thickness of t_{fer} and relative permeability μ_{fer}. For a coil in

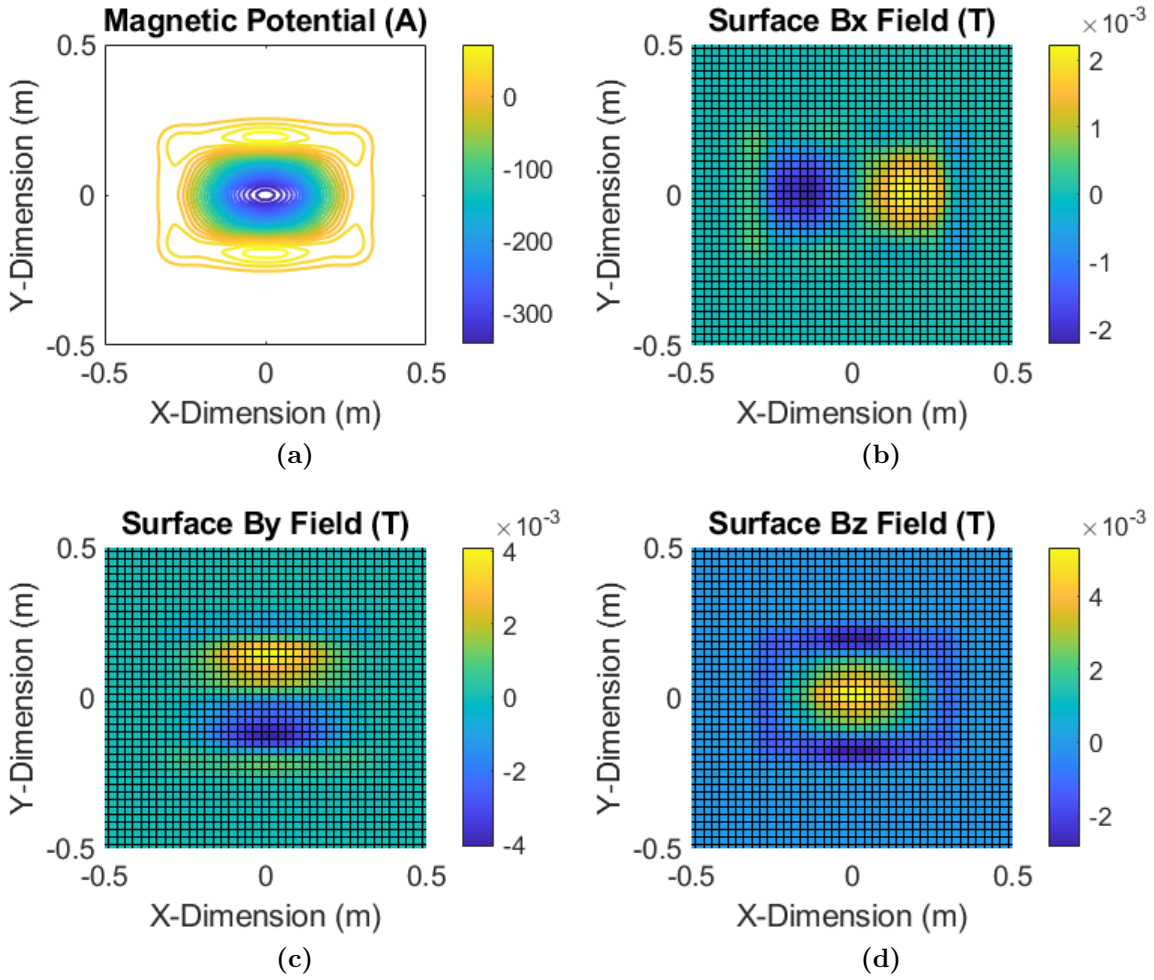

Figure 3.10: Coil geometry and fields of the candidate 6.6 kW coil: (a) Contours of the magnetic scalar potential of the coil. Surface fields of the coil with a current of 17.3 A in the (b) x-direction, (c) y-direction, and (d) z-direction.

the x-y plane, the average fields are

$$B_{x,fer}(x,y) = \sum_{m=1}^{2N-1}\sum_{n=1}^{2N-1} \frac{-\mu_0 j k_x \psi(k_x,k_y) e^{j(k_x x + k_y y)}}{\gamma t_{fer}} (1 - e^{-\gamma t_{fer}\mu_r}) \tag{3.45}$$

$$B_{y,fer}(x,y) = \sum_{m=1}^{2N-1}\sum_{n=1}^{2N-1} \frac{-\mu_0 j k_y \psi(k_x,k_y) e^{j(k_x x + k_y y)}}{\gamma t_{fer}} (1 - e^{-\gamma t_{fer}\mu_r}) \tag{3.46}$$

$$B_{z,fer}(x,y) = \sum_{m=1}^{2N-1}\sum_{n=1}^{2N-1} -\mu_0 \psi(k_x,k_y) e^{j(k_x x + k_y y)} (1 - e^{-\gamma t_{fer}\mu_r}) \tag{3.47}$$

for fields in the x, y, and z directions, respectively. Here, the Fourier components of B_x and B_y are divided by t_{fer} as they are each orthogonal to the z-axis, whereas B_z is parallel and thus not divided by t_{fer}. Then the average peak flux density in the ferrite, $B_{avg,fer}(x,y)$, is computed as the vector sum of the field components,

$$B_{avg,fer}(x,y) = \sqrt{(B_{x,fer}(x,y))^2 + (B_{y,fer}(x,y))^2 + (B_{z,fer}(x,y))^2}. \tag{3.48}$$

An example of this calculation is seen for the demonstrator coil in Figure 3.10a with a primary current of 17.3 A at 85 kHz. As detailed in the following chapter and in Appendix A.1, two different thicknesses of ferrite were used: 2.7 mm on the outside and 5 mm on the inside. This leads to lower flux density and less loss in the middle of the coil.

3.5.3 Inverter and Rectifier Losses

In the demonstrator WPT system, a high-frequency full-bridge inverter drives the primary resonant tank. The secondary side is connected to a full-wave diode rectifier. The SiC MOSFETs in the inverter and SiC Schottky diodes in the rectifier produce losses in the system. The first loss mechanism of the full-bridge inverter is caused by the MOSFET resistance. For MOSFETs, this is given as R_{DS}. In a full-bridge inverter, the primary RMS current I_1 will flow through two devices for most of the switching period. Therefore, the conduction loss of the switching devices is given by

$$P_{R_{DS}} = 2I_{1,RMS}^2 R_{DS}. \tag{3.49}$$

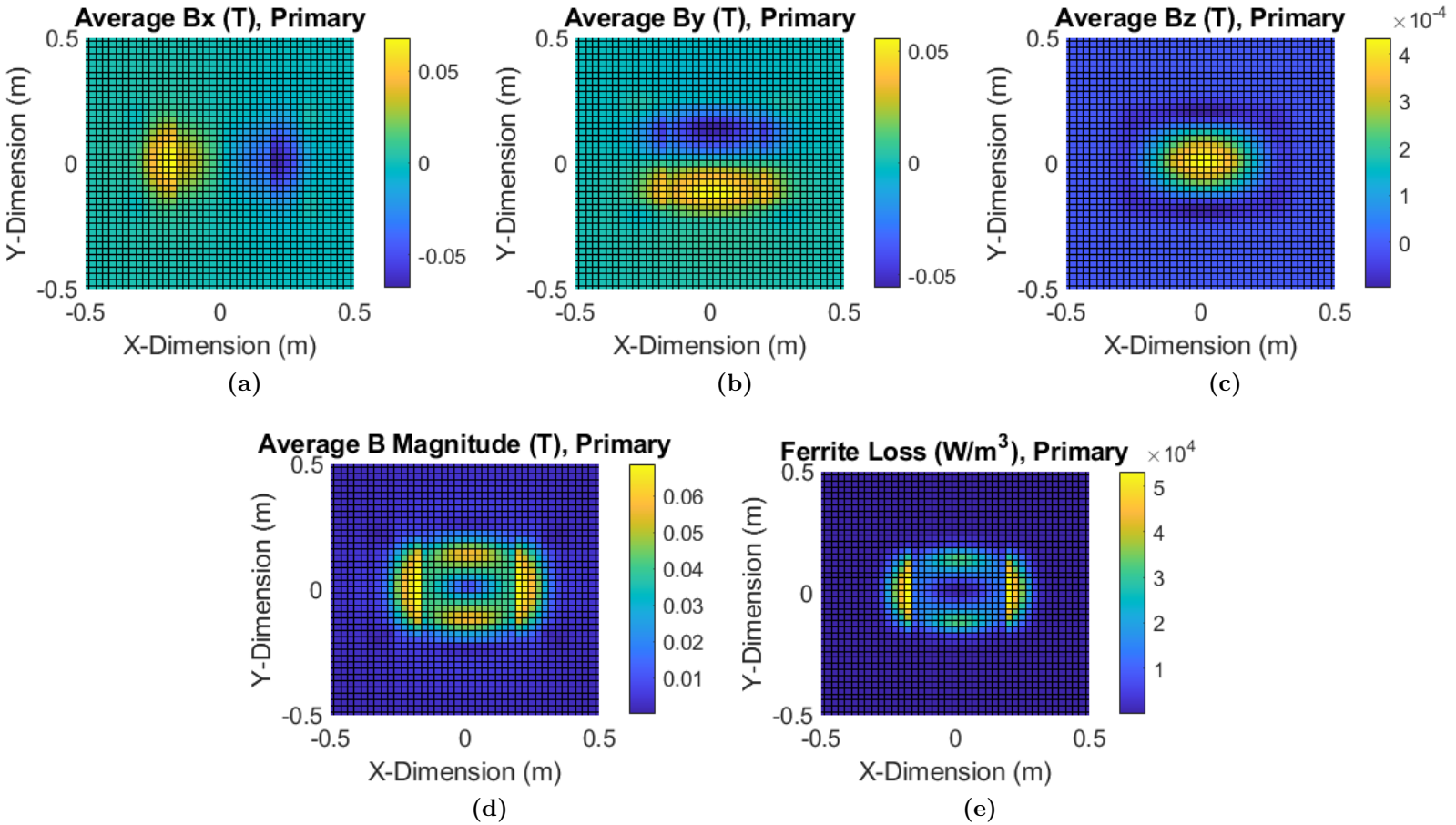

Figure 3.11: Ferrite flux of the 6.6 kW coil derived in FAM: Average RMS fields in primary ferrite coil with a current of 17.3 A in the (a) x-direction, (b) y-direction, and (c) z-direction. (d) The RMS magnitude of the ferrite flux. (e) The spatial specific power loss of the primary coil ferrite at 85 kHz for C_m = 92.66e-3, α = 1.045, and β = 2.440 at T_{fer}= 20°C. Here the inner ferrite is 5 mm and the outer ferrite is 2.7 mm, leading to lower peak fields and lower specific power loss in the middle section.

Likewise, on the secondary side, the secondary RMS current $I_{2,RMS}$ will flow through the forward voltage of the diodes V_f and diode resistance R_f to produce a loss,

$$P_{diode} = 2V_f I_{2,avg} + 2I_{2,RMS}^2 R_f. \tag{3.50}$$

In the demonstrator system, the diode device has two diodes in a common cathode configuration such that the normal diode on-resistance is halved. The reverse-recovery losses of the diodes are negligible as Schottky diodes are used. The average diode forward current is calculated by

$$I_{2,avg} = \frac{2\sqrt{2}}{\pi} I_{2,RMS} \tag{3.51}$$

The second loss mechanism present in full-bridge inverters in WPT is switching loss. The primary mechanism for this is the device output capacitance C_{oss}. In a hard-switching transition of the switch-node voltage from the DC-link voltage $V_{1,DC}$ to zero, the voltage across C_{oss} is reduced to zero and the charge is passed through R_{DS} as loss. In this case, the C_{oss} power loss in the full-bridge inverter is

$$P_{C_{oss}} = 4V_{1,DC}^2 C_{oss} f, \tag{3.52}$$

where f is the switching frequency of the inverter.

In the demonstrator system, this loss is often avoided by operating the WPT system such that the input impedance seen by the full-bridge Z_{in} is inductive and by using soft-switching transitions and dead-time intervals. In this mode of operation, the device capacitances are commutated by the coil RMS current $I_{1,RMS}$. This commutation period is often brief for the large currents present in high-power WPT systems. After this, the current flows through the body or anti-parallel diodes of the device until the end of the dead-time period, reducing the voltage of the device to nearly zero before the dead-time ends and the gate voltage is applied. The input impedance characteristics of a series-series WPT system will be reviewed in later sections.

To assess the performance of the inverter and rectifier as a function of current in comparison with datasheet values, the temperature of the heatsink and fan of the case, and

voltage of the shorted half-bridge MOSFETs and diodes were taken. These measurements are summarized and compared to the datasheet values in Figure 3.12. Here, the MOSFETs had similar resistance to the low-temperature datasheet values, but the diodes had greater on-resistance than the low-temperature manufacturer curve. This data was used to determine the diode and MOSFET parameters given in Table 4.5.

3.5.4 Coil Turn Discretization

When limited to a single-layer coil, the number of turns must be chosen so that the conductors can physically be placed on the surface of the coil in a single layer with wire diameters d_{out}. This value is given in datasheets by the wire manufacturer and includes the outer insulation, coating, and conductors. This can be assured by relating the wire diameter and current to the maximum value of $K_{mag}(x, y, 0)$, K_{max}

$$\frac{\max \Psi(x, y, 0) - \min \Psi(x, y, 0))}{N_T d_{out}} = \frac{I_{RMS}}{d_{out}} < K_{max}. \tag{3.53}$$

Since this depends on d_{out}, the number of turns that violate this condition varies per gauge of wire. For a given power level, the product of voltage and current remains approximately the same, but the impedance ratio varies based on the selection of N_T. As an example, the coil current and voltage for the coil of Figure 3.7a are plotted in Figure 3.13. In these plots, multiple litz wire diameters are considered to illustrate the limitation of (3.53). Here, larger gauges of wire will be limited to higher $I_{1,RMS}$ and $I_{2,RMS}$ than smaller gauges. For example, the selection of smaller gauges of wire and more turns may be favorable to reduce inverter currents when considering the inverter device R_{DS} loss.

3.5.5 Compensation Component Losses

Compensation components are critical to making efficient WPT systems. Without them, the input impedance of the WPT system is nearly all reactive and the feasibility of high-power WPT systems is limited. Power capacitors such as the ones used in the WPT system are designed to have small, but non-zero series resistance and dielectric losses. The ratio of real power, or loss in this case, to reactive power is expressed as the tangent of the angle ϕ of the

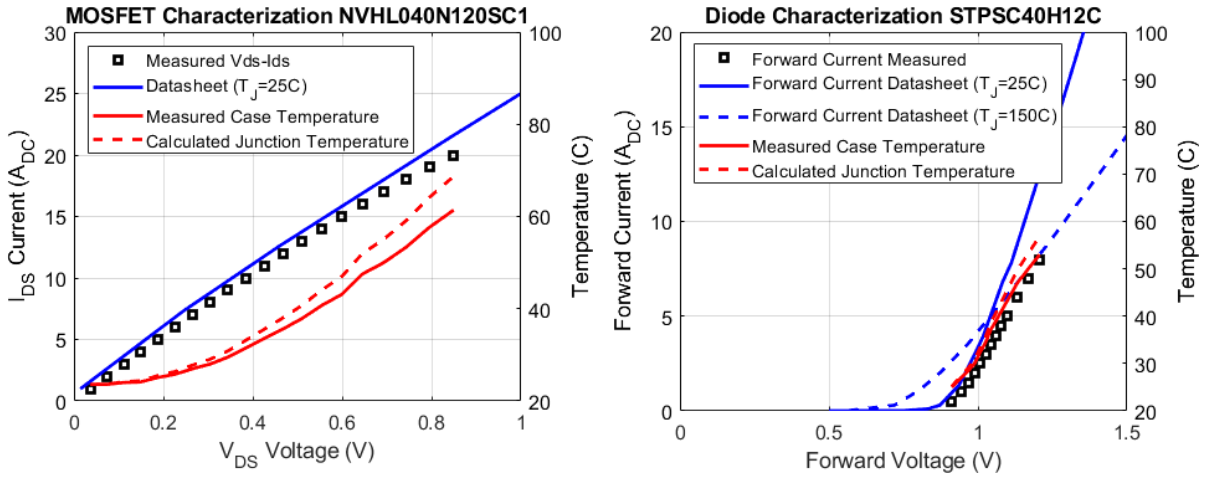

(a) (b)

Figure 3.12: Temperature and voltage measurements as a function of DC current for the (a) inverter SiC MOSFETs and the (b) rectifier SiC Schottky diodes.

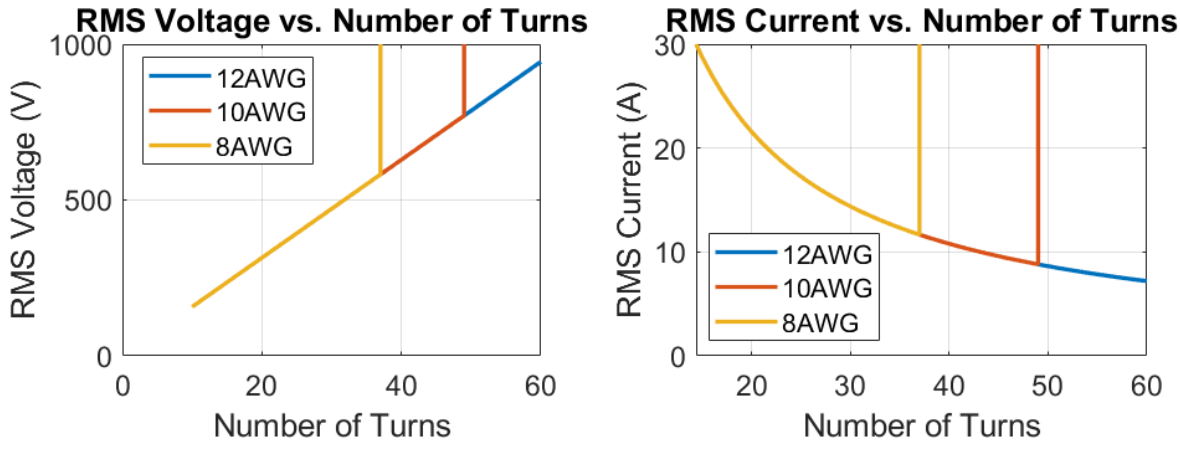

(a) (b)

Figure 3.13: Ideal RMS (a) voltage and (b) current for the coil geometry of Figure 3.7a at a power level of 6.6 kW. In these plots, the voltage or current is set as a large number when the condition of Equation 3.53 is violated.

vector sum of the real power loss P_c and reactive power Q_c in the capacitor, or the dissipation factor (DF).

$$\tan\phi = P_c/Q_c \tag{3.54}$$

The real power loss of resonant capacitors is comprised of both dielectric loss and conduction loss. For polypropylene-based capacitors, the dielectric component of the dissipation factor (DF) remains constant with frequency around 10^{-4} to 2×10^{-4}. The conduction loss component of the DF, however, scales with frequency so that the total DF increases with frequency, as illustrated in Figure 3.14a which compares the nominal DF of film capacitors from [90] to measurements of a resonant capacitor bank of three film capacitors. Here, the measured DF of the capacitors is about half of the nominal curve, but about five times greater than the nominal value. For a known dissipation factor, $\tan\phi(f)$, the ESR of the resonant capacitors R_C and the total power loss P_c are

$$R_C = \frac{\tan\phi(f)}{\omega C} \tag{3.55}$$

$$P_c = I_{1,RMS}^2 R_{c1} + I_{2,RMS}^2 R_{c2}. \tag{3.56}$$

A summary of the equivalent DFs of a few types of Illinois Capacitors film capacitors is given in Figure 3.14b. The lower dissipation of the high-density resonant capacitors of the HC and LC types compared to the traditional through-hole PSB-RSB capacitors is apparent. As given, high-density, conduction-cooled resonant capacitors such as HC1, HC2, LC2 display a lower DF than standard PP film capacitors, such as the PSB-RSB series, which are not optimized for high-current and voltage applications. This equates to high quality factors and low equivalent series resistance (ESR). For example, the HC2 0.66 µF capacitor has ratings of 700 V(rms) and 400 A(rms) and a rated ESR of 0.4 mΩ at 100 kHz at 25°C with a volume of 61608 mm^3. In comparison, the 4-lead PSB 0.68 µF capacitor (part number 684PSB202K4R) has ratings of 700 V(rms) and 22 A(rms) and an ESR of 3.6 mΩ with a volume of 77625 mm^3 or around 126% the volume of the HC2 capacitor. To overcome current or voltage limitations, many of these capacitors can be placed in series and

parallel to make a higher capacitance value or to withstand a higher current. However, these additional external connections will increase the ESR of the capacitor bank.

It is also possible to include additional capacitors or inductors in the compensation network. In this case, the inductor loss can be computed with similar equations as presented in the previous sections for AC conduction losses and magnetic component loss. Likewise, the power losses in the additional capacitors can be computed with (3.56).

3.5.6 Series-Series System Circuit Model

A diagram of a series-series compensated WPT system is shown in Figure 3.15. With an equivalent AC load resistance on the secondary side R_L, the circuit is modeled as

$$\begin{bmatrix} \mathbf{V}_1 \\ 0 \end{bmatrix} = \begin{bmatrix} Z_1 & -j\omega M \\ -j\omega M & Z_2 \end{bmatrix} \begin{bmatrix} \mathbf{I}_1 \\ \mathbf{I}_2 \end{bmatrix}. \tag{3.57}$$

$$Z_1 = 2R_{DS} + R_{C1} + R_{11} + j\omega L_1 + 1/(j\omega C_1) \tag{3.58}$$

$$Z_2 = 2R_f + R_{C2} + R_{22} + R_L + j\omega L_2 + 1/(j\omega C_2) \tag{3.59}$$

As seen in Figure 3.15, the parasitic resistance of the primary and secondary, R_1 and R_2 respectively, are

$$R_1 = 2R_{DS} + R_{C1} + R_{11} \tag{3.60}$$

$$R_2 = 2R_f + R_{C2} + R_{22} \tag{3.61}$$

The input voltage and equivalent AC load resistance are found by the first-harmonic approximation of a square wave as a function of the DC input voltage $V_{1,DC}$ and the DC output load resistance $R_{L,DC}$. The input voltage phasor $\mathbf{V}_1$ is defined to have a phase of 0°. The RMS currents of the system $I_{1,RMS}$ and $I_{2,RMS}$ and the RMS input voltage $V_{1,RMS}$ can be found by dividing the magnitude of $\mathbf{I}_1$, $\mathbf{I}_2$, and $\mathbf{V}_1$ by $\sqrt{2}$, respectively.

$$R_L = \frac{8}{\pi^2} R_{L,DC} \tag{3.62}$$

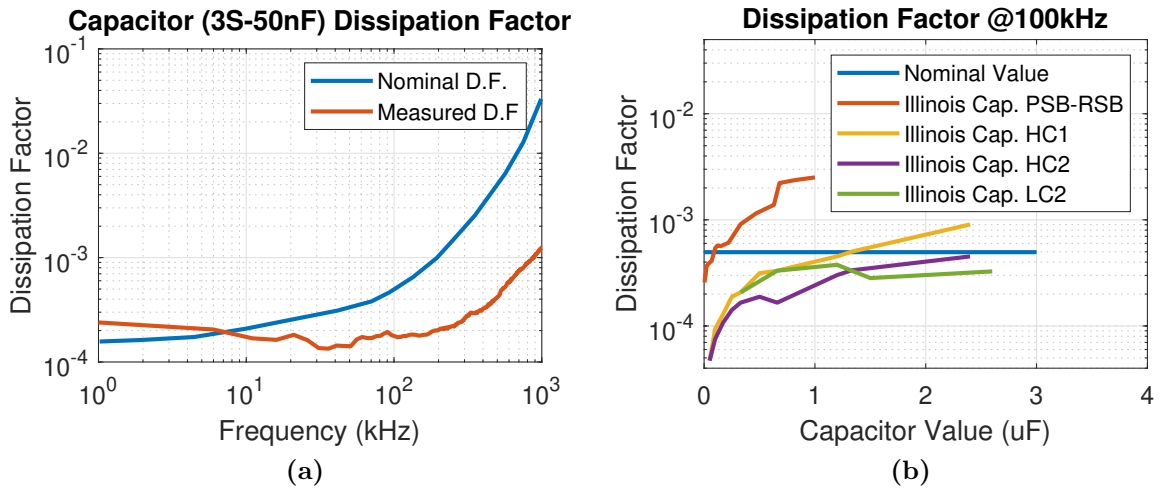

Figure 3.14: Resonant capacitor dissipation factors: (a) The frequency-dependent dissipation factor (DF) of polypropylene (PP) capacitors as in [90] compared to the measured DF of the HC1 capacitor bank with 3, 50 nF capacitors in series. (b) Equivalent DF of Illinois Capacitor film capacitors derived from datasheet values.

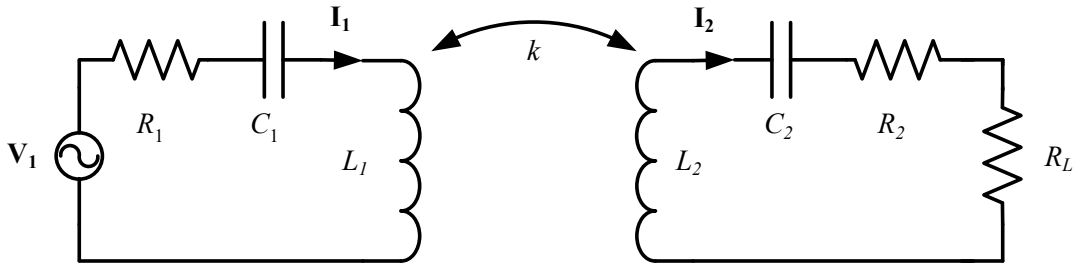

Figure 3.15: Circuit diagram of a series-series compensated WPT system.

$$V_{1,RMS} = \frac{2\sqrt{2}}{\pi} V_{1,DC} \tag{3.63}$$

Likewise, the DC output voltage can be found by

$$V_{2,DC} = \frac{\pi}{2\sqrt{2}} I_2 R_L - 2V_f. \tag{3.64}$$

In this linear circuit model, the resistances due to the ferrite losses are neglected. In the final loss calculation, the ferrite losses are calculated from the currents found by this linear model. By inverting this matrix, the input impedance of the system is

$$Z_{in} = \frac{Z_1 Z_2 + (\omega M)^2}{Z_2}. \tag{3.65}$$

To assure the zero-voltage switching of the inverter switches, the frequency and load of the WPT system is chosen so the input impedance of the primary coil will be inductive such that

$$2C_{oss}(V_{DC,1})V_{DC,1} = -\int_0^{\text{ang}(Z_{in})/\omega} \sqrt{2} I_1 \sin\left(\omega t - \text{ang}(Z_{in})\right) dt. \tag{3.66}$$

This is done by choosing an operating frequency slightly greater than the resonant frequency of the tank. For the measured inductance values at 210 mm with three 50 nF compensation capacitors in series with the primary and secondary, the input impedance magnitude and phase are plotted as a function of frequency and load resistance in Figure 3.16.

Summary

In this chapter, an optimization method based on the Fourier Basis functions coefficients was detailed and used to derive geometries in the tradeoff of stray field and current magnitude. Field, inductance, and loss models built upon the same Fourier modeling approach were also given including the calculation of ferrite flux density and loss and external proximity effect loss. Measurements of a set of two tripolar, air-core coils were performed as validation of the inductance and field modeling approaches and FEA simulations of two of the outputs from

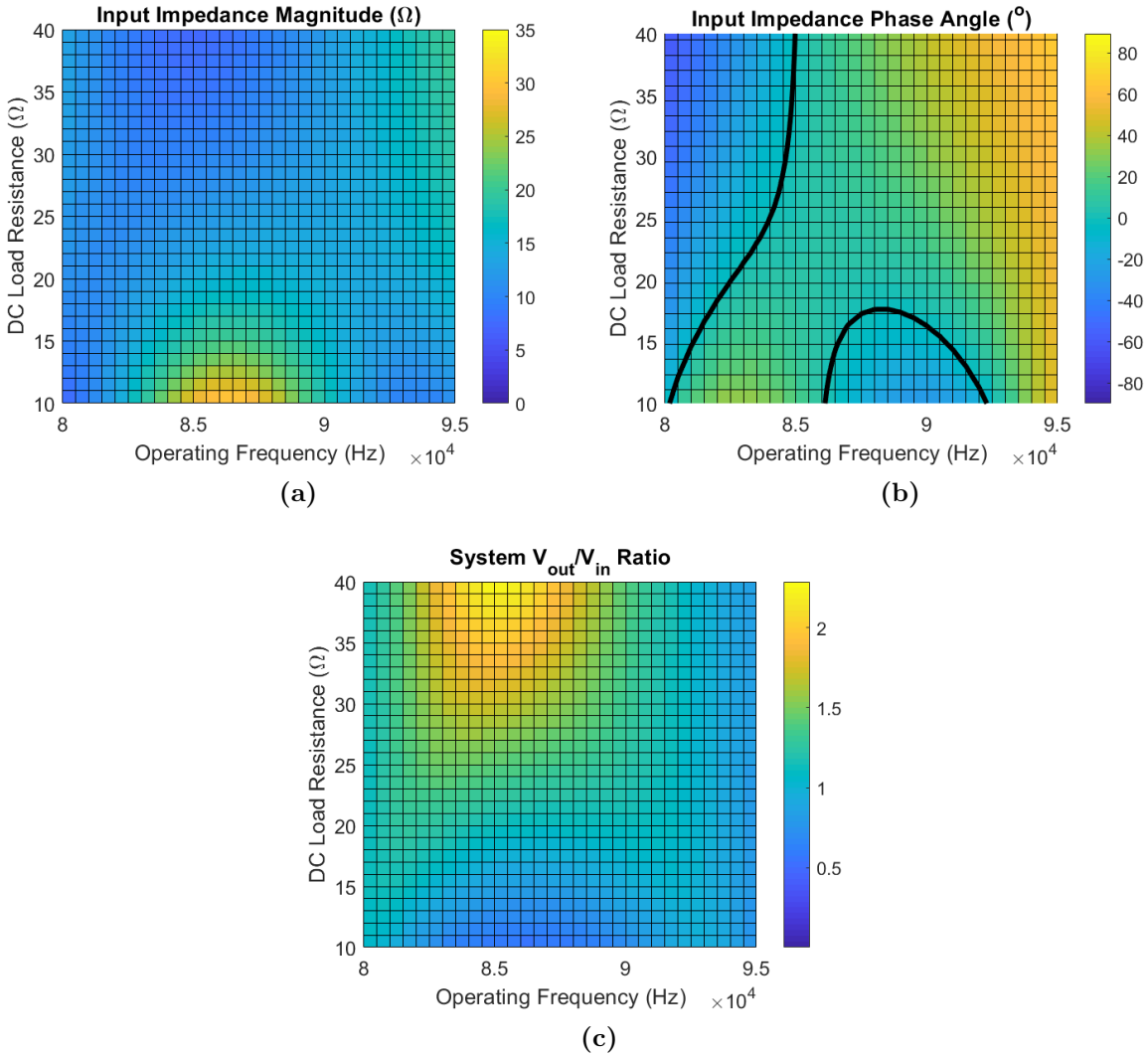

Figure 3.16: Calculated input impedance and voltage transfer ratio for the demonstrator system when tuned for 86.5 kHz. (a) Input impedance magnitude, (b) Input impedance phase angle with black contour at zero degrees, (c) Voltage transfer ratio of the system.

the optimization sweep were compared to model outputs. In the next chapter, the shielded rectangular geometry of Figure 3.7a is constructed with ferrite backing to experimentally validate the model outputs.

Chapter 4

Experimental Validation of a 6.6 kW Demonstrator

With the experimental system and models described in the previous sections, two candidate geometries were obtained for further evaluation as seen in Figure 4.1. The shielded rectangular coil was selected from these two to be built, and a series of tests were performed to compare the loss and field models with the experimental values. A summary of values measured in the testing are listed in Tables 4.1 and 4.2 . The airgaps were chosen based on the nominal ground clearance classes of J2954 as in Table 1.1.

The proof-of-concept demonstrator was extensively tested at 86.5 kHz, the nominal operating frequency, across varying airgaps, misalignments, and input voltages. A power level of 6.7 kW was tested at a 210 mm airgap at alignment to reach the nominal power level and assess thermal effects. At other airgaps and alignments, test points with reduced power levels were taken so that an electronic load could be used in shunt to control the output load resistance. At the other two tuning frequencies, 50.5 kHz and 121.5 kHz, the efficiencies and fields were measured at alignment to assess the impact of varying frequency compared to the nominal frequency of 86.5 kHz.

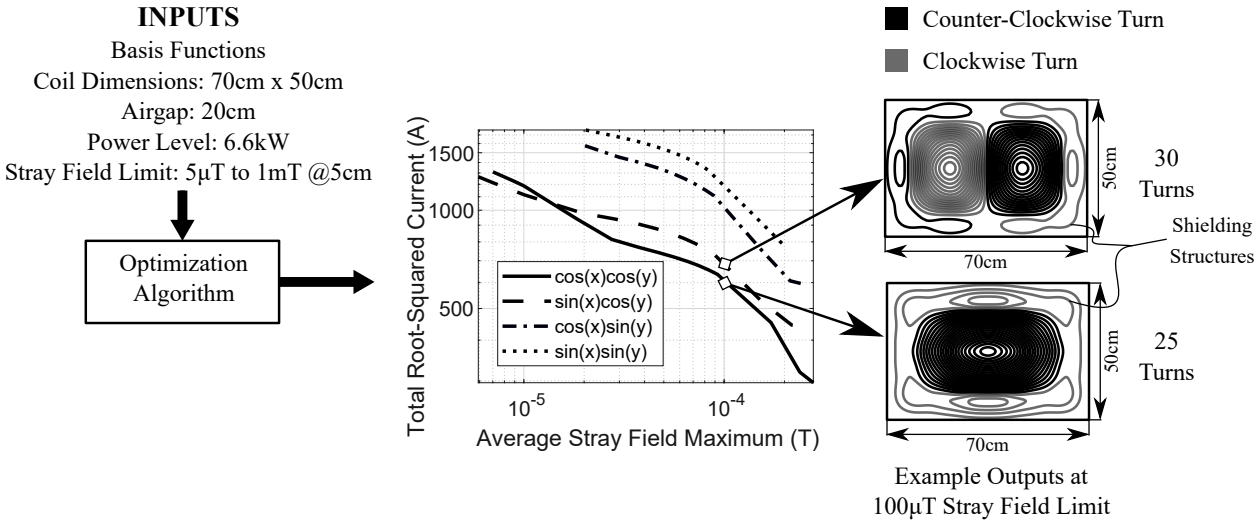

Figure 4.1: Design process used to derive coil geometries. As discussed before, the two geometries were derived from optimization outputs at $B_{stray,lim} = 100$ μT.

Table 4.1: Demonstrator Specifications and Measured Values at 86.5kHz

Parameter	Measured Values	
DC Input Voltage	50-600 V	
DC Output Power	≤6.7 kW	
Air Gap	125, 210, 250 mm	
Misalignment (X)	-10 cm, 0 cm	
Misalignment (Y)	-7.5 cm, 0 cm	
Misalignment (Rotation)	0°, 15°, 45°	
Peak Efficiency (DC-DC), Aligned	125 mm	97.6%
	210 mm	95.6%
	250 mm	93.1%
Aligned Stray Field Magnitude 6.6 kW, 86.5 kHz (Scaled Measurements at 0.8 m, [X,Y])	125 mm	1.8 μT, 1.4 μT
	210 mm	4.4 μT, 3.6 μT
	250 mm	6.5 μT, 4.5 μT

4.1 Test Setup Construction

The 6.6 kW demonstrator was built to evaluate one of the candidate coil geometries found in the optimization process and to validate the loss and field models with experimental measurements. The overall setup can be seen in Figure 4.2 and consists of a set of two matched planar coils, two compensation capacitor banks, and power electronics consisting of four half-bridge modules, eight gate driver boards, and a control board FPGA. Field measurements were taken with a 3D printed sensor cubic wound with magnet wire. A part count and bill of materials are included in Table 2.

4.1.1 6.6 kW Demonstrator Construction

One of the two identical coils is shown in Figure 4.3a. Each coil is a sandwich structure comprised, top to bottom, of a polycarbonate coil former, ferrite tiles of two thicknesses, hardboard spacers, and an aluminum sheet held together with nylon bolts and reinforced tape. The dimensional drawing of the coils can be found in Appendix A.1. The airgap holder in Figure 4.3b was made out of wood and nylon bolts to suspend one of the coils at varying airgaps. The four threaded nylon rods allow for the quick adaptation of the airgap and support the upper coil from the bottom.

Litz wire was used to wind the coils symmetrically as shown in Figure 4.3c. The total length of the wire in each coil was measured to be 29.8 m, with 24.8 m in the coils themselves. The calculated value from the model was 24.5 m in the coil contours themselves. This difference is accounted for in the loss modeling of the system.

4.1.2 Capacitor Bank Construction

The compensation capacitors are constructed of 50 nF HC1 high-density resonant capacitors from Illinois Capacitor [90]. Due to the need to reach high voltage levels, multiple capacitors are placed in series to reach higher voltages. The capacitors may also be placed in parallel to change the tuning of the system. To achieve this flexibility, the capacitor bank shown in Figure 4.4 was constructed out of 1/16 inch (1.59 mm) 110 copper sheets. An identical

Table 4.2: Summary of Measured Values at Other Frequencies

Parameter	Measured Values		
DC Input Voltage	≤200 V		
DC Output Power	≤750 W		
Air Gap	125, 210, 250 mm		
Misalignment (X)	0 cm		
Misalignment (Y)	0 cm		
Operating Frequency		50.5 kHz	121.5 kHz
Peak Efficiency (DC-DC), Aligned	125 mm	96.5%	95.6%
	210 mm	92.2%	94.8%
	250 mm	88.9%	92.6%
Aligned Stray Field Magnitude 6.6kW (Scaled Measurements, 0.8 m [X,Y])	125 mm	1.9 µT, 1.7 µT	2.0 µT, 1.4 µT
	210 mm	5.1 µT, 4.4 µT	4.4 µT, 2.8 µT
	250 mm	7.4 µT, 6.1 µT	5.6 µT, 4.2 µT

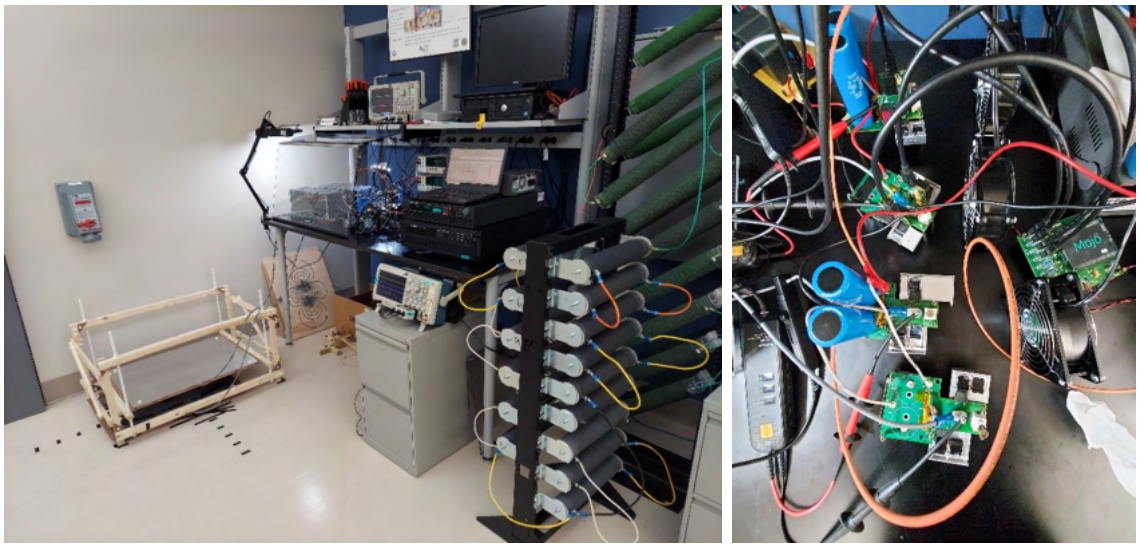

(a) **(b)**

Figure 4.2: Test bench setup for the 6.6 kW demonstrator. (a) Overall test bench with WPT coils, compensation capacitors, inverters and rectifiers, multimeters, power supplies, an electronic load, and wirewound resistors from left to right. (b) Closeup of inverter and rectifier half-bridge modules and control board.

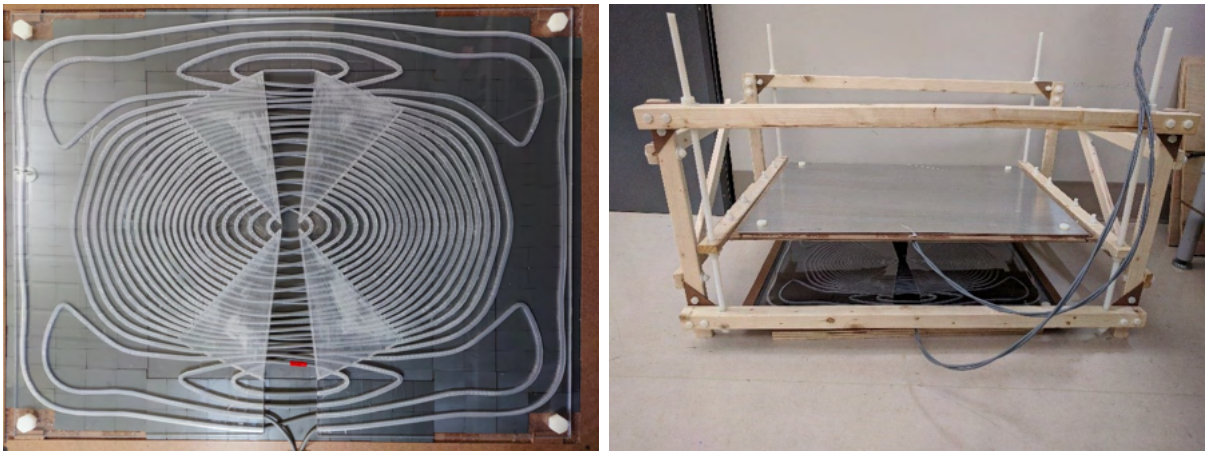

(a) (b)

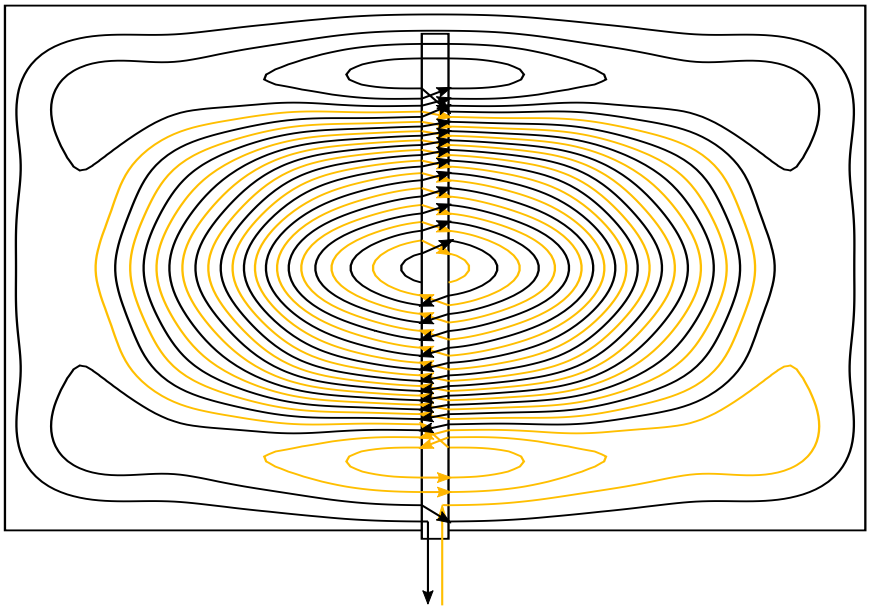

(c)

Figure 4.3: 6.6 kW demonstrator construction: (a) Demonstrator 6.6 kW coil. (b) Airgap holder used to set varying airgap and misalignments. (c) Winding pattern of the coil. Here the orange turns go into the coil and the black turns go out of the structure.

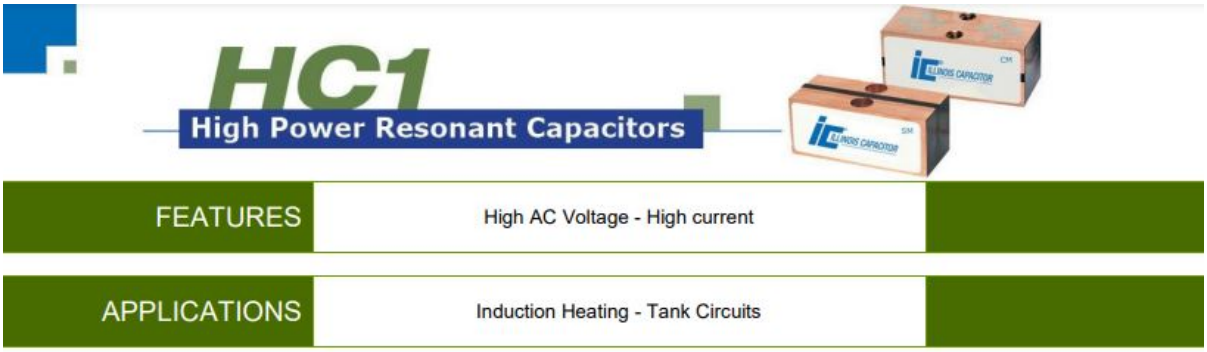

KVAR	150
CAPACITANCE TOLERANCE	+/-10%
MAXIMUM CORE TEMPERATURE	+85°C
SURFACE TEMPERATURE	+45°C (Above 45°C the KVAR rating must be de-rated by 2.25%/°C)
CONSTRUCTION	Self-healing
SELF INDUCTANCE	< 3 nH
DIELECTRIC	Polypropylene
FLAME RETARDANT	UL94V0

Standard part listing

Capacitance (µF)	VAC	IC part number	Maximum RMS current (A)	MAX power kvar	Frequency range (kHz)	ESR (mΩ) 100kHz, +25°C	Dimensions (mm)			Terminal Style
							B	H	L	
0.05	1000	503HC1102K2CM6	200	150	478-700	1.5	30.2	30	68	2CM6
		503HC1102K2SM6								2SM6

(a)

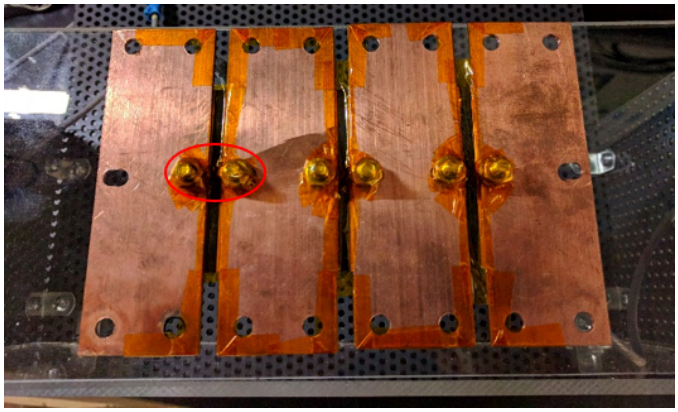

(b)

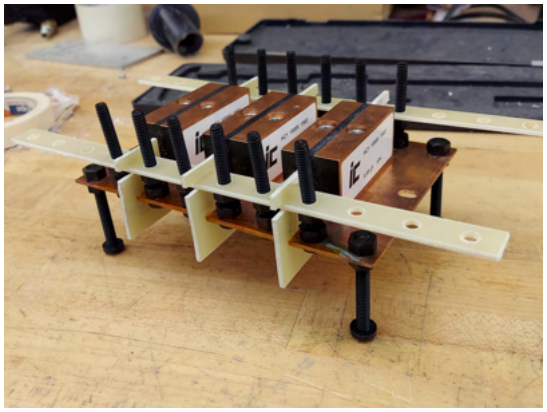

(c)

Figure 4.4: Capacitor bank construction: (a) Datasheet of the Illnois Capacitor HC1 50 nF capacitors used in the capacitor bank [90]. (b) Underside of capacitor bank with three capacitors in series. The area where arcing was observed without the FR4 fins and Mylar tape is encircled in red. (c) The assembled capacitor bank with FR4 fins.

bank was constructed and placed on the secondary side to provided series-series tuning for the system. Detailed mechanical drawings are provided in Appendix A.1.

It was found that the area between the nuts on the underside of the capacitors provided a path for an arc to form and required additional voltage insulation. This was especially the case where the corners of the nuts were facing each other. To resolve this issue, FR4 fins were made to provide additional voltage insulation between the capacitor bolts on top of Mylar tape. These are held in place by long pieces of FR4 aligning the busbars and nylon bolts. The assembly is enclosed in a PVC and plexiglass safety box.

4.1.3 Sensor Cubic

A sensor cubic was made to measure the fields of the system during operation for comparison with model values. The probe design is similar to [22], but scaled to achieve higher sensitivity. The voltage induced in the sensor windings is given by

$$V_{meas} = NA\frac{dB}{dt}. \tag{4.1}$$

The CAD model, printed and wound sensor cubic, and field measurement setup are shown in Figure 4.5a. The impedances of the three windings were measured with an impedance analyzer and are plotted in Figure 4.6. Due to the high-frequency self-resonance of the sensor windings, an RC filter was used to damp the high-frequency voltages. The effect of the RC filter is included in the calculation of the stray field from the operating frequency. The parameters of the cubic and RC-filter are given in Table 4.3.

4.2 Surface Field Measurements

After the coil set was manufactured, measurements were taken of the surface field of the coils for comparison to the model output. These measurements captured the magnitude of the B_z component of the surface field on a 5 cm grid by measuring the induced voltage in a sensing coil. For the test, an 85 kHz current was produced by a power amplifier and function generator. An image of this test is given in Figure 4.7. The parameters of the sensing coil

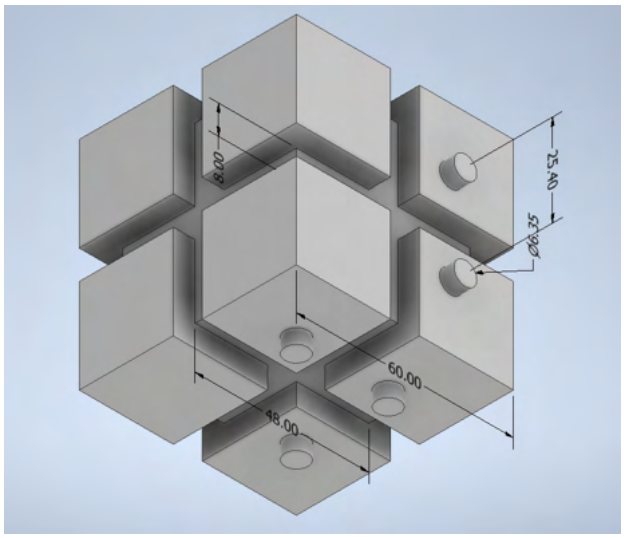

(a)

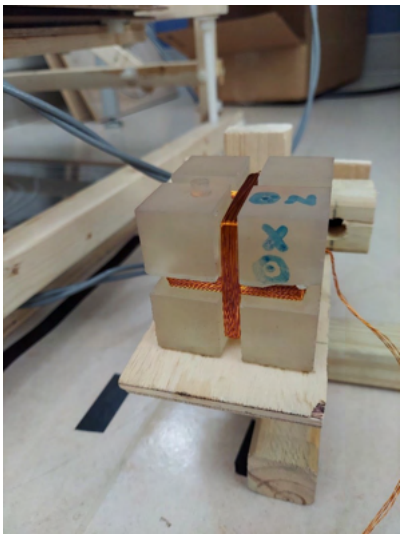

(b)

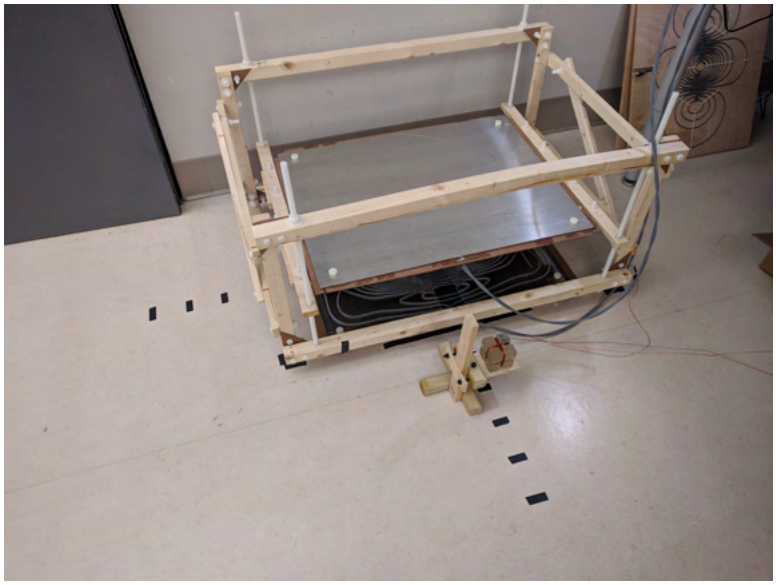

(c)

Figure 4.5: Field measurement setup for the 6.6 kW demonstrator: (a) CAD model of the custom field sensor cubic of Table 4.3. (b) 3D printed field sensor on adjustable wooden stand (c) Field measurement setup.

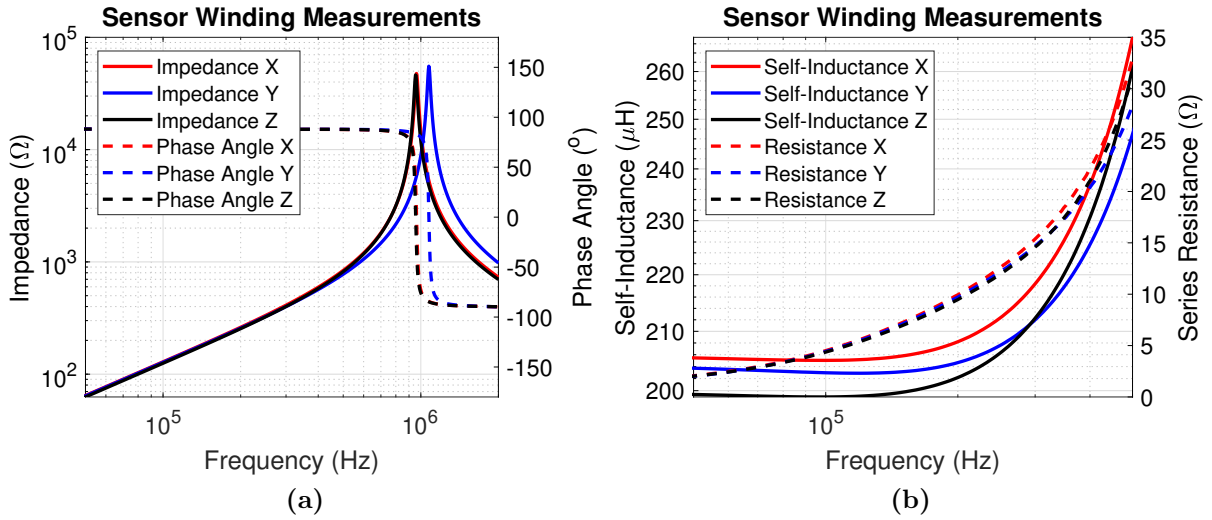

Figure 4.6: Field sensor cubic impedance: (a) Measured impedance and phase of the three sensor windings. (b) Measured inductance and resistance of the three sensor windings.

Table 4.3: Sensor Cubic Values

Parameter	Value	
Magnet Wire AWG	30 AWG	
Number of Turns	$N = 45$ turns	
Turn Area	$A = 23.04$ cm^2	
Field Sensitivity (dV/dB)	50.5 kHz	32.9 mV/μT
	86.5 kHz	56.4 mV/μT
	121.5 kHz	79.2 mV/μT
RC Filter Values	R =1.6 kΩ	
	C =300 pF	
RC Corner Frequency	300 kHz	

are given in Table 4.4. As shown, the magnitudes of the measured fields match well to the model. Most error is due to the averaging of the fields within the sensing coil area vs. the point-wise field of the model.

4.3 Experimental System Measurements

With the experimental system and the models described in the previous sections, a series of tests were performed to compare the loss and field models with the experimental values. The parameters used to model the system performance are given in Table 4.5. In all cases, the airgap and alignment of the system were set by a speed square, meter stick, and level. With this measurement method, some error in misalignment or airgap is possible and errors up to +/- 10 mm or +/- 10° were observed in repeated measurements, especially when setting precise translational and rotational misalignment. Likewise, when manually measuring the fields using the setup in Figure 4.5c, the X-Y position and the vertical location relative to the center of the airgap was prone to some error. Plots of the field measurements can be found in Appendix B.

Two power supplies were used in the tests: a Keysight N8935A for the high-power tests and a BK Precision PVS60085MR for the lower-power tests. A BK Precision 8612 electronic load was used alone or in parallel with the wirewound resistors for the low-power tests. For the high-power tests, the wirewound resistor bank alone was used. Due to the limited availability of the Keysight N8935A power supply during testing, many test points are limited by the current rating of the BK Precision power supply: 600 V, 8.5 A, 3 kW. The system waveforms were obtained with a Tektronix MSO4104B-L and the field voltages were obtained with a Tektronix MDO3104. The DC current and voltage measurements used to derive efficiency were obtained by multimeter or power supply current measurements and by multimeter Kelvin connections, respectively. For these series of tests, the system was run in open-loop with constant load resistance.

Table 4.4: Surface Field Sensor Parameters

Parameter	Value	
Magnet Wire AWG	26 AWG	
Number of Turns	$N = 45$ turns	
Turn Area	$A = 7.55$ cm^2	
Field Sensitivity (dV/dB)	85 kHz	18.1 mV/µT

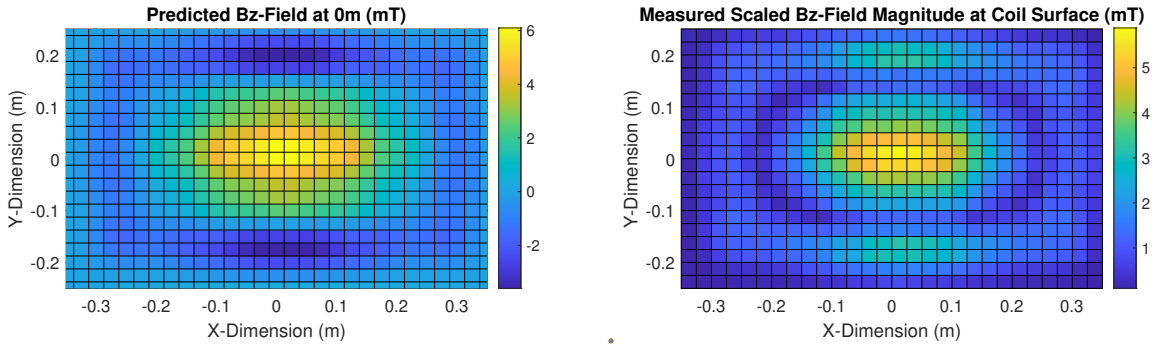

(a) **(b)**

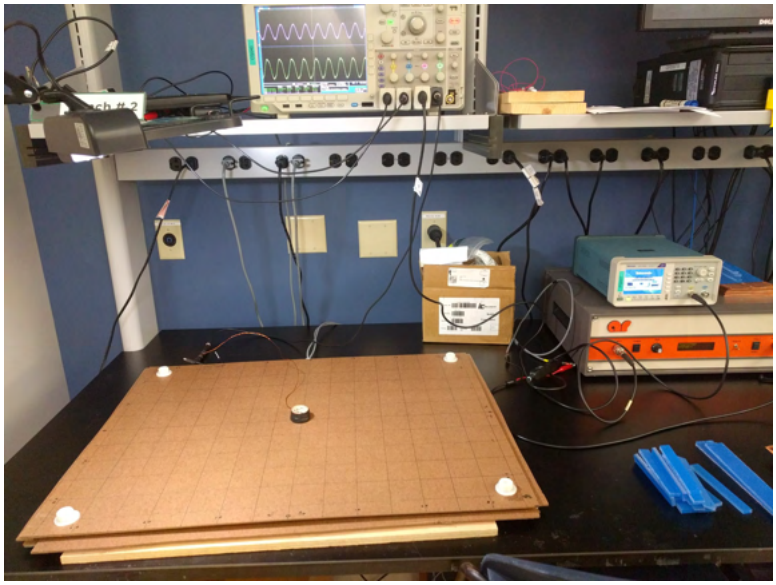

(c)

Figure 4.7: Surface field measurement of 6.6 kW coil: (a) Predicted surface B_z of coil. (b) Scaled measured surface B_z of coil. (c) Measurement setup with power amplifier.

Table 4.5: Loss Model Parameter Definitions and Values

Parameters		Value	Note
Ferrite Steinmetz Parameters		$\mu_r = 2000$ $C_m = 92.116\text{e-}3$ mW/cm^3 α =1.045 β =2.440	Ferroxcube 3C95 Technical Datasheet
Ferrite Temperature Coefficients		$C_t = 1.332$ $C_{t1} = 0.0079$ $C_{t2} = 4.62\text{e-}5$	Ferroxcube 3C95 Technical Datasheet
Temperature of Ferrite		T_{fer} =20°C	Observed Ferrite Temperature
Ferrite Thickness		$t_{fer} = 2.7$ mm (outer) $t_{fer} = 5$ mm (inner)	PLT38/25/2.7 PLT64/50/5
Litz Wire	Outer Wire Diameter Number of Strands Strand Diameter Bunching Operations Wire Length	$d_{out} = 3.8$ mm $n = 1100$ $d_{str} = 0.0787$ mm $N_b = 1$ $N_c = 2$ $L_T = 29.8$ m	NEW 10 AWG (5x5/44/40) Technical Datasheet Measured Value
Compensation Capacitor		$\tan\delta$ see Figure 3.14	Manufacturer Curve
Inverter On-Resistance		R_{DS} =45 mΩ	ON Semiconductor NVHL040N120SC1 Datasheet
Diode Model Curve Fit		$V_f = 0.913$ V $R_f = 36.6$ mΩ/2	Curve Fit of Meas.
Temperature Coefficient of Copper		$C_{Cu,t} = +0.393\%/°\text{C}$	
Temperature of Copper		$T_{Cu} = 38°\text{C}$	Maximum Observed Wire Temp.
Gap Between Ferrite and Wire Plane		$z_g = 7.5$ mm	Estimated Distance

4.3.1 Impedance Measurements

In Table 4.6, the measured and calculated inductances of the system are compared. The measurements were obtained with an Agilent Technologies E4990A impedance analyzer. As measured, the self-inductance of the coils will change as a function of airgap due to the presence of ferrite across the airgap. The FAM model also captures this effect. This change in self-inductance will slightly change the resonant frequency of the tank. To account for this effect, the operating frequency is chosen such that the input impedance is inductive for the largest airgap, when the coil self-inductances are lowest and the tank resonant frequency is the highest. The airgap used in this document is defined as the magnetic airgap of the system, the distance between the ferrite of the coils. The ground clearance of the coils will be approximately 1/2 in (12.7 mm) less than this value due to the thickness of the coil former.

In Figure 4.8, the measured series tank impedances of the primary and secondary tanks are shown when tuned for the 50.5 kHz, 86.5 kHz, and 121.5 kHz operating points. To achieve the necessary voltage ratings and the nominal resonant frequency of 85 kHz, three 50 nF capacitors were used. The 50.5 kHz and 121.5 kHz frequencies were then chosen to be compatible with alternative combinations of 50 nF capacitors. The different tuning configurations were obtained by modifying the capacitor banks in the following manner:

- 50.5 kHz: 2 Series of 2 Parallel 50 nF Capacitors = 50 nF
- 86.5 kHz: 3 Series of 50 nF Capacitors = 16.6 nF
- 121.5 kHz: 6 Series of 50 nF Capacitors = 8.3 nF

The parasitic series resonances of the tanks were seen to produce a high-frequency resonant point in the tanks, as seen in the later test results. This current may cause Electromagnetic Interference or Electromagnetic Compatibility (EMI/EMC) compliance issues and losses. This is especially seen in the high-impedance 121.5 kHz operating point at 125 mm, where the high-frequency current was approximately 1/10th of the primary current at the nominal frequency. This motivates the investigation of the impact of different tuning networks and different winding approaches on EMI/EMC compliance. Due to the

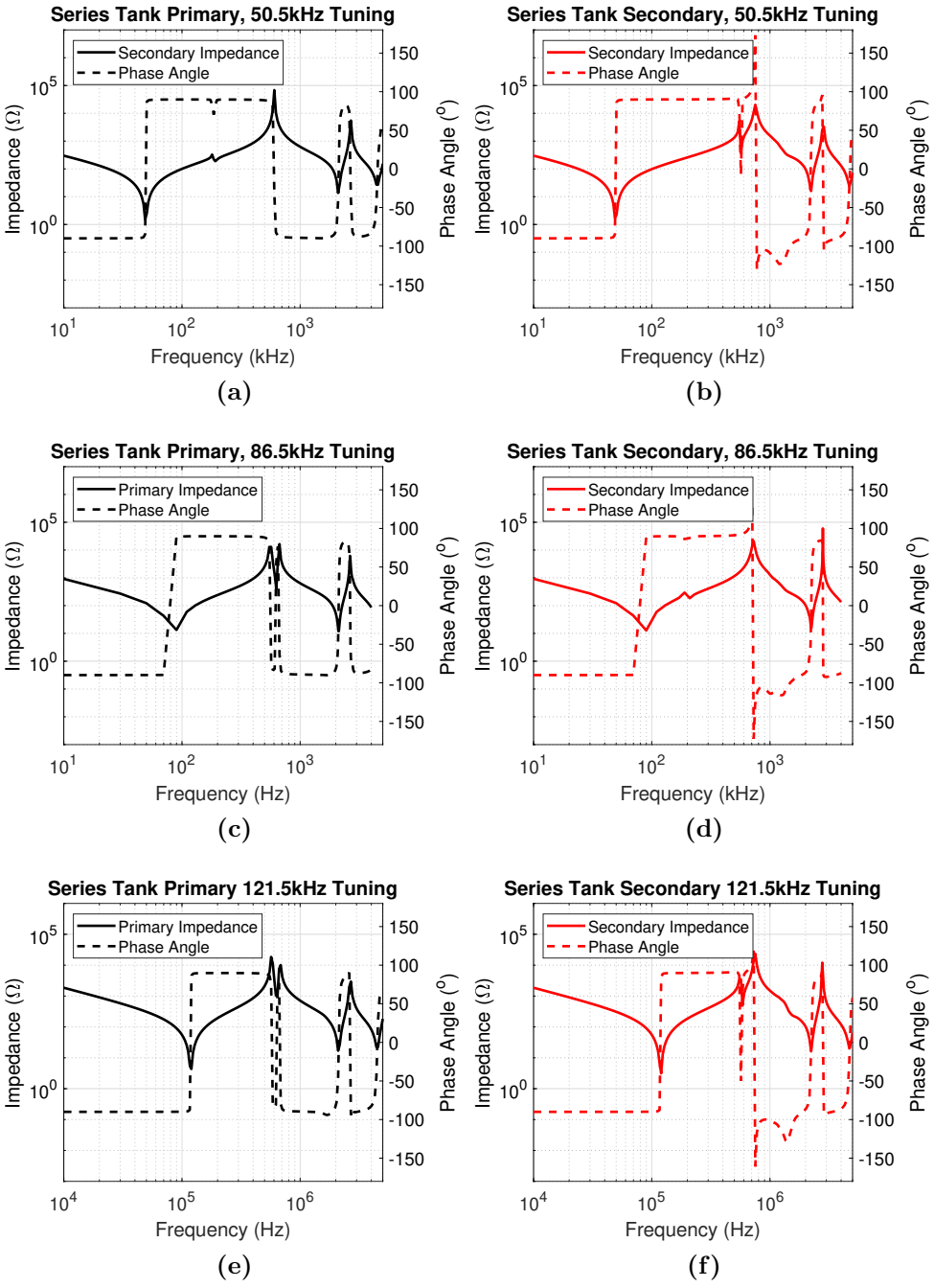

Figure 4.8: Tank impedance of the 6.6 kW system: (a) primary and (b) secondary tanks at 50.5 kHz tuning, the (c) primary and (d) secondary tanks at 86.5 kHz tuning, and the (e) primary and (f) secondary tanks at 121.5 kHz tuning.

spacing of the frequency sweep, the behavior around the resonant points may not capture the impedance of the resonant point, where the tank impedance is equal to the series resistance.

4.3.2 Measurements at 50.5 kHz

A series of tests were performed at 50.5 kHz to assess the stray field and efficiency. At this frequency, the impedance of the system was lower than the other frequencies, requiring higher currents. This limited the output power of the test to under 1 kW as in Figure 4.10. This lower impedance reduced the efficiency compared to the 86.5 kHz operating frequency. The increase current also increased the measured stray field of the system as in Table 4.7. Complete field measurements are in Appendix B. Efficiency measurements of the system at 125 mm, 210 mm, and 250 mm are shown in Figures 4.9, 4.11, and 4.13 respectively. Waveforms of the system are given for the 125 mm, 210 mm, and 250 mm airgaps at alignment in Figures 4.10, 4.12, and 4.14, respectively.

In these results, the peak efficiency as a function of load shifts as the power level and input voltage increases as in Figures 4.9a, 4.11a, and 4.13a. This is mainly due to the efficiency of the rectifier at low power levels dominated by the forward voltage of the diodes. At higher power levels, this effect is less pronounced compared to the other loss mechanisms.

4.3.3 Measurements at 86.5kHz

A series of tests at 86.5 kHz were performed at alignment and misalignment to confirm the models at the nominal operating frequency range. At an alignment and airgap of 210 mm, the system was tested at full power to 6.7 kW as in Figure 4.17. The frequency of this initial test was set to 86 kHz instead of 86.5 kHz. It was found that the increased frequency was needed to achieve better soft switching over misalignment and other airgaps for the other test points. Thermal images of the coil and power electronics were also taken to assess the thermal effects on the system in Figures 4.17d, 4.17e. Efficiency measurements of the system at 125 mm, 210 mm, and 250 mm are shown in Figures 4.16, 4.18, and 4.20 respectively. Waveforms of the system are given for the 125 mm, 210 mm, and 250 mm airgaps at alignment in Figures 4.15, 4.17, and 4.19 respectively. Stray field measurements at

Table 4.6: Calculated Inductance Values vs. Measurements

Airgap	Parameter	Model	Measured	Error (%)
125mm	Self Inductance L_1, L_2	224.9 µH	218.9 µH, 217.2 µH	2.7%, 3.5%
	Mutual Inductance M	82.6 µH	79.9 µH	3.3%
210mm	Self Inductance L_1, L_2	204.5 µH	205.4 µH, 203.8 µH	-0.4%, 0.3%
	Mutual Inductance M	31.9 µH	30.2 µH	5.3%
250mm	Self Inductance L_1, L_2	201.7 µH	200.3 µH, 199.7 µH	0.7%, 1.0%
	Mutual Inductance M	21.7 µH	20.0 µH	7.8%

Table 4.7: Summary of Scaled Stray Field (RMS) Measurements at 0.8 m, 50.5 kHz and 6.6 kW

Airgap	Scaled Measured Values (X,Y)
125 mm	1.9 µT, 1.7 µT
210 mm	5.1 µT, 4.4 µT
250 mm	7.4 µT, 6.1 µT

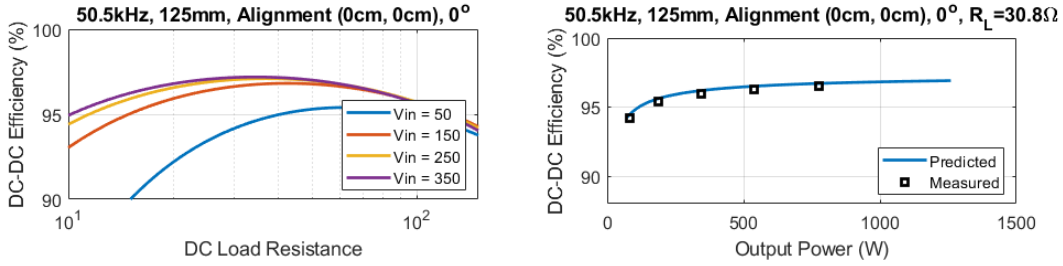

(a) **(b)**

Figure 4.9: Experimental results and model outputs at 50.5 kHz, 125 mm. (a) Modeled efficiency of system over load resistance at alignment. (b) Model efficiency vs. measurement at alignment.

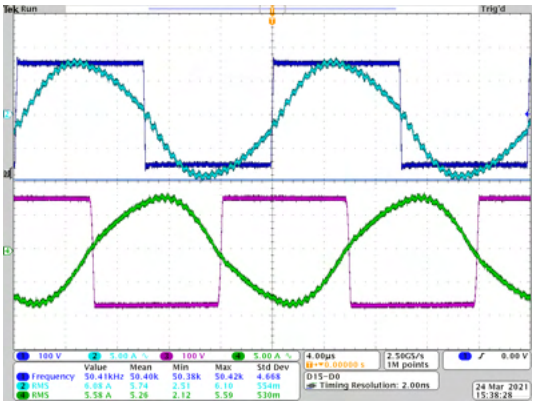

(a)

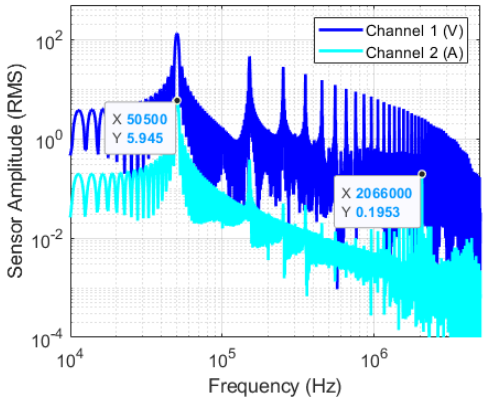

(b)

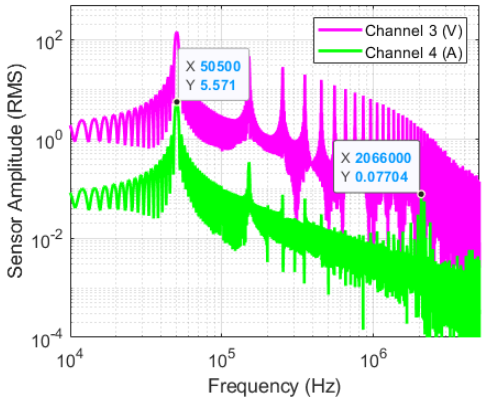

(c)

Figure 4.10: Experimental waveforms at 777 W and 50.5 kHz, 125 mm at alignment. (a) Waveforms of switch node voltages and currents. CH1: Blue primary switch node voltage, CH2: cyan primary current, CH3: magenta secondary switch node voltage, and CH4: green secondary current. (b) Frequency components of CH1 and CH2. (c) Frequency components of CH3 and CH4.

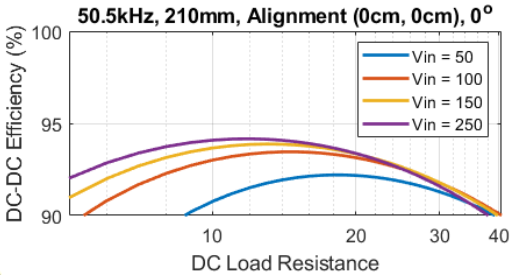

(a)

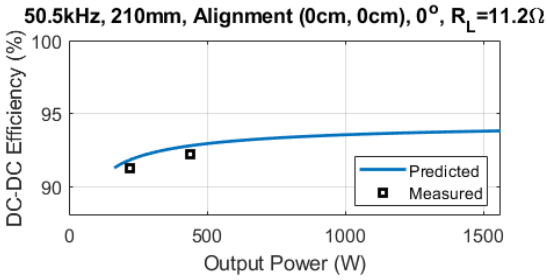

(b)

Figure 4.11: Experimental results and model outputs at 50.5 kHz, 210 mm. (a) Modeled efficiency of system over load resistance at alignment. (b) Model efficiency vs. measurement at alignment.

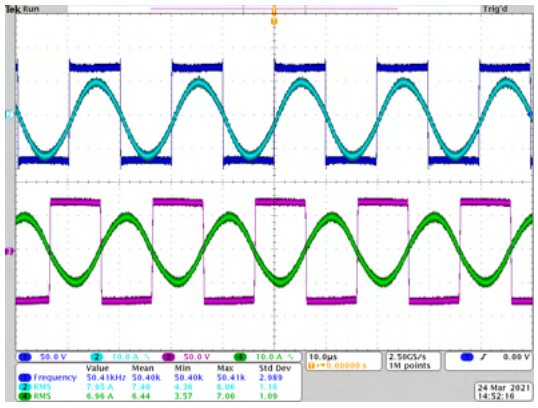

(a)

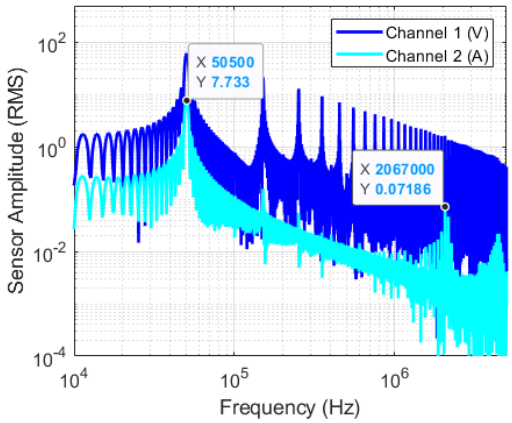

(b)

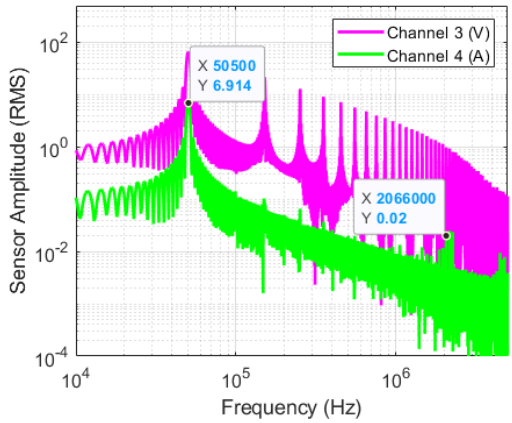

(c)

Figure 4.12: Experimental waveforms at 438 W and 50.5 kHz, 210 mm at alignment. (a) Waveforms of switch node voltages and currents. CH1: Blue primary switch node voltage, CH2: cyan primary current, CH3: magenta secondary switch node voltage, and CH4: green secondary current. (b) Frequency components of CH1 and CH2. (c) Frequency components of CH3 and CH4.

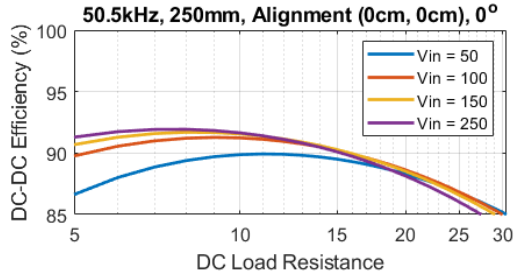

(a)

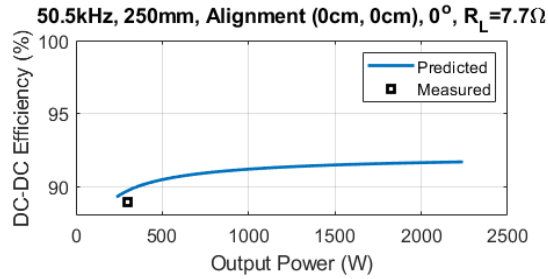

(b)

Figure 4.13: Experimental results and model outputs at 50.5 kHz, 250 mm. (a) Modeled efficiency of system over load resistance at alignment. (b) Model efficiency vs. Measurement at alignment.

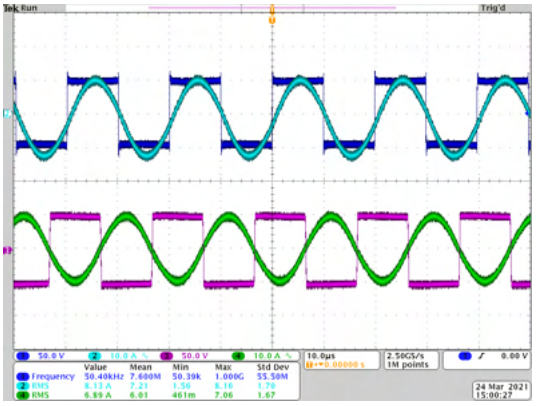

(a)

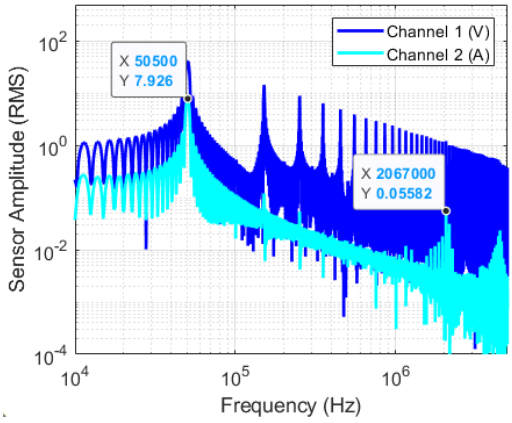

(b)

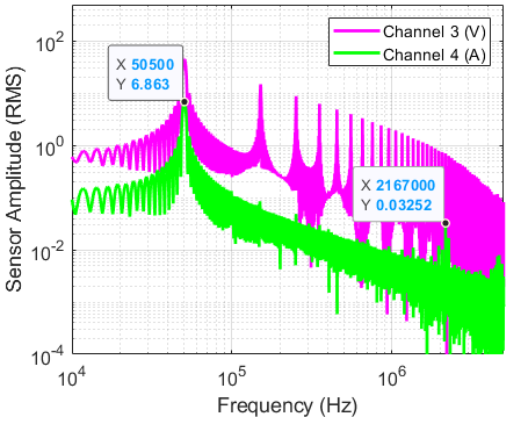

(c)

Figure 4.14: Experimental waveforms at 297 W and 50.5 kHz, 250 mm at alignment. (a) Waveforms of switch node voltages and currents. CH1: Blue primary switch node voltage, CH2: cyan primary current, CH3: magenta secondary switch node voltage, and CH4: green secondary current. (b) Frequency components of CH1 and CH2. (c) Frequency components of CH3 and CH4.

alignment and misalignment are summarized in Table 4.8. The complete field measurements are given in Appendix B.

At the 86.5 kHz operating point, the input impedance of the system was high, especially at the 125 mm airgap operating point. This drove the coil current lower, reducing the overall losses and driving efficiency to a peak of 97.6% DC-DC efficiency when aligned at 125 mm airgap. High-frequency parasitic resonances in the coils were also low at this point compared to the 121.5 kHz operating frequency.

4.3.4 Measurements at 121.5 kHz

Tests at 121.5 kHz were performed at alignment and misalignment to confirm the models at the nominal operating frequency range. Efficiency measurements of the system at 125 mm, 210 mm, and 250 mm are shown in Figures 4.21, 4.24, and 4.26 respectively. Waveforms of the system are given for the 125 mm, 210 mm, and 250 mm airgaps at alignment in Figures 4.22, 4.23, and 4.25 respectively. Stray field measurements at alignment are summarized in Table 4.9. The complete field measurements are given in Appendix B.

At the 121.5 kHz operating point, the parasitic resonance of the coils produced a high-frequency current that lowered the overall efficiency of the system, especially when the input impedance of the system was high as in Figure 4.22. In the test points, a harmonic current was observed at 2.06 MHz, close to the parasitic self-resonant frequency of the coils measured in Figure 4.8. The 2.06 MHz frequency is close to the 17th harmonic of 121.5 kHz, whereas it is close to the 24th harmonic of 86.5 kHz, which is minimal with square-wave excitation. This high-frequency current lowers the efficiency by producing the additional losses estimated in Figures 4.21b, 4.24b, 4.26b. The lower efficiency slightly increases the required fundamental current relative to what would be predicted in the models of the WPT system that are based on the first-harmonic approximation. The increased fundamental current increases the fields present in the system in the high-impedance operating points, making the 121.5 kHz stray fields similar to those of the 86.5kHz operating frequency as seen in Tables 4.1, 4.2.

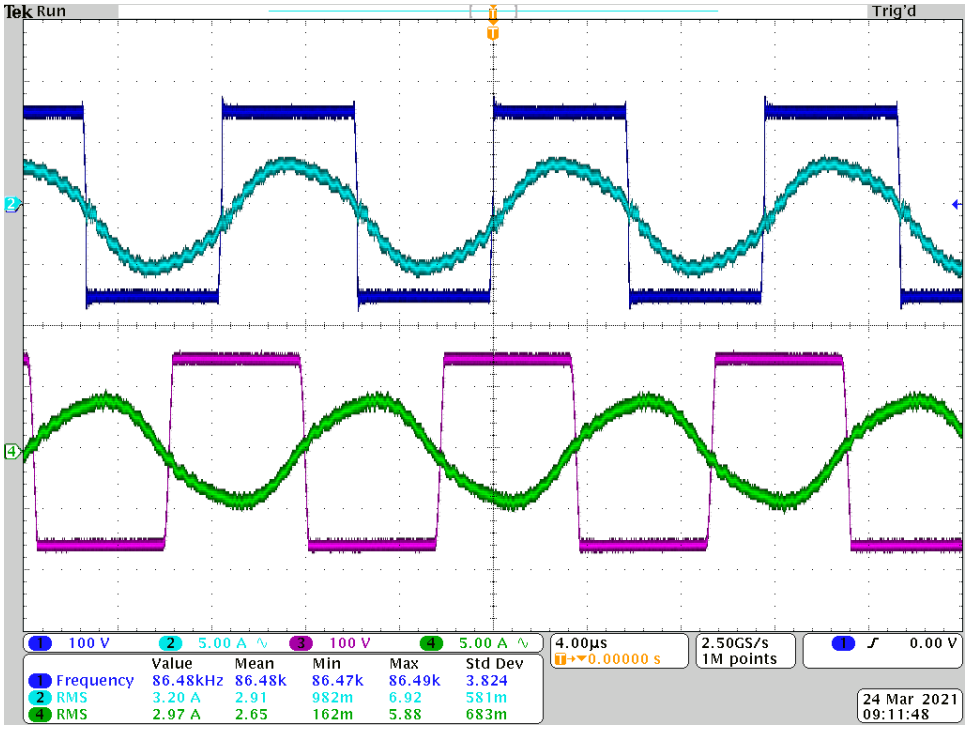

(a)

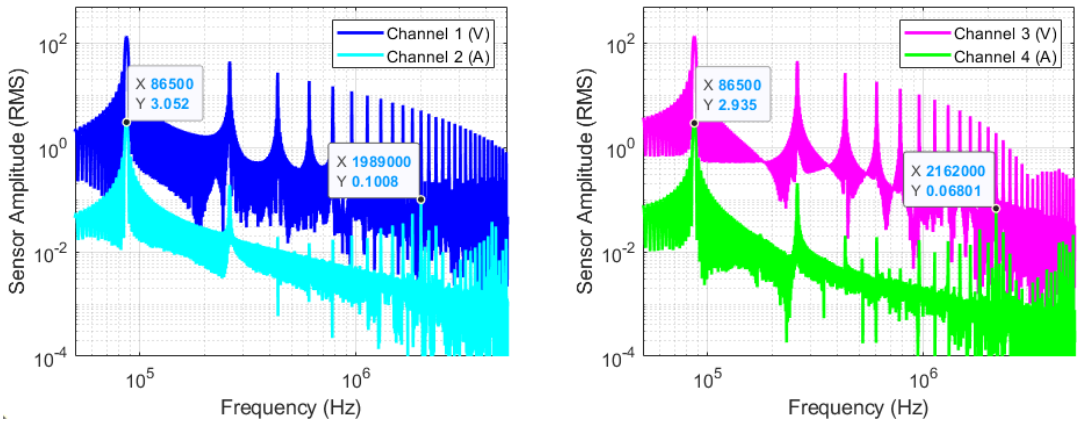

(b) (c)

Figure 4.15: Experimental waveforms at 369 W and 86.5 kHz, 125 mm at alignment. (a) Waveforms of switch node voltages and currents. CH1: Blue primary switch node voltage, CH2: cyan primary current, CH3: magenta secondary switch node voltage, and CH4: green secondary current. (b) Frequency components of CH1 and CH2. (c) Frequency components of CH3 and CH4.

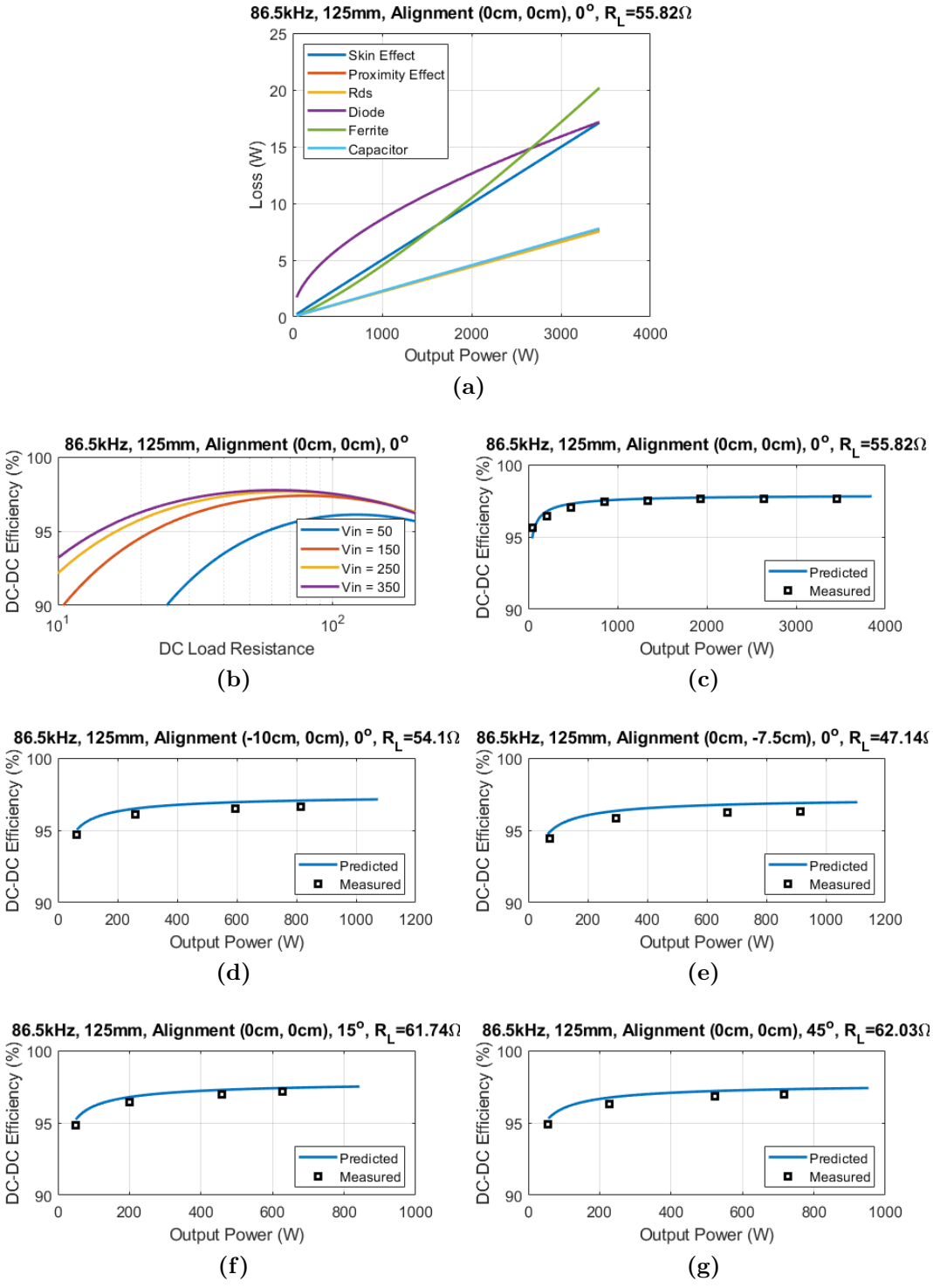

Figure 4.16: Experimental results and model outputs at 86.5 kHz, 125 mm. (a) Loss breakdown of the system at alignment over varying output resistances. (b) Modeled efficiency of the system over load resistance at alignment. (c) Model efficiency vs. Measurement at alignment. (d) at -10 cm in the X-direction (e) at -7.5 cm in the Y-direction, (f) at 15° rotation, and (g) at 45° rotation.

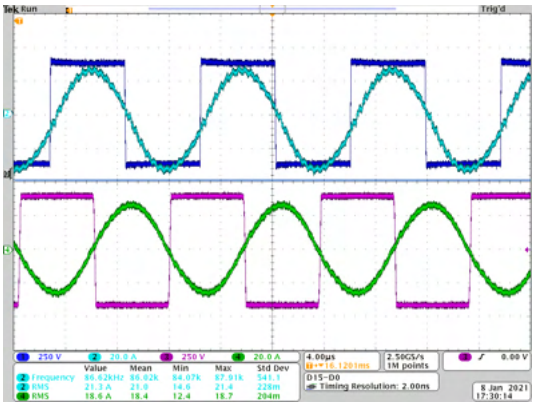

(a)

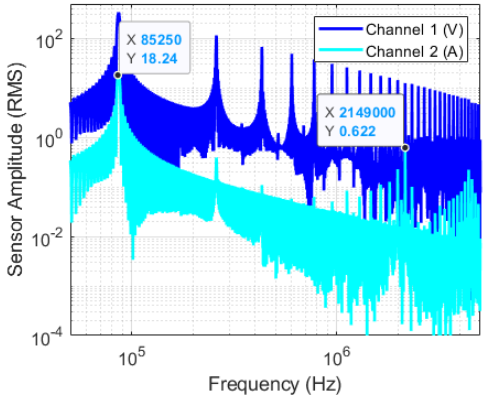

(b)

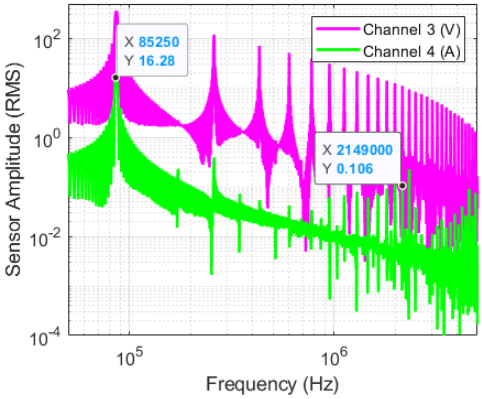

(c)

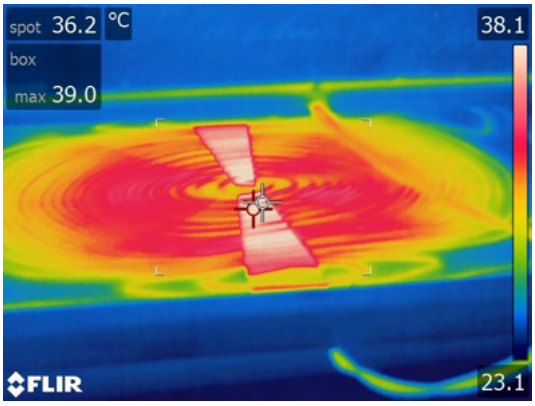

(d)

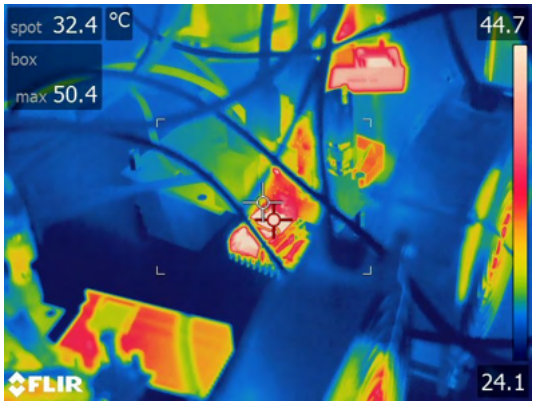

(e)

Figure 4.17: Experimental results at 6.7 kW and 86 kHz, 210 mm at alignment. (a) Waveforms of switch node voltages and currents. CH1: Blue primary switch node voltage, CH2: cyan primary current, CH3: magenta secondary switch node voltage, and CH4: green secondary current. (b) Frequency components of CH1 and CH2. (c) Frequency components of CH3 and CH4. (d) Thermal image of secondary coil showing a maximum wire temperature of 39°C. (e) Thermal image of the inverter (top) and rectifier (bottom) heat sinks.

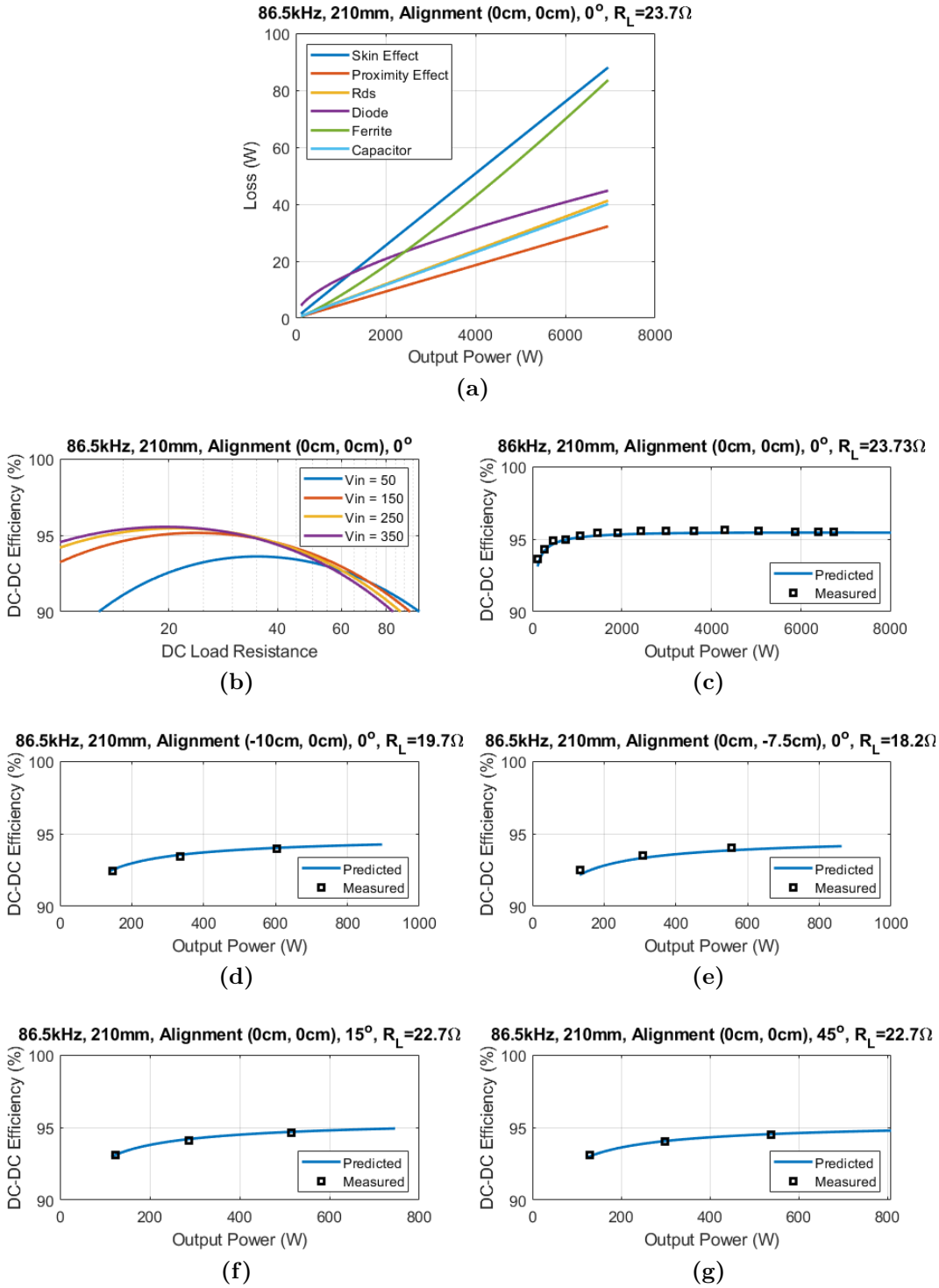

Figure 4.18: Experimental results and model outputs at 86.5 kHz, 210 mm. (a) Loss breakdown of the system at alignment over varying output resistances. (b) Modeled efficiency of system over load resistance at alignment. (c) Model efficiency vs. Measurement at alignment. (d) at -10cm in the X-direction (e) at -7.5 cm in the Y-direction, (f) at 15° rotation, and (g) at 45° rotation.

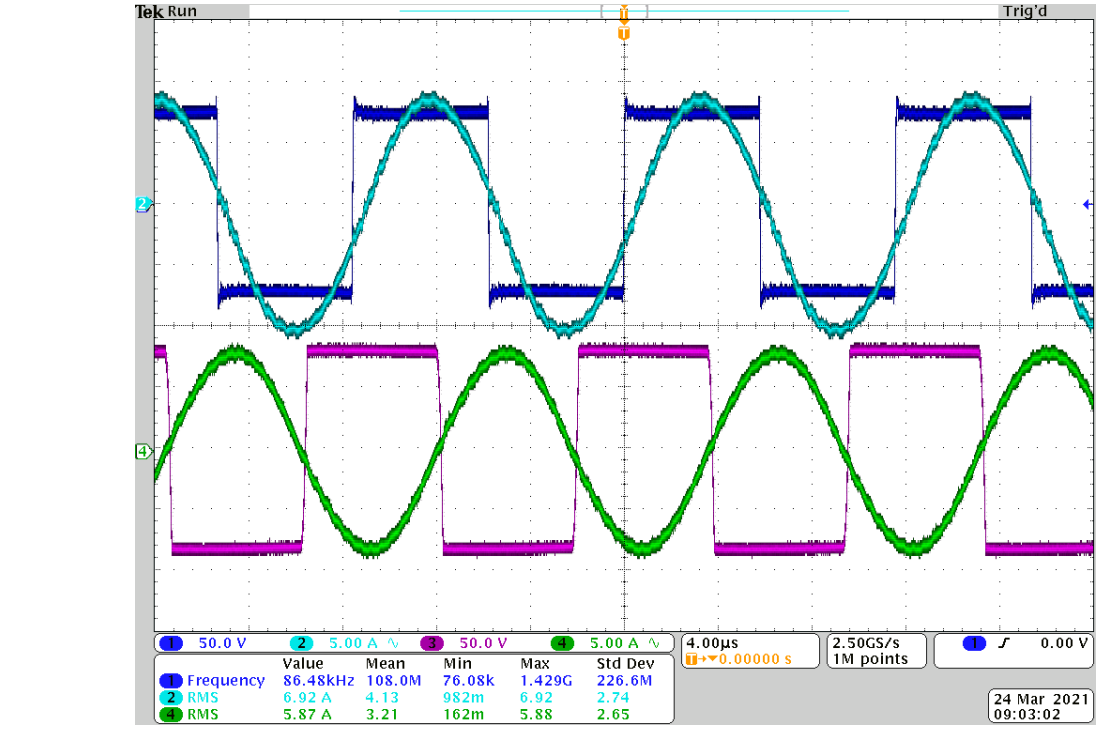

(a)

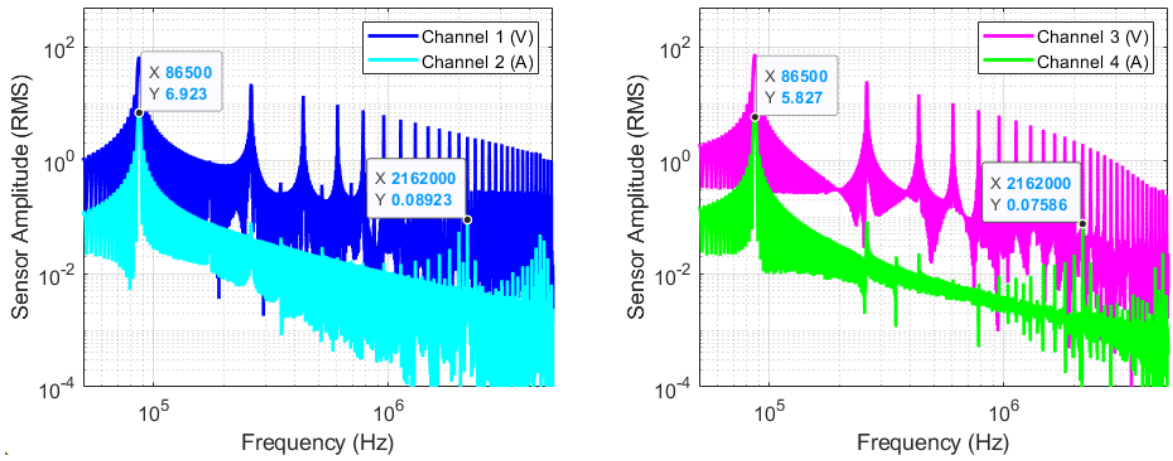

(b) (c)

Figure 4.19: Experimental results at 421 W and 86.5 kHz, 250 mm at alignment. (a) Waveforms of switch node voltages and currents. CH1: Blue primary switch node voltage, CH2: cyan primary current, CH3: magenta secondary switch node voltage, and CH4: green secondary current. (b) Frequency components of CH1 and CH2. (c) Frequency components of CH3 and CH4.

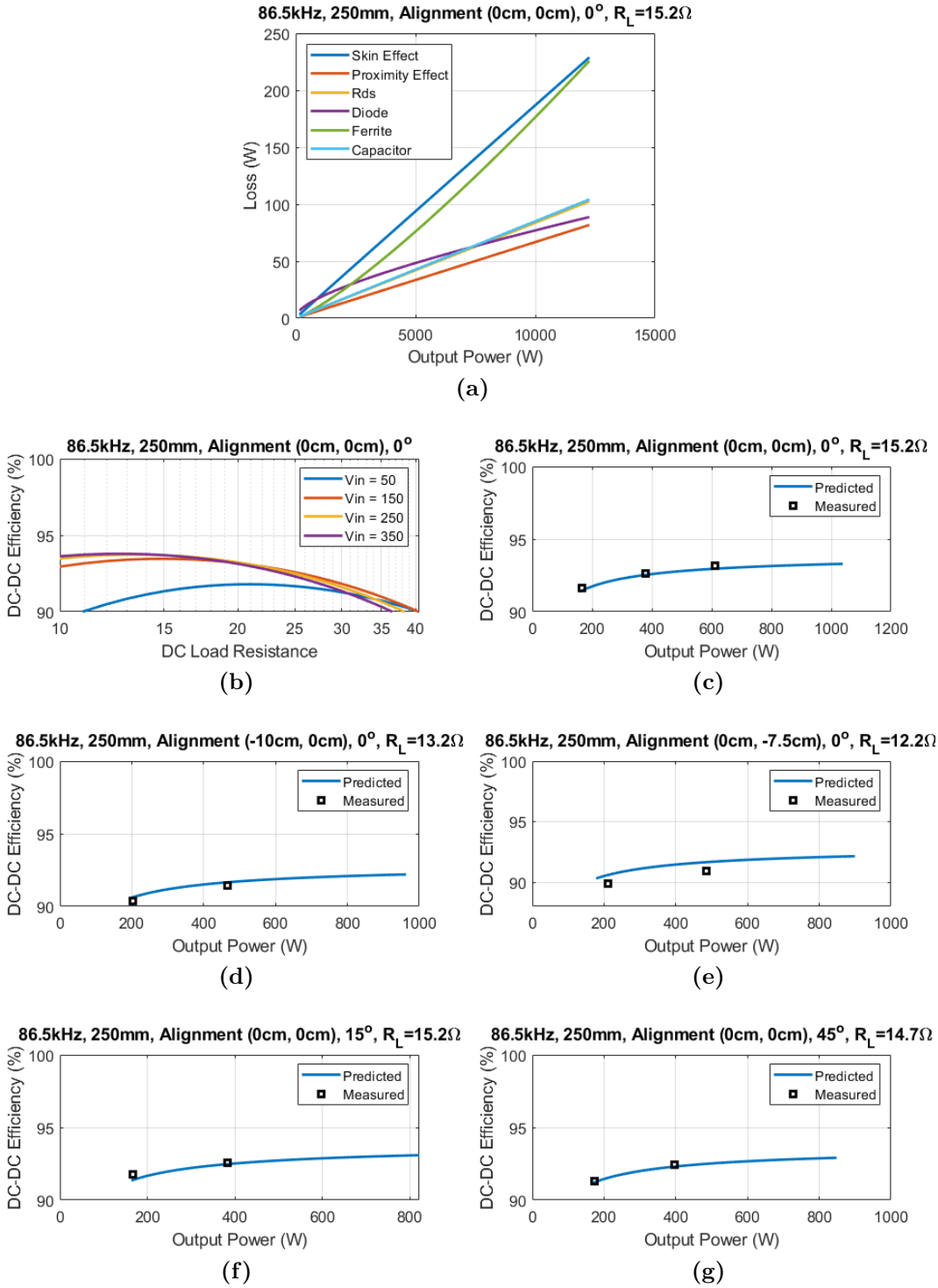

Figure 4.20: Experimental results and model outputs at 86.5 kHz, 250 mm. (a) Loss breakdown of the system at alignment over varying output resistances. (b) Modeled efficiency of system over load resistance at alignment. (c) Model efficiency vs. Measurement at alignment. (d) at -10 cm in the X-direction (e) at -7.5 cm in the Y-direction, (f) at 15° rotation, and (g) at 45° rotation.

Table 4.8: Summary of Scaled Stray Field (RMS) Measurements (X,Y) at 0.8 m, 86.5 kHz and 6.6 kW

Misalignment (X,Y) Airgap	0 cm, 0 cm	-10 cm, 0 cm	0 cm, -7.5 cm
125 mm	1.8 µT, 1.4 µT	4.5 µT, 1.8 µT	2.1 µT, 3.1 µT
210 mm	4.4 µT, 3.6 µT	6.6 µT, 4.2 µT	4.5 µT, 5.6 µT
250 mm	6.5 µT, 4.5 µT	8.9 µT, 5.3 µT	6.6 µT, 7.2 µT

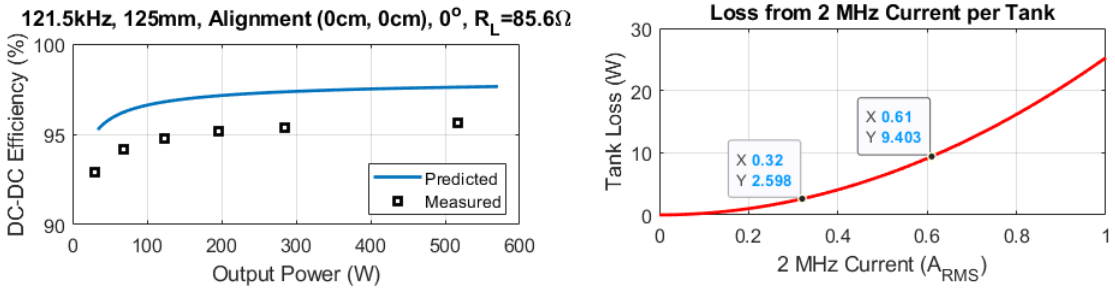

(a) **(b)**

Figure 4.21: Experimental results and model outputs at 121.5 kHz, 125 mm. (a) Experimental measurements vs model without high-frequency current impact and (b) impact estimate.

Table 4.9: Summary of Scaled Stray Field Measurements (RMS) at 0.8 m, 121.5 kHz and 6.6 kW

Airgap	Scaled Measured Values (X,Y)
125 mm	2.0 µT, 1.4 µT
210 mm	4.4 µT, 2.8 µT
250 mm	5.6 µT, 4.2 µT

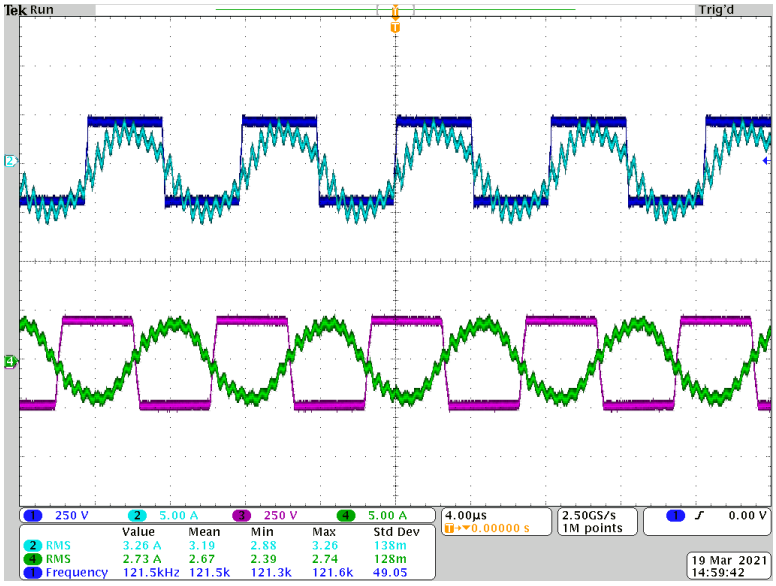

(a)

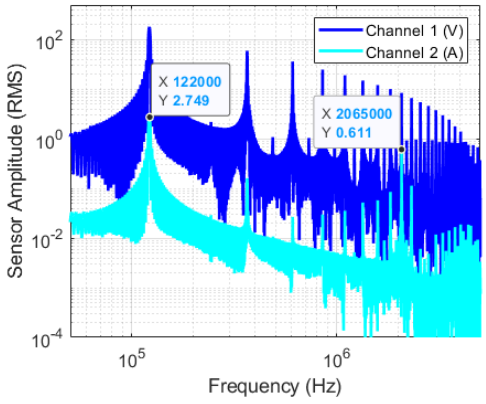

(b)

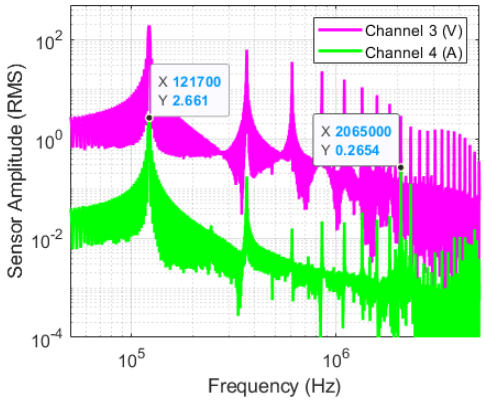

(c)

Figure 4.22: Experimental results at 518 W and 121.5 kHz, 125 mm at alignment. (a) Waveforms of switch node voltages and currents. CH1: Blue primary switch node voltage, CH2: cyan primary current, CH3: magenta secondary switch node voltage, and CH4: green secondary current. (b) Frequency components of CH1 and CH2. (c) Frequency components of CH3 and CH4.

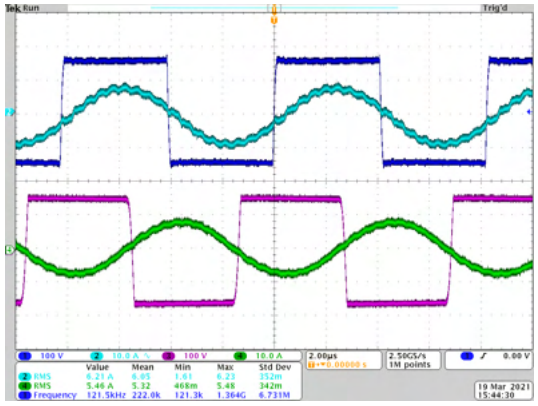

(a)

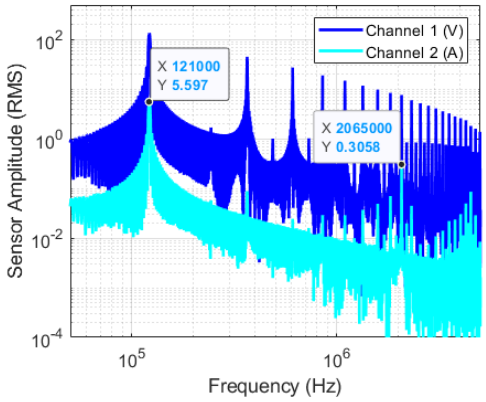

(b)

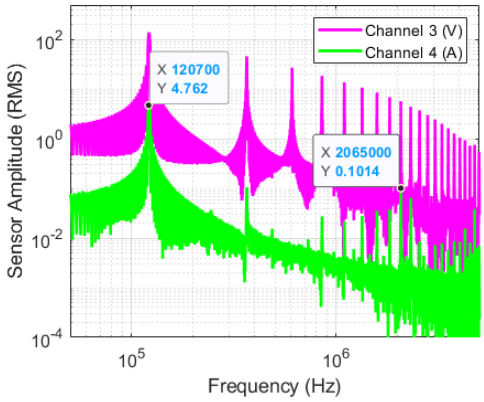

(c)

Figure 4.23: Experimental results at 744 W and 121.5 kHz, 210 mm at alignment. (a) Waveforms of switch node voltages and currents. CH1: Blue primary switch node voltage, CH2: cyan primary current, CH3: magenta secondary switch node voltage, and CH4: green secondary current. (b) Frequency components of CH1 and CH2. (c) Frequency components of CH3 and CH4.

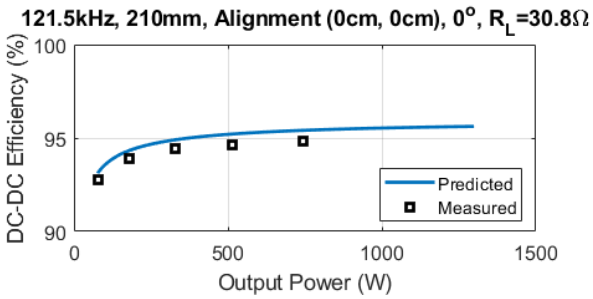

(a)

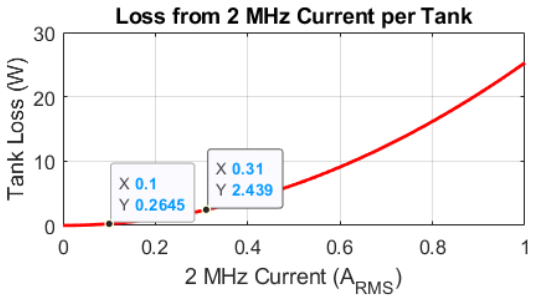

(b)

Figure 4.24: Experimental results and model outputs at 121.5 kHz, 210 mm. (a) Experimental measurements vs model without high-frequency current impact and (b) impact estimate.

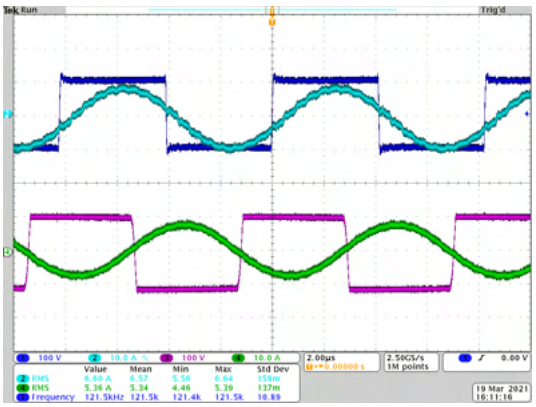

(a)

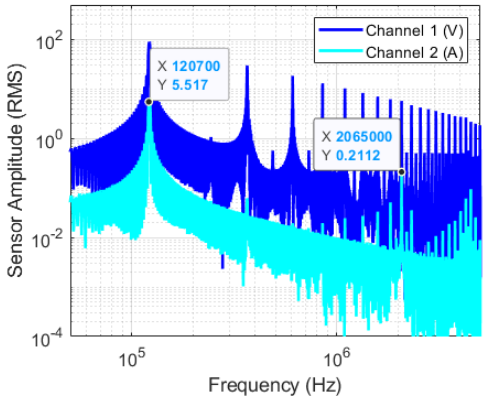

(b)

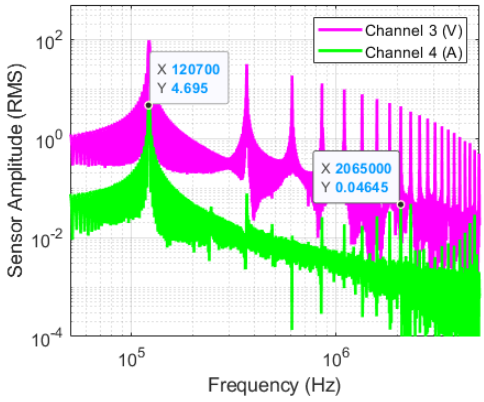

(c)

Figure 4.25: Experimental results at 503 W and 250 mm at alignment. (a) Waveforms of switch node voltages and currents. CH1: Blue primary switch node voltage, CH2: cyan primary current, CH3: magenta secondary switch node voltage, and CH4: green secondary current. (b) Frequency components of CH1 and CH2. (c) Frequency components of CH3 and CH4.

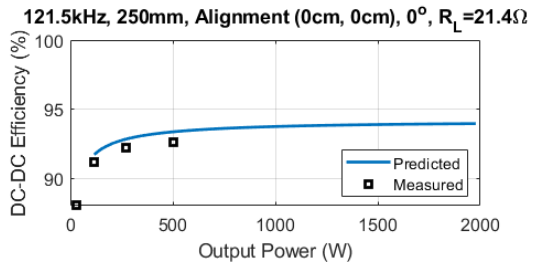

(a)

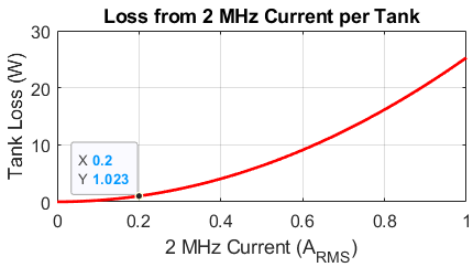

(b)

Figure 4.26: (a) Experimental results and model outputs at 121.5 kHz, 250 mm. Experimental measurements vs model without high-frequency current impact and (b) impact estimate.

Summary

In this chapter, details of the construction and testing of a 6.6 kW demonstrator are given. The measurements show high-efficiency operation over a variety of misalignments and airgaps as well as low stray fields, especially at the lowest 125 mm airgap. Overall the models matched well to the measured values. The 50.5 kHz frequency lowered the impedance of the system, increasing the amount of current required for a given power level and decreasing efficiency relative to the 86.5 kHz frequency. This is expected as the coil turns and conductors were chosen for the 86.5 kHz, not 50.5 kHz. At the higher operating frequency of 121.5 kHz, a parasitic resonance caused a high-frequency ripple which induced additional losses in the system compared to the model prediction. The rise in temperature of the wire and power electronics were captured by thermal camera. Although relatively minor at 6.6 kW, these effects will scale with power level to much higher values for power levels comparable to DC fast charging.

Chapter 5

Design and Testing of High-Power WPT Demonstrators

With the knowledge and model validation from the low power 6.6 kW demonstrator, the loss models and geometry optimization were used to design a system with a nominal power level of 120 kW. The general design targets for this system are given in Table 5.1. The power density targets, 250 kW/m^2 and 4 kW/kg, are based on the systems reviewed in Table 2.1. To far exceed the area-related power density target and help achieve the power density target, a coil area of 0.4 m by 0.5 m was chosen for a power density of around 600 kW/m^2. The realized demonstrator achieved a power density of 530 kW/m^2 and 4.1 kW/kg. Achieving higher power levels and power density required improvements in thermal, mechanical and magnetic performance relative to the 6.6 kW demonstrator. It was more critical to achieve high efficiency at high power levels as large losses would limit the power density by requiring more active cooling or larger component sizes to ensure acceptable operating temperatures. Therefore, improvements to the low-power design were made by analyzing cost, weight, and loss; implementing indirect backside cooling of the coil and capacitors; encapsulating the litz wire and ferrite; and designing a new capacitor bank with better insulation, alignment, and packaging. A Generation 1 (Gen. 1) demonstrator was designed, built, and tested, and then a second Generation 2 (Gen. 2) demonstrator was built to improve on the first, yielding a DC/DC efficiency of 97.2% at 120.1 kW output power at alignment and a 125 mm airgap.

During testing of the first Gen. 1 120 kW demonstrator, higher than expected losses were observed, lowering the efficiency from an expected 96% DC/DC efficiency to 93% DC/DC efficiency due to decreases in coil-coil efficiency at high power levels. These losses made it difficult to effectively cool the system. The analysis of these unexpected losses led to modifications in the Gen. 2 demonstrator, including important changes to the encapsulation material, ferrite layout, and litz wire routing through the ferrite.

5.1 FAM Optimization Outputs

Using methodology and loss modeling similar to that of the low-power demonstrator, an optimization of Fourier basis functions was performed using the parameters summarized in Table 5.2. Here, the same stray field limits used in the optimization of the 6.6 kW demonstrator, $B_{str,lim}$ from 5 µT to 1 mT, were used. The optimization considers stray field measurement extents of $x_{meas} = 0.6$ m and $y_{meas} = 0.6$ m and coil extents of $x_{ext} = 0.4$ m and $y_{ext} = 0.5$ m. The airgap distance is kept to the same $z_{gap} = 0.21$ m as before and the power level is $P = 120$ kW. The optimization outputs are shown in Figure 5.3. Here, the $\cos x \sin y$ basis function has the lowest current to achieve 120 kW at low stray field limits. Using the same $B_{str,lim} = 100$ µT limit as before, the output for $\cos x \sin y$ is seen in Figure 5.3c.

Using this optimization output, the number of turns, thickness of the ferrite, and litz wire size were iterated and the final design was chosen based on cost, weight, and acceptable operation and efficiency over misalignment using the application design targets in Table 5.1. This design process is illustrated in Figure 5.1 and compared with a conventional design process. After the geometry is chosen from the optimization outputs, it is discretized into a number of turns. The optimization is done with an airgap of $z_{gap} = 0.21$ m, but aligned operation at the lowest airgap of the target range, $z_{gap} = 0.125$ m, is considered in the choice of the number of turns. This maximum coupling condition sets the upper limit of the input impedance of the system, which is constrained by the inverter voltage rating. The bipolar geometry also requires an even number of turns. The impact of the number of turns on the nominal current and voltage at unity gain with an airgap of 125 mm at alignment is plotted in Figure 5.2. The choice of 14 turns supports efficient operation at the nominal 120 kW

Table 5.1: Design Targets for the 120 kW Demonstrator

Design Target	Value
Peak Power Level	120 kW
Inverter Input Voltage	$\leq$ 900 V
Battery Voltage Range	400-820 Vdc
DC/DC Efficiency	$\geq$ 95%
Maximum Stray Fields at 0.8 m	$\leq$27 µT(rms)
Power Density	$\geq$ 250 kW/m^2 $\geq$ 4 kW/kg
Ground Clearance	125 mm, 152.4 mm
Misalignment Tolerance	+/- 10 cm (X-axis) +/- 7.5 cm (Y-axis)

Table 5.2: The FAM Optimization Parameters for the 120 kW Demonstrator

FAM Optimization Parameters	Value
Power Level	$P = 120$ kW
Stray Field Limit	$B_{str,lim}$ =5 µT to 1 mT
Field Measurement Extents	$x_{meas} = 0.6$ m and $y_{meas} = 0.6$ m
Coil Extents	$x_{ext} = 0.4$ m and $y_{ext} = 0.5$ m
Airgap	$z_{gap} = 0.21$ m

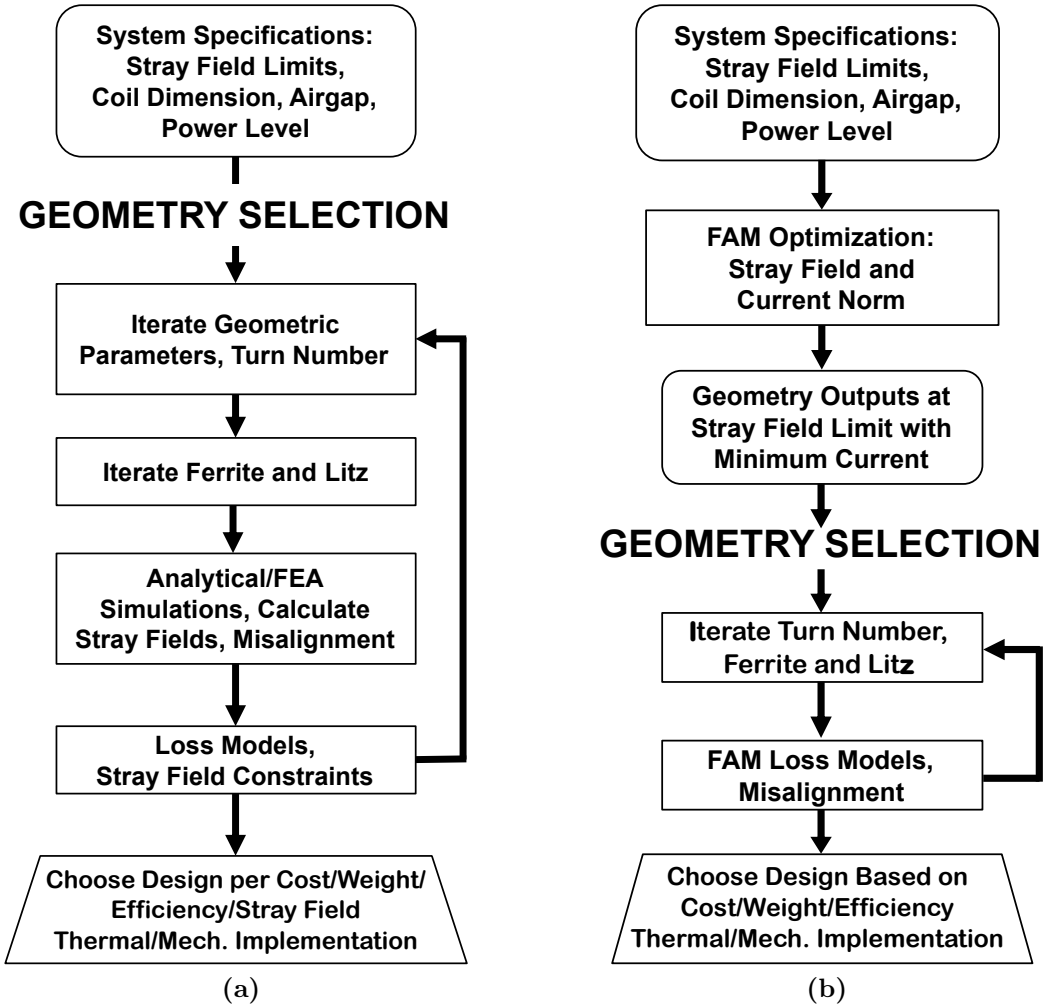

Figure 5.1: Comparison of the conventional design processes and the FAM design method. (a) Flowchart of some conventional design processes using FEA or analytical methods constrained to specific geometries. (b) Flowchart of the FAM design framework where the geometry is chosen through the optimization of the stray field and the current norm first and then used in post-processing steps.

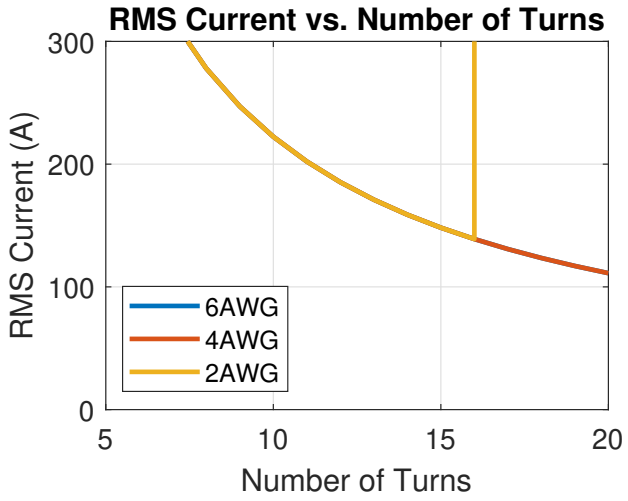

(a)

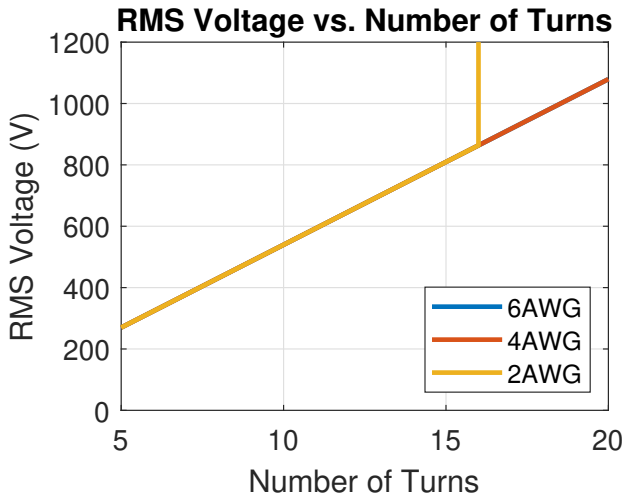

(b)

Figure 5.2: The effect of the number of turns on the (a) nominal RMS current and (b) voltages at 120 kW output power, 125 mm airgap, and alignment for the $\cos x \sin y$ output at $B_{str,avg}$ =100 µT.

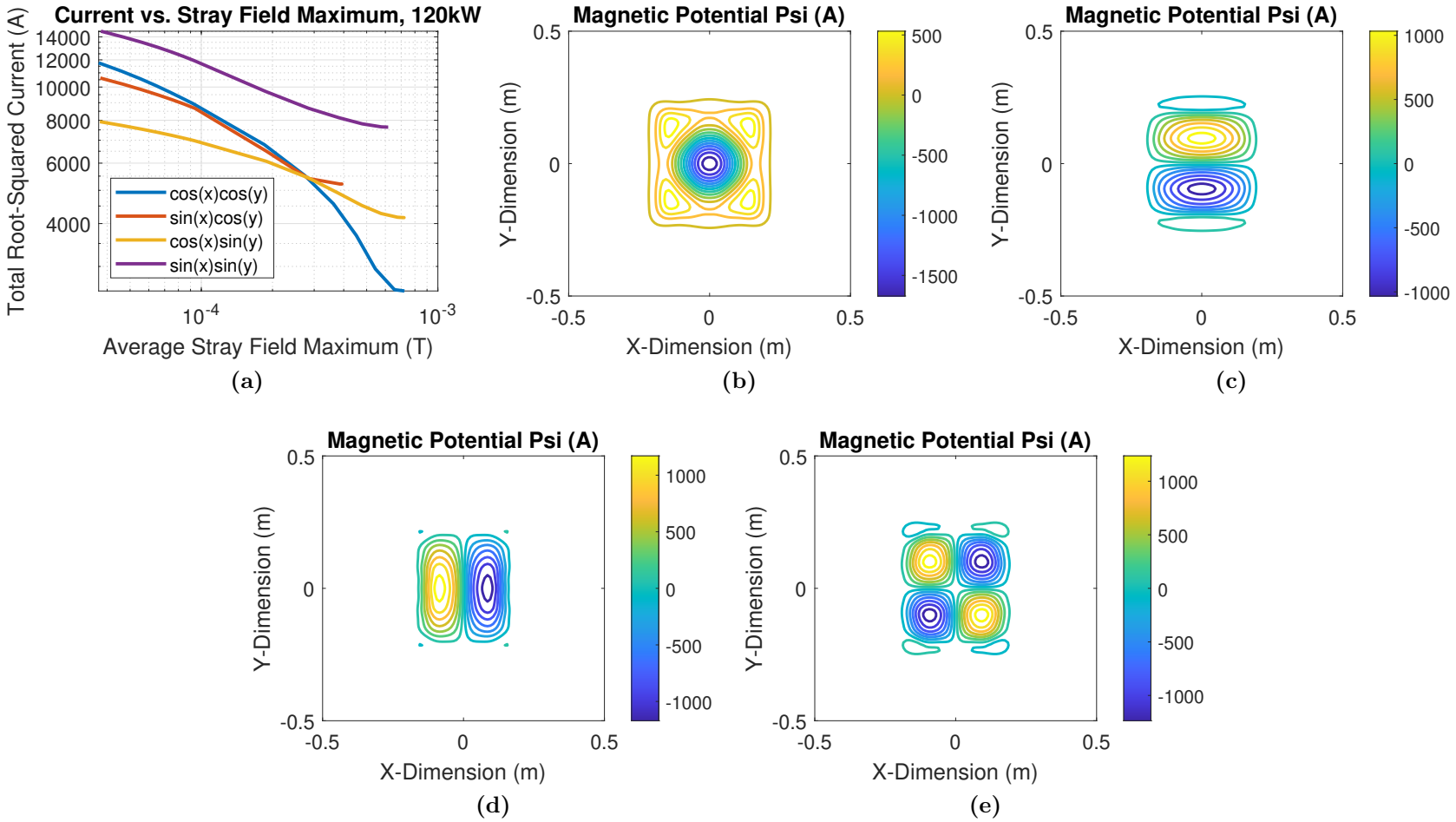

Figure 5.3: FAM optimization for the 120 kW system. (a) Sweep of the basis functions for 120kW design using the parameters $x_{meas} = 0.6$ m and $y_{meas} = 0.6$ m, $z_{gap} = 0.21$ m, and $P = 120$ kW. Scalar potential contours of the (b) $\cos x \cos y$, (c) $\cos x \sin y$, (d) $\sin x \cos y$, and (e) $\sin x \sin y$ outputs with $B_{str,avg}$ =100 µT and 14 turns.

power level with 1.2 kV switching devices with a $\leq$ 900 V inverter DC-link voltage and near-unity voltage gain near the upper end of the 400-820 Vdc battery voltage range. The input and output voltages at unity gain lower at larger airgaps or with misalignment. As discussed further in Chapter 6, depending on the platform battery voltage range, fast charging profile, and ground clearance, the ideal number of turns may be adapted with the same general geometry to optimize efficiency.

5.2 Cost, Weight, and Efficiency Optimization

From the geometry and turn selection of Figure 5.3c, the selection of the conductor type and ferrite thickness is performed with a tradeoff analysis of cost, weight, and loss. In research work, determining the costs of components in scale production is often difficult. Therefore, the cost modeling of this work is done with low-volume prices obtained from manufacturers. At higher volumes, the costs would scale downward. In this analysis, the litz cost model developed in [52] is normalized by quotes of litz wire from New England Wire Technologies at 5000 ft order quantity with equivalent cable gauges of 16 AWG to 2 AWG. Cost is modeled as the price per 1000 ft of litz, C_{Litz}. Similarly, the cost of ferrite per kilogram with a quantity of 1000, as obtained from Digikey, is used in the analysis. These prices were obtained in June 2021.

As introduced in [52], litz wire cost models in the form

$$C_{Litz} = M\left(C_0 + n_{str}d_c^2(1 + \frac{k_1}{d_c^6} + \frac{k_2}{d_c^2})\right) \tag{5.1}$$

where $k_1 = 1.1 \times 10^{-26}$, and $k_2 = 2 \times 10^{-9}$ are curve fit coefficients defined by [52] and $M = 1.15 \times 10^8$ and $C_0 = 9 \times 10^{-6}$ according to the curve fit of the prices as in Figure 5.4a.

The price of the ferrite per kilogram C_{fer} was also modeled as a curve fit as in Figure 5.4b. As shown, the price was very linear with respect to the weight. The cost of Ferroxcube 3C95 ferrite was roughly \$47/kg. The price of TDK N95 ferrite, a ferrite material similar in temperature range and loss performance to Ferroxcube 3C95, was determined to be higher at \$63.4/kg with similar losses as in Figure 5.5 such that the 3C95 material was chosen with

a thickness of 1 cm of ferrite or around 9.8 kg. Similar to the approach of [53], further lightweighting was achieved by reducing the ferrite to 5 mm thickness in the outer region of the ferrite sheet to reduce the weight to around 6.0 kg. This increases the ferrite loss per side from around 161 W to 267 W. The inner region dimension was chosen by using a 6 by 2 grid of 50.8 mm by 64.0 mm ferrite tiles for an overall 30.7 cm by 13.0 cm area. The comparison of the flux density is given in Figure 5.6.

In Figure 5.7, the result of a sweep of litz wire size is plotted in terms of weight, loss, and cost. In these plots, the length of the wire is kept constant at 10.8 m, the length calculated from the contours of the coil geometry, and different gauges of wire are swept according to manufacturer standard litz constructions from 16 AWG to 2 AWG standard gauges of 38 AWG to 44 AWG strands, resulting in points from left to right, respectively. The loss model parameters are given in Table 5.6. Here, as the equivalent gauge of wire is increased more insulated strands of wire are added in parallel which decreases the DC resistance, which normally would decrease the AC resistance and loss of the wire. However, in this case the proximity effect loss from these additional strands offsets and eventually overcomes the decrease in DC resistance in larger gauge of litz wire, especially with the thicker 38 AWG and 40 AWG stranding. This limits the benefit of the thicker equivalent gauges of wire from the loss, cost, and weight perspective. From this analysis, litz wire with equivalent 4 AWG gauge and 42 AWG stranding was chosen as the wire for the demonstrator.

5.3 Thermal Modeling, Testing, and Design

As reviewed in Chapter 2, the passive cooling of WPT systems, especially in the case of buried GAs, does not prevent high temperatures in WPT coils. Therefore, active cooling methods were considered to maintain low steady-state temperatures and increase the operating time and lifetime of the WPT system. To better understand the impact and requirements for the cooling of high-power WPT coils, the area-related heat dissipation of a coil is a function of the coil-to-coil power level P, the coil quality factor Q, and the coupling coefficient of the coils k. The coupling coefficient is strongly a function of the geometric mean length (GML) of the coils l_{GM} relative to the airgap [35]. As often derived in the literature, at optimum

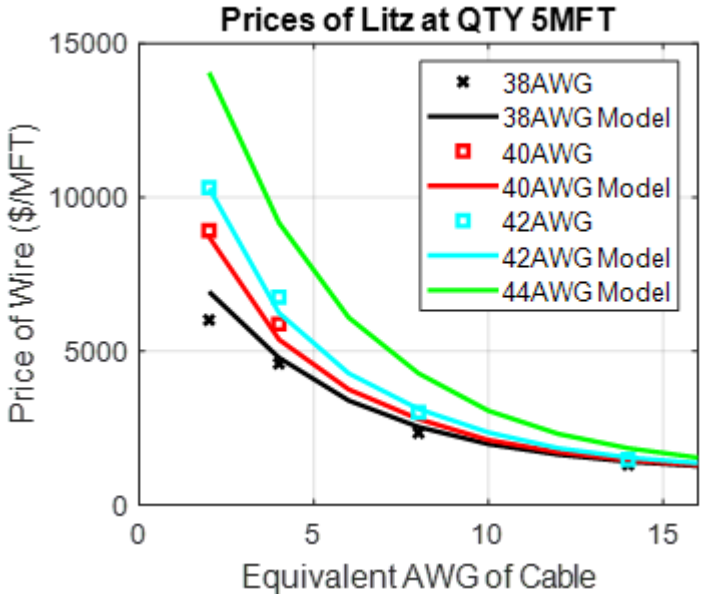

(a)

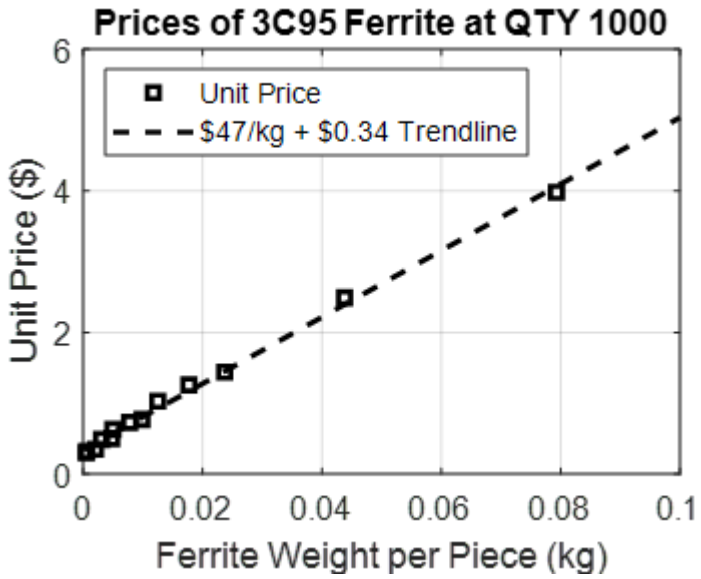

(b)

Figure 5.4: Comparison of the (a) litz and (b) ferrite cost models with low-volume manufacturer and distributor prices.

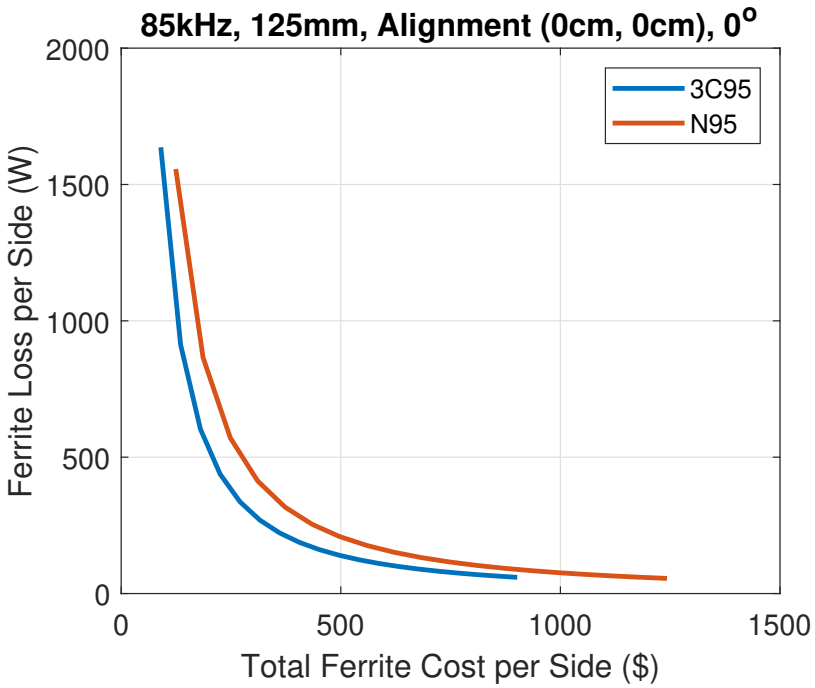

(a)

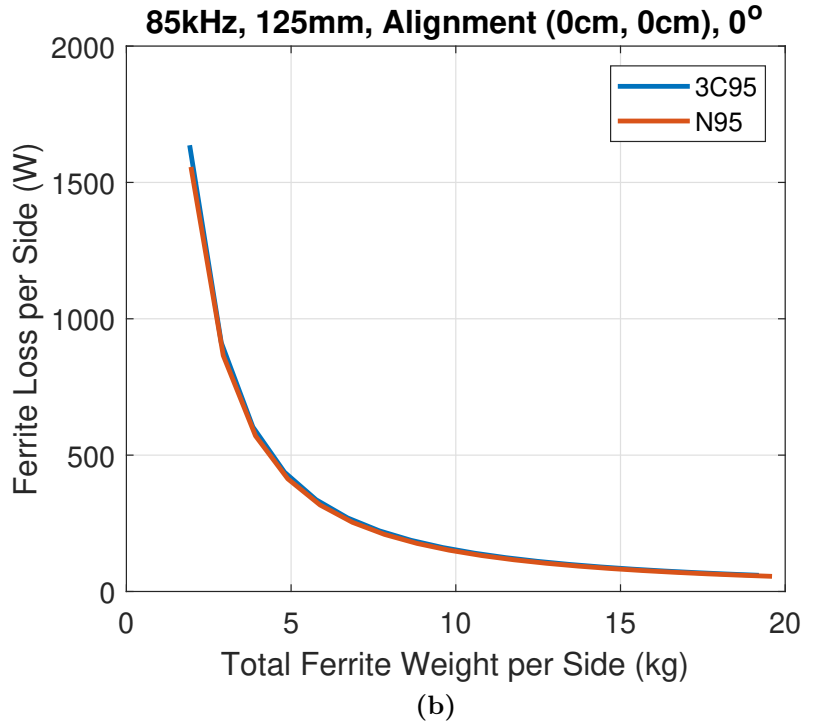

(b)

Figure 5.5: Comparison of the ideal ferrite losses per manufacturer Steinmetz equation coefficient and the weight of Ferroxcube 3C95 material and N95 material. (a) Comparison of the cost of the material vs. loss. (b) Comparison of the losses of the materials as a function of weight.

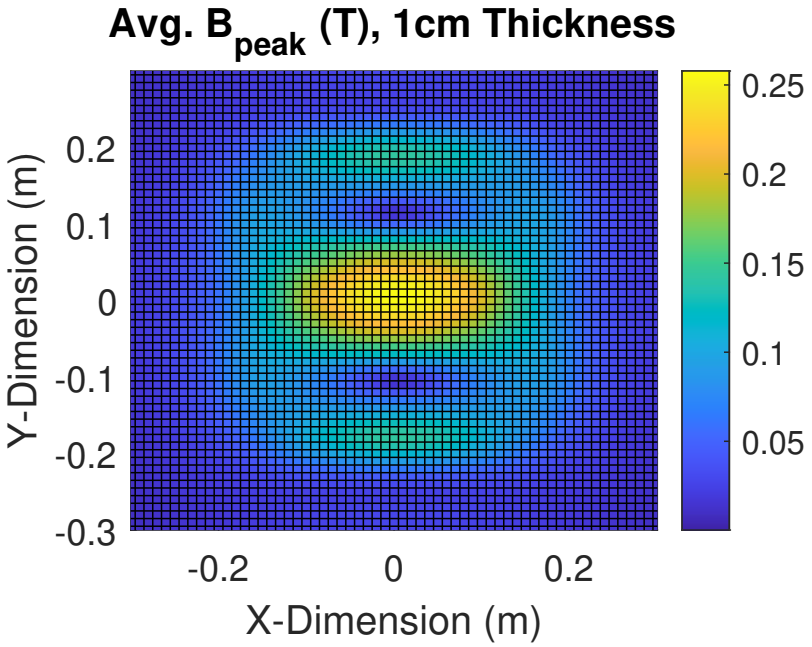

(a)

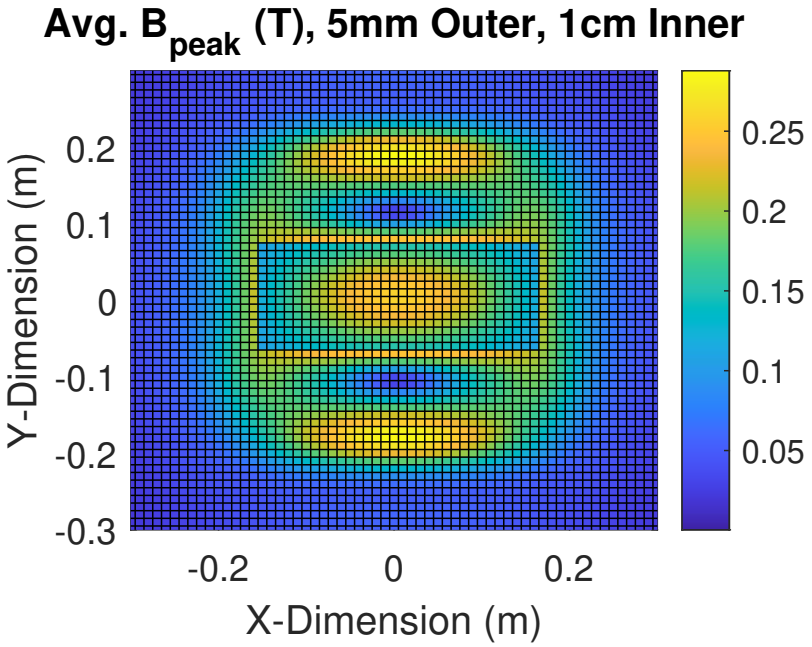

(b)

Figure 5.6: Comparison of the ferrite flux density at 120 kW with a 125 mm airgap at alignment. (a) Ferrite flux density with a fixed 1 cm ferrite thickness throughout. (b) Ferrite flux density with an inner 30.7 cm by 13.0 cm region of 1 cm ferrite thickness and an outer ferrite thickness of 5 mm.

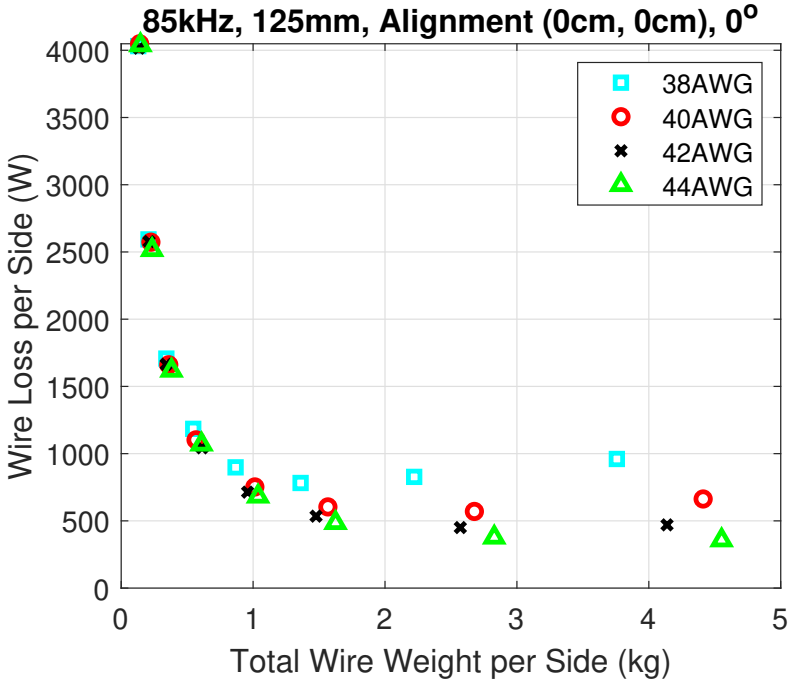

(a)

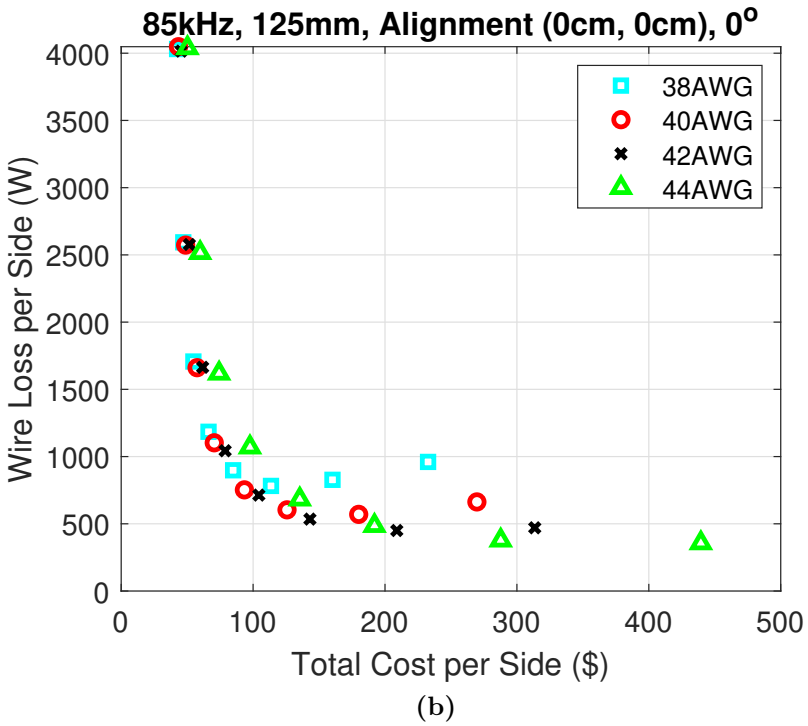

(b)

Figure 5.7: The loss, cost, and weight of different litz wire diameters and stranding. The overall cable size is swept from 16 AWG to 2 AWG equivalents from left to right. (a) Weight and loss plot. (b) Cost and loss plot.

loading and matched coils, the coil-coil efficiency can be calculated as [35, 22].

$$\eta = \frac{k^2Q^2}{\left(1+\sqrt{1+k^2Q^2}\right)^2} \approx 1 - \frac{2}{kQ}. \tag{5.2}$$

Therefore, for a given power level and area-related heat transfer coefficient h_T, the surface temperature increase ΔT is

$$\Delta T = \frac{P}{kQh_T l_{GM}^2}. \tag{5.3}$$

As an example, for square WPT coils with a quality factor of $Q = 600$ at an airgap of 210 mm, the temperature rise of the coils at various power levels will be a function of h_T and l_{GM} as in Figure 5.8a. This plot assumes that only the surface area of one side of the coil is available for cooling. Here, the coupling coefficient of the system is determined by the Fourier Analysis Method (FAM) optimization of this work with no field constraint. The four heat transfer coefficients here are examples of convective heat transfer coefficients as in Table 5.3. To achieve higher power levels, such as 50 kW, 120 kW, and 270 kW, high heat transfer coefficients are needed to limit the temperature rise. For conductive cooling, the heat transfer is governed by the thermal conductivity of the material, κ_{th}, and thickness, t, as in

$$h_T = \frac{\kappa_{th}}{t}. \tag{5.4}$$

The thermal resistance R_{th} of each layer of area A is then

$$R_{th} = \frac{1}{h_T A} = \frac{t}{\kappa_{th} A}. \tag{5.5}$$

For indirect backside cooling with 1 cm of ferrite in the ideal case, 350 W/m^{2}K is the upper limit for h_T given the 3.5 W/mK thermal conductivity of the material. This relatively high heat transfer potential through the ferrite motivates further exploration of the backside cooling of the coil through the ferrite. As reviewed in Section 2.5, there are also several other advantages to backside cooling in the automotive context as the coolant can be electrically insulated and shielded from fields and voltages present in the coil assembly.

Table 5.3: Overview of Area-Related Heat Transfer Coefficients [91]

Heat Transfer Type	Typical Heat Transfer Coefficient (W/m^2K)
Natural Air Conv. Vertical Wall	5
Forced Air Conv. at 5 m/s	30
Forced Air Conv. at >30 m/s	100
Conduction through 1cm 3C95 Ferrite (3.5 W/mK)	350
Water at 2 m/s over a Flat Plate	590
Water at 19 m/s through 20 mm I.D. Tube	34500

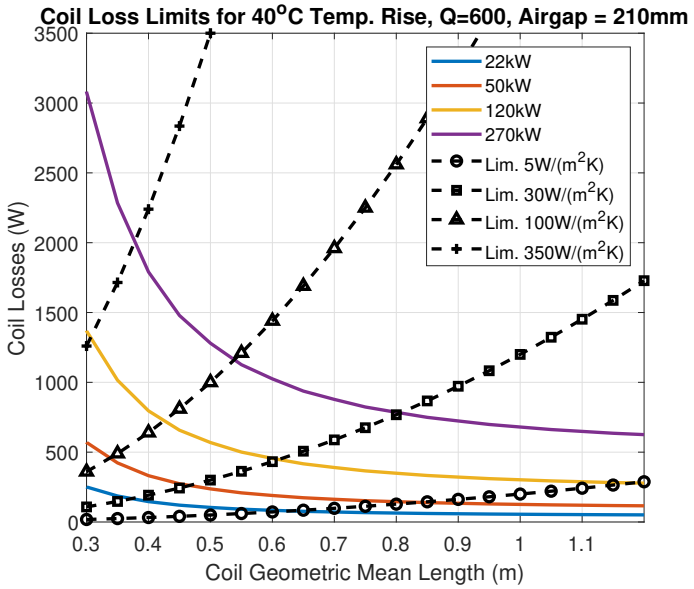

(a)

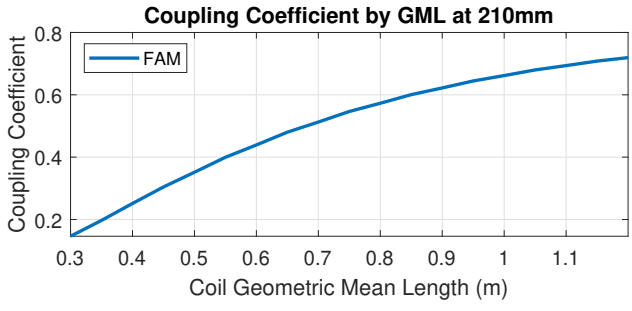

(b)

Figure 5.8: Basic assessment of the temperature rise of square coils with fixed quality factors. (a) Thermal limits of coils with a constant quality factor as a function of the power level and heat transfer coefficient for a temperature rise of 40°C. (b) Coupling coefficient of square coils as a function of GML as derived by FAM optimization.

5.3.1 Modeling and Testing of the Backside-Cooled Coil Assembly

To assess the feasibility of cooling the WPT coil through cold plates mounted on the back of the ferrite, a series of simulations and tests were performed. The test coil was a 10 cm diameter single-layer spiral coil constructed of the same wire as the 6.6 kW demonstrator. The 5 mm thick coil was placed on top of two layers of the 5 mm thick, 3C95 ferrite used in the 6.6 kW demonstrator for 1 cm total thickness. The assembly was placed in a aluminum tray and potted after thermal grease was applied between and under the ferrite layers to reduce the interface contact resistance. The thermal epoxy used to pot the assembly was MGChem 834HTC high thermal conductivity epoxy with a rated thermal conductivity of 0.94 W/mK. The heatsink was an Advanced Thermal Systems ATS-TCP-1003 heatsink. Dimensional drawings are shown in Figure 5.9d.

The FEA simulation of this arrangement was performed to predict the temperature rise of the coil assembly. For this simulation, a total power loss of 16 W was set in the coil volume and a constant temperature boundary condition was imposed on the underside of the aluminum heatsink. The thermal conductivity of the coil volume was set to 1 W/mK to model the low transverse conductivity of the litz wire [64]. The outputs from the simulation can be seen in Figure 5.10. As seen, the temperature rise of the top of the coil is around 10 K, leading to a total thermal resistance of 0.625 K/W. The simulated heat transfer coefficient related to the area of the 10 cm diameter coil is 203 W/m^{2}K. This lower than the ideal value of 350 W/m^{2}K for the 1 cm thick ferrite as the wire and epoxy layer adds thermal resistance. For comparison, simplifying the wire loss to be centered in the 5 mm thickness of the 1 W/mK wire and epoxy layer and using only the area of the 10 cm coil for the layers shown in Figure 5.9a produces a thermal resistance of 0.693 K/W.

Testing was performed on the test article in the lab to compare the simulation outputs. For the testing, a chiller was used to pump the coolant at rate of 2 gpm (7.57 lpm) and regulate the coolant temperature to 22^{o}C. Heat was generated by running a 40 A DC current through the coil, producing around 16 W of loss by Kelvin measurement. Two fiber optic temperature probes were used to take the temperatures of the top of the coil and top of the heatsink. The results of the tests are shown in Figure 5.11. In the test, the temperature rise

of the test assembly over that of the heatsink was also around 10 K, equating to a thermal resistance of 0.625 K/W which is close to the predicted FEA simulation value and simplified calculation.

The results of this testing and modeling demonstrate that high area-related heat transfer coefficients of 200 W/m^{2}K may be obtained with the backside cooling of ferrites. Given the analysis previously, this would conservatively equate to geometric mean coil lengths as low as 40 cm to 50 cm for a 120 kW system for a temperature rise of 40 K.

5.3.2 Small-Scale Testing of Buried-Tube Liquid Cooling

In the 120 kW demonstrator, liquid cooling is integrated into the structure of the coil enclosure. In conventional liquid-cooled heatsink design, copper tubes are either press fit into aluminum to achieve good thermal contact or placed into channels and buried with a thermally-conductive epoxy. The buried tube method produces more thermal resistance between the tubing and the metal, but requires fewer specialized tools to construct. Therefore, the buried tube heatsink was chosen for the 120 kW demonstrator.

To implement this in the demonstrator design, copper tubing is bent to fit into channels milled into the aluminum. The entrance and exit of the copper tube into the channels are sealed with a high-temperature rubber washer and silicone sealant to prevent the epoxy from leaking out while curing. The edges of the channels are taped with high-temperature, removable tape to keep the backside surfaces clear of epoxy, and the epoxy is then poured over the tubing to cover it.

The thermal resistance of copper tubing buried in thermally-conductive material to the surrounding aluminum channels can be approximated by the thermal resistance R_{cyl} from the inside surface to the exterior surface of a hollow cylinder of inner radius r_1 and outer radius r_2, a thermal conductivity of κ_{th}, and a length L. The thermal resistance of this configuration is logarithmic and is known as [91]

$$R_{cyl} = \frac{\ln r_2/r_1}{2\pi L \kappa_{th}}. \tag{5.6}$$

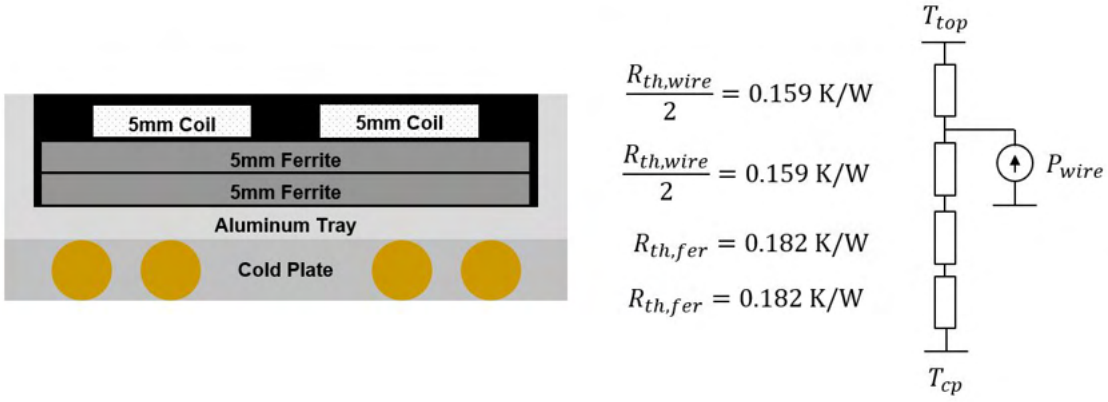

(a)

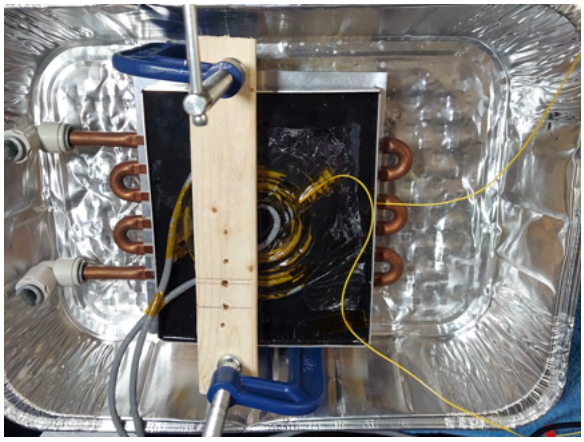

(b)

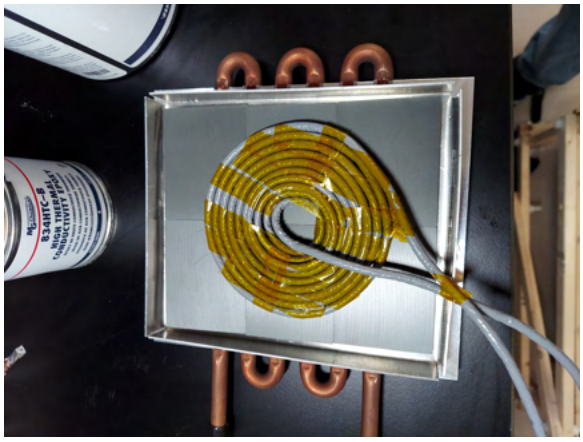

(c)

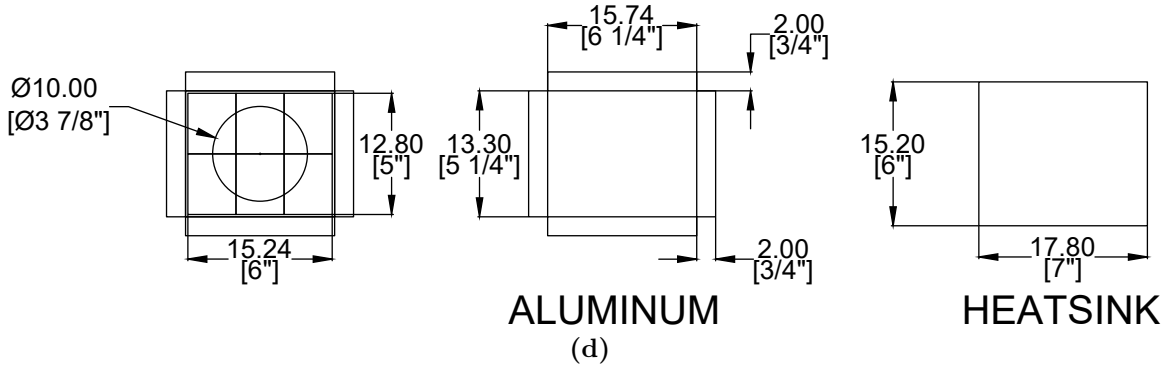

(d)

Figure 5.9: The small-scale thermal test used to determine the effectiveness of backside cooling. (a) Layer diagram of thermal test coil assembly with approximate thermal resistance based on the coil area. (b) Picture of the potted and (c) unpotted coil assembly on the heat sink. (d) Dimensional drawing of the thermal test assembly.

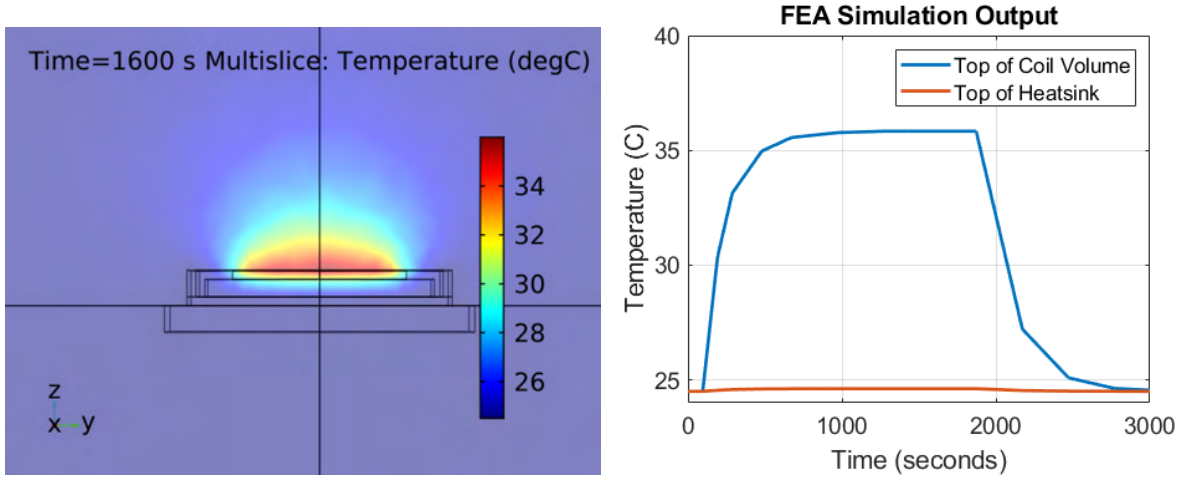

(a) (b)

Figure 5.10: FEA thermal simulation of the test coil assembly: (a) Modeled temperature gradient on the Y-Z plane at the end of the time period. (b) Plot of the simulated temperature over time.

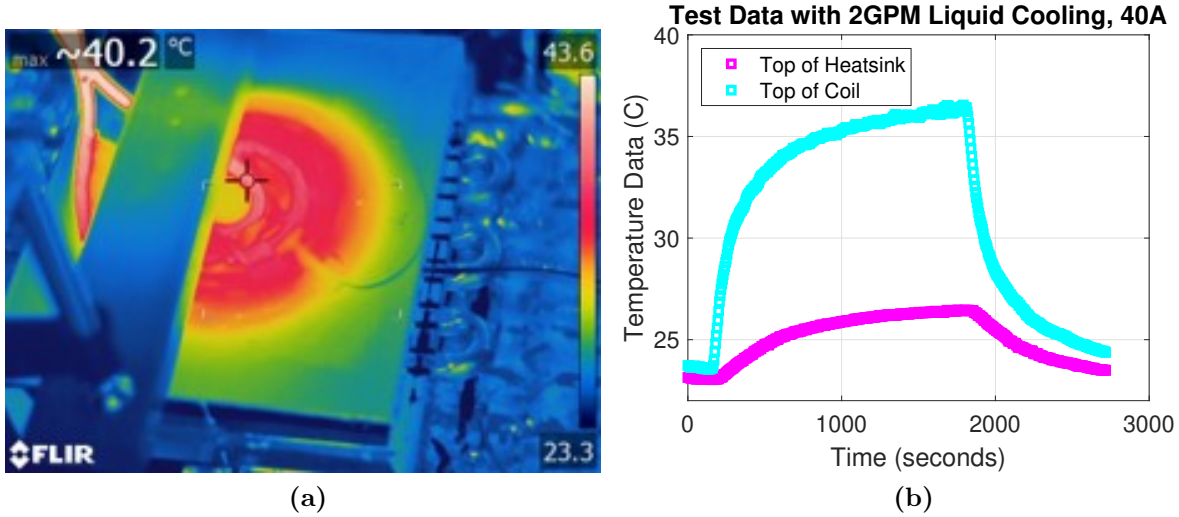

(a) (b)

Figure 5.11: Thermal measurements of the test coil assembly: (a) Thermal image of the coil at 1600 seconds. (b) Measured temperatures of the test coil assembly.

With the tubing radius of 5/16", channel radius of 3/8", length of tubing in the channels of 18", epoxy thermal resistance κ_{th} =1.2 W/mK, the approximate resistance of the tubing to the aluminum is 0.06 K/W.

A small-scale test was performed to assess the mechanical construction of the buried copper tube heatsink. A 6" x 6" block of aluminum was machined with channels of slightly varying depths as shown in Figure 5.12a. The centerline spacing of the channels was 1-3/8" as in the demonstrator. This results from the 11/16" bend radius made by standard 5/16" tubing bender tools. The threaded holes were drilled and tapped to mount 11 precision resistors in Figure 5.12b. Current was passed through these resistors to produce a known amount of loss on the aluminum block. Copper tubes with a 5/16" outer diameter were placed in the channels, sealed with rubber washers and silicone, and buried and cured with Aremco-Bond 2315 epoxy.

Current was passed through the 11 precision resistors to produce 129.9 W of loss. With 1.7 gpm (6.4 lpm) of water-glycol coolant at a 20°C temperature setpoint, a steady-state temperature rise of a 5 K was measured on the aluminum plate at 5 minutes using a thermal camera aimed at a strip of black electrical tape. The tape was placed to provide a high emmisivity surface on the low emmisivity aluminum surface. This rise equates to a 0.038 K/W thermal resistance to plate.

To further isolate the cooling of the heatsink from the contribution of the ambient environment, another test was performed without coolant flow. In this test, 36.4 W of loss from the resistors produced a steady-state temperature rise of 25 K at 10 minutes, which is an equivalent thermal resistance of 0.68 K/W, which is the resistance of the plate to the ambient environment. This thermal resistance is parallel to the resistance of the plate to the tubing. Therefore, the thermal resistance of the plate to the coolant is 0.04 K/W isolated from ambient cooling effects, slightly lower than the approximate value of 0.06 K/W.

This test shows that the buried tube implementation for the 120 kW demonstrator is effective. Compared to the Advanced Thermal Solutions ATS-TCP-1001, which uses press fit 3/8" copper tubing with four 6" passes similar to the test piece has a datasheet value of 0.025 K/W thermal resistance to plate with a a coolant flow of 1.5 gallons per minute.

This datasheet value likely includes ambient cooling effects and should be compared with the 0.038 K/W value obtained in the tests.

5.3.3 Fourier Modeling of Heat Transfer in the Coil Assembly

With the concept of backside cooling established, the modeling of heat transfer in the 120 kW coil assemblies can be performed. Since the coil current and ferrite fields are already expressed in the Fourier domain, it is convenient to express and analyze the heat transfer and temperature rise in the Fourier analysis framework. Fourier's equation for heat flux is

$$q = -\kappa_{th} \nabla T, \tag{5.7}$$

where q is the heat density in W/m^2, κ_{th} is the thermal conductivity in W/mK and T is the temperature in K. As a simplification, the heat generated by the wire and ferrite can be each grouped at a surface in the middle of the wire and the ferrite thicknesses, respectively. With this simplification of no internal heat generation [91]

$$\nabla^2 T = 0 \tag{5.8}$$

$$\frac{d^2 T}{dz^2} - (k_x^2 + k_y^2) T = 0. \tag{5.9}$$

The solution of this equation takes the form

$$T = Ae^{-\gamma z} + Be^{\gamma z}. \tag{5.10}$$

Combining this with Fourier's equation, the steady-state temperature on the surface of at material of thickness z_m is

$$T(k_x, k_y, z_m) = \frac{q(k_x, k_y)}{\kappa_{th} \gamma \coth \gamma z_m} + T(k_x, k_y, 0). \tag{5.11}$$

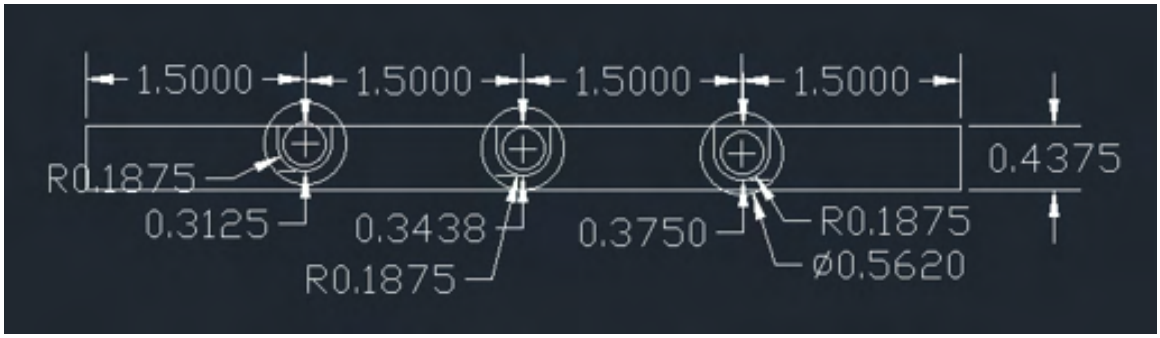

(a)

(b)

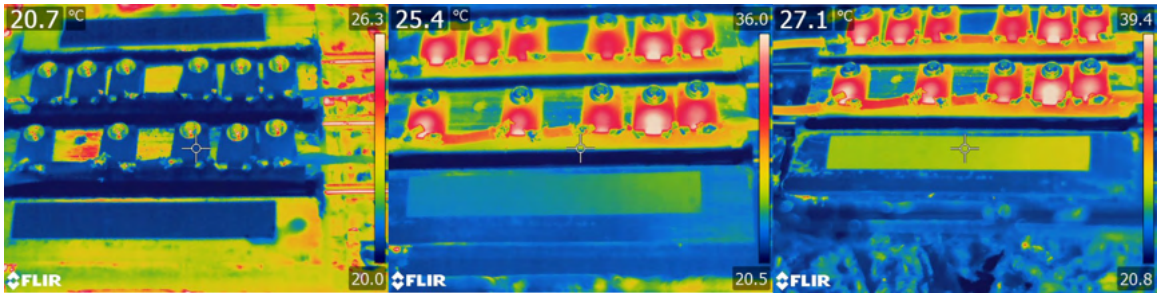

(c)

Figure 5.12: Test of a buried tube heatsink implementation considering different tube burial depths. (a) Drawing of the small-scale test piece used to measure the thermal conductivity of the coolant to the aluminum. (b) Picture of the assembled test piece with precision resistors mounted on the surface with thermal grease. (c) Thermal images before and during testing.

Therefore, with heat expressed in the Fourier domain and a known boundary condition at the bottom of the material, $T(k_x, k_y, 0)$, the temperature is calculated for each Fourier component and then transformed into the spatial domain to find the overall temperature.

Using the interface of the heatsink and the ferrite as a constant temperature boundary condition, this calculation for the Gen. 2 GA at 125 mm with an alignment of (10 cm, 7.5 cm) at 120 kW is performed as shown in Figure 5.13. This is the maximum misalignment specified in the SAE J2954 standard [24]. The heat produced in the GA at this operating point is approximately 1200 W of wire loss and 800 W of ferrite loss. The wire layer is approximately 1 cm thick and the ferrite layer is 1 cm in the center region and 5 mm thick elsewhere. The wire layer was given a uniform thermal conductivity of 3 W/mK to match the Cooltherm SC320 thermal conductivity. The loss density of the wire is derived from the squared current density distribution normalized to the calculated total loss.

FEA simulations of the coil assembly were performed to compare to the modeling results in Figure 5.14. These simulations use a constant temperature boundary in the channels to model the effect of the copper tubing. The worst-case losses in the coil were modeled at the nominal power level of 120 kW with each modeled loss evenly distributed throughout the volumes of the litz wire, ferrite, and capacitors, respectively. As seen, the temperature of the center of the wire increases to around 75°C over 20 minutes of operation relative to the constant 20°C temperature imposed on the tubing channel surfaces. As seen, the maximum temperature in the coil assembly is in the center of the bipolar structure. Here, many closely spaced windings with conduction losses are in contact with 1 cm of ferrite instead of the 5 mm in the outer areas with higher equivalent thermal resistance to the cooled aluminum enclosure.

As shown, the model-derived and FEA-derived thermal performance of the 120 kW system show the possibility of steady-state operation at 120 kW with a wire temperature rise of 55°C relative to the channel surfaces. This relates to a temperature rise in the center of the coil of around 0.0275 K/W accounting for the 1200 W of wire loss and 800 W of ferrite loss used in the models. Some additional thermal resistance between the copper tubing and the enclosure channels because of the encapsulant used to interface the copper tubing and

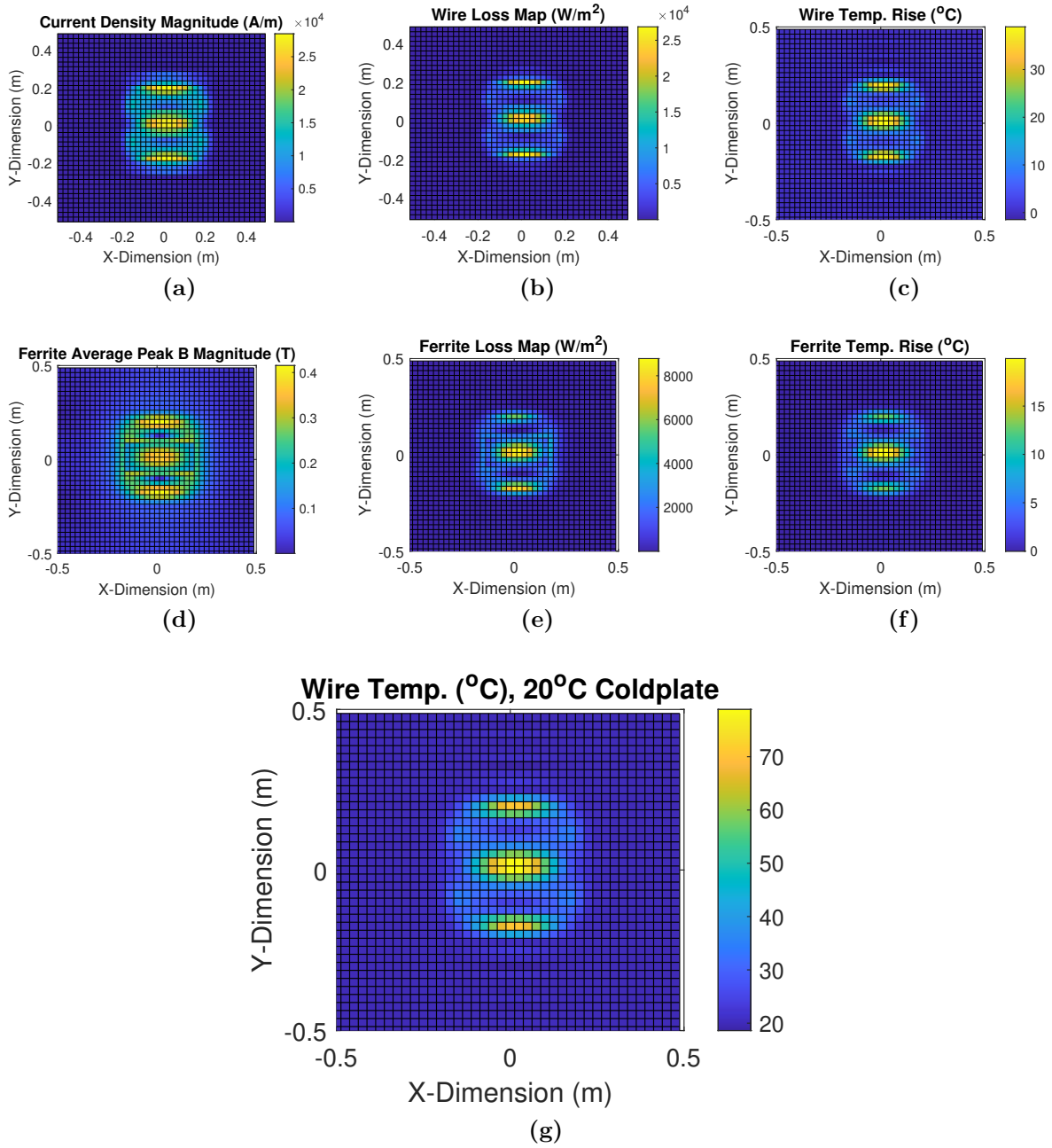

Figure 5.13: FAM steady-state heat transfer modeling of the Gen. 2 120 kW coil at maximum misalignment with the modeled worst-case losses at 120 kW: 1200 W of wire loss and 800 W of ferrite loss. (a) Gen. 2 current density magnitude. (b) Wire loss density derived from the current density. (c) Wire temperature rise with the losses centered in the 1 cm thickness of the wire layer. (d) Peak ferrite flux density. (e) Ferrite loss density. (f) Ferrite temperature rise with the losses centered in the inner and outer ferrite thicknesses.(g) Overall temperature at the surface of the wire with a coldplate temperature of 20°C.

the enclosure. The thermal resistance of the coolant to the tubing is a function of the flow rate and pressure as discussed in Section 5.8.4.

5.4 Encapsulant Material and Residual Stress

The thermal interface and mechanical adhesion of litz wire, ferrite, aluminum enclosure, and copper tubing in the 120 kW demonstrators are achieved with thermally conductive encapsulation materials. Encapsulants for electronic components and motors are widely available [92]. Due to high alternating electric and magnetic fields within the coil area, the encapsulants used in coils for inductive charging system are nonmagnetic and nonconductive to keep eddy current loss to a minimum while having high thermal conductivity. Due to the electric fields present between coil turns, the dielectric breakdown strength and dielectric dissipation factor are also of interest. In terms of mechanical properties, high tensile strength and adhesion are preferable to keep components in place in the ground assembly and in the vehicle assembly where the ferrite and wire weight may be supported by the encapsulant to the aluminum, ferrite, and wire against shock, driving forces, and vibrations. Lastly, other mechanical properties related to residual stress such as thermal expansion, cure shrinkage, and Young's modulus must be considered to prevent unwanted stresses on components.

In the development and testing of the 120 kW demonstrator, two types of encapsulants were chosen and tested: first the epoxy Aremco-Bond 2315 for the Gen. 1 demonstrator and then the silicone elastomer Cooltherm SC-320 for the Gen. 2 demonstrator. The cured properties of these two materials are compared with ferrite and aluminum in Table 5.4. The Young's Modulus values for the encapsulant materials are extrapolated from the hardness values in the datasheet by the methodology of [93]. With their relatively high thermal conductivity, both materials were able to effectively conduct heat away from the coil materials and provide mechanical support, but Aremco Bond 2315 caused higher ferrite losses by placing compressive stresses in the ferrite. As discussed and tested in [94], placing large stresses on MnZn ferrite is known to have several deleterious effects on the magnetic performance including lower permeability, lower saturation flux, and increased hysteresis loss.

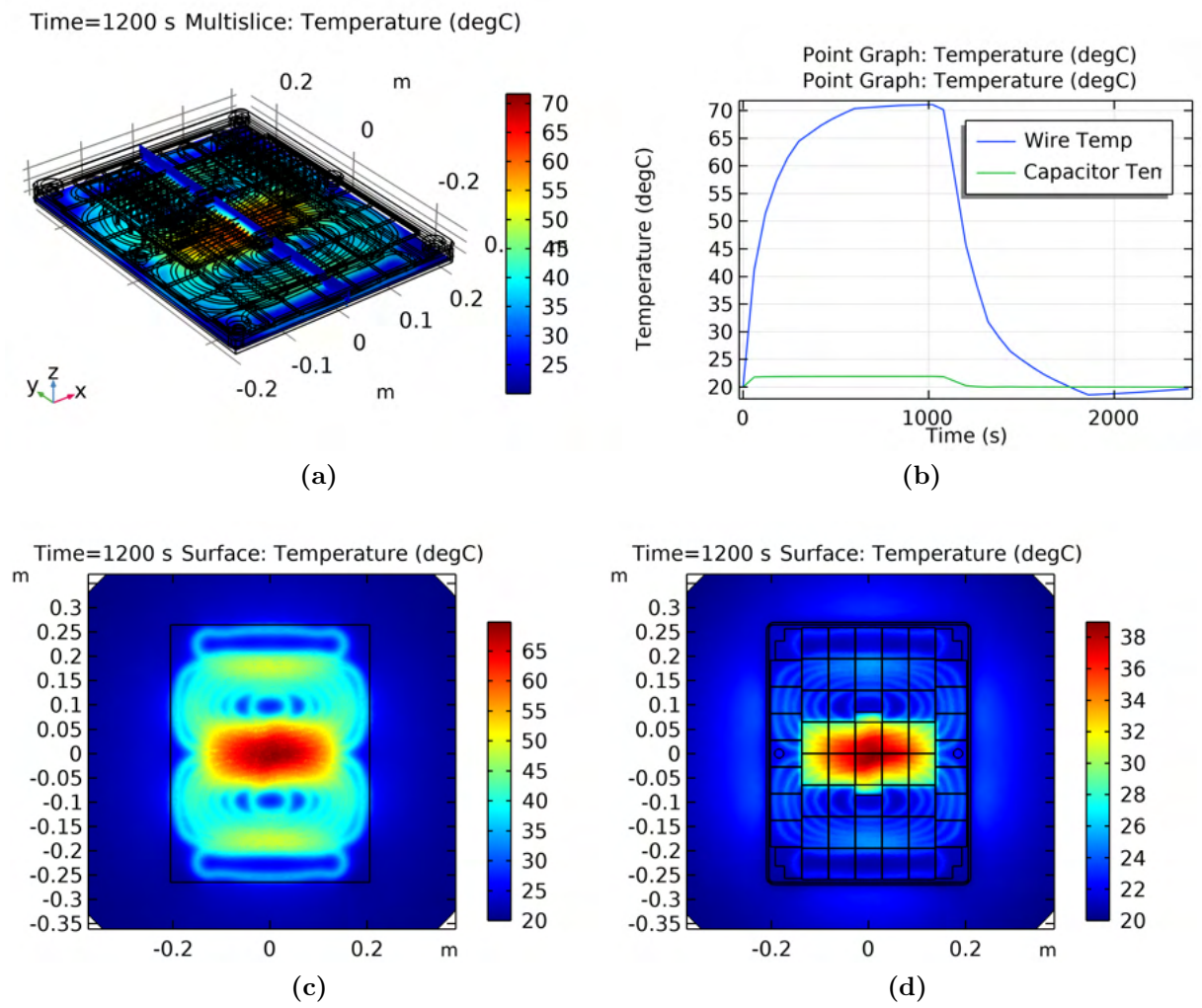

Figure 5.14: Thermal FEA simulations of the Gen. 2 120 kW coil at maximum misalignment with the modeled worst-case losses at 120 kW with 20 minutes of operation: 1200 W of wire loss, 600 W of capacitor loss, and 800 W of ferrite loss. (a) Isometric view of the simulation after 20 minutes. (b) Temperature over time of the center of the wire and one of the backside capacitors. (c) Temperature distribution on the surface of the wire. (d) Temperature distribution 2.5 mm from the surface of the ferrite.

For example, with a compressive stress of 53.36 MPa, the loss in the ferrite at 100 kHz and 100 mT and 100°C was almost five-times than when no compressive stress was applied [94].

These additional losses motivated the construction of a second demonstrator with the Cooltherm SC-320 to reduce the stress on the ferrite and implement other improvements. The Cooltherm SC-320 encapsulant has higher thermal conductivity, lower shrinkage, and lower cured hardness than the Aremco 2315, which causes less stress on the ferrite but also has lower tensile strength than the Aremco Bond 2315, making the cured coil more susceptible to forces and vibration.

The compressive stress on the ferrite is caused by two primary mechanisms: chemical shrinkage and differences in thermal expansion coefficients. The first of these, chemical shrinkage, occurs when the encapsulants cure and undergo chemical changes. Many neat or unfilled epoxies shrink 1% to 5% when cured, while some ceramic-filled epoxies such as Aremco-Bond 2315 epoxy shrink less. In contrast, most silicone elastomers such as Cooltherm SC-320 have minimal shrinkage. The stress $\sigma_{shr,s}$ caused by the cure shrinkage S is a function of the volume ratios and Young's moduli of the encapsulant and ferrite, ϕ_e and ϕ_f respectively, and E_e and E_f [95].

$$\sigma_{shr,s} = S\left(\frac{E_f}{1+\frac{\phi_f}{\phi_e}\frac{E_f}{E_e}}\right) \tag{5.12}$$

The second is caused by curing the coil at high temperature followed by cooling. When cooling, the differences in thermal expansion coefficients of the encapsulant and ferrite, which is a metal-oxide ceramic, are multiplied by the difference in the curing temperature and final temperature. Similar to cure shrinkage, the stress $\sigma_{shr,c}$ induced by the difference in thermal expansion coefficient α_e and α_f at a temperature T when cured at T_{cure} is

$$\sigma_{shr,c} = (\alpha_e - \alpha_f)(T - T_{cure})\left(\frac{E_f}{1+\frac{\phi_f}{\phi_e}\frac{E_f}{E_e}}\right). \tag{5.13}$$

The room temperature stress on ferrite caused by encapsulation in Cooltherm SC-320, Aremco-Bond 2315, or aluminum when cured at 120°C is shown in Figure 5.15. Both material manufacturers specify this curing temperature as an option for fast single-temperature curing

profiles. In the Gen. 1 and Gen. 2 demonstrators, a wire and encapsulant layer thickness of 1 cm, ferrite layer thickness of 1 cm in the inner region and 5 mm in the outer region, and aluminum thickness of approximately 1 cm in the inner region and 1.5 cm in the outer region are used. This leads to a range of ferrite to encapsulant ratio of 1 in the inner region and 0.5 in the outer region and a ferrite to aluminum ratio of 1 in the inner region and 0.33 in the outer region. Aluminum is included as the ferrite is bonded to the aluminum by the encapsulant and its differences in thermal expansion coefficients relative to the ferrite adds to the total stress on the ferrite. In these plots, ferrite, Aremco 2315, and aluminum have high Young's moduli such that small strains in the materials cause large stresses in the materials. For the 120 kW demonstrator, the simplified thermo-mechanical FEA simulations shown in Figure 5.16 show the development of large mechanical stresses of around 40-60 MPa from thermal shrinkage effects alone.

5.4.1 Validation of the Effect of Compressive Stresses on Ferrite

To confirm the presence of higher ferrite losses caused by compressive stress, a small-scale planar coil was made in order to compare losses with and without the Aremco 2315 epoxy. The small-scale coil is shown in Figure 5.18. Dimensional drawings of the coil are given in Appendix C.1. In the small-scale coil, a cavity in an aluminum block was machined to fit a layer of 2.7 mm ferrite, a 5 mm thick coil made of 8-turns of 10 AWG litz wire with 38 AWG strands, and a layer of 5 mm ferrite attached to an aluminum sheet held in place by bars of FR4. A notch was cut into the 5 mm ferrite to allow the passage of the coil leads such that the coil lays flat.

The sheet of 5 mm ferrite added above the coil increased the self-inductance of the coil; increasing the flux density in the 2.7 mm ferrite layer per unit current and increasing the ratio of ferrite hysteresis loss to wire loss. The bottom 2.7 mm ferrite layer was subjected to stresses when the 2315 epoxy was cured around them. As in the first 120 kW demonstrator, a thin layer of Aremco 2315 is poured and spread on the aluminum to adhere the ferrite to the aluminum, the 2.7 mm ferrite tiles were placed, an additional 2315 epoxy layer was poured to cover the 2.7 mm ferrite, the top 5 mm layer bonded to a thin aluminum sheet and the coil was placed in the cavity, the FR4 bars were fastened in place with nylon bolts, and

Table 5.4: Thermo-mechanical properties of encapsulants and coil materials

	Aremco-Bond 2315	Cooltherm SC-320	MnZn Ferrite	Aluminum 6061-T6
Thermal Conductivity (W/mK)	1.2	3.0	3.5	167
Thermal Expansion (10^{-6}/K)	34	110	10	23.6
Young's Modulus (Hardness)	4.2 GPa (Shore D 92)	3.1 MPa (Shore A 54)	90-150 GPa	69 GPa
Ultimate Tensile Strength (MPa)	84.8	2.16	20-65	310
Cure Shrinkage	0.3%	N/A	N/A	N/A
Curing Cycle	120°C/6 hours	25°C/24 hours or 125°C/1 hour	N/A	N/A

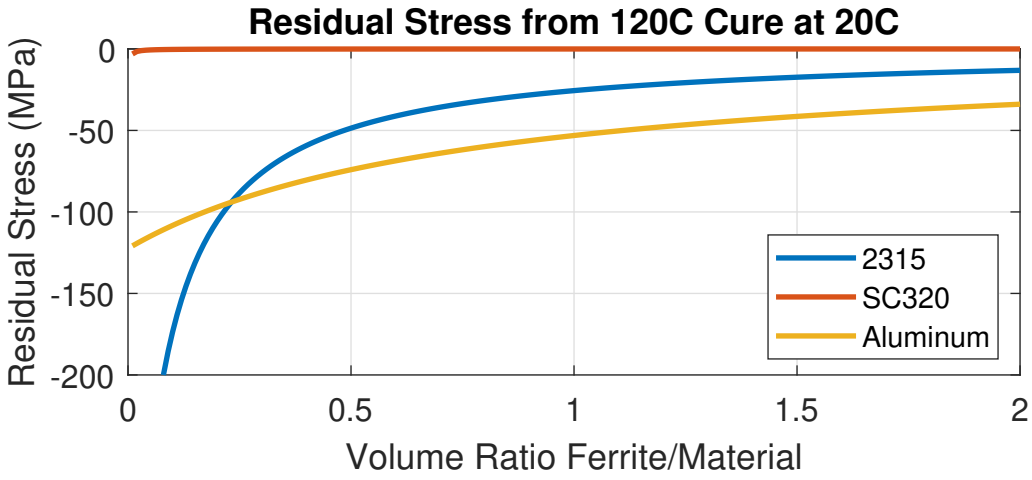

Figure 5.15: Compressive stress at 20°C on ferrite from a 120°C cure as a function of the volume ratio of ferrite to the encasing material.

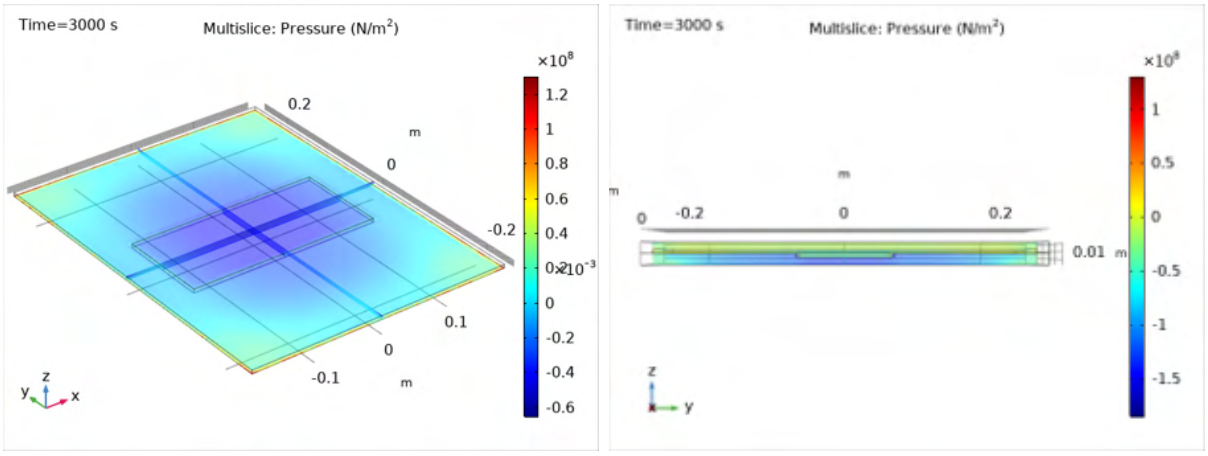

(a) **(b)**

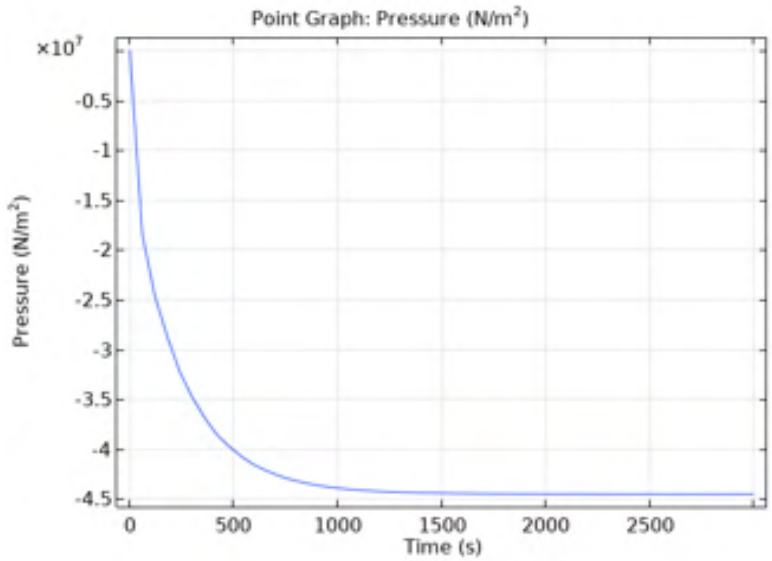

(c)

Figure 5.16: FEA simulation of the compressive stresses in the ferrite in the 120 kW demonstrator caused by the aluminum and Aremco 2315 Epoxy from a 120°C cure. (a) Isometric view of the resultant stress in the middle of the ferrite sheet. (b) Side view of the simulation output. Here, the aluminum is below the ferrite and the epoxy is above. The double layer of ferrite of 10 mm thickness in the middle of the coil is shown in the middle of the rest of the 5 mm thick sheet. (c) Plot of compressive stress at the point in the center of the 10 mm double-layer ferrite sheet.

the assembly was cured at 120°C for 6 hours. Measurements were taken with and without the epoxy to compare losses.

FEA simulations were performed to estimate the compressive stress, flux density, and ferrite loss of the small-scale coil. The results of these simulations are shown for both magnetic and mechanical simulations in Figure 5.17. Here the peak current of 20 A(rms) in the 8-turn coil generated a peak flux-density of 225 mT in the 2.7 mm layer of ferrite. The FEA mechanical simulation predicted a ferrite stress of 50-100 MPa in the 2.7 mm layer of ferrite.

Loss measurements were taken with a WT1800 Yokogawa power analyzer and a AETechron 7794 power amplifier as a function of current at the resonant point of a series tank comprised of the coil assembly and film capacitors. Taking measurements near the resonant point allowed for higher power factor measurements by compensating the large reactive component of the coil impedance. This led to better accuracy than if the inductor alone was measured. The low series impedance of the tank at resonance also increases the current capability of the power amplifier used in the tests, which is limited by the voltage of the amplifier. Different measurement frequencies were achieved by varying the number of capacitors in series. Slightly different resonant frequencies were also measured to evaluate the effect of decreased power factor due to the shift of the resonant point from the decrease of the self-inductance of the cured and uncured coil. Multiple measurements were taken to explore the effect of temperature on the measurements.

As seen in Figure 5.19, the self-inductance of the coil decreased after curing from around 27.2 µH to 22.2 µH as in Figure 5.19a. With an airgap of 5 mm, this decrease may be from a drop in the magnetic permeability of the ferrite from stress [94]. With the drop in self-inductance, there is less flux in the ferrite per unit of current, potentially decreasing the core loss as a function of current. The magnitude of this difference can be estimated by the $\beta = 2.44$ term of the 3C95 ferrite. Using the ratio of the inductance raised to the β as in the Steinmetz equation yields a decrease in the hysteresis loss of 64%. However, as seen in Figures 5.19b and 5.19c, the tank losses approximately double for the cured coil relative to the uncured coil. After subtracting the linear losses of the wire and capacitor resistances, the ferrite hysteresis loss after curing is almost three times higher than before

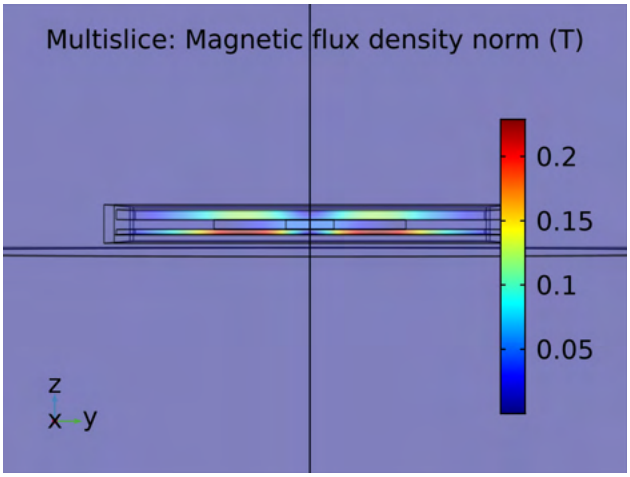

(a)

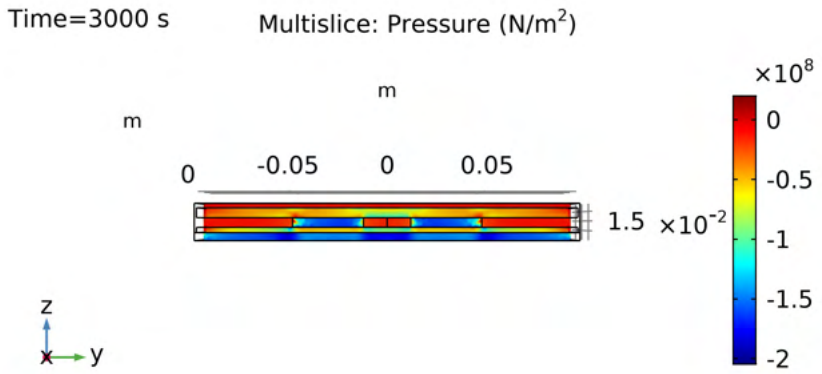

(b)

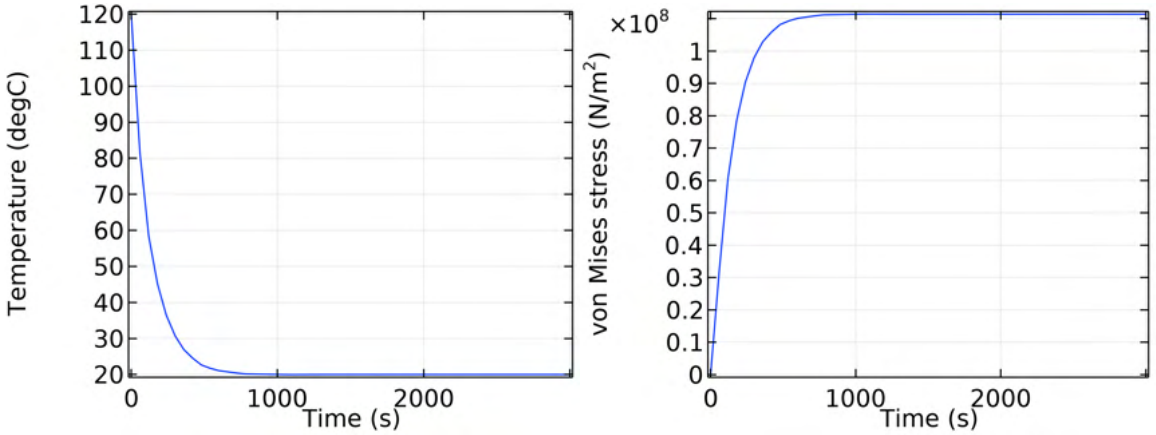

(c) (d)

Figure 5.17: FEA simulation of the small-scale coil for the compression effect test. (a) Peak flux density in the coil with 20 A(rms) of coil current. (b) Stresses induced by thermal contraction of the materials from 120°C to 20°C. (c) Temperature at the center of the 2.7 mm ferrite sheet over time. (d) Stress in the center of the 2.7 mm ferrite sheet over time.

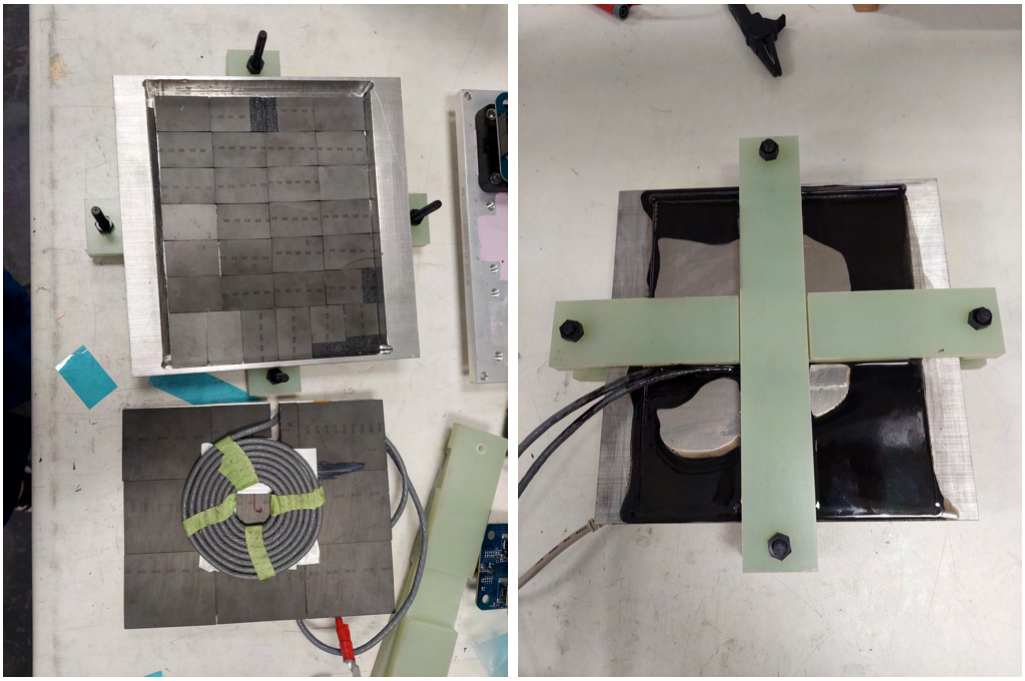

(a) **(b)**

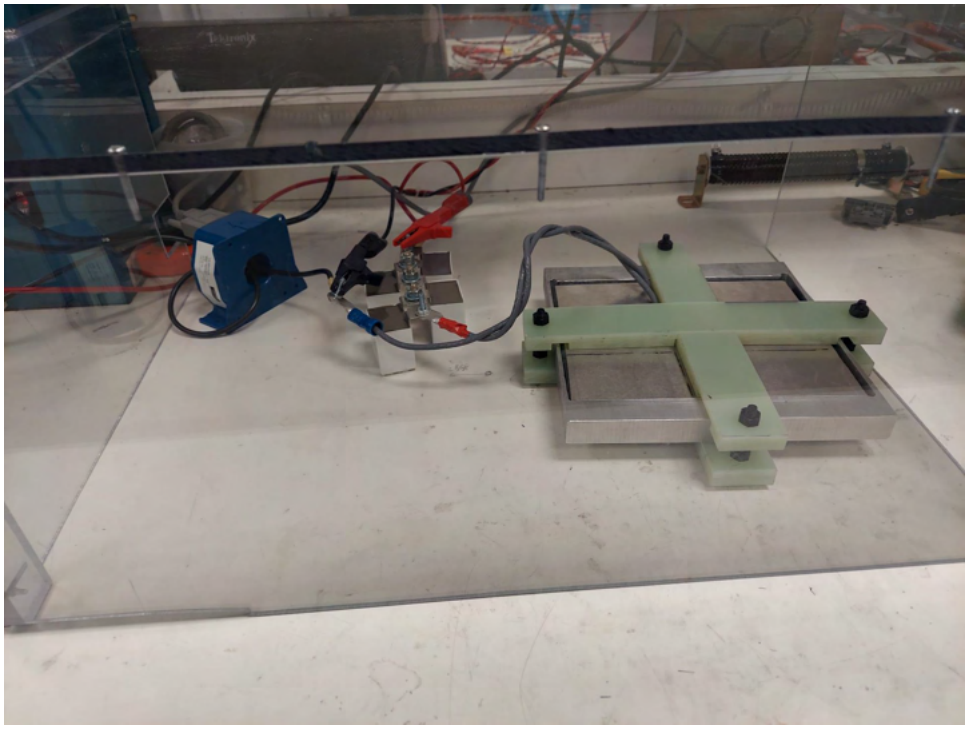

(c)

Figure 5.18: The small-scale coil test article used to verify the compressive stress effect of the Aremco 2315 epoxy on the ferrite hysteresis loss. (a) Top and bottom parts of the assembly. (b) The cured assembly. (c) Loss measurement test setup with resonant film capacitors.

curing and almost five times higher when corrected for the decrease in self-inductance as in Figures 5.19d and 5.19e.

5.5 Circulating Flux and Flux Concentrations

It is imperative that the magnetics of high-power inductive components operate very efficiently to prevent high temperatures or hot spots, especially when limiting the amount of magnetic material or ferrite in the system to reduce cost or weight. Therefore, care must be taken in the physical construction of the modeled ferrite and coil design to avoid additional losses. Instead of the continuous, unbroken sheet of ferrite assumed by the ferrite loss models in the FAM, discrete ferrite tiles were used instead of a continuous sheet of ferrite and openings or passthroughs in the ferrite were made to route the litz wire to the backside capacitors. The analysis of these details showed enough impact so that changes were made in the Gen. 2 coils to avoid additional losses.

The use of discrete ferrite tiles in the 120 kW demonstrators places many small air gaps within the ferrite sheet. Depending on the location of these gaps, localized concentrations of flux may occur possibly causing hot spots within the ferrite. As discussed in [45], for rectangular tiles or bars of ferrite, these concentrations are avoided by limiting the number of "T" intersections, where the corners of two tiles face the long side of a third tile due to offset and instead using "cross" intersection with four corners with all the tiles aligned. The authors also suggest to limit the number of cut tiles with non-machined irregular edges. In the Gen. 1 ferrite layout, several locations for flux concentrations were found, making it necessary to modify the layout in the Gen. 2 layout to allow a consistent ferrite pattern with more ideal "cross" intersections. Comparison of the two ferrite patterns is shown in Figure 5.20. Here, flux concentrations around "T" intersections are seen in the Gen. 1 layout and are reduced in the simplified Gen. 2 layout. The Gen. 2 layout produces higher flux density in the tiles close to the passthroughs due to inner corners cut into the ferrite to accommodate the openings. Smaller tiles are also used in the Gen. 2 simulation to match the dimensions of the parts. In the Gen. 1 coil design, all simulations were done with 64 mm x 54 mm x 5 mm tiles instead of the actual 64 mm x 50.8 mm x 5 mm tiles used

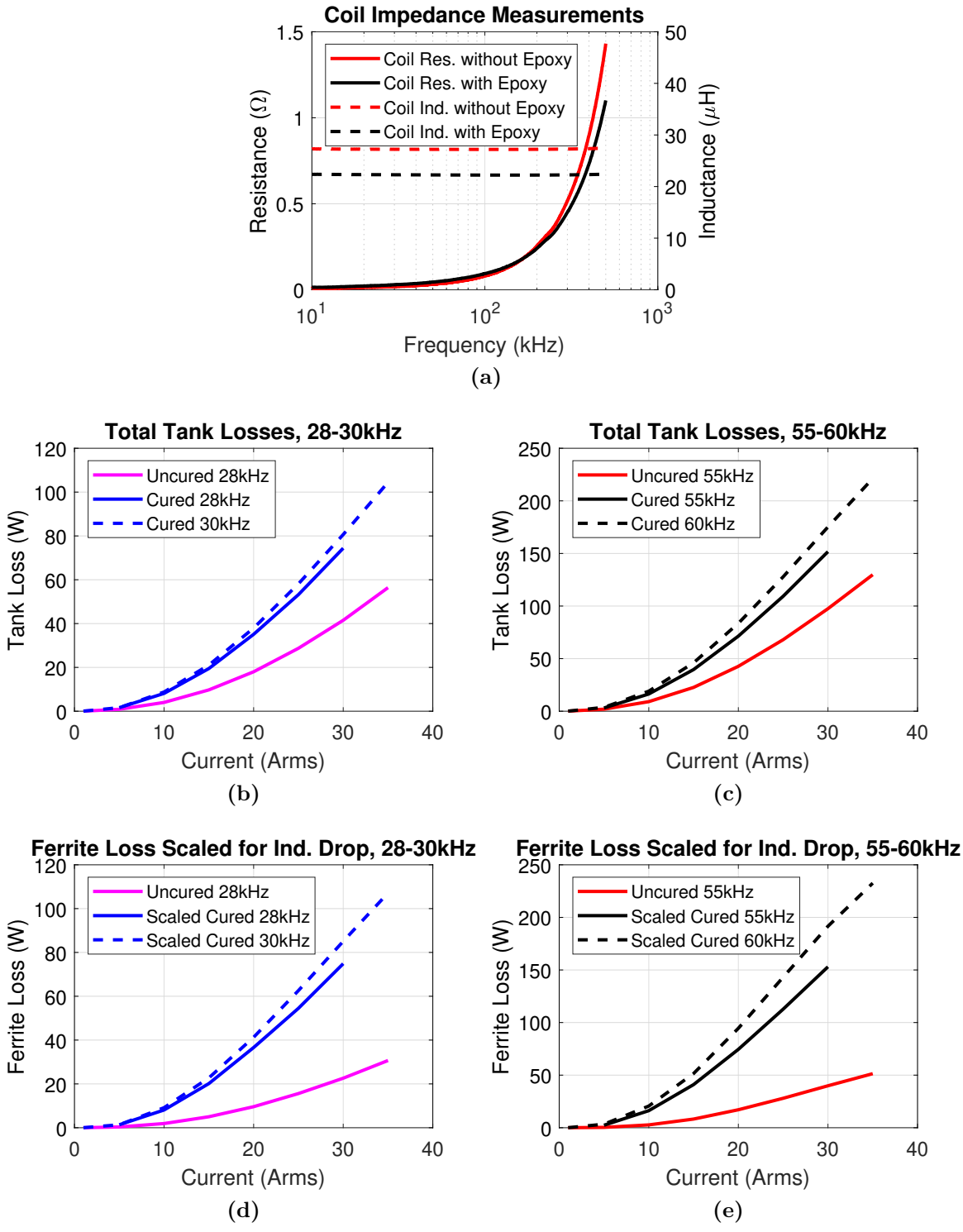

Figure 5.19: Measurements of impedance and loss of the small-scale coil. (a) Impedance measurements of the coil before and after curing with epoxy. (b) Tank losses before and after curing with epoxy with the 30 kHz tank. (c) Tank losses before and after curing with epoxy with the 60 kHz tank. Estimated ferrite loss without the loss from the measured tank resistance loss scaled for the drop in inductance with the (d) 30 kHz and (e) 60 kHz tank.

in the demonstrators. The difference in dimensions was due to an error in transcribing the dimensions from the datasheet from a different part variation.

In both Gen. 1 and Gen. 2 demonstrators, litz wire passes through openings in the aluminum enclosure and ferrite from the frontside to the backside of the enclosure where the compensation capacitors are mounted. Routing the wire in this manner reduces the need for additional coil area outside the ferrite to route the wires and minimizes the high-frequency conductor length. However, this requires a gap in the ferrite sheet which may lead to flux concentrations and higher overall ferrite loss than in an unbroken ferrite layer of the same thickness. Additionally, if the net current passing through each opening is non-zero, the ferrite sheet provides a low-reluctance path for circulating flux to form around the openings or passthroughs in the plane of the ferrite. As also discussed in [45], this flux does not contribute to the coupling of the coils and results in additional ferrite loss. This loss, as with most other ferrite losses, is nonlinear and minimally present in low-amplitude measurements, such as coil or tank resistance measurements with an impedance analyzer.

Circulating flux can be avoided by adding gaps between the ferrite tiles to increase the reluctance of the path, which slightly decreases the coupling of the coils [45], or by making the total passthrough current equal to zero. This is best accomplished by having both the incoming and outgoing wires pass through the ferrite sheet together such that their currents cancel. In the Gen. 1 coils, two separate passthroughs resulted in circulating flux around each opening. When this occurs, the circulating current is additive between the openings as in Figure 5.21. In the Gen. 2 coils, the litz wire was rerouted to return through a single passthrough. FEA simulations were performed as shown in Figure 5.22 to estimate the impact of the circulating current on the ferrite loss and to explore options for rerouting the litz wire or notching the ferrite to eliminate the circulating current. There were two main options explored: making a notch in the center ferrite between the Gen. 1 openings to pass the wire underneath the coil to a single passthrough and passing the wire over the coil to a single passthrough by extending a hole in the coil former. Each case was simulated at the peak flux from the nominal coil current of 164 A(rms) and a volume integral of the flux density to the $\beta = 2.44$ term of the 3C95 ferrite to determine the relative impact on the ferrite loss compared to the base case as in Table 5.5. As shown, the use of a notch

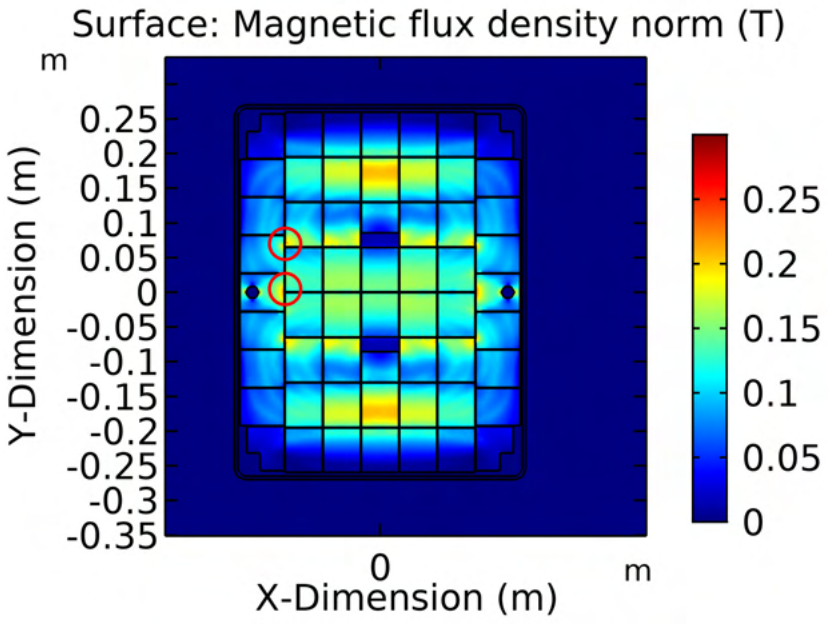

(a)

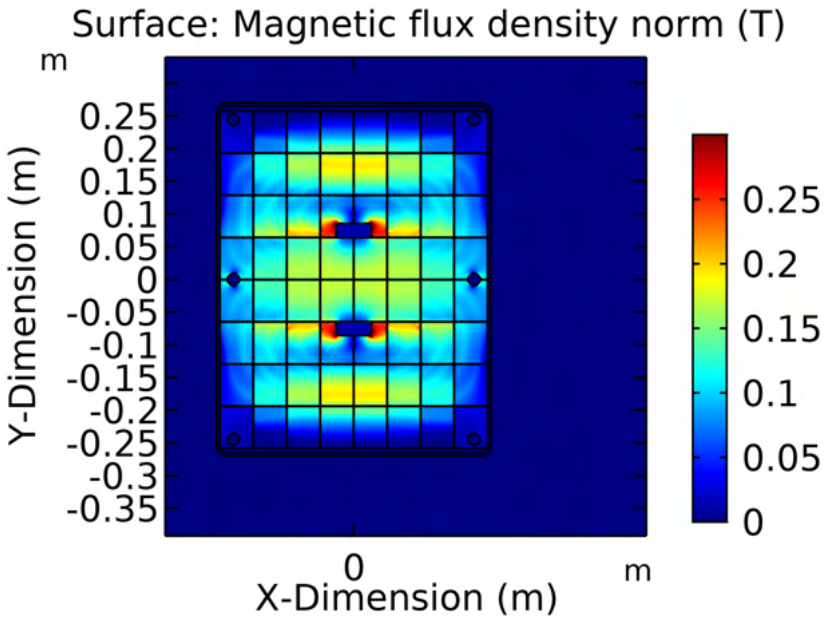

(b)

Figure 5.20: FEA simulations of ferrite layouts for the (a) Gen. 1 coil assemblies with two "T" intersections labeled with red circles and the (b) Gen. 2 coil assemblies. Both flux density plots are taken at 2.5 mm from the surface of the ferrite at the peak flux of the nominal 164 A(rms) coil current.

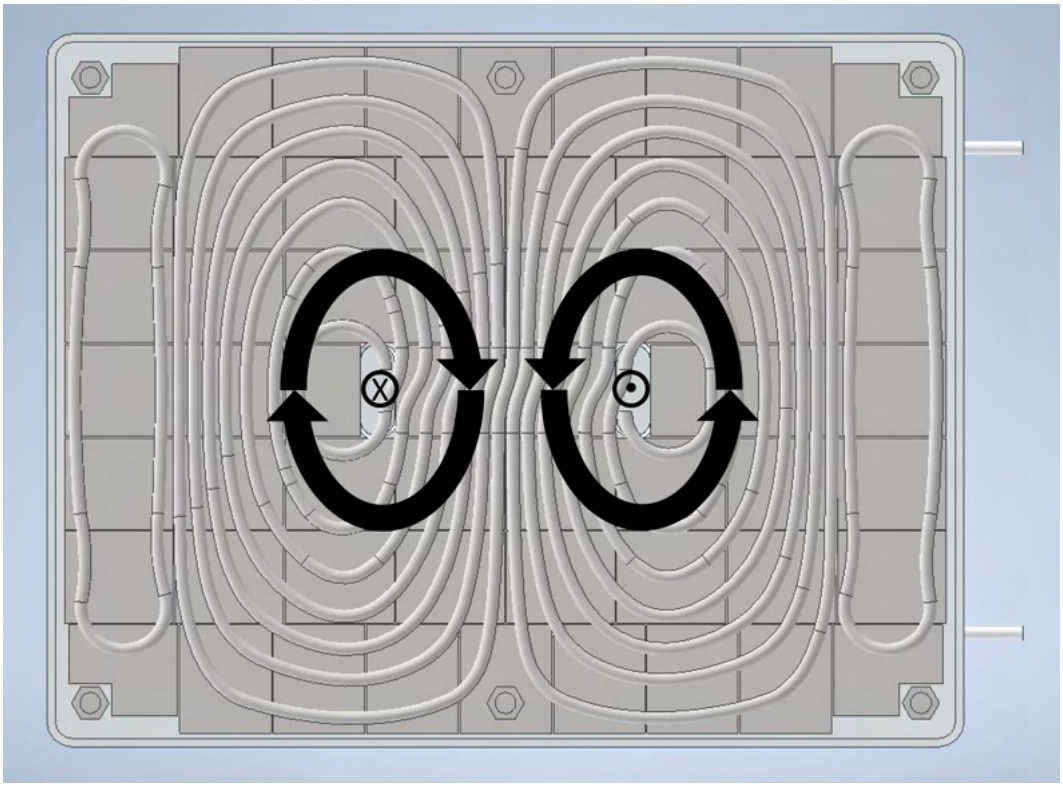

Figure 5.21: The formation of circulating flux in the Gen. 1 ferrite sheet from two separate lead currents entering and leaving through separate passthroughs.

Table 5.5: Comparison of Ferrite Loss from FEA Simulations of the Different Passthrough Options of Figure 5.22 with the Gen. 2 Ferrite Layout and Coil Current of 164 A(rms)

Simulation	Peak $\boldsymbol{B}^{2.44}$ Volume Integral	Relative Loss
Baseline Two Openings	10.4e-6	-
Two Openings with Center Notch	7.0e-6	-32.7%
One Opening with Center Notch	6.6e-6	-36.5%
One Opening with Passover Routing	6.4e-6	-38.5%

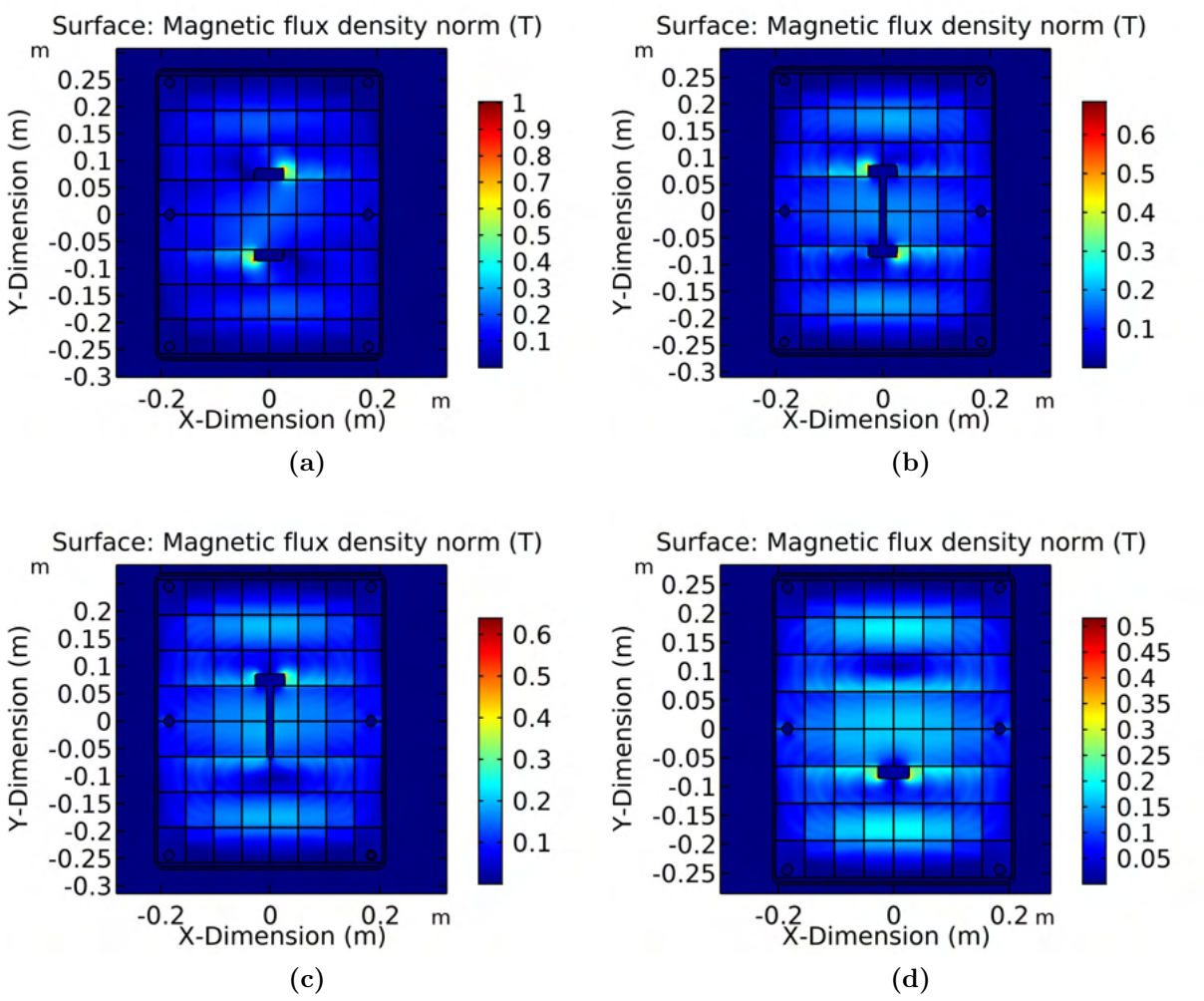

Figure 5.22: FEA simulation outputs of the flux density 2.5 mm from the surface of the ferrite with different options to reduce the circulating flux. (a) Baseline case with two openings and separate wire passthroughs, (b) two openings with a 0.5" width center notch in the ferrite and separate wire passthroughs, (c) one opening with a 0.5" width center notch in the ferrite, and (d) the best case with one opening and no notches.

to eliminate the main circulating flux path is effective, but does slightly increase the loss relative to the best case with an unbroken sheet of ferrite with the return wire routed over the center conductors, as was done in the Gen. 2 coil assembly. This provided the least amount of loss of the options, but required a notch cut in the polycarbonate coil former to accommodate the wire routing change.

5.6 Construction of the Gen. 1 and Gen. 2 Demonstrators

The Gen. 1 coil assemblies were constructed and tested to validate the FAM loss, field, and thermal modeling at high power levels. Tests were performed on Gen. 1 assemblies to measure performance under different misalignment and load conditions. These measurements led to additional analysis and modifications to the Gen. 1 design for the Gen. 2 coil assemblies. As detailed in the previous sections, these changes were made to improve the efficiency by simplifying the ferrite layout, reducing the compressive stress on the ferrite caused by the encapsulant, and reducing the ferrite loss caused by circulating flux by rerouting the litz wire leads to pass through one opening in the ferrite. The same capacitor bank and compression plates were used in the Gen. 1 and Gen. 2 coil assemblies.

Overall, the Gen. 1 and Gen. 2 designs were very similar in construction and comprised of a polycarbonate cover and coil former, a litz wire coil, a layer of ferrite, an aluminum enclosure, copper tubing, and the capacitor banks. A layout of these parts can be seen in Figure 5.23. A cost and weight breakdown of one of the Gen. 2 assemblies is seen in Figure 5.24. Here, the ferrite, litz wire, and encapsulant are only 20% and 41% of the cost and weight of the assembly, respectively, while the capacitor banks comprise 42% of the cost and 22% of the weight of the assemblies. The detailed bill of materials of one Gen. 2 system assembly is given in Appendix C.2. As seen, the cost and weight of custom-built components, such as the enclosure, coil former, compression plates, and resonant capacitor banks, are large. Many opportunities for cost and weight reductions still exist in the enclosure

and capacitor bank design for production at scale. The volume purchasing of components will further reduce the cost.

In Figure 5.23b, the system is shown with an ORNL designed rectifier mounted on the back of the enclosure. Enough room was left on the back of the enclosure to mount a rectifier to have a "single-box" assembly. However, in the benchtop tests of this work, both the inverter and rectifier were placed on a table and connected to the assemblies with litz wire leads for ease of access and measurement as seen in the test setup in Figure 5.25.

5.6.1 Construction of Gen. 1 Coil Assemblies

The Gen. 1 coil assemblies were constructed using Aremco 2315 epoxy as the encapsulant on both the back and front sides of the enclosure. Each cure of this black-colored epoxy required a cure time of 6 hours at 120°C such that a large oven was needed to cure the entire coil assembly in multiple steps. In each use of the Aremco 2315 epoxy, the resin and hardener parts were mixed and then degassed in a vacuum chamber to eliminate air bubbles. Several images of the process are shown in Figure 5.26 including the setting of the copper tubing, layout of the ferrite, and encapsulation of the tubing, coil and ferrite. In Figure 5.26a, the end result of the tubing preparatory work is shown. The tubing was bent with a hand tool to shape; pressed into the channels with strips and sheets of wood, clamps, and weights; and set with room-temperature epoxy. The layout of the ferrite tiles in the Gen. 1 coils is shown in Figure 5.26b. The layout differs slightly from the original due to the slight difference in tile width used in the CAD design and simulations compared to the actual tile width. This led to the rotation of some tiles and the addition of some cut pieces as spacers. Likewise, layout and numbering of the ferrite was done to match tolerances between tiles and ensure all pieces would fit before applying encapsulant.

5.6.2 Construction of the Gen. 2 Coil Assemblies

The Gen. 2 coils were constructed using Lord Cooltherm SC-320 as the encapsulant. Cooltherm SC-320 is a pink-colored silicone elastomer that can be cured at room temperature for a nominal 24 hours. The design and construction of the Gen. 2 coil assemblies were similar

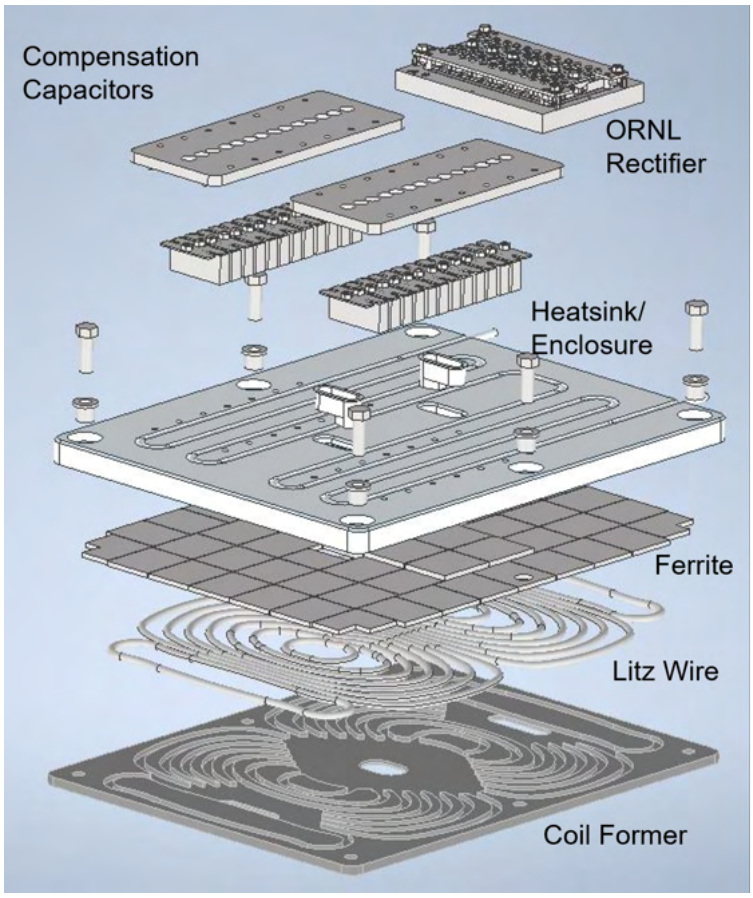

(a)

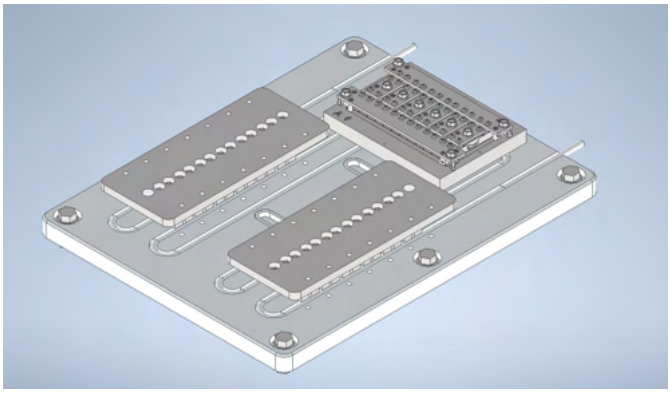

(b)

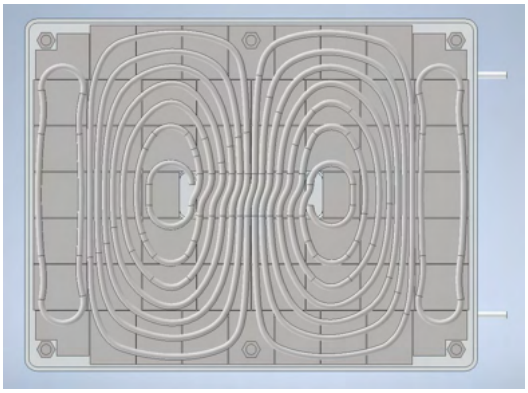

(c)

Figure 5.23: CAD layout of the Gen. 1 coil assembly. (a) Exploded view of the different layers used in the coil assembly. (b) Top view of the assembly with a sample rectifier mounted on the backside of the coil enclosure. (c) Bottom view of the litz wire coil and ferrite.

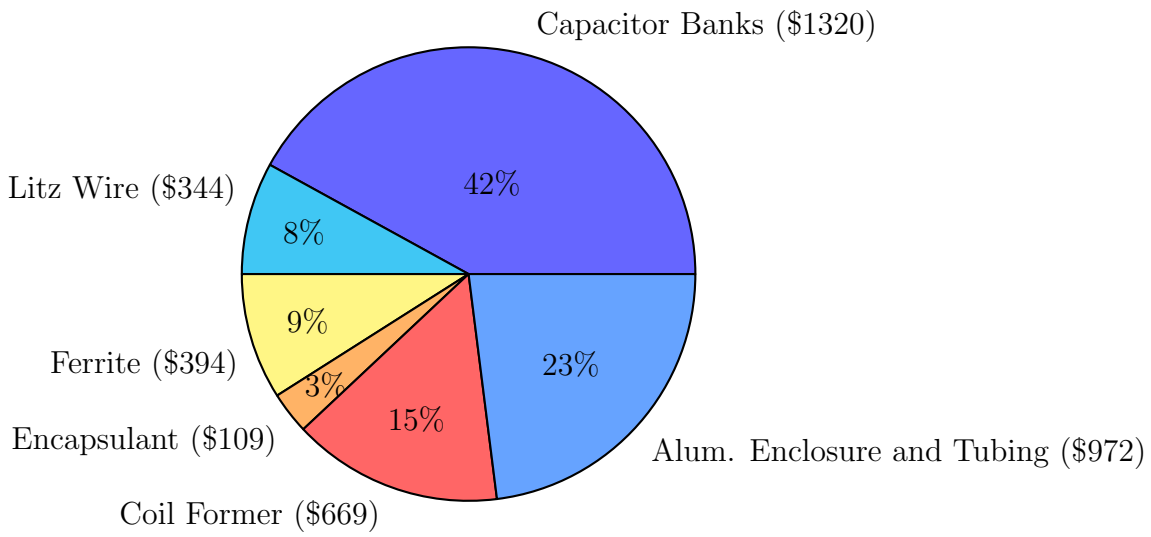

(a)

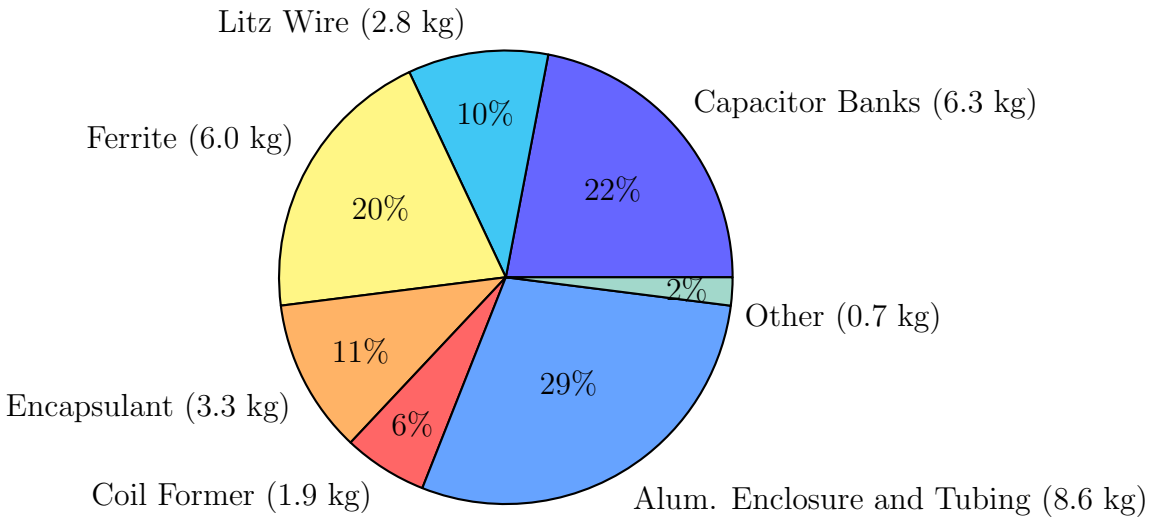

(b)

Figure 5.24: Breakdown of the (a) cost and (b) weight of one of the Gen. 2 demonstrator coil assemblies.

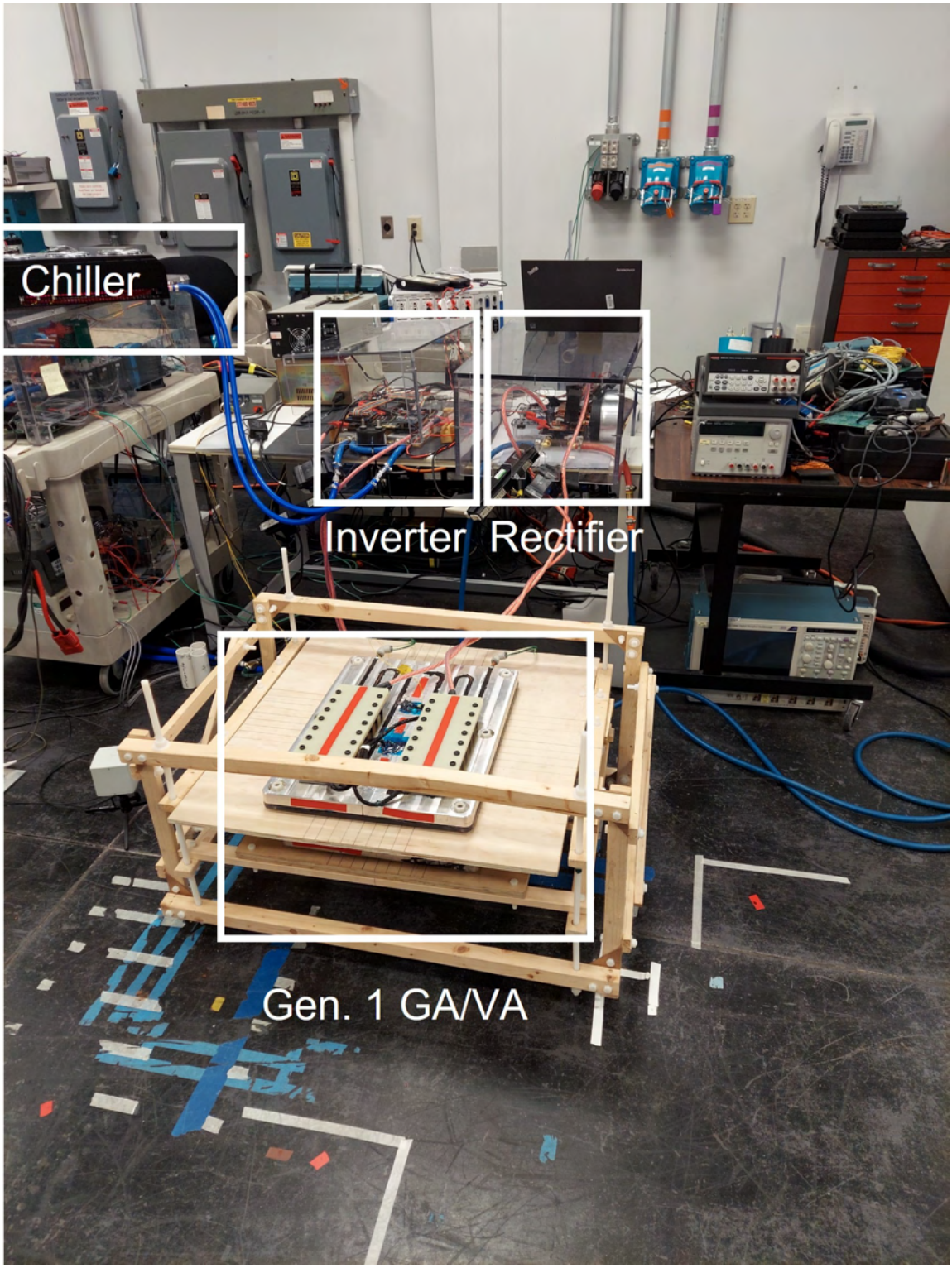

Figure 5.25: Overall test setup used for the Gen. 1 assemblies. Here, the ORNL inverter and rectifier and the top of the Gen. 1 coil vehicle assembly are visible as well as the chiller used to cool the inverter during the test.

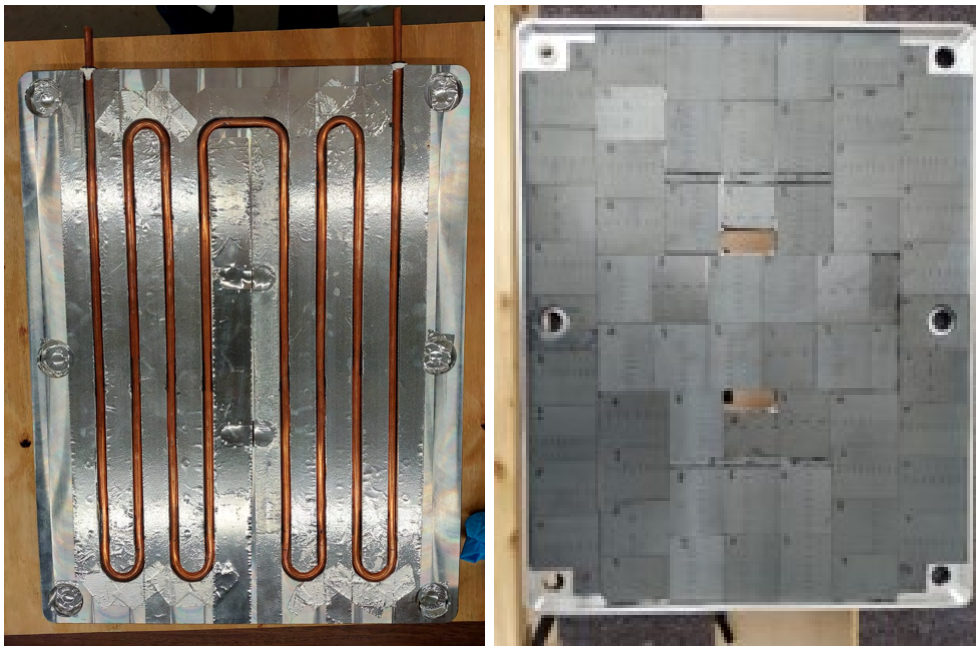

(a) (b)

(c)

Figure 5.26: Construction of the Gen. 1 120 kW coil assemblies. (a) Bent tubing pressed and bonded into the channels in the aluminum enclosure. (b) Ferrite layout and numbering of the Gen. 1 coil assembly with a similar layout used in the other coil. (c) Multiple images of tubing, ferrite and coil encapsulation, degassing of the epoxy, wound coil former, and front sides of the finished Gen. 1 coils.

to that of the Gen. 1 assemblies, but with improvements. In the Gen. 2 demonstrator, the tubing channels were widened by 1/8" to make fitting the tubing in place easier. The inner section of the cavity was widened to accommodate the correct ferrite tile dimensions and the overall ferrite layout was simplified. A passthrough was also eliminated such that both wires were routed together through one opening. This required an additional notch cut into the middle of the polycarbonate coil former. Additionally, better tape was used to keep the wire in place on the coil former when flipped upside down. This tape enabled the wound coil former to be flipped and placed directly on top of a layer of encapsulant poured on top of the ferrite. This was done directly after placing the ferrite on top of a thin layer of encapsulant without the need to cure beforehand as in the Gen. 1 demonstrator.

Images of the Gen. 2 assembly process are shown in Figure 5.27. The cutting of the ferrite tiles in Figure 5.27c was accomplished more cleanly than in the Gen. 1 assembly by the use of a wet tile saw with a continuous diamond blade. This method made precise cuts to the ferrite and prevented the ferrite from shattering from thermal shock as when cutting with a rotary tool in the Gen. 1 construction.

5.6.3 Capacitor Assembly and Mounting

In both the Gen. 1 and Gen. 2 coil assemblies, 12 compensation capacitors, the 1 µF Celem CSM 150/300 conduction cooled capacitors with maximum ratings of 700 V(rms) and 450 A(rms) were connected to the coil in series and divided into two banks of 6 capacitors each. Copper bus bars connect the capacitors with torqued bolts, washers, and nuts as in Figure 5.28a. Cooling of the capacitors is accomplished by thermal contact with the cooled aluminum enclosure through large, insulating thermal pads with clamping force supplied by the compression plates. The compression plates in Figure 5.28b are made of G10 and align the capacitors and busbars that fit in the raised notches on the plates. The compression plates are attached and screwed into threaded holes in the aluminum to provide adequate clamping force for thermal contact. The nuts on top of the busbars fit into holes in the plates, which prevents creepage paths between the corners of the nuts, as seen in the 6.6 kW demonstrator. A layer of mylar tape on the bottom of the capacitors and between the nuts on top of the busbars provides additional insulation.

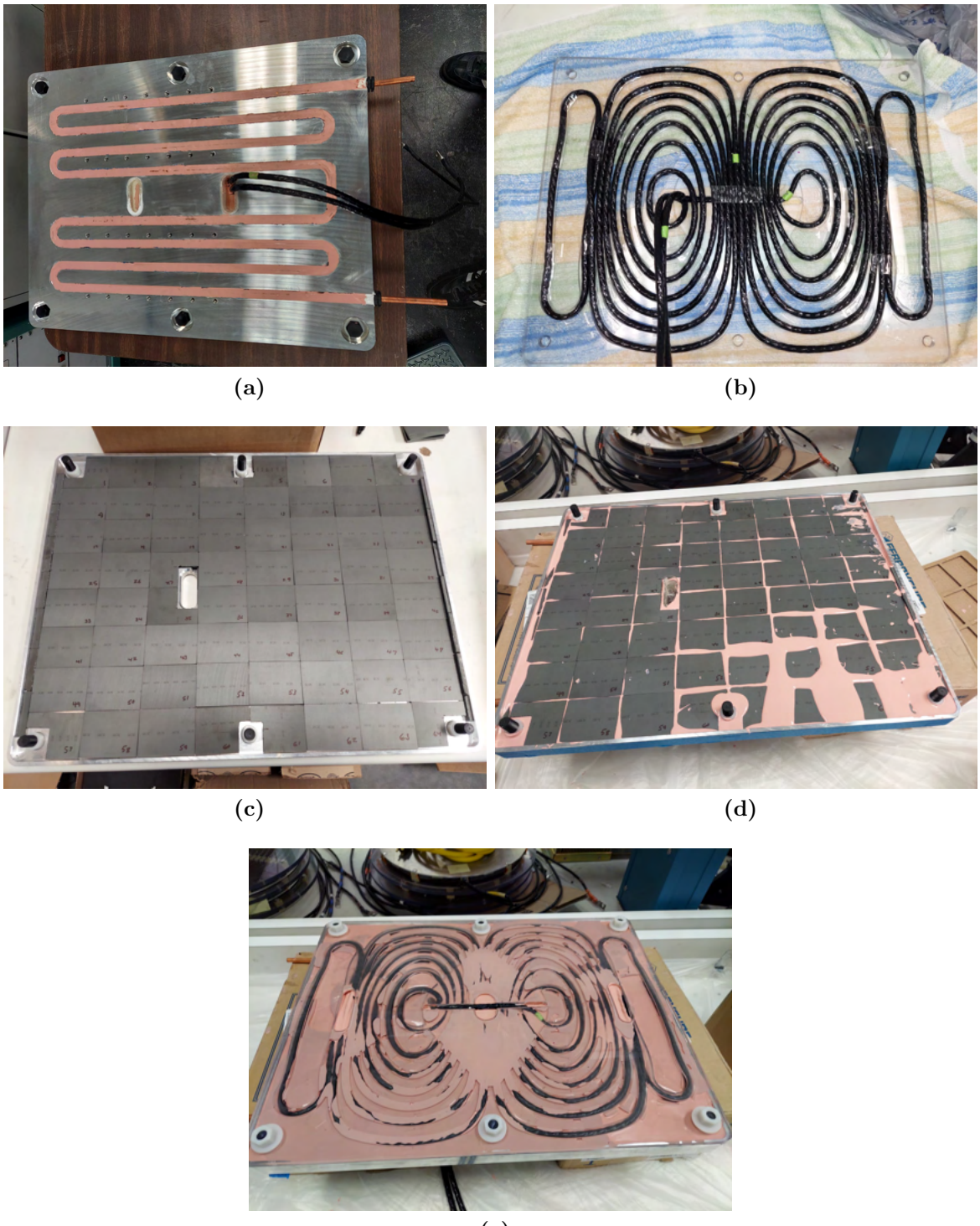

Figure 5.27: Construction of the Gen. 2 120 kW coil assemblies. (a) Bent tubing pressed and bonded into the channels in the aluminum enclosure and covered with encapsulant. (b) Coil former with routed wire taped in place. (c) Ferrite layout and numbering of one of the Gen. 2 coil assemblies. (d) Encapsulation of the ferrite before the 5 mm layer and coil former were added. (e) Frontside of a cured Gen. 2 coil.

This compensation capacitor bank design has several benefits. Conductive cooling of each capacitor is accomplished while keeping the busbars and fasteners away from the aluminum enclosure. The alignment of the capacitors and busbars in series arrangement, which is normally difficult due to the single-bolt package of the capacitors, is resolved by the notches in the compression plate. Finally, the capacitors are mounted close to the wire passthroughs, reducing the need for extra wire for leads or additional heatsink weight in the system.

5.7 Simulation Model

A series of simulations were performed in PLECS to compare the test data with the modeled values. In these simulations, values for the self and mutual inductance as well as the resonant capacitor capacitance were imported into the model. To include losses at the fundamental frequency and from the higher-order, odd harmonic currents in the tank, the frequency-dependent resistance of the conductors and resonant capacitors were included. The ferrite losses were imported as a function of both frequency and amplitude as a linearized resistance only at the fundamental harmonic of current. Overall, the current is highly sinusoidal and most of the loss comes from the fundamental frequency. At the 120 kW operating point, the fundamental current in the GA was 167 A(rms), with 3rd harmonic of 5 A(rms) and 5th harmonic of 1 A(rms), yielding a total harmonic distortion of approximately 3%. The difference between the Steinmetz equation and the improved generalized Steinmetz equation (iGSE) [96] using the waveform data is less than 5%. These values, derived using the parameters in Table 5.6 result in the resistances plotted in Figure 5.30. The measured impedance of the litz wire leads to and from the inverter and rectifier and the GA and VA as in Figure 5.39b are tabulated at the harmonics in Table 5.6 and was added to the resistance and inductance used in the simulations. The leads are shown as additional inductance in the overall circuit diagram with inductance of L_{lead} and resistance of R_{lead} in Figure 5.29.

A benefit of PLECS as a simulation tool is the inclusion of device thermal effects on conduction and switching losses both in hard and soft-switching operating conditions and deadtime intervals t_{dt} used in the tests. PLECS accomplishes this by including temperature-dependent conduction and switching loss models for devices with lookup table or equations

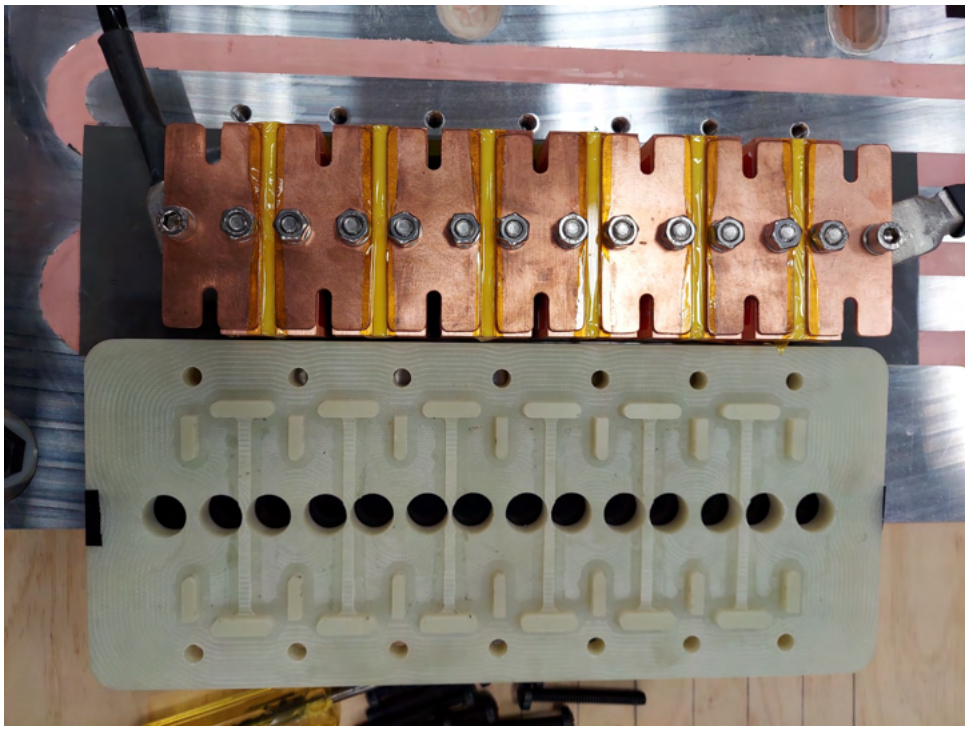

(a)

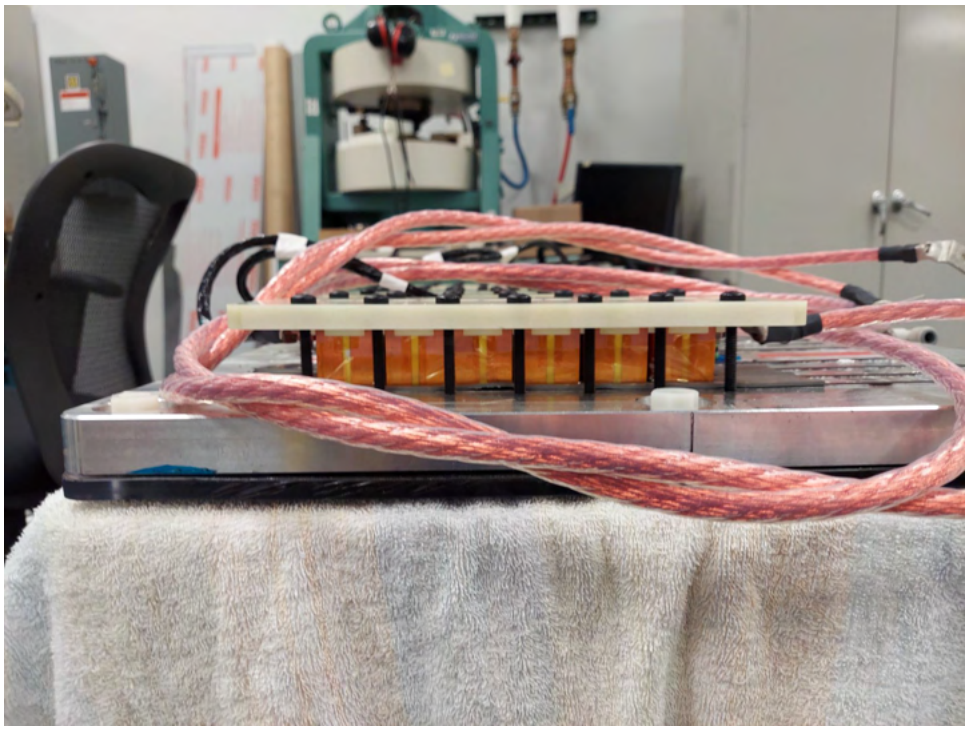

(b)

Figure 5.28: The compensation capacitor bank used in the Gen. 1 and Gen. 2 coil assemblies. (a) View of the disassembled compression plate, bus bars, and capacitors. (b) Side view of the assembled capacitor bank mounted on the Gen. 1 coil assembly.

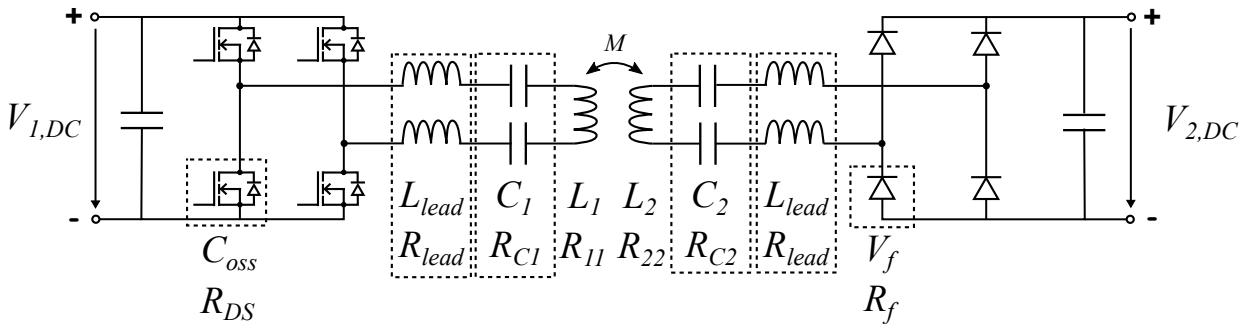

Figure 5.29: The Gen. 1 and Gen. 2 circuit schematic labeled with component parameters. Both demonstrator systems consisted of matched, series-series compensated coils driven by a MOSFET full-bridge inverter with a diode rectifier.

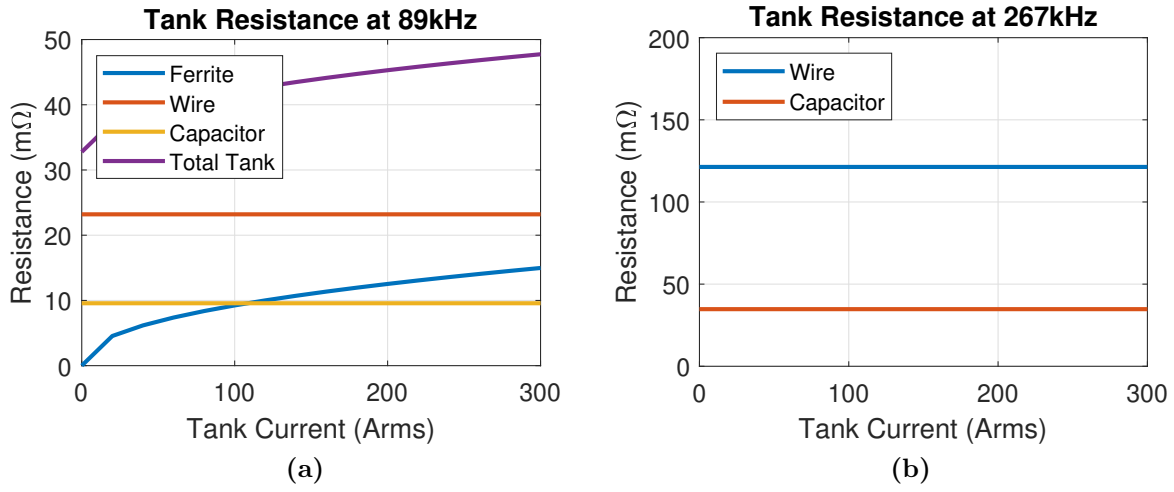

Figure 5.30: Modeled resistance values used in the PLECS simulations at the first two odd harmonics. (a) The modeled resistance values at 89 kHz and (b) 267 kHz.

Table 5.6: Model Parameter Descriptions and Values

Parameters		Value
Ferrite Steinmetz Parameters Ferroxcube 3C95 20 kHz-150 kHz		$\mu_r = 3000$ $C_m = 92.1\text{e-}3$ mW/cm^3 $\alpha = 1.045$; $\beta = 2.440$ $C_t = 1.332$; $C_{t1} = 0.0079$; $C_{t2} = 4.62\text{e-}5$
Temperature of Ferrite		$T_{fer} = 19$°C
Ferrite Thickness		$t_{fer} = 5$ mm (outer) $t_{fer} = 10$ mm (inner), 307mm x 130mm
Litz Wire	Outer Diameter Number of Strands Strand Diameter Cabling Operations Wire Length	$d_{out} = 8$ mm $n = 6750$ $d_{str} = 0.0635$ mm $N_b = 2$ $N_c = 1$ $L_T = 11.9$ m
Measured Lead Inductance and Resistance		$L_{lead} = 1.465$µH, $R_{lead} = 5$ mΩ, 89 kHz 24 mΩ, 267 kHz 55 mΩ, 445 kHz 102 mΩ, 623 kHz 163 mΩ, 801 kHz 235 mΩ, 979 kHz
Inverter Parameters CAS325M12HM2 Module Gate Drive Board CGD1700HB3P-HM3		$R_{DS} = 4$ mΩ $C_{oss} = 1.54$ nF $t_{dt} = 600$ ns $V_{GS} = -4/+15$ V
Rectifier Device Curve Fit BSM300D12P2E001 Module Diode		$V_f = 0.9$ V $R_f = 3$ mΩ
Heatsink (HS) Thermal Resistance Coolant (Liq.) Temperature		0.014 (HS/Liq.)+0.035 (Case/HS Rohm) °C/W 25°C
Copper Wire Resistivity at 20°C		$\rho_{Cu} = 1.724\text{e-}8$ Ω-m
Temperature Coefficient, Copper		$C_{Cu,t} = +0.393$ %/°C
Temperature of Copper		$T_{Cu} = 40$ °C
Gap Between Ferrite and Wire Planes		$z_g = 6.5$ mm

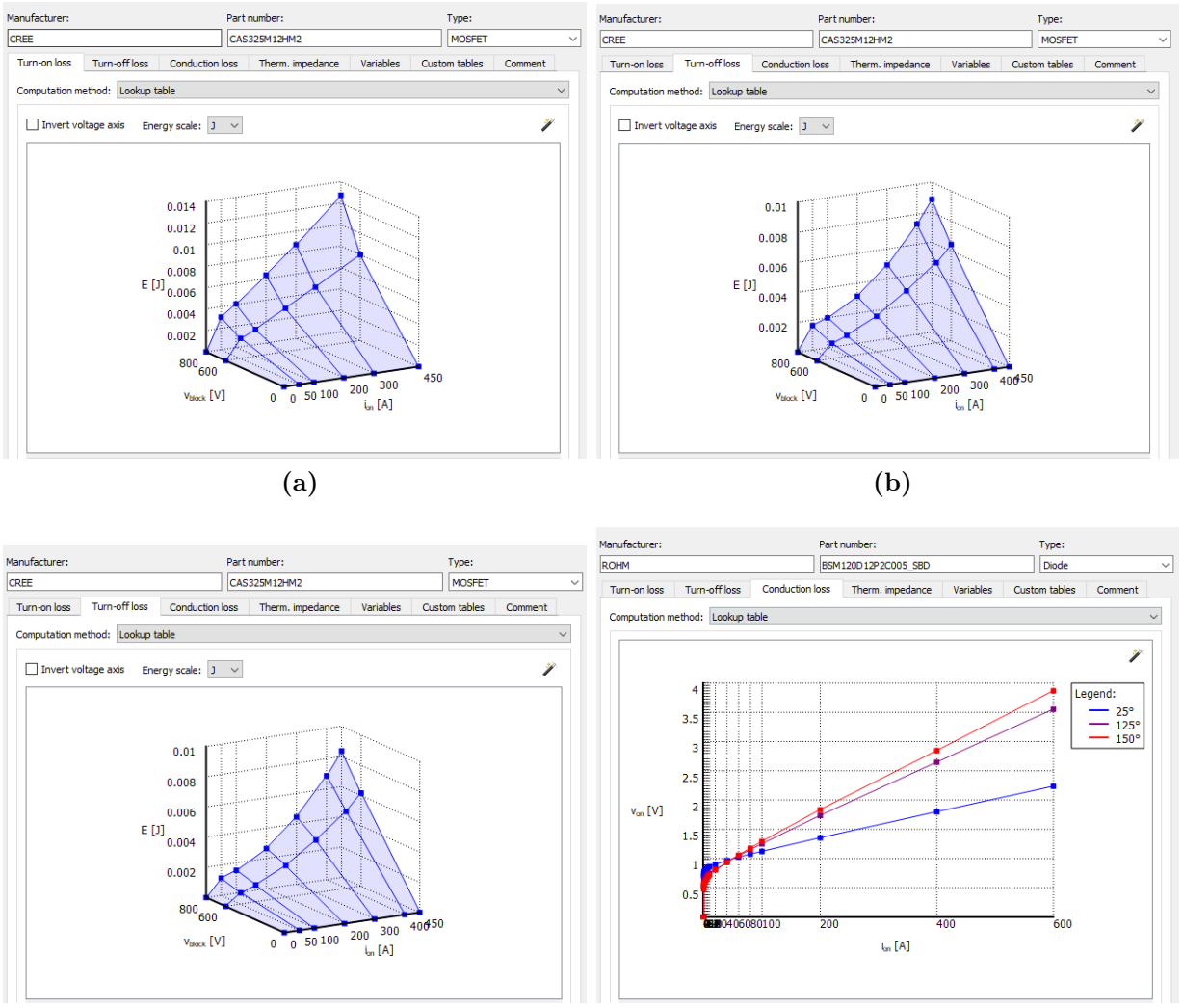

Figure 5.31: The switching loss values for the Cree CAS325M12HM2 module used in the PLECS simulations: (a) E_{on} under hard-switching conditions and E_{off} under (b) hard-switching and (c) soft-switching conditions. (d) Conduction loss values used for the Rohm BSM300D12P2E001 per datasheet values.

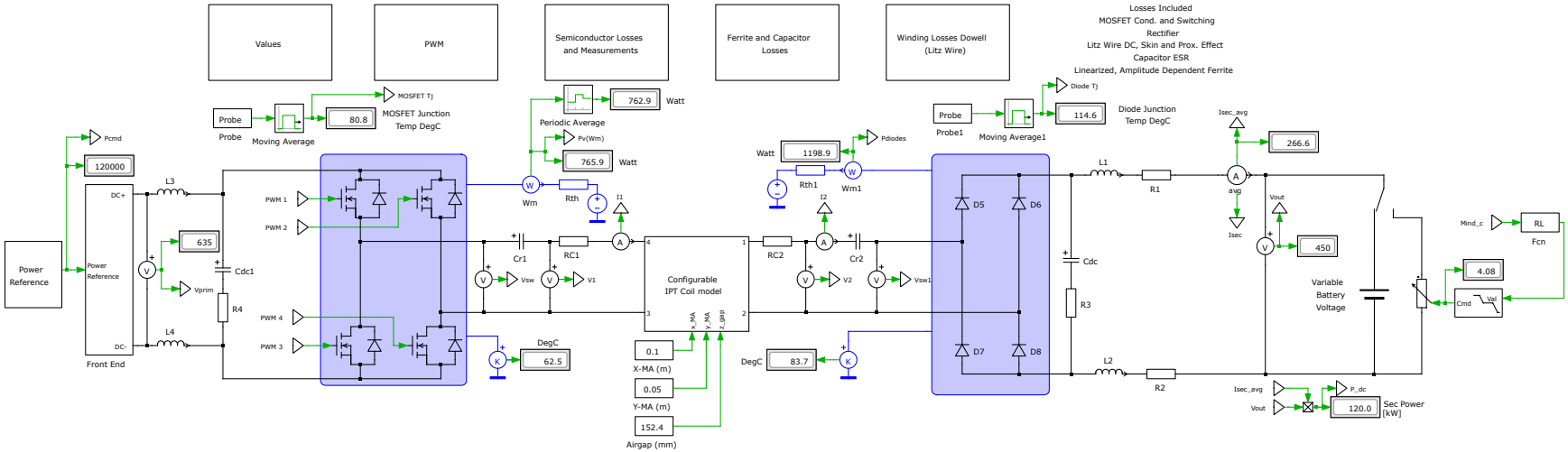

Figure 5.32: The top-level schematic of the PLECS simulation.

and varying the temperature as a function of the losses as the solver time steps through the simulation period.

The 1.2 kV SiC MOSFET half-bridge modules Wolfspeed/Cree CAS325M12HM2 and Rohm BSM300D12P2E001 were used in the inverter and rectifier, respectively, the thermal models of the device are shown in Figure 5.31. The thermal capacitance of the devices was reduced in order to achieve steady-state temperatures quickly. The overall simulation schematic is shown in Figure 5.32 and the litz and switching loss sub-schematics are in Figure 5.33. The simulation used a 3D lookup table of the modeled mutual inductance values as a function of x and y-axis misalignment and airgap inputs. A 1D lookup table of values for the modeled self-inductance of the GA and VA coils added with the measured lead inductance was also included as a function of airgap.

Device switching losses are dependent on many factors, such as power loop inductance and gate driver specifications, voltage, layout, and gate resistance values, but datasheets often only provide switching losses for one set of tests under hard switching conditions. In soft-switching operation, the energy of the device output capacitance $E_{Coss} = \frac{1}{2}C_{oss}V_{DS}^2$ is stored during the turn-off of the device and recovered during the zero-voltage turn-on transition. To extrapolate values from manufacturer data for use in modeling soft-switching losses, the turn-off loss in each period when soft-switching, $E_{off,ss}$, is approximated from the datasheet hard-switching turn-off loss, E_{off}, by [97]

$$E_{off,ss} = E_{off} - E_{Coss}. \tag{5.14}$$

For the Cree/Wolfspeed CAS325M12HM, the C_{oss} value was used to derive the soft-switching turn-off loss table in Figure 5.31c from the datasheet hard-switching turn-off loss in Figure 5.31b with a gate drive voltage of -5/+20 V. In the tests, the Cree/Wolfspeed gate driver board CGD1700HB3P-HM3 was used with a gate drive voltage V_{GS} of -4/+15 V compared to the nominal -5/+20 V gate drive voltage specified in the device datasheet. This causes a slight increase in the nominal on-state resistance to R_{DS} =4 mΩ in the datasheet plots and was accounted for in the PLECS model. However, only switching loss plots for -5/+20 V were given and so the -5/+20 V values were used in the PLECS model.

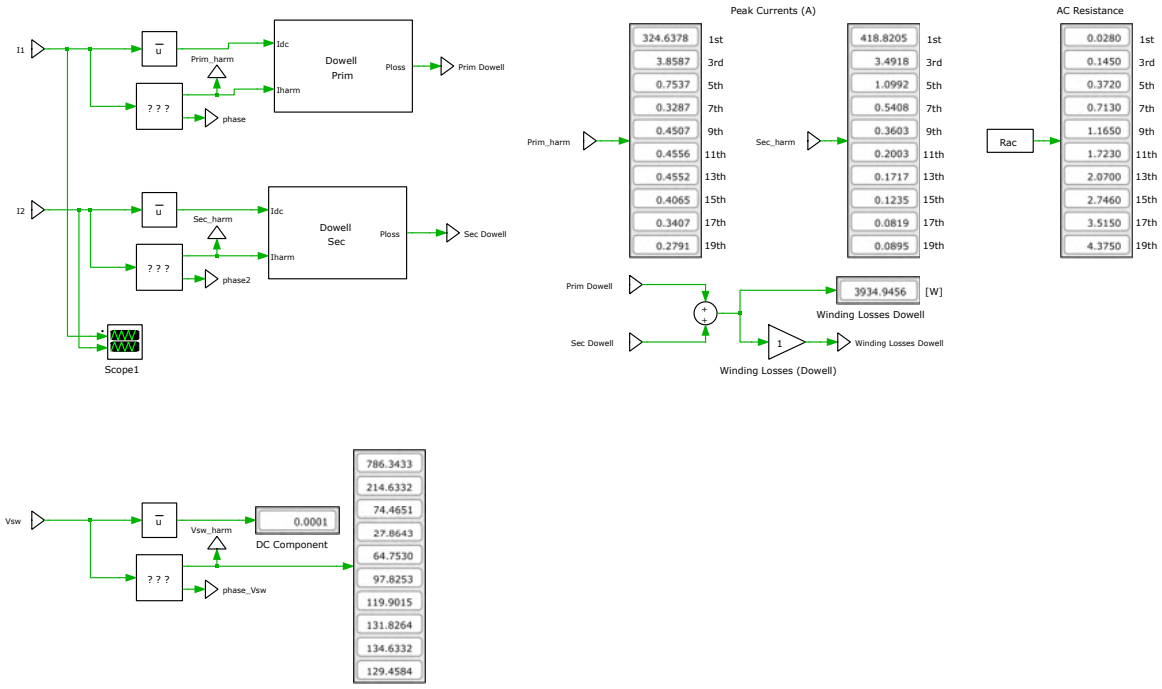

(a)

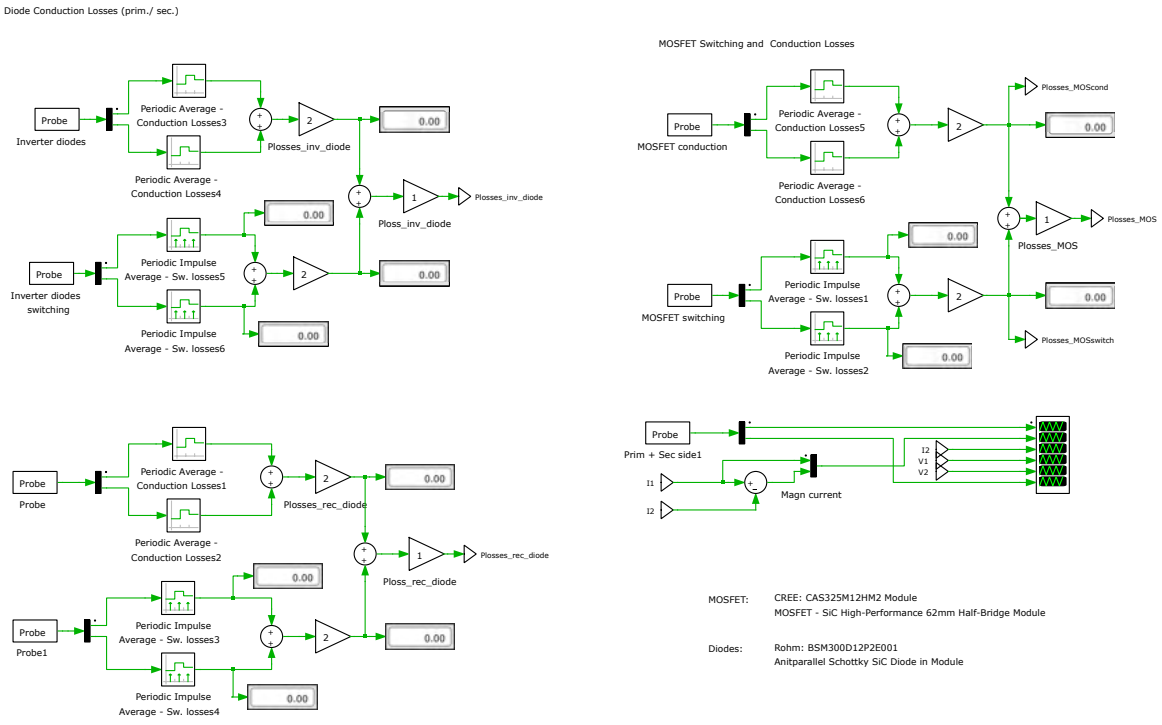

(b)

Figure 5.33: Subdiagrams of the PLECS simulation model including the (a) litz wire and (b) switching loss calculations.

The hard switching operation of the inverter was not extensively tested and validated, but was observed in some test points during frequency sweeps. For example, the 600 V output test at (5 cm, 0 cm) in Figures 5.47c and 5.47d was hard-switching throughout all test points because the switching frequency was set to 85 kHz below the resonant point instead of 89 kHz. This is why the "HS 600 V" curves do not sit evenly between the 400 V and 800 V curves in the plots. The waveform and power analyzer screenshots of 600 V hard-switching at 13.1 kW output power are shown in Figure 5.34 as an example of the inverter ringing and capacitive power factor.

5.8 Testing of the Gen. 1 and Gen. 2 Demonstrators

Testing and measurements of the Gen. 1 and Gen. 2 demonstrators were done using the facilities, equipment, inverters, and rectifiers at Oak Ridge National Laboratory (ORNL). Measurements of impedance, mutual inductances over misalignment, waveforms, stray fields, and efficiencies of the Gen. 1 and Gen. 2 assemblies were taken with comparison to modeled values given for the Gen. 2 system. The performance of the Gen. 1 and Gen. 2 coils was tested at an airgap of 125 mm over different alignments at operating points with close to unity gain, such that the coils had similar currents, and with fixed 400 V and 600 V output voltages to explore operating points with mismatched loading and current. In Section 5.8.1, impedance measurements of the Gen. 1 and Gen. 2 system are shown and compared with the modeled values. In Sections 5.8.2 and 5.8.3, the efficiency and stray field near unity gain with the Gen. 1 system are given. The same for the Gen. 2 system is in Sections 5.8.4 and 5.8.5. The tests of the Gen. 2 system at non-unity gain operation at 400 V and 600 V are summarized in Appendix D and later discussed in Chapter 6.

Images of the overall of the test setup, inverter, and rectifier are given in Figure 5.35. A Hioki PW6001 power analyzer was used to capture the voltage, current, and losses. To capture coil currents, the Hioki CT6904A current sensor was used with datasheet phase compensation. During some of the tests, this allowed the losses of each stage to be measured with accurate higher-frequency AC power measurements at the output of the inverter and input of the rectifier. Test points at high power levels were achieved for short durations such

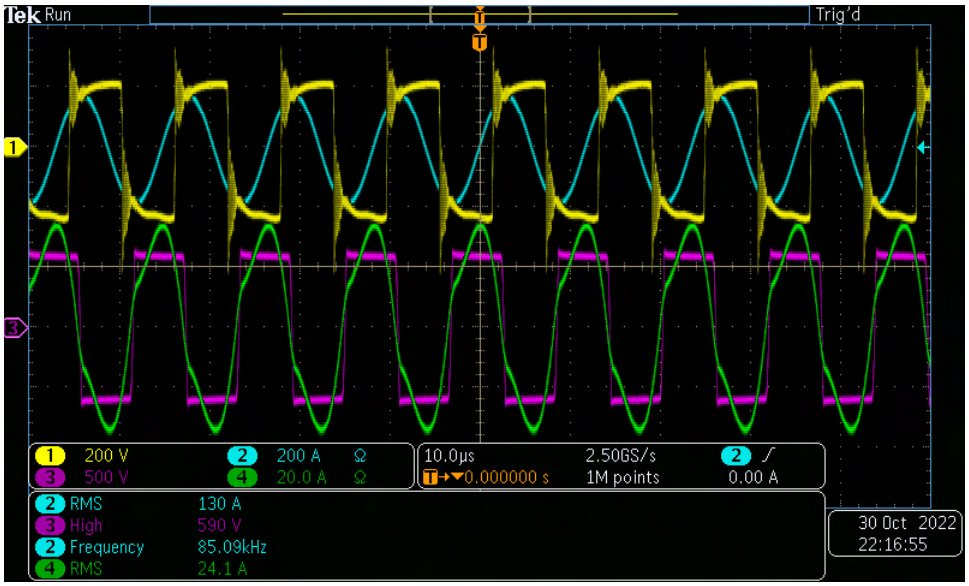

(a)

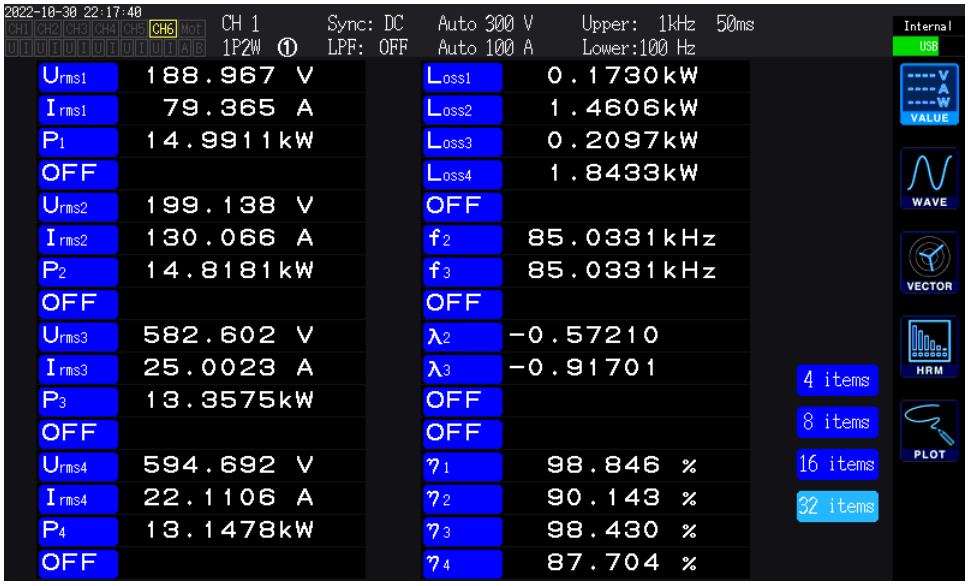

(b)

Figure 5.34: Gen. 2 system test at 600 V output voltage and 13.1 kW output power at an alignment of (5 cm, 0 cm), and a 125 mm airgap (grid offset of (-7 mm, -5 mm)). This test point has inverter hard-switching due to a 85 kHz switching frequency which is below the resonant point of the tanks. (a) Waveforms with significant ringing of the inverter switch node on Channel 1 and (b) power analyzer screenshot with the capacitive inverter power factor seen in the negative λ_2 measurement.

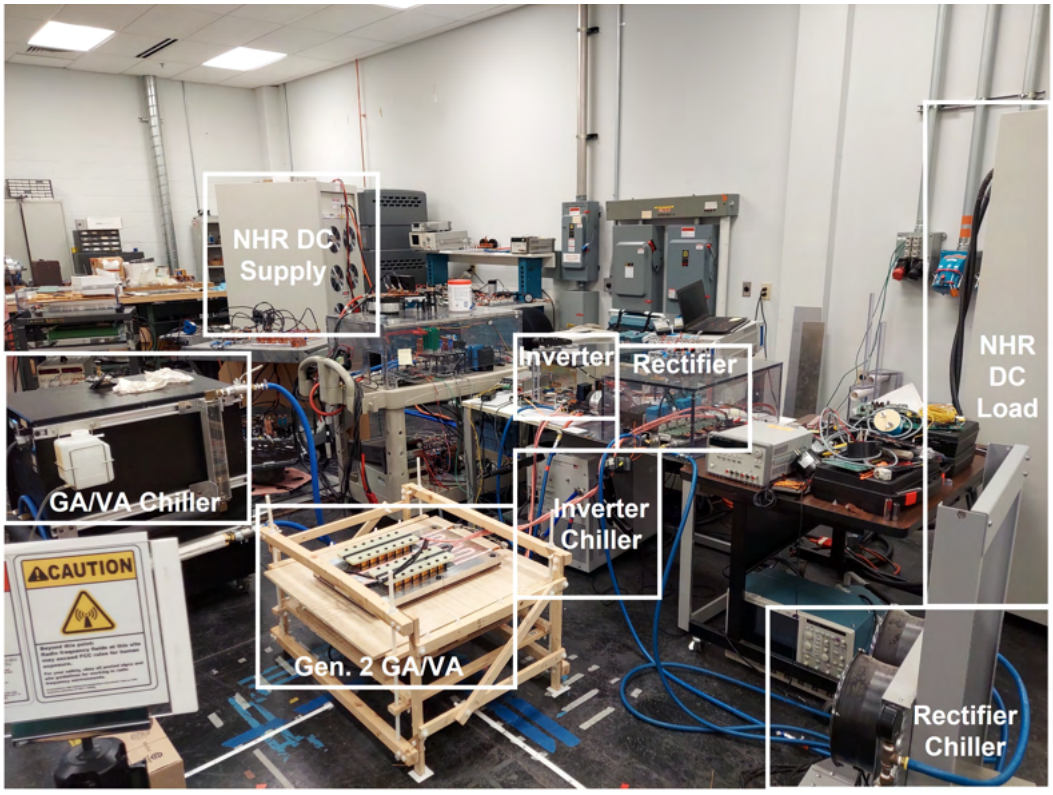

(a)

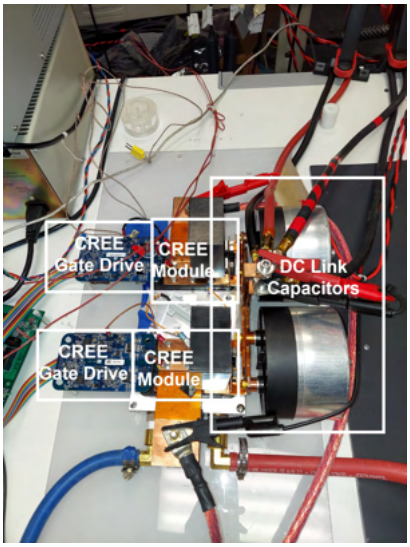

(b)

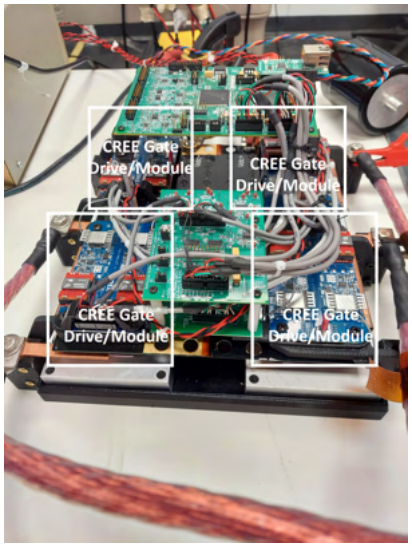

(c)

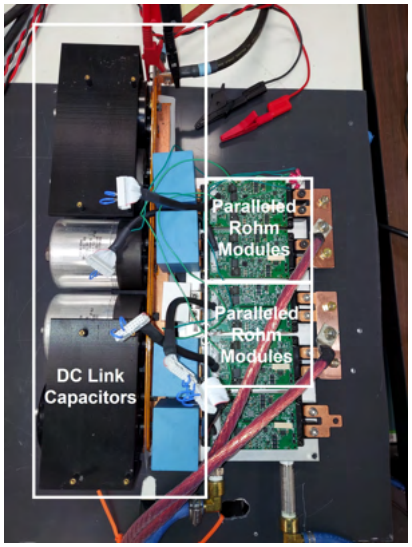

(d)

Figure 5.35: Images of the Gen. 2 test setup. (a) Overall test setup including 100kW DC sources on the input and output of the system, chillers, and airgap holder. (b) ORNL 120kW full bridge inverter, (c) ORNL 2X full bridge inverter with four half-bridge modules, and (d) ORNL Rohm module converter used as the test rectifier.

that the temperatures in the GA and VA remained low. During the tests, the four-channel Omega FOB100 fiber optic thermometer was used. This type of temperature probe is not affected by EMI from the fields of the WPT system such that temperature measurements could be taken during the tests. Temperatures were typically measured on the GA and VA on the surfaces of the resonant capacitors and at the center of the coil geometry on the surface of the outer insulation of the litz wire cable.

5.8.1 Impedance and Mutual Inductance Measurements

Impedance measurements of the Gen. 1 and Gen. 2 coil assemblies were taken using LCR meters and impedance analyzers. To assess the effects of curing on the coils, measurements were taken before and after curing the coils with encapsulant. The self-inductance and resistances of the Gen. 1 and Gen. 2 coils are shown in Figure 5.36. Different instruments, the Aligent E4990A and the Omicron Lab Bode 100, were used in the measurements of the Gen. 1 and Gen. 2 systems respectively. The modeled values for self-inductance and resistance are compared with the measured values in Table 5.7 using an LCR meter with a lead length of 11.9 m (39 ft). These values vary slightly from the values in Figure 5.36. Measurements were taken with the coils aligned at an air gap of 125 mm and the presence of ferrite across the airgap slightly increases the self-inductance values.

The mutual inductance of the coils was found by measuring the inductance of the series combination of the coils over different misalignments and subtracting the measured self-inductance of the coils. Mutual inductance measurements compared to the modeled values from the FAM are shown in Figure 5.37. As seen, the measured values were within 10% of the modeled values for all misalignment points. For both the Gen. 1 and Gen. 2 coils, there was a trend in the error that positive X and Y-axis misalignment related to higher measured mutual inductance relative to the model. This was due to an approximate -7 mm offset in the VA grid on the X-axis and a -5 mm offset on the Y-axis. Introducing this offset to the modeled values reduced the error to within 5% as in Figure 5.38.

In both demonstrators, two capacitor banks with a series combination of twelve 1 µF Celem CSM150/300 capacitors were used to form a series tank with the GA and VA coils. The capacitance and series resistance of one of these capacitor banks are given in

Figure 5.39a and compared to the modeled values in Table 5.8. As seen, the capacitance of the capacitors are affected by a parasitic resonance such that the capacitance increases with frequency, especially above 100 kHz. The two Gen. 2 tank impedances are also shown in Figures 5.39c and 5.39d, with some parasitic resonances seen in the MHz range. There is a difference in the series resistance measurements with the LCR meter in Table 5.8 and the Bode 100 impedance analyzer measurements in Figure 5.39a possibly due to differences in the setup or calibration of the two instruments.

The measured inductance and series resistance of the leads is also plotted in Figure 5.39b. This measurement is important as the leads add significant resistance and self-inductance to the GA and VA tanks and effects the resonant point of the tank and overall system efficiency. Therefore, the lead impedance is included in the simulations and modeling to match the parasitics in the test setup. Some of the difference in series resistance and self-inductance of the Gen. 1 and Gen. 2 coils can be accounted for in the additional six feet of lead length of the Gen. 1 coils compared to that of the Gen. 2 coils when the measurements were taken.

5.8.2 Gen. 1 Efficiency and Thermal Measurements

The Gen. 1 GA and VA were tested up to 90 kW output power over a variety of loading conditions and misalignments. For the aligned condition with near-unity gain with constant output resistance, the test results are plotted in Figure 5.40. In Figure 5.40a, the efficiency of each stage is shown. In these measurements, phase compensation of the high-frequency current probes was not performed, which led to some inaccuracy of the power factor, AC power, and efficiency measurement of the stages. The overall DC/DC efficiency is based on DC-link measurements and is not affected by the phase error of the current probes. However, the separately measured inverter, coil-coil, and rectifier efficiencies are still included, as they clearly show the decrease in coil-coil efficiency as the power level increases and the lower rectifier efficiency associated with the rectifier forward voltage drop.

At low power levels, the coil-coil efficiency is high, matching the low-amplitude measurements of resistance and impedance of the Gen. 1 GA and VA. At high power levels,

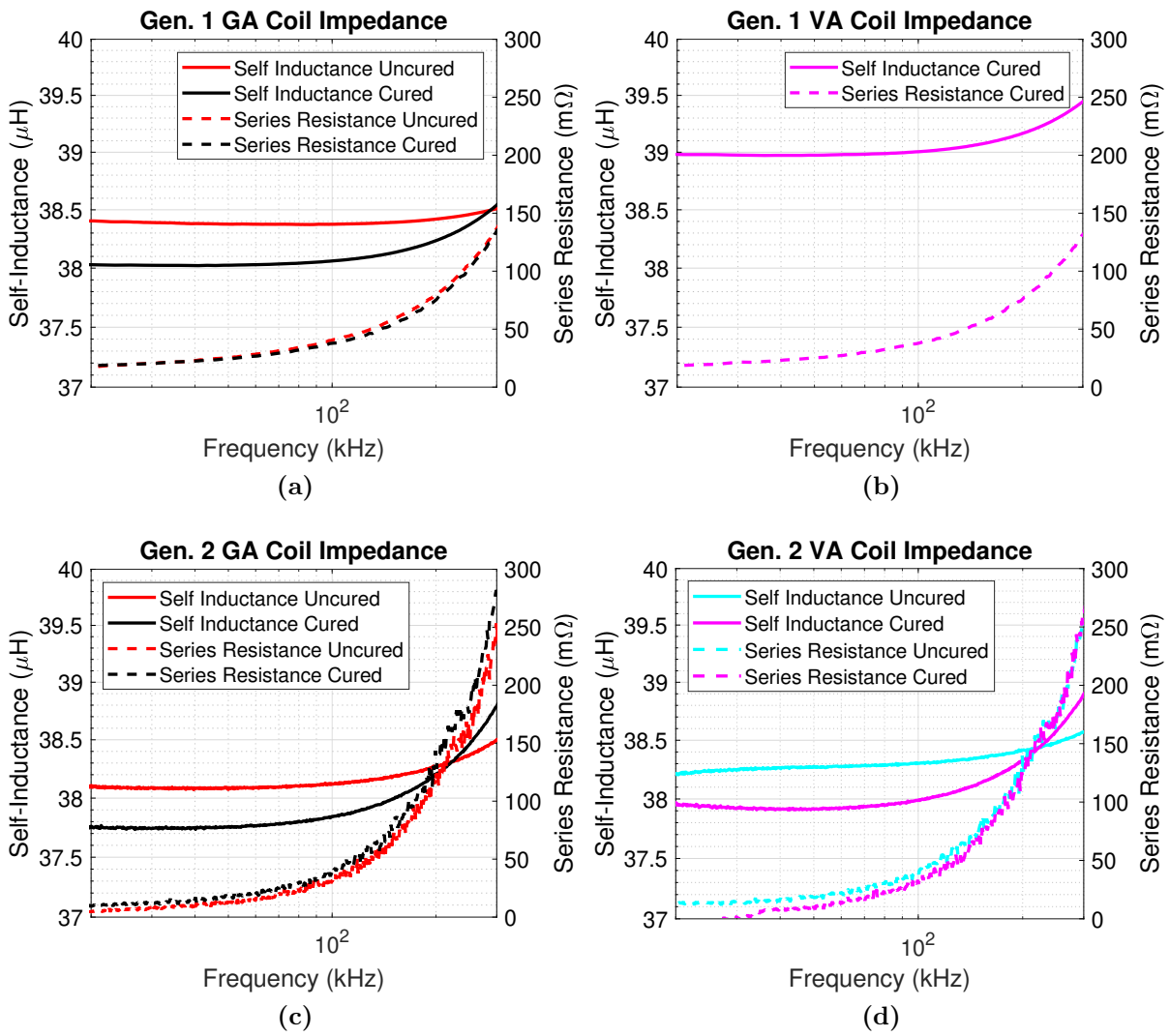

Figure 5.36: Measured self-inductance and series resistance of the uncured and cured coils without the presence of the other coil. (a) Cured and uncured measurements of the Gen. 1 GA coil. (b) Cured measurements of the Gen. 1 VA coil. In this case, measurements were only taken after assembly and were not captured before curing. (c) Measurements of the uncured and cured Gen. 2 GA coil. (d) Measurements of the uncured and cured Gen. 2 VA coil.

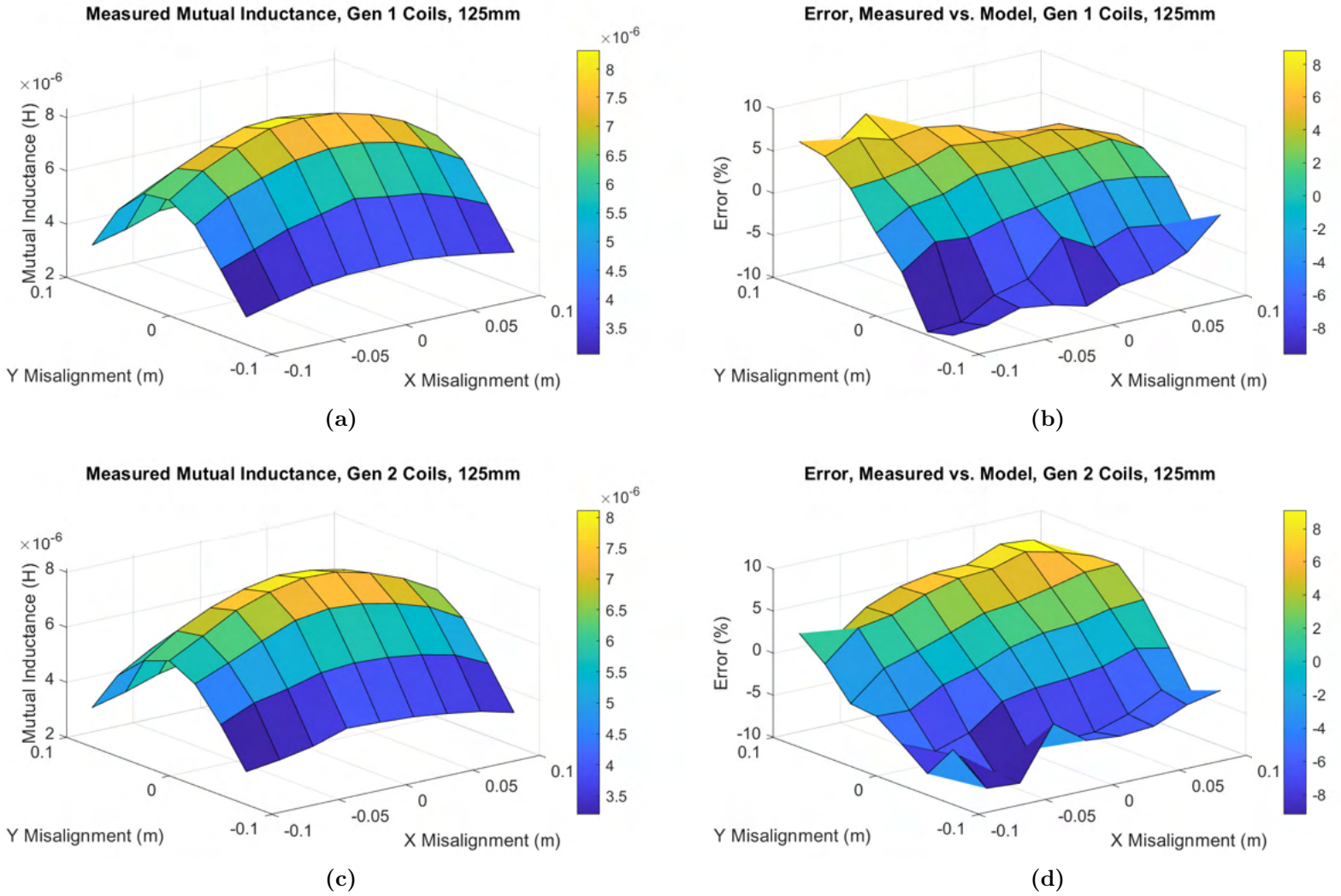

Figure 5.37: Measured mutual inductance of the Gen. 1 and Gen. 2 coil compared to the modeled values. (a) Measured mutual inductance of the Gen. 1 coils and (b) error compared to the modeled values. (c) Measured mutual inductance of the Gen. 2 coils and (d) error compared to modeled values.

the coil-coil efficiency plot has perturbations in efficiency. This is due to pulsed measurements and the effect of temperature on the coil efficiency. Measurements after a resting time at higher temperatures led to slightly higher efficiencies. The component temperatures during a few of the higher power test points up to 91.8 kW are plotted in Figure 5.40b. In the temperature measurements, it was observed that the wire temperatures continued to increase after the system was turned off for a short period of time, suggesting that the ferrite temperature might have been higher than that of the wire. As mentioned in Section 5.4, higher overall temperatures closer to the curing temperature of the Aremco 2315 epoxy should reduce the stress on the ferrite and decrease ferrite loss. Higher ferrite temperature up to around 100°C for Ferroxcube 3C95 also leads to lower ferrite loss.

A three minute duration test at 60 kW was performed to assess the system temperatures. For this test, the coils were cooled with a VWR 1175MD chiller with glycol-water coolant at a pressure of 9 psi (62.1 kPa), coolant flow rate of of 1 lpm, and set point of 19°C, with the GA and VA coolant tubes in series. The test data are shown in 5.41. Some cracking noises that may have been caused by thermal expansion were heard during the tests. As seen, the temperatures of the GA and VA coils rapidly rise from 20°C to around 62.4°C and 56.4°C, respectively. The temperatures of the GA and VA capacitors stay lower with temperatures reaching a maximum of around 30°C. Due to the low coolant flow rate, the temperatures take around 21 minutes to return to close to the starting temperatures. The data suggests that much of the loss is in the GA and VA assemblies and that the flow rate of 1 lpm is not high enough. The continued increase in temperature after the end of the three-minute period at 60 kW, as also seen in Figure 5.40b, again suggests that the ferrite beneath the wire may be hotter than the wire itself.

A summary of the measured Gen. 1 DC/DC efficiency at other alignments is given in Table 5.9 at the highest power levels achieved compared to the modeled values. As seen, the measured DC/DC efficiency is much lower than modeled as a result of the rapid drop-off in coil-coil efficiency.

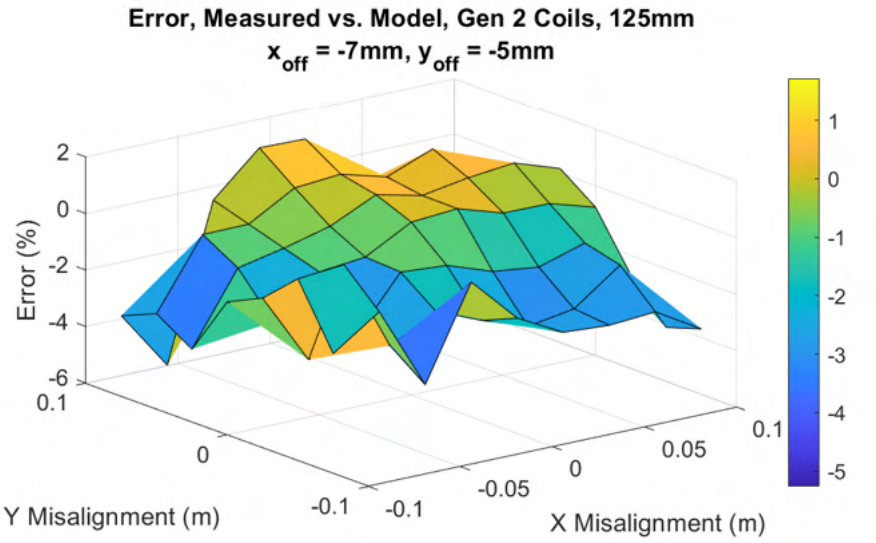

Figure 5.38: Mutual inductance measured vs. modeled error with -7 mm X-axis and -5 mm Y-axis offset.

Table 5.7: Measured vs. Modeled Gen. 1 and Gen. 2 Self-Inductance and Resistance Aligned at 125 mm Airgap from LCR Meter at 85 kHz

	Self-Inductance (L_1, L_2)		Series Resistance (R_{11}, R_{22})		
	Measured (GA, VA)	Modeled (Coil Only 10.2m)	Measured (GA, VA)	Modeled (Coil Only 10.2m)	Modeled (With Leads 11.9m)
Gen. 1	37.9µH, 38.1µH	37.4µH	35mΩ, 36mΩ	19.7mΩ	23mΩ
Gen. 2	38.9µH, 39.1µH	37.4µH	23mΩ, 16mΩ	19.7mΩ	23mΩ

Table 5.8: Measured vs. Modeled Capacitor Bank Impedance at 85kHz by LCR Meter (Celem CSM 150/300)

	Series Capacitance (C_1, C_2)		Series Resistance (R_{C1}, R_{C2})	
	Measured (GA, VA)	Nominal	Measured (GA, VA)	Modeled
12S-1 µF Bank	84.1 nF, 84.1 nF	83.3 nF	9 mΩ, 10 mΩ	9.6 mΩ

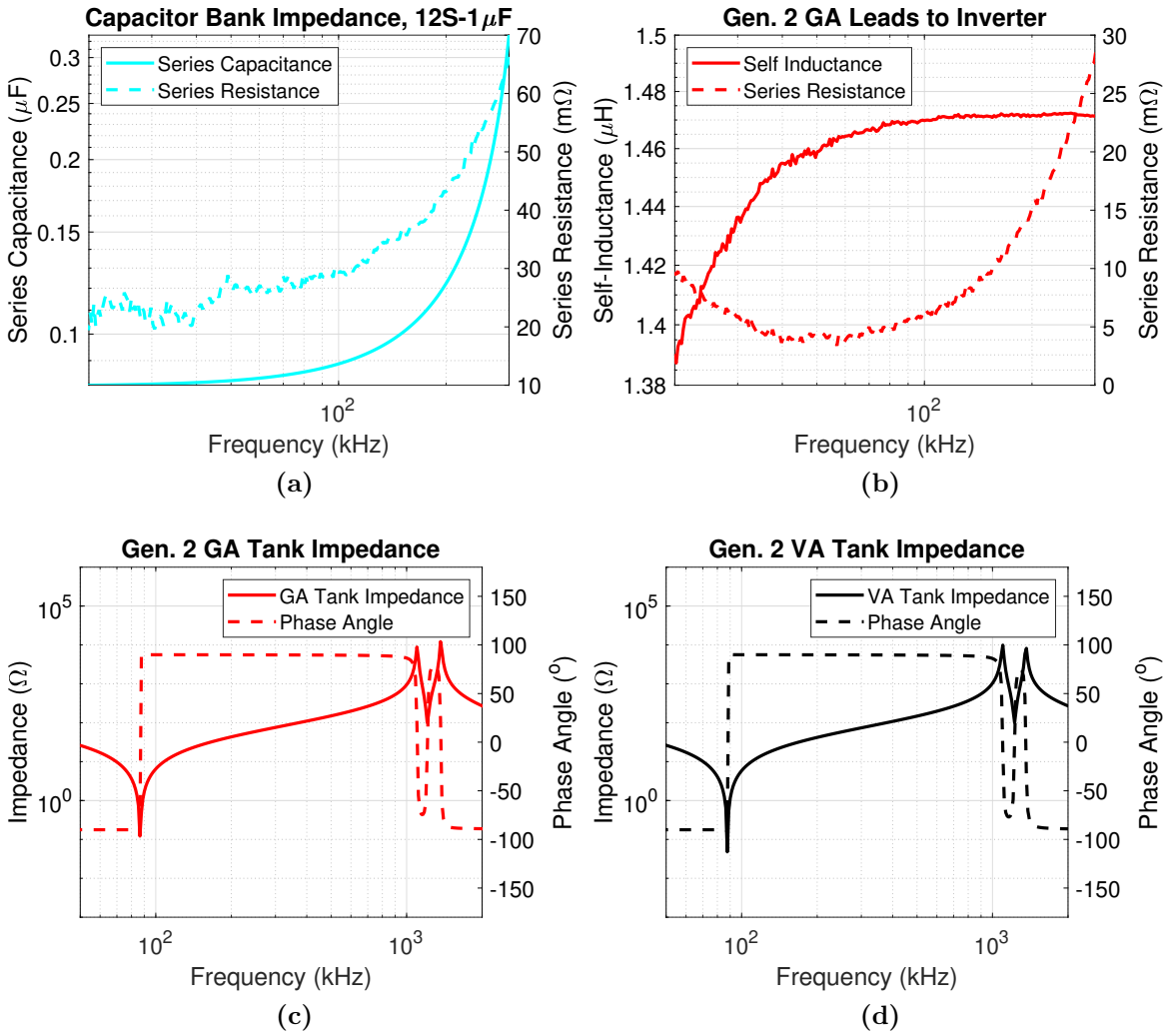

Figure 5.39: Measurements of the tank elements comprised of twelve 1μF Celem CSM 150/300 capacitors and series tank impedance with the Gen. 2 coils. (a) Measured capacitor bank series capacitance and resistance. (b) Measured lead impedance to and from the GA and VA to the inverter and rectifier. (c) Cured measurements of the Gen. 2 GA tank. (d) Cured measurements of the Gen. 2 VA tank.

Table 5.9: Summary of the measured and modeled DC/DC efficiency of the Gen. 1 system at different alignments at an airgap of 125 mm. Grid offset of (-7 mm, -5 mm).

Alignment (X,Y)	DC Output Resistance	Power Level	Meas. DC/DC Eff.	Model DC/DC Eff.
(0cm, 0cm)	6.8 Ω	91.8 kW	93.3%	96.3%
(5cm, 0cm)	5.9 Ω	48.5 kW	93.3%	96.2%
(10cm, 0cm)	5.5 Ω	46.7 kW	91.8%	95.3%
(0cm, 5cm)	5.5 Ω	44.2 kW	92.1%	95.2%

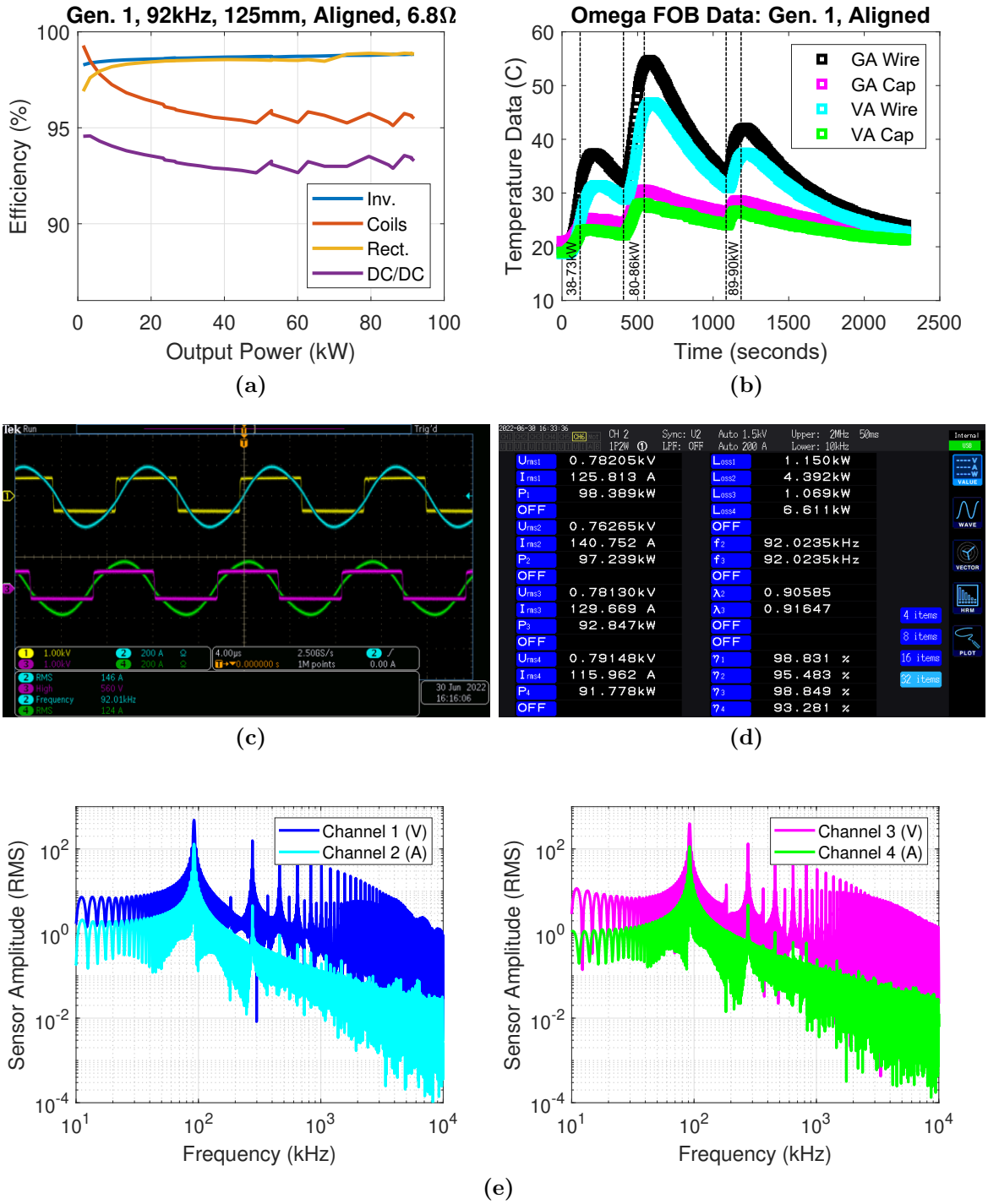

Figure 5.40: Test of the Gen. 1 system at alignment (grid offset of (-7 mm, -5 mm)) and 125 mm. (a) Efficiency breakdown up to 91.8 kW output power. (b) Thermal measurements of the system during testing points around 91.8 kW. (c) Waveforms at 91.8 kW output. (d) Power analyzer screenshot at 91.8 kW. (e) FFT of the waveforms at 91.8 kW.

5.8.3 Gen. 1 Stray Field Measurements

To assess the stray field performance of the Gen. 1 demonstrator, the fields of the system were measured at a distance of 80 cm away from the center of the airgap with a NARDA EHP-200A field probe. The fields at a power level of 50 kW at alignment are shown in Figure 5.42 and a summary of the measured fields at the fundamental frequency at all alignments is given in Table 5.10. As shown, the fields increase on both axes under misaligned conditions, but more significantly on the axis in the direction of offset. The stray field is comprised of fields in the X, Y, and Z directions. Although these B_x, B_y, and B_z components may not be in phase, the vector sum of the three is often used as the total worst-case magnetic field used to compare with the reference values in the standards [27].

5.8.4 Gen. 2 Efficiency and Thermal Measurements

The Gen. 1 system achieved acceptable stray field performance, but with lower efficiency than expected. After analyzing the measured losses of the Gen. 1 system, several modifications were made in the Gen. 2 system including different encapsulant as in Section 5.4, and a improved ferrite layout and a single passthrough in the ferrite for the coil leads as in Section 5.5. The Gen. 2 coil assemblies were then constructed and tested to measure the effect of these modifications.

The Gen. 2 demonstrator was tested up to 120 kW in various alignments. Equipment similar to that in the Gen. 1 tests was used to measure efficiency and temperatures. For the aligned condition up to 120 kW, the system efficiencies are shown in Figure 5.44. The measurements are compared to the modeled efficiency as derived in PLECS using the parameters in Table 5.6. In the PLECS simulation, the modeled inductances were used, leading to a small error in the calculation of current and gain as in Figure 5.44b. For this test sweep, the Hioki PW6001 power analyzer and current probes were set up with phase compensation so that the breakdown between the inverter, coil-coil, and rectifier efficiency is more accurate than in the Gen. 1 tests. The power analyzer screen shot and waveforms of the system at 120 kW are shown in Figure 5.45.

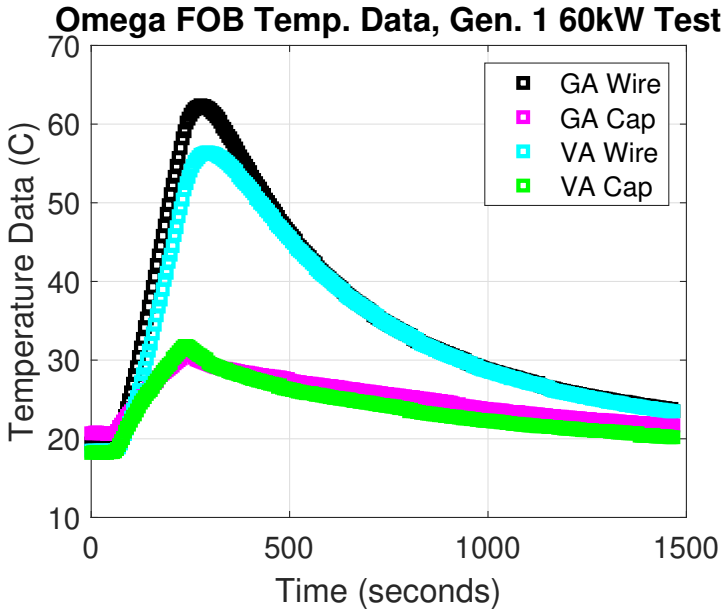

Figure 5.41: 60 kW 3 minute duration testing and cooling of the Gen. 1 system at alignment with measured grid offset of (-7 mm, -5 mm), and 125 mm airgap.

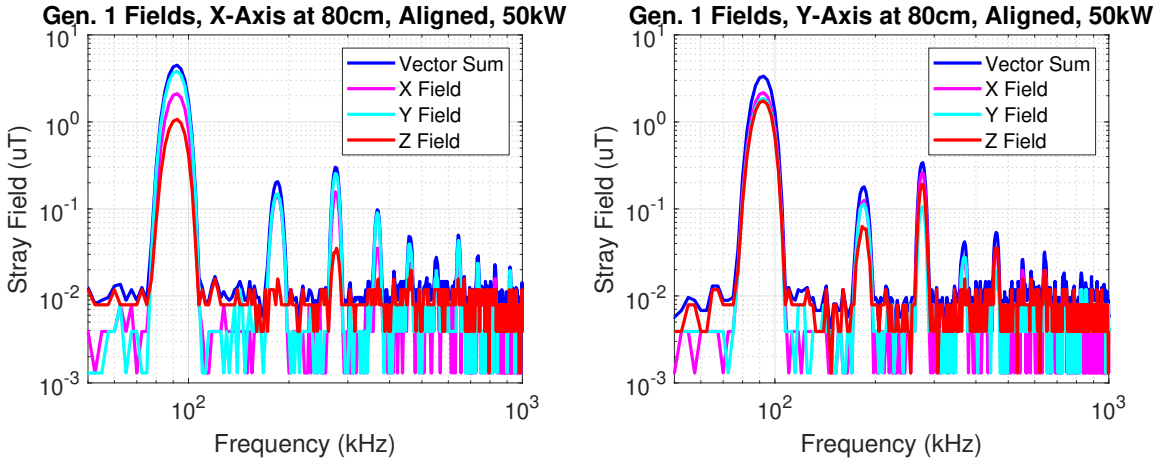

(a) **(b)**

Figure 5.42: Field measurements at the middle of the airgap at 80 cm distances at of the Gen. 1 system at alignment with an output power of 50 kW. (a) FFT of X-axis fields and (b) Y-axis fields.

As seen, the inverter and rectifier efficiencies increase with power level to a peak of 99.6%. Meanwhile, the coil-coil efficiency starts around 98.2% at low power and gradually decreases to 97.4% at the peak power of 120 kW. The effect of the ferrite loss can be clearly seen in the increased coil-coil loss at higher current and output power. The comparison of the overall modeled and measured coil-coil loss in Figure 5.44d suggests that the ferrite losses may increase faster at high power levels than those modeled. These sets of tests were pulsed measurements such that the temperatures of the GA and VA did not rise very much and thermal effects are likely small. The efficiencies near unity gain measured at other misalignments are summarized in Table 5.11. Plots of these tests with comparisons to the modeled values are found in Appendix D.

To increase the pressure and flow rate of the coolant through the coils, a building chiller with the GA and VA tubing in parallel was used for some of the initial tests at a supply pressure of around 15 psi (103.4 kPa). For high power and duration testing, a larger chiller, the Bay Voltex MCHT100 was used to provide a higher pressure of 32 psi (220.6 kPa) and flow rate of 7.1 lpm (1.88 gpm) for around 3.6 lpm (0.95 gpm) through each assembly at a temperature setpoint of 19°C. The pressure for the benchtop demonstrator includes the length of hose to and from the coils and the 5/16" (inner diameter 0.215" or 5.46 mm) copper tubing of the coil assemblies, which was around 13 ft (4 m) per assembly, and quick-connect fittings, so not all the pressure drop was from the assembly tubing itself. However, even at relatively low flow rates of 3 lpm, the Reynolds number for 50/50 water glycol flow in 0.215" inner diameter copper tubing (assumed roughness of 0.0015 mm) is 2591, leading to turbulent flow and a high pressure drop of 12.5 psi (86.2 kPa) following the methodology of [91]. The estimated pressure drop of the coil assembly alone is plotted in Figure 5.43 assuming turbulent flow at a Reynolds number over 2000. The pressure drop is higher than would be desirable for an automotive part, but could be made lower with larger tubing diameter and fewer passes of tubing.

With better cooling in place, a 15 minute, 50 kW output power test was performed at alignment to assess the steady state temperature and overall thermal performance of the system. Using a fiber-optic thermometer, the temperatures of the GA and VA are measured during the test. Likewise, the power analyzer was used to record the measurement data

Table 5.10: Measured RMS stray field (B_x, B_y, B_z) of the Gen. 1 system at an airgap of 125 mm. Misalignment toward probes. Grid offset of (-7 mm, -5 mm).

Alignment (X,Y)	Measurement Output Power	X-axis at 80 cm (Scaled 120 kW Field)	Y-axis at 80 cm (Scaled 120 kW Field)
(0cm, 0cm)	50.0 kW	3.81μT, 2.11μT, 1.07μT (5.90μT, 3.27μT, 1.66μT)	1.87μT, 2.17μT, 1.74μT (2.90μT, 3.36μT, 2.70μT)
(5cm, 0cm)	48.4 kW	4.32μT, 2.73μT , 1.23μT (6.80μT, 4.30μT, 1.94μT)	1.92μT, 2.07μT, 1.77μT (3.02μT, 3.26μT, 2.79μT)
(10cm, 0cm)	46.7 kW	5.93μT, 4.12μT, 1.60μT (9.51μT, 6.60μT, 2.56μT)	2.29μT, 2.39μT, 2.06μT (3.67μT, 3.83μT, 3.30μT)
(0cm, 5cm)	44.2 kW	3.77μT, 2.35μT, 1.15μT (6.21μT, 3.87μT, 1.89μT)	2.05μT, 2.29μT, 2.11μT (3.38μT, 3.77μT, 3.48μT)

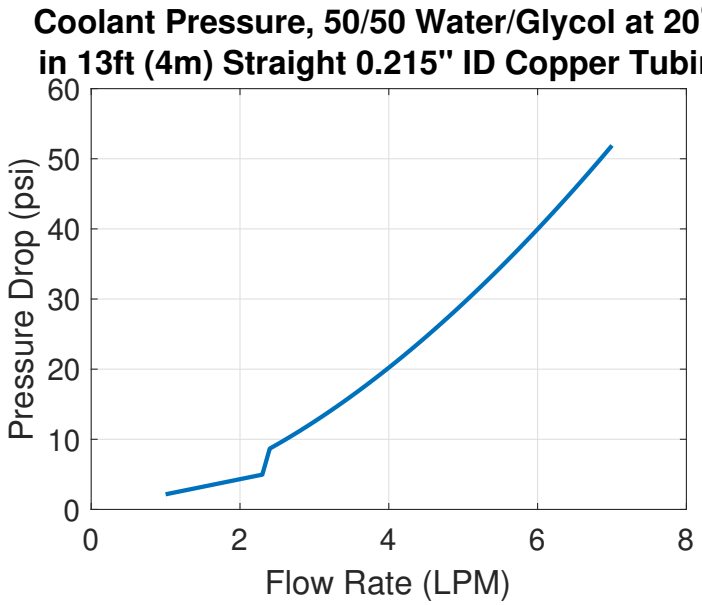

Figure 5.43: Estimated coolant pressure drop at 20°C from one Gen. 1 or Gen. 2 assembly assuming 13 ft of straight copper tubing with an inner diameter 0.215" (5.46 mm).

Table 5.11: Summary of the DC/DC efficiency of the Gen. 2 demonstrator near unity gain at different alignments at an airgap of 125 mm. Grid offset of (-7 mm, -5 mm).

Alignment (X,Y)	DC Load	Power Level	Meas. DC/DC Eff.	Model DC/DC Eff.
(0cm, 0cm)	5.9 Ω	120.4 kW	96.6%	96.7%
(5cm, 0cm)	5.9 Ω	64.2 kW	96.6%	96.8%
(10cm, 0cm)	5.9 Ω	52.7 kW	95.9%	96.0%
(0cm, 5cm)	5.0 Ω	51.2 kW	96.1%	96.2%
(10cm, 5cm)	4.1 Ω	51.7 kW	95.2%	95.1%

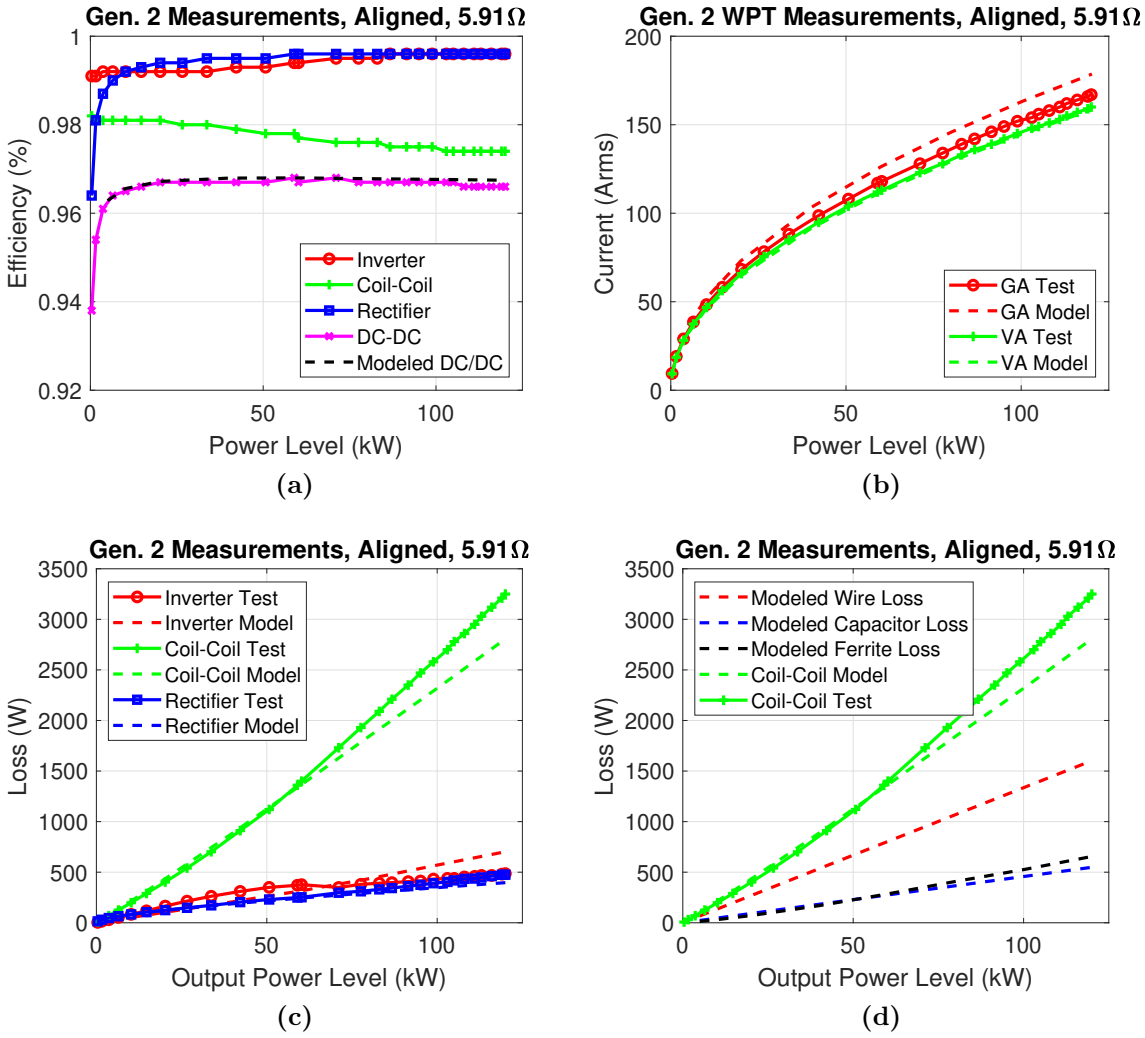

Figure 5.44: Testing of the Gen. 2 system at alignment (grid offset of (-7 mm, -5 mm)) and 125 mm. (a) Efficiency breakdown vs. output power. (b) Measured vs. modeled GA and VA current. (c) Measured vs. modeled system losses. (d) Breakdown of the modeled coil-coil losses vs. measured.

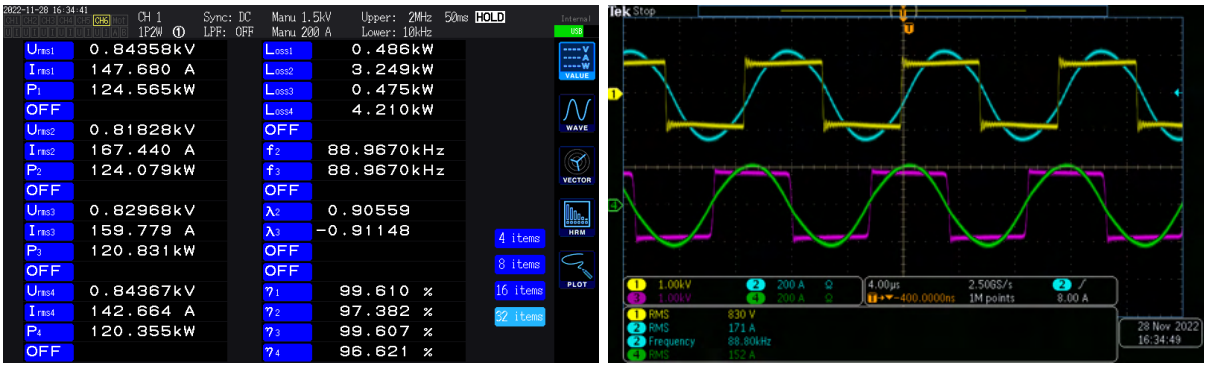

(a)

(b)

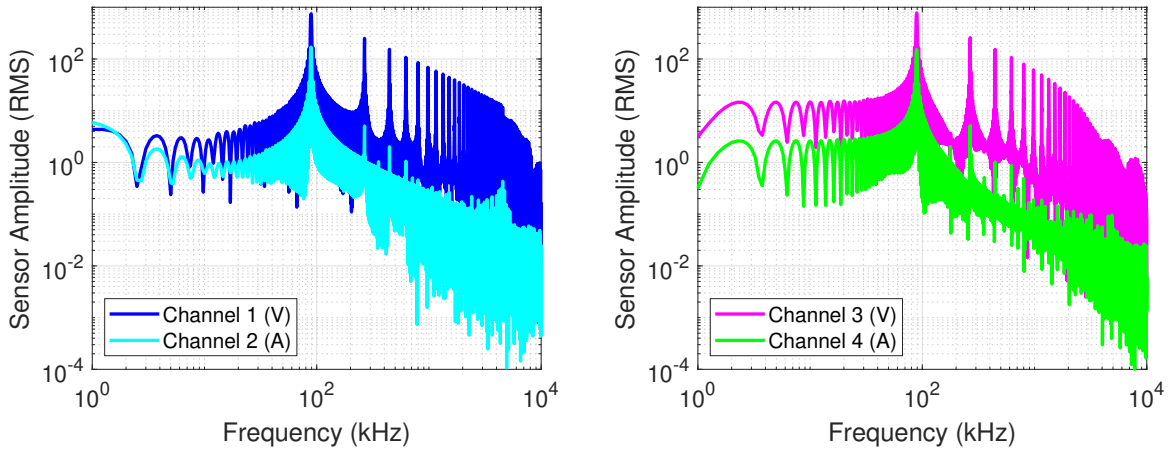

(c)

Figure 5.45: Measurements of the Gen. 2 demonstrator at alignment with a 125 mm airgap (grid offset of (-7 mm, -5 mm)) at an output power of 120 kW. (a) Power analyzer screenshot, (b) waveforms, and (c) FFT of the waveform data.

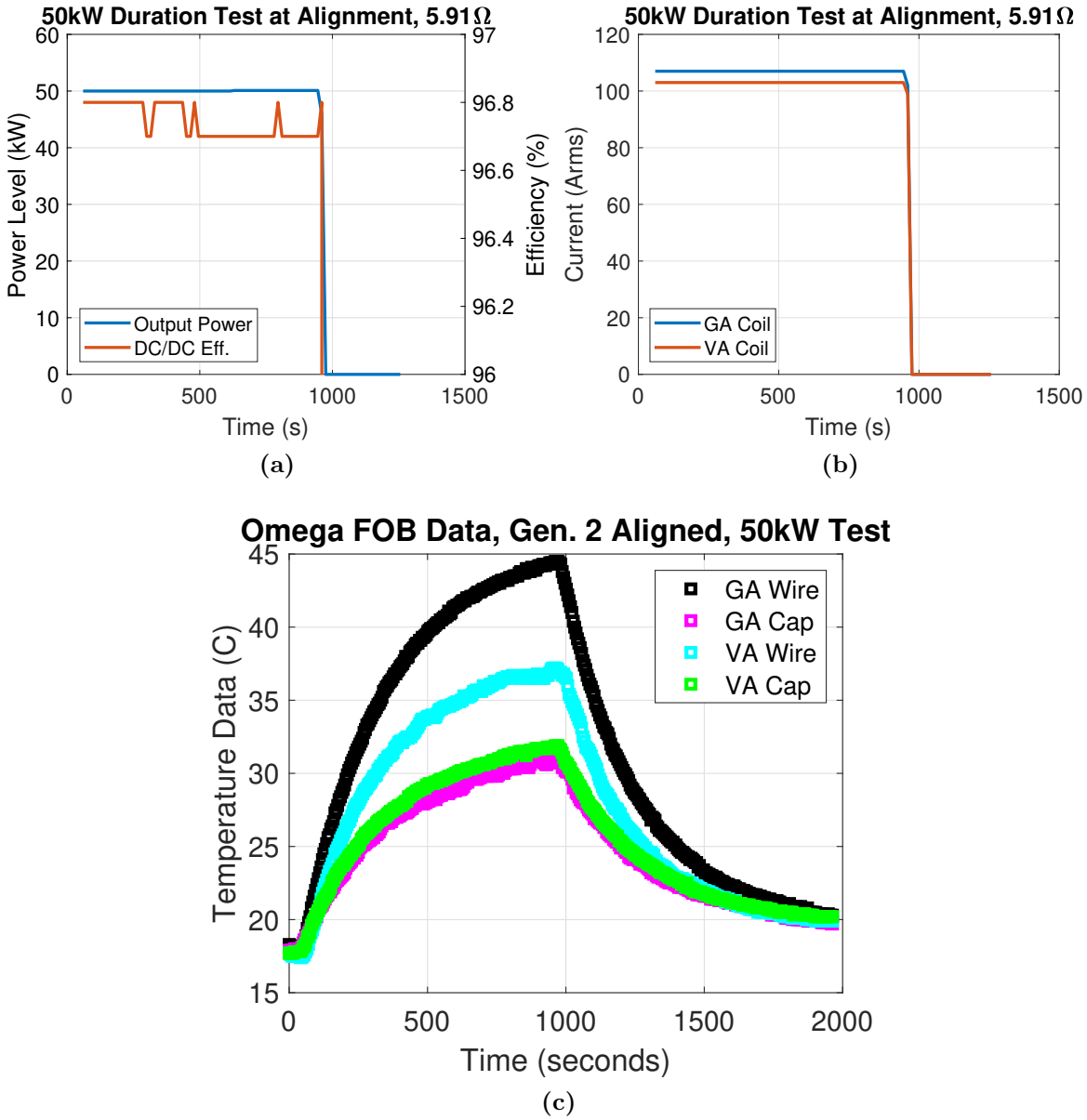

Figure 5.46: Measurements of the Gen. 2 demonstrator from the 50 kW, 15-minute duration test. Power transfer starts at the 60 second mark. (a) Measured output power and DC/DC efficiency during the test. (b) Measured GA and VA currents during the test. (c) Measured temperatures.

at 15 second intervals. These data are summarized in Figure 5.46. As seen, the DC/DC efficiency for this test dropped slightly from 96.8% to 96.7% over the 15 minute interval. During the test, after the power and voltages were verified to be zero, the temperatures of the large DC-link film capacitors on the inverter were observed to be very high (Cornell Dubilier/Illinois Capacitor 947D601K901DCRS 600 µF). The reason for this may be that these capacitors were not in direct thermal contact with any actively cooled components and were operating at the upper end of their nominal frequency range.

At the 50 kW test point, the ferrite, capacitor and wire loss between GA and VA together are modeled to be 225 W, 229 W, and 668 W, respectively, for a total of 1.1 kW. With a measured rise in wire temperature of around 25°C and 18°C at the center of the GA and VA windings, respectively. This relates to between 0.040 K/W and 0.056 K/W at the center of the coil geometry where the temperatures were measured. This is much greater than the FEA simulation in Figure 5.14 where an assumed 1200 W of wire loss and 800 W of ferrite loss caused a 45 K wire temperature rise in the center of the geometry, around 0.023 K/W. However, it is also seen that the capacitor temperatures also rise around 11 K during the test. The capacitors are mounted and compressed to the surface of the aluminum enclosure on top of 2 mm silicone thermal pads. From the datasheet values, the thermal resistance of the capacitors to the GA and VA aluminum enclosure would be 0.021 K/W, relating to only 2.4 K of temperature rise from the heat of the capacitors themselves. The rest of the temperature rise of around 8.6 K may come from the rise in the aluminum enclosure temperature. With this accounted for, the rise in temperature relative to enclosure temperature would be between 0.021 K/W and 0.037 K/W at the center of the coil geometry, much closer to the modeled value. The predicted thermal resistance of 0.006 K/W for the resistance of the coolant to the aluminum enclosure would account for 3.4 K. A relatively low flow rate of 3.6 lpm (0.95 gpm) through each of the GA and VA would tend to increase this resistance.

The Gen. 2 demonstrator was also tested and modeled with fixed output voltage loads to evaluate the performance of the system when connected to a battery. These conditions often result in mismatched GA and VA currents and non-unity gain operation which lowers the coil-coil efficiency. Additionally, when the equivalent output resistance decreases below

the bifurcation limit, the input impedance of the system will become capacitive, leading to inverter hard-switching. For the series-series compensated Gen. 2 demonstrator, this condition occurs when [22, 98]

$$k > \frac{R_L}{\omega_s L_2}, \tag{5.15}$$

which is where $R_L < \omega_s M$ and below unity gain for matched GA and VA where $L_1 = L_2$. In the fast-charging application explored here, this may occur at ideal alignment and low airgaps when high power is requested at low SoC and battery voltages such as in the low-voltage, high-power operating regions at a 125 mm airgap.

The measured and modeled performance of the Gen. 2 demonstrator at an airgap of 125 mm with fixed output voltages of 400 V, 600 V, and 800 V are plotted at alignment and (5 cm, 0 cm) in Figure 5.47. To represent hard switching in the models, the inverter devices in the PLECS simulation were switched from soft-switching to hard-switching device models to calculate the switching losses when operating below the bifurcation limit. The efficiency decreases from hard-switching are clearly seen in the plots. The rest of the fixed output voltage tests at various misalignments at a 125 mm airgap are given in Appendix D. The summary of the measurements over misalignment are plotted in Figure 5.48.

A second set of measurements at constant output voltage were taken with the inverter shown in Figure 5.35c at the same airgap and alignment points. This "ORNL 2X Inverter" as published in [99] has four 1.2 kV SiC MOSFET half-bridge modules Wolfspeed/Cree CAS325M12HM2 modules for two modules in parallel per leg of the full bridge inverter which lowers the conduction loss and temperature rise of the devices relative to the other inverter. This slightly improved the inverter and rectifier efficiency relative to the previous tests and enabled higher GA coil current which occurs at the higher output voltages. Out of caution considering the thermal limits of the first inverter seen in the 50 kW duration test, these large currents precluded the 800 V output voltage tests in the first series of test, but were feasible with the 2X Inverter. The data is plotted in Figure 5.49 over output power at alignment and (5 cm, 0 cm) and Figure 5.50 over misalignment. As before, the plots of the full set of tests are given in Appendix D. For the inverter modeling, the number

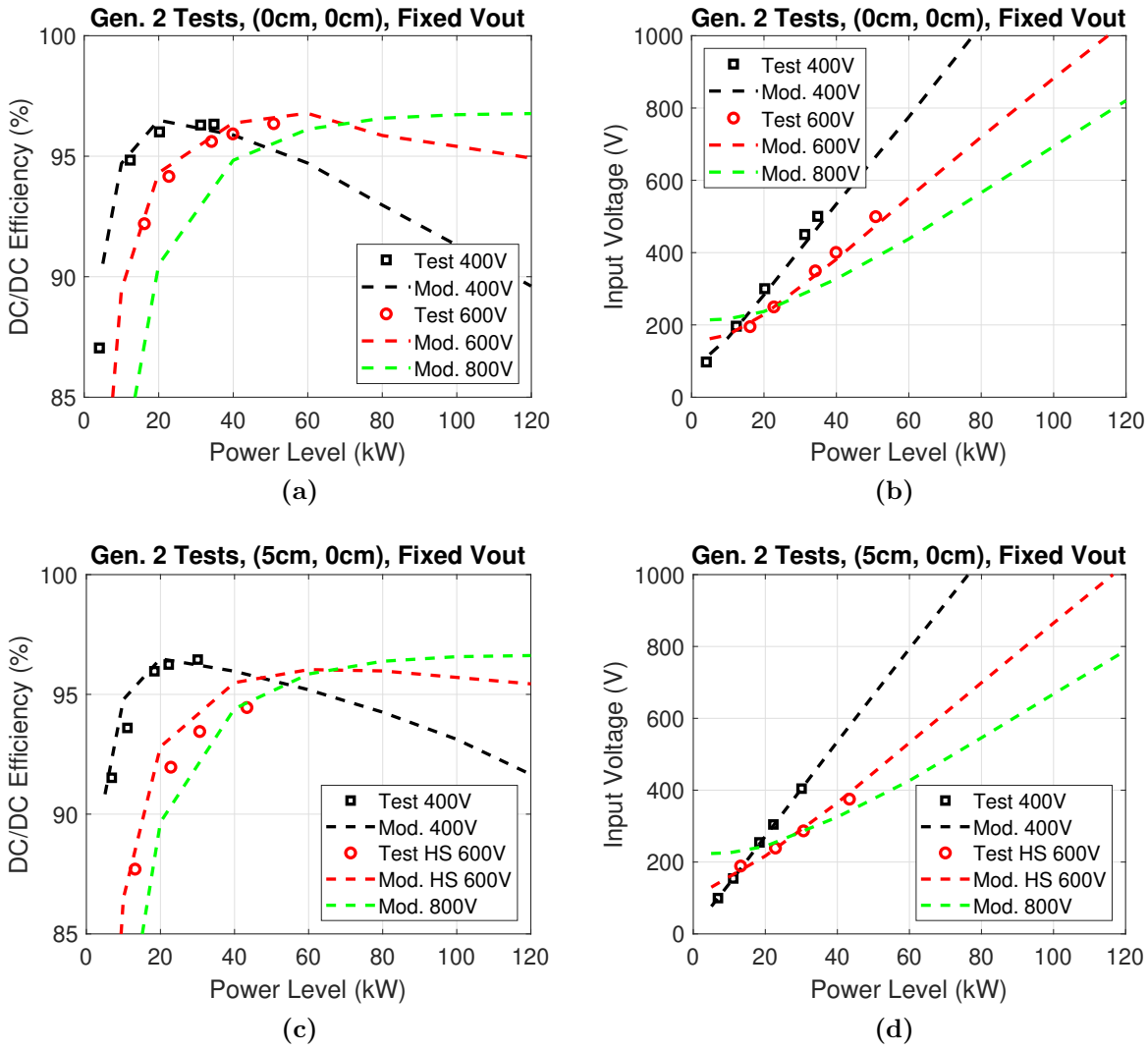

Figure 5.47: Tests of the Gen. 2 demonstrator at different alignments compared to modeled values at fixed output voltages (grid offset of (-7 mm, -5 mm)) and an airgap of 125 mm. (a) DC/DC efficiency and (b) output power vs. input voltage at (0 cm, 0 cm). (c) DC/DC efficiency and (d) output power vs. input voltage at (5 cm, 0 cm).

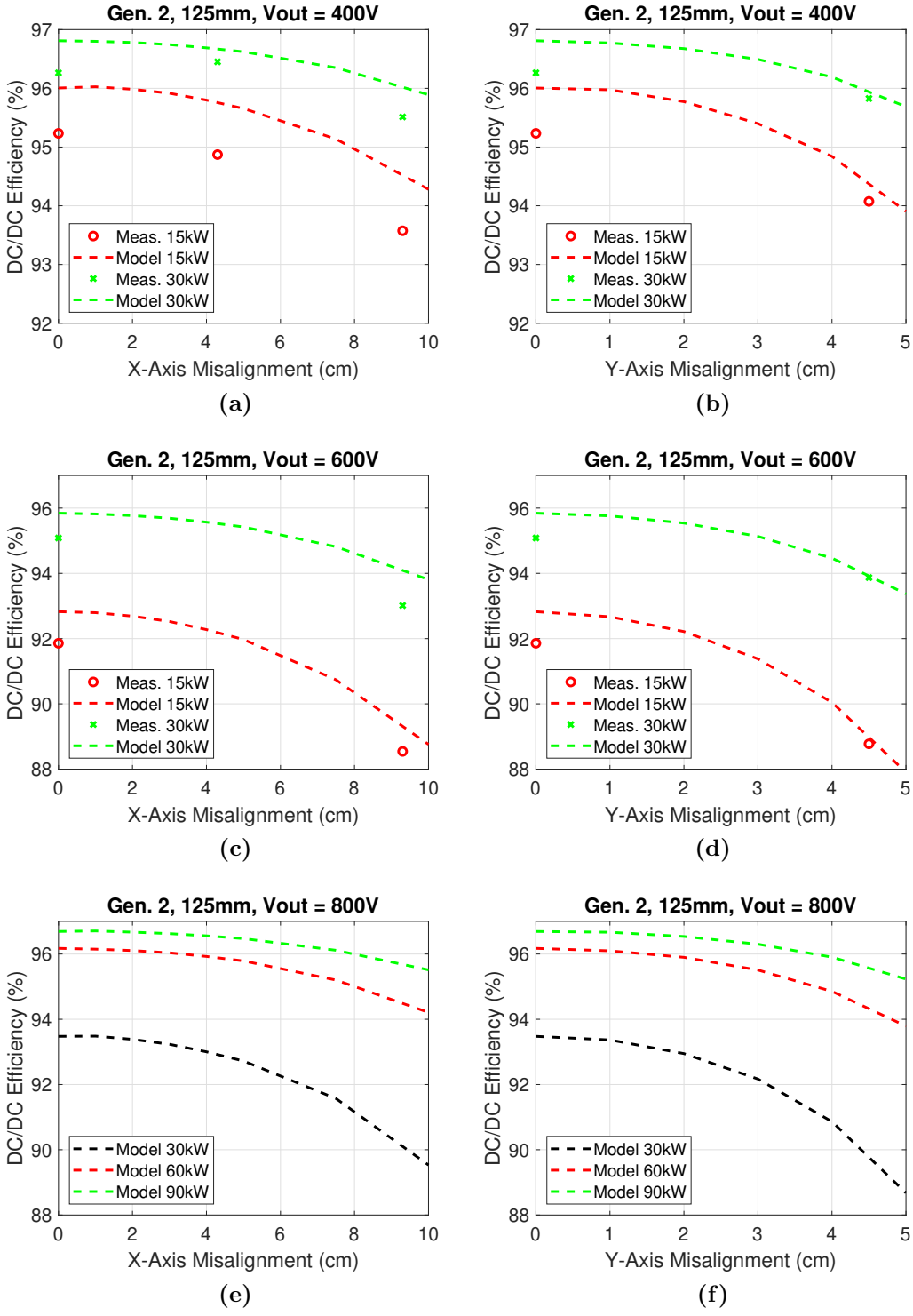

Figure 5.48: Interpolated measurements of the Gen. 2 demonstrator at constant power over alignment compared to modeled values at fixed output voltages and an airgap of 125 mm. DC/DC efficiency at 400 V output over (a) X-misalignment and (b) Y-misalignment. DC/DC efficiency at 600 V output over (c) X-misalignment and (d) Y-misalignment. DC/DC efficiency at 800 V output over (e) X-misalignment and (f) Y-misalignment.

of devices in the PLECS simulation was doubled and the heatsink thermal resistance and GA lead resistance were halved from the values in Table 5.6.

The measured vs. modeled loss breakdowns at alignment over the three voltages are shown in Figure 5.51. As seen, much of the difference between the measured and modeled loss at low power levels is caused by differences in the modeled and measured inverter loss when operating with low power factor. Slight differences in the measured and modeled GA current, which is caused by some error in the mutual inductance used in the PLECS simulation, also accounts for some of the difference between the measured and modeled inverter and coil-coil losses. The slightly different mutual inductance with the constant output voltage clamps the GA current to a nearly constant value slightly higher than the measured GA current. After accounting for this mainly constant difference in GA current, the modeled coil-coil losses matches the measured values well. Overall, with the 2X Inverter, the peak DC/DC efficiency at alignment improved to 97.3% at 93 kW output power at 807V compared to the 96.7% peak efficiency seen with the first inverter due to the increased inverter efficiency of the 2X Inverter and better coil-coil efficiency from the doubled GA leads. A final sweep to 120 kW at alignment with constant output resistance produced a DC/DC efficiency of 97.2% in this arrangement as in Figure 5.52.

5.8.5 Gen. 2 Stray Field Measurements

Stray field measurements were taken during operation with the same NARDA EHP-200A probe used in the Gen. 1 field measurements. In Table 5.12, the measured fields at 80 cm at the fundamental are summarized and scaled to a common reference power level of 120 kW for comparison. All of these tests were performed at similar power levels and were taken at a distance of 80 cm away from the center of the GA at the middle of the airgap between the GA and VA. In the table, the highest stray field was the B_y component in the worst-case misalignment (10 cm, 5 cm) measured on the X-axis. As expected, stray fields increase with misalignment, especially when the misalignment places the probe closer to the VA such as in the (10 cm, 0 cm) measurements.

Later in the testing of the Gen. 2 system, a second series of stray field measurements was taken at alignment over different power levels and at different measurement distances.

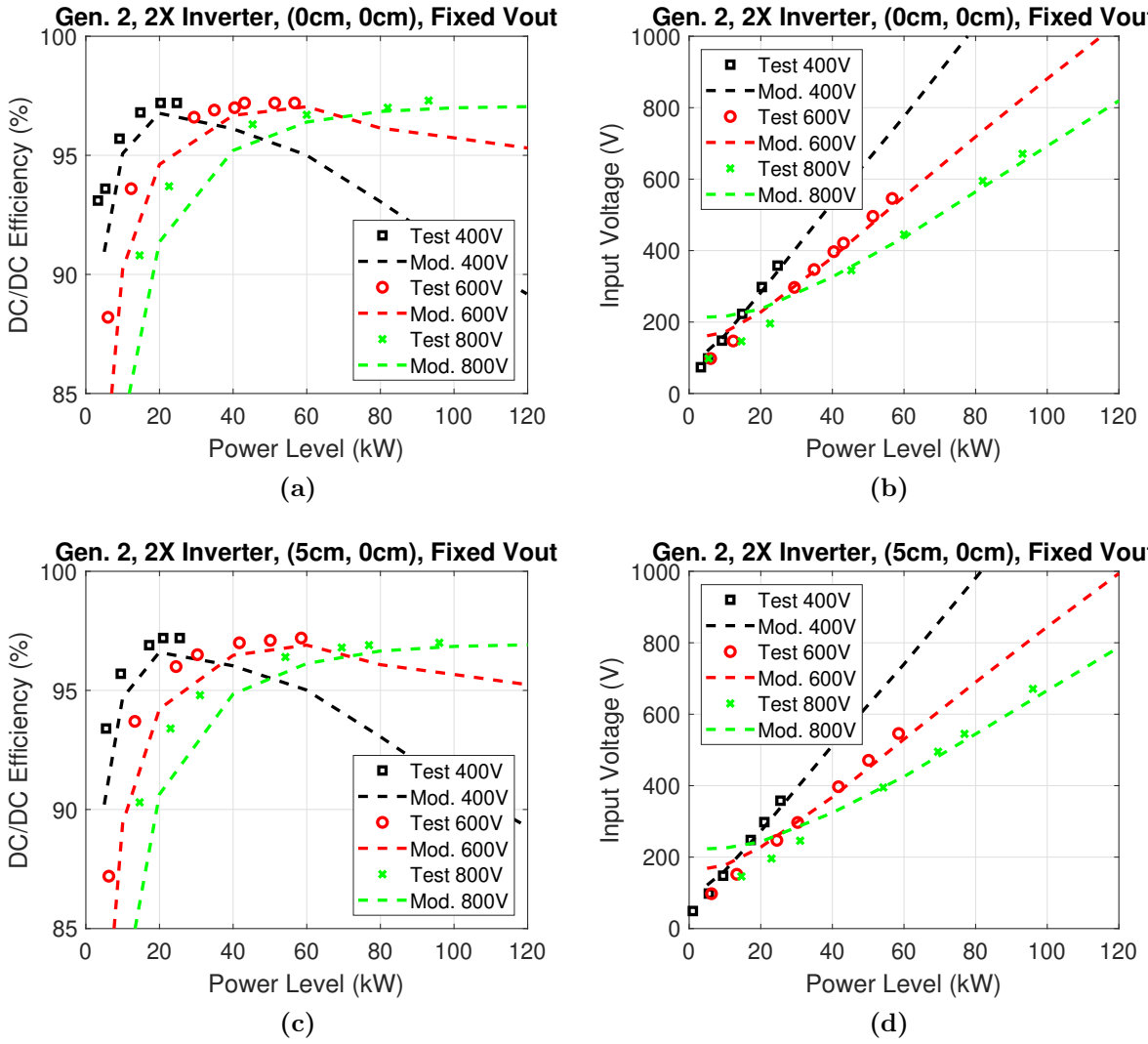

Figure 5.49: Tests of the Gen. 2 demonstrator with the 2X Inverter at different alignments compared to modeled values at fixed output voltages (grid offset of (-7 mm, -5 mm)) and an airgap of 125 mm. (a) DC/DC efficiency and (b) output power vs. input voltage at (0 cm, 0 cm). (c) DC/DC efficiency and (d) output power vs. input voltage at (5 cm, 0 cm).

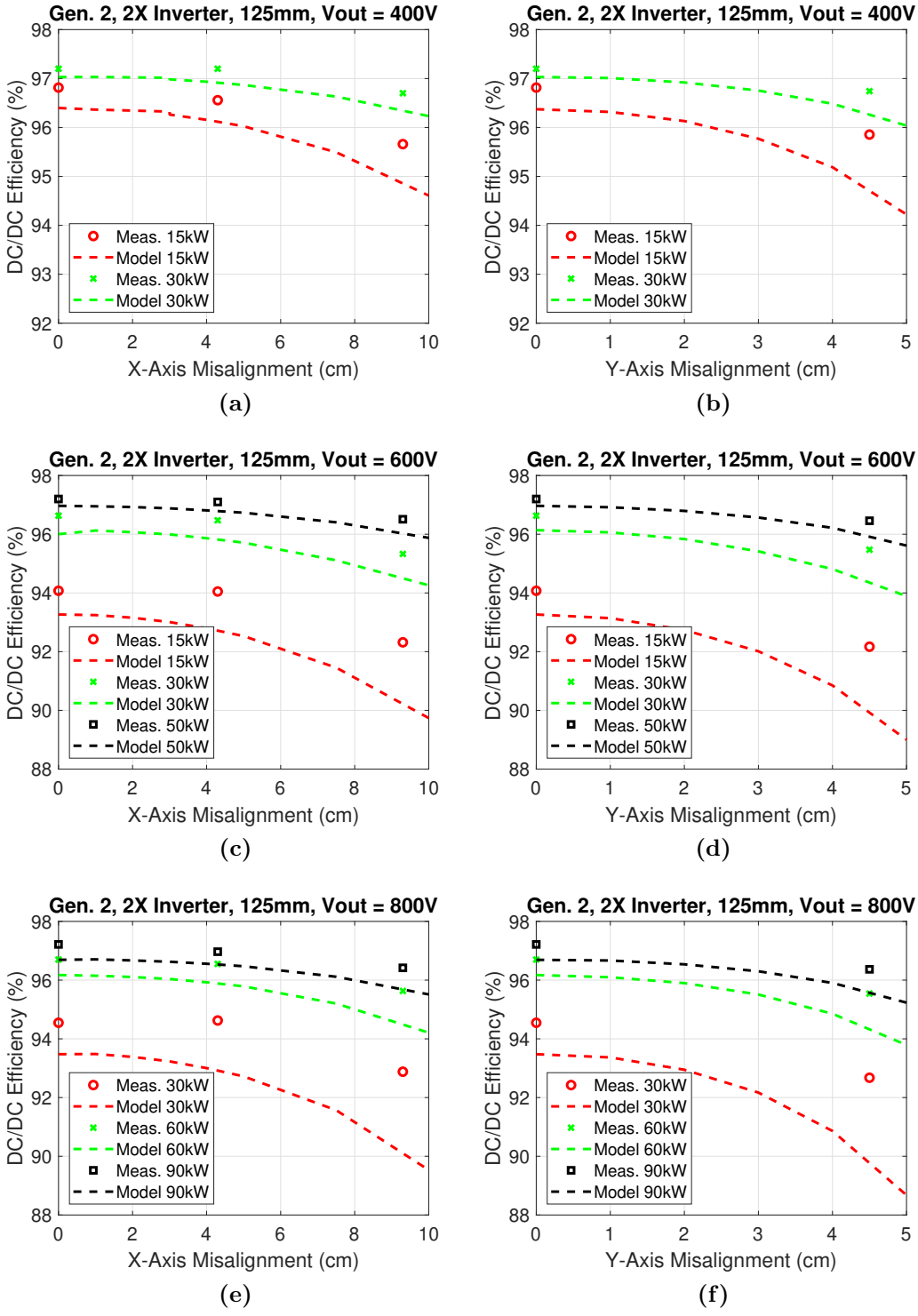

Figure 5.50: Interpolated measurements of the Gen. 2 demonstrator with the 2X Inverter over alignment compared to modeled values at fixed output voltages and an airgap of 125 mm. DC/DC efficiency at 400 V output over (a) X-misalignment and (b) Y-misalignment. DC/DC efficiency at 600 V output over (c) X-misalignment and (d) Y-misalignment. DC/DC efficiency at 800 V output over (e) X-misalignment and (f) Y-misalignment.

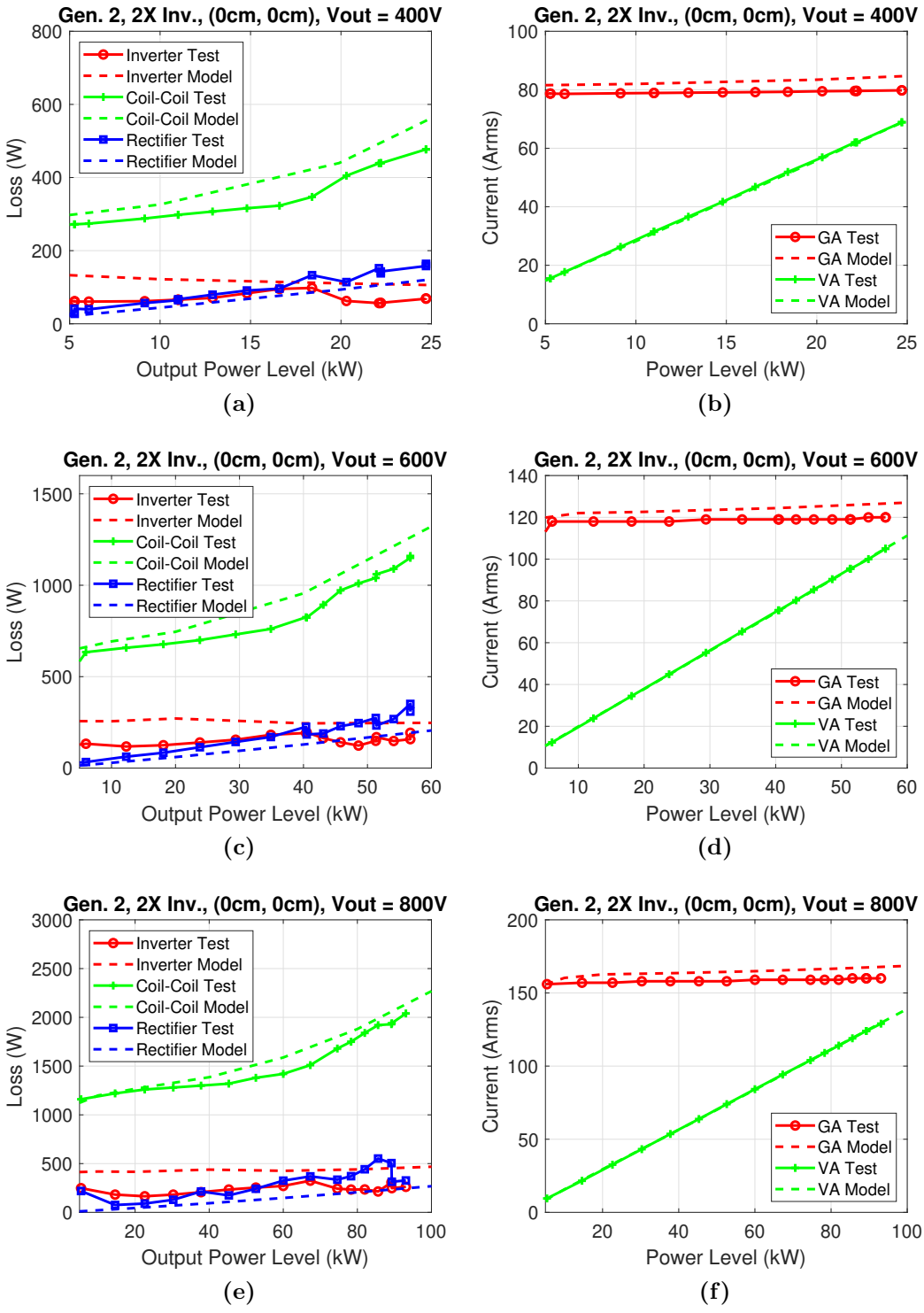

Figure 5.51: Loss breakdown of the Gen. 2 demonstrator with the 2X Inverter at alignment (grid offset of (-7 mm, -5 mm)) and an airgap of 125 mm with constant output voltage: Measured vs. modeled (a) losses and (b) coil current at 400 V output. Measured vs. modeled (c) losses and (d) coil current at 600 V output. Measured vs. modeled (e) losses and (f) coil current at 800 V output.

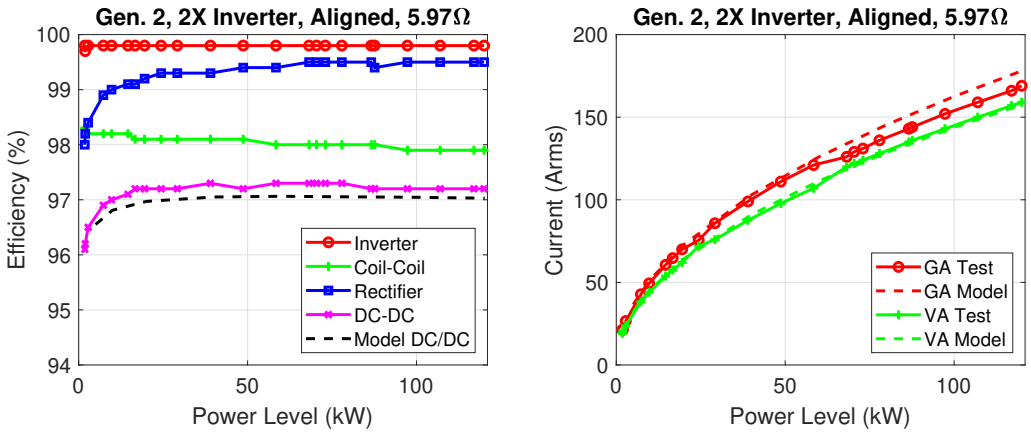

(a) (b)

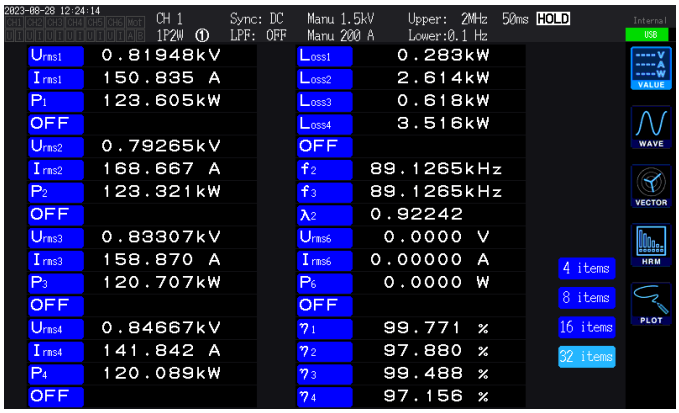

(c)

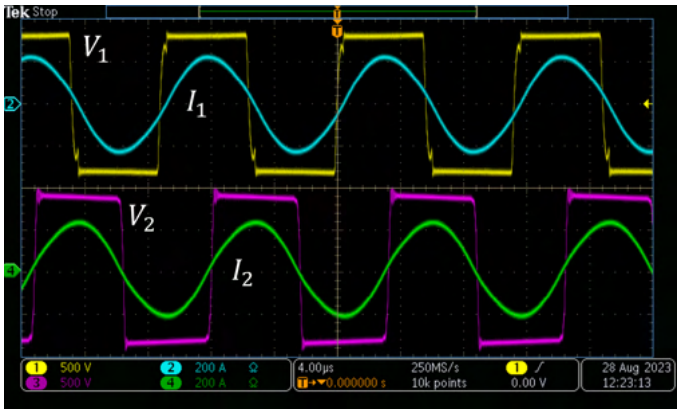

(d)

Figure 5.52: Loss breakdown of the Gen. 2 demonstrator with the 2X Inverter at alignment (grid offset of (-7 mm, -5 mm)) and an airgap of 125 mm with constant output resistance: Measured vs. modeled (a) Efficiency and (b) coil current up to 120 kW output. (c) Power analyzer and (d) waveforms at 120 kW.

One set of measurements focused on validating the scaling of field with power level with measurements at 50 kW, 75 kW, 100 kW, and 120 kW. These measurements are summarized in Table 5.13. The fields at 80 cm at 100 kW are plotted in Figure 5.53. In these measurements, new positioning markings were laid out as in Figure 5.54 to place the NARDA probe along the axes. Some increase of the fields were observed compared to the first set of measurements. Some of this increase may be due to the new markings placing the probe to be slightly closer than in the first measurements. From the manual of the NARDA probe used in the measurements, it was also learned that the X, Y, and Z magnetic field sensors, which are located on three orthogonal faces of the 9.2 cm x 9.2 cm x 109 cm cubic probe, have an offset of around 4.2 cm from the centerpoint of the probe. Therefore the orientation of the probe affects the measurements.

A set of measurements were taken at distances of 60 cm, 80 cm, and 100 cm. These fields are plotted as a function of distance in Figure 5.55 and compared to the FAM and FEA-derived values. The plots from the FEA simulation used in these comparisons are shown in Figure 5.56. In these plots, the stray field in the Y-direction at the center of the airgap is dominated by the B_z field and the stray field in the X-direction at the center of the airgap is dominated by the B_y field.

As seen, the FAM-derived fields match the FEA modeled values relatively well, but both the magneto-static FEA simulation and the FAM-derived values underestimate the measured fields far away from the center of the coils. This may be due to positional offset in the measurements along the axes, as shown by the error bars on the measured points, such as with the 4.2 cm offset in the sensors from the centerpoint of the probe. As shown in the FEA simulation outputs in Figure 5.56, slight offsets in the other directions orthogonal to each of the axes may result in large variations of the measured field. This is probably why some B_x and B_z fields were measured on the X-axis and B_x fields were measured on the Y-axis although those fields on those axes should ideally be zero.

The measured stray field of the Gen. 2 demonstrator is very low compared to previous work. As summarized in Table 2.1, with an airgap to GML of 0.262 at an airgap of 125 mm, the measured stray field at 3.4 µT and 3.5 µT on the X and Y axes, respectively, leads to stray field to power level ratios of 3.26 $kW^{0.5}/\mu T$ and 3.14 $kW^{0.5}/\mu T$. In comparison,

Table 5.12: Measured and scaled RMS stray field (B_x, B_y, B_z) of the Gen. 2 demonstrator at an airgap of 125 mm. Misalignment toward probes. Grid offset of (-7 mm, -5 mm).

Alignment (X,Y)	Measurement Output Power	X-axis at 80 cm (Scaled 120 kW Field)	Y-axis at 80 cm (Scaled 120 kW Field)
(0 cm, 0 cm)	49.0 kW	1.11µT, 1.51µT, 1.05µT (1.74µT, 2.36µT, 1.64µT)	0.36µT, 1.04µT, 1.14µT (0.56µT, 1.63µT, 1.78µT)
(5 cm, 0 cm)	49.0 kW	1.09µT, 1.88µT, 1.26µT (1.71µT, 2.94µT, 1.97µT)	0.40µT, 1.13µT, 1.17µT (0.63µT, 1.77µT, 1.83µT)
(10 cm, 0 cm)	47.4 kW	0.96µT, 2.92µT, 1.55µT (1.53µT, 4.65µT, 2.47µT)	0.70µT, 1.52µT, 1.39µT (1.11µT, 2.42µT, 2.21µT)
(0 cm, 5 cm)	45.9 kW	1.20µT, 1.65µT, 1.18µT (1.94µT, 2.67µT, 1.91µT)	0.57µT, 1.51µT, 1.51µT (0.92µT, 2.44µT, 2.44µT)
(10 cm, 5 cm)	53.9 kW	1.41µT, 3.86µT, 1.98µT (2.10µT, 5.76µT, 2.95µT)	1.06µT, 2.58µT, 2.09µT (1.58µT, 3.85µT, 3.12µT)

Table 5.13: Measured and scaled RMS stray field (B_x, B_y, B_z) of the Gen. 2 demonstrator at an airgap of 125 mm at alignment at different power levels. Grid offset of (-7 mm, -5 mm).

Alignment (X,Y)	Measurement Output Power	X-axis at 80 cm (Scaled 120 kW Field)	Y-axis at 80 cm (Scaled 120 kW Field)
(0 cm, 0 cm)	48.9 kW	0.81µT, 2.04µT, 0.88µT (1.27µT, 3.20µT, 1.38µT)	0.48µT, 1.80µT, 1.24µT (0.75µT, 2.82µT, 1.94µT)
(0 cm, 0 cm)	73.0 kW	1.02µT, 2.39µT, 1.03µT (1.31µT, 3.06µT, 1.32µT)	0.57µT, 2.18µT, 1.47µT (0.73µT, 2.80µT, 1.88µT)
(0 cm, 0 cm)	97.3 kW	1.17µT, 2.77µT, 1.18µT (1.30µT, 3.08µT, 1.31µT)	0.74µT, 2.76µT, 1.77µT (0.82µT, 3.07µT, 1.97µT)
(0 cm, 0 cm)	120.1 kW	1.02µT, 2.93µT, 1.27µT (1.02µT, 2.93µT, 1.27µT)	0.78µT, 2.86µT, 1.83µT (0.78µT, 2.86µT, 1.83µT)

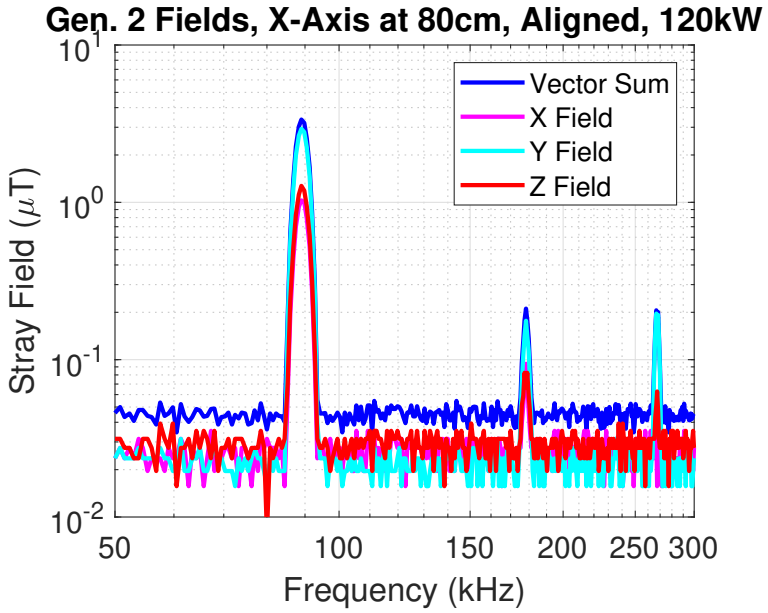

(a)

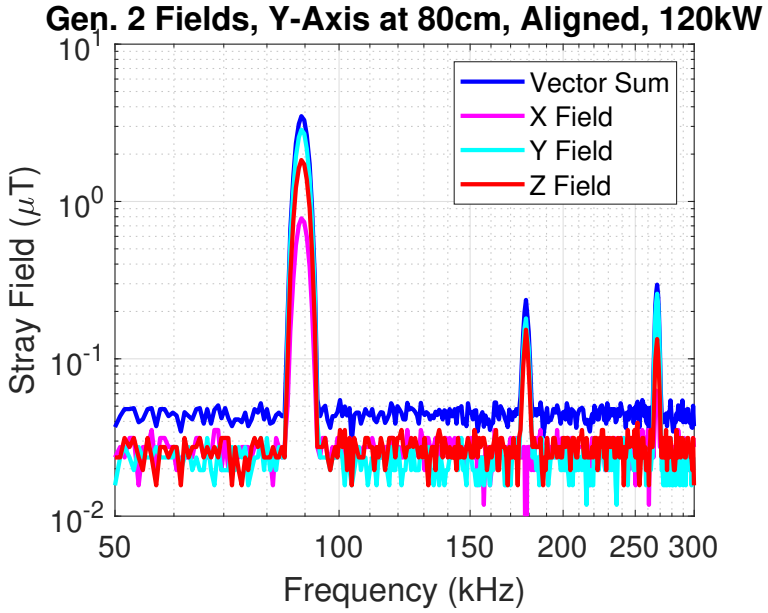

(b)

Figure 5.53: Field measurements of the Gen. 2 demonstrator at alignment at 120 kW. Measured fields on the (a) X-axis and (b) Y-axis at 80 cm. Here, fields are seen at the fundamental frequency of 89 kHz, and the 2nd and 3rd harmonics.

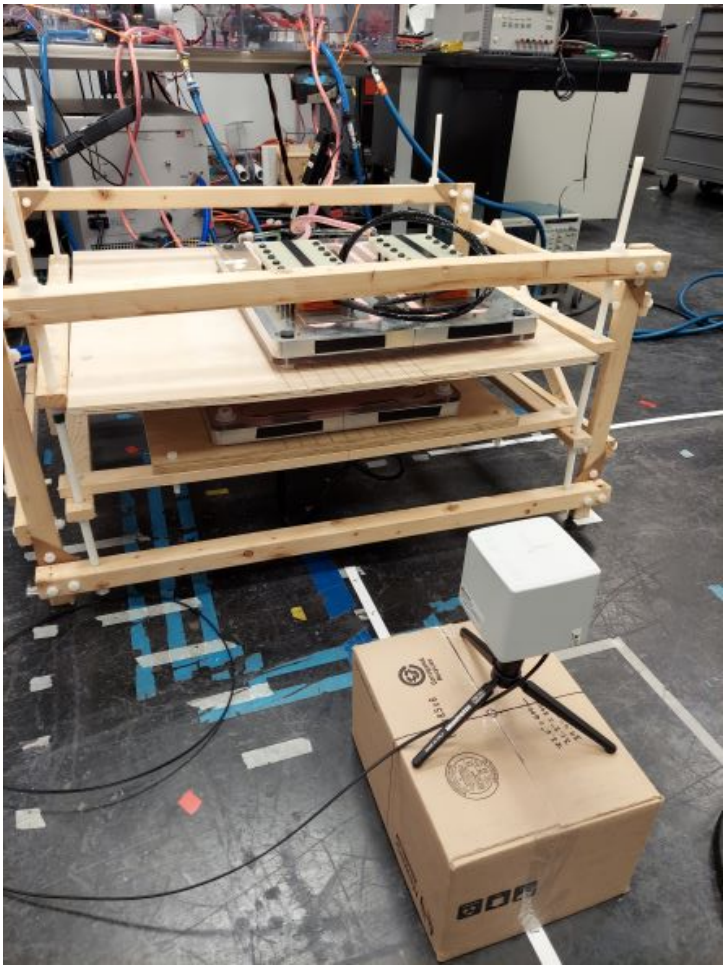

Figure 5.54: Field measurement setup of the Gen. 2 demonstrator. Here a box was used to elevate the probe to the middle of the airgap and tape was placed with markings at distances of 60 cm, 80 cm, and 100 cm on the X and Y axes.

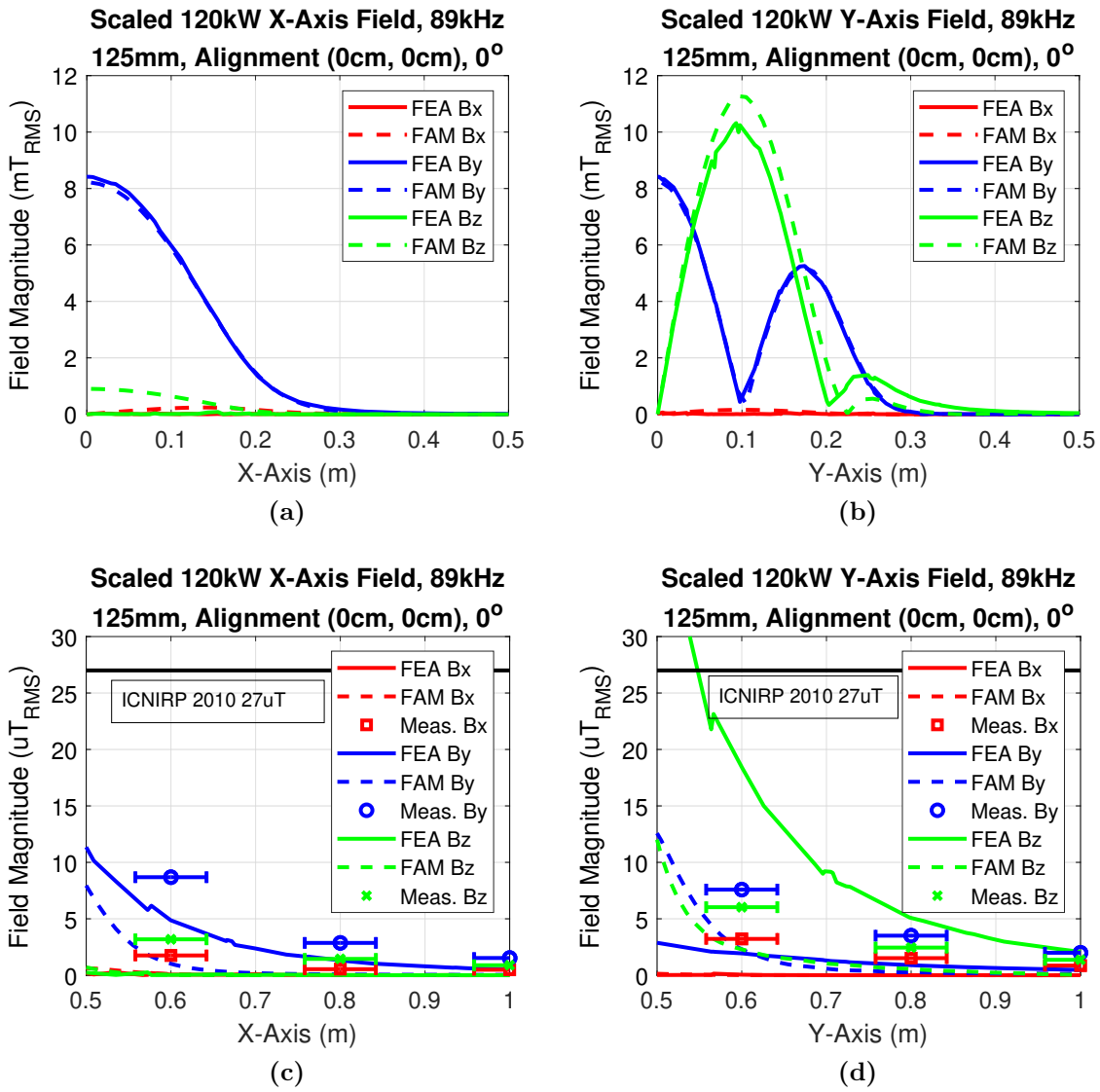

Figure 5.55: Measured and modeled fields of the Gen. 2 demonstrator aligned at 125 mm and 120 kW. FEA and FAM-derived fields at the fundamental close to the center of the GA and VA airgap on the (a) X-axis and (b) Y-axis. Modeled vs. measured small-magnitude stray fields from 50 cm to 100 cm on the (c) X-axis and (d) Y-axis with 4.2 cm positioning error bars on the axial positions of the measurements. These plots show that the system meets the 27 µT(rms) ICNIRP field limit [27] even at 60 cm.

the 6.6 kW demonstrator achieved a stray field ratios on the X and Y axis, respectively, of 1.43 $kW^{0.5}/\mu T$ and 1.84 $kW^{0.5}/\mu T$ at 125 mm with an airgap to GML ratio of 0.203. Even at maximum misalignment, the Gen. 2 system achieves ratios of 1.49 $kW^{0.5}/\mu T$ and 1.94 $kW^{0.5}/\mu T$.

5.9 Summary

In this chapter, a shielded bipolar geometry selected from FAM optimization outputs was used in the design of two 120 kW proof-of-concept demonstrators to demonstrate the ability of a FAM-generated coil geometry in an efficient, low-stray field, and high power system. Using the FAM geometry output, component selections and design work were done to reduce the cost, weight, and temperature rise of the assembly components and backside cooling was integrated to produce the Gen. 1 demonstrator. The testing of the Gen. 1 demonstrator yielded lower efficiency than expected, and further analysis resulted in a Gen. 2 demonstrator with lower encapsulation stress, a single passthrough to reduce circulating flux, and improved ferrite layout. The Gen. 2 demonstrator was tested up to 120 kW and demonstrated very low stray field at high power levels while achieving a DC/DC efficiency of 97.2% at 120 kW at alignment at an airgap of 125 mm. At 120 kW, the vector sum of the stray field at 80 cm was 3.4 µT and 3.5 µT on the X and Y axes, well below the 27 µT ICNIRP stray field limit.

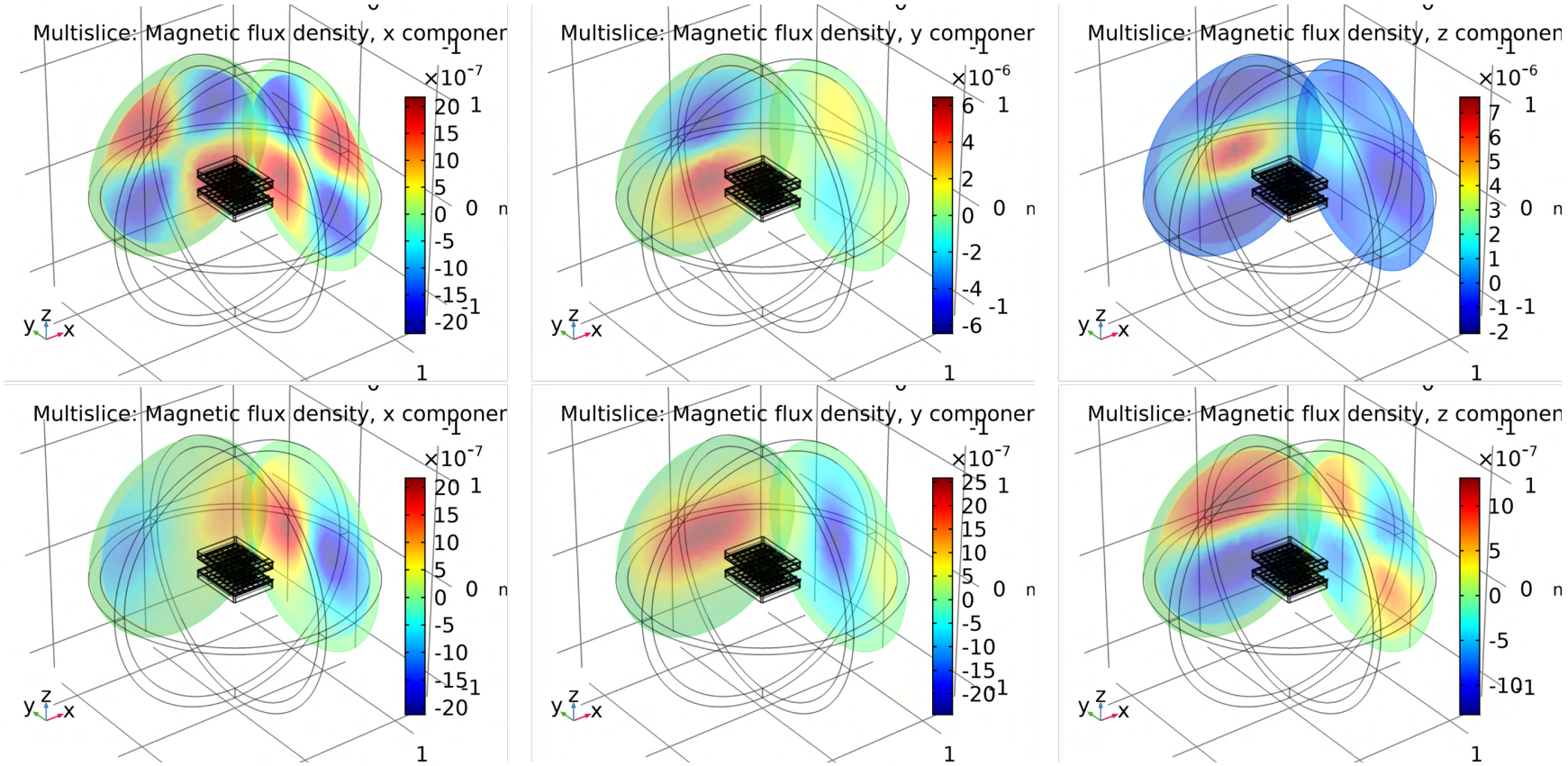

Figure 5.56: FEA of the Gen. 2 stray field (T) at alignment at a 120 kW output power at planes on the X and Y axes at 80 cm. The top row of the plots is at the point of time in the period when the B_z components in the middle of the airgap are maximized, and the bottom plots are when the B_x and B_y components in the middle of the airgap are maximized.

Chapter 6

Fast Charging and Interoperability Analysis

The Gen. 2, 120 kW demonstrator detailed in the previous chapter was able to achieve high efficiency and low stray field operation. However, the analysis of the performance of the system over a broad range of conditions is needed to assess the application of the system to wireless fast charging. For a fast charging application, the system must have acceptable operation in terms of stray field, EMI, and efficiency over misalignment with different platform ground clearances, power level, and a wide range of battery voltages. The interoperability of the Gen. 2 geometry with other geometries is also important, and the coupling and compatibility of different types of coil geometries to the Gen. 2 system must be considered as VAs may vary in size and geometry to suit the space, power level and output voltage requirements of different vehicle platforms.

In this chapter, the performance of the Gen. 2 proof-of-concept demonstrator is mapped to the end-use application of fast charging an electric vehicle. The impact of mismatched loading, different airgaps, and fixed output voltage operation is established. This includes an overview of methods to extend efficient operation and soft-switching over a wider range of loads. FAM modeling is also used to import and analyze geometries and assess their interoperability to the Gen. 2 coil geometry.

6.1 Fast Charging Analysis of the Gen. 2 Demonstrator

As reviewed previously, the wireless stage, such as the Gen. 2 120 kW demonstrator developed and tested in this work, can serve a similar purpose as an isolated DC/DC converter in conductive fast charging systems. This stage provides galvanic isolation between the vehicle chassis and the grid in several fast-charger topologies as reviewed in [10]. Instead of the closed-form transformer used in many AC-link isolated DC/DC converters, the wireless charger uses a loosely coupled transformer separated by a physical airgap. As such, the wireless system should be able to operate throughout the current and battery voltage range of the EV fast charging profiles even as the coupling of the GA and VA changes over the misalignment and airgap range.

Fast charging profiles for electric vehicles vary widely, but all manufacturers continue to achieve higher power levels. Examples of several fast charging profiles are shown in Figure 6.1. Despite their differences, all profiles demand high power at low battery state of charge (SoC) and ramp down power at higher battery SoCs as battery temperatures and voltages increase. These profiles represent a large range of output impedance over the SoC range beginning at low equivalent load resistance at low SoC and battery voltages with high power and current and ending at high load resistance at high SoC and battery voltages with low power and current. Battery management systems (BMS) may allow higher power levels at higher SoCs if the battery pack temperatures were lower, such as when starting a charging session at higher SoCs with a preconditioned battery. The combination of the output power range and battery voltages establish a wide operating range of where wireless systems may need to operate in a fast charging application.

To match the 120 kW nominal power level of the Gen. 2 demonstrator, the fast charging profile of the Volkswagen ID.4 was chosen for the analysis. This profile, as seen in Figure 6.1 peaks at around 130 kW. As mentioned previously, the number of turns used in the Gen. 2 demonstrator was chosen to make the nominal output voltage at full power around 800 V at 125 mm to make full use of 1.2 kV devices on the inverter and rectifier. Therefore, instead of the 240 V to 400 V nominal ID.4 battery voltage range, a doubled range of around 480 V to

800 V is used. This range is representative of 800 V and other higher-voltage EV batteries such as in the Porsche Taycan, Audi e-tron GTS, Hyundai Ioniq 5, and Lucid Air. The resulting battery voltage and equivalent load for an output power range of 1 kW to 120 kW and the sample charging profile are plotted in Figure 6.2a. Here, the equivalent load ranges from around 2 Ω to 15 Ω.

6.1.1 Operating Bounds and Efficiency Contours

The performance of the Gen. 2 system over this operating range was then modeled using the validated PLECS model of the Gen. 2 120 kW demonstrator detailed in Section 5.7 with the two module, 120 kW inverter. The efficiency contours of the Gen. 2 system at 125 mm and 152.4 mm airgaps as seen in Figures 6.2 and 6.3 were found by simulating the operating points in Table 6.1 and interpolating between them. The contours were bound to areas where the input voltages and device temperature limits were satisfied as labeled.

At the 125 mm airgap, the output current and power level at low battery voltages was especially limited by bifurcation, which caused hard switching and device temperatures in the inverter and high input voltages that went beyond the 900 V limit. Depending on the parasitic inductance of the inverter, hard-switching with high input voltage may also exceed the voltage limits of the devices. At the 152.4 mm airgap, the system bifurcates at a lower output impedance, leading to the full 120 kW rated power at low output voltages. However, with lower coupling under heavily misaligned conditions, the inverter current at high output voltages is very high even at low power, so that the inverter device temperature limit is exceeded at the 850 V output point for the (10 cm, 0 cm) and (0 cm, 5 cm) alignments, and at the 650 V point and beyond for the (10 cm, 5 cm) alignment.

6.2 Methods to Improve Operating Range Performance

As seen in Figures 6.2 and 6.3, the EV fast charging application requires operation over a wide range of battery voltages over different misalignment and power levels. This may lead to high

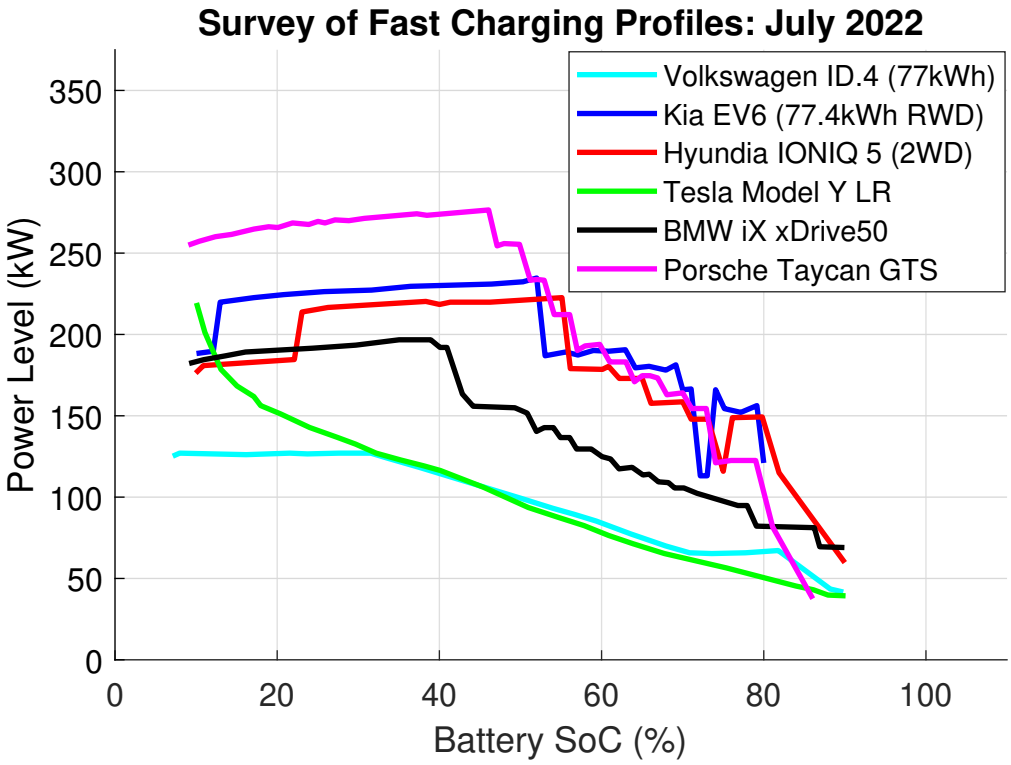

Figure 6.1: Survey of various fast passenger EV charging profiles as of July 2022 [100].

Table 6.1: Operating Range and Simulated Points with Table 5.6 Loss Parameters

Output Power Range	5 kW - 120 kW
Battery Voltage Range	480 V - 800 V
Simulated Points 125 mm	5, 10, 20, 40, 60, 80, 100, 120 (kW) 400, 600, 800 (V)
Simulated Points 152.4 mm	5, 10, 20, 40, 60, 80, 100, 120 (kW) 350, 450, 550, 650, 750, 850 (V)
Inverter DC-Link Voltage Range	$\leq$900 V
Inverter/Rectifier Junction Temp.	$<$150°C
X-Direction Misalignment	+/- 10 cm
Y-Direction Misalignment	+/- 5 cm

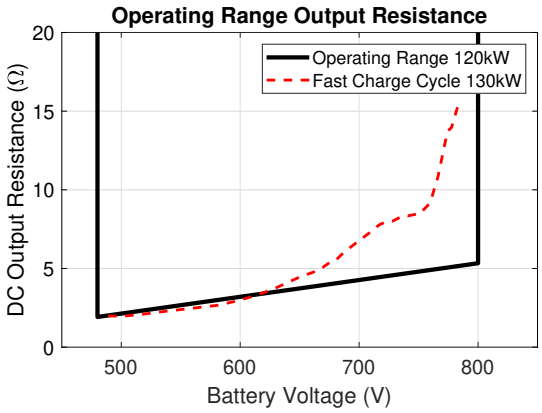

(a)

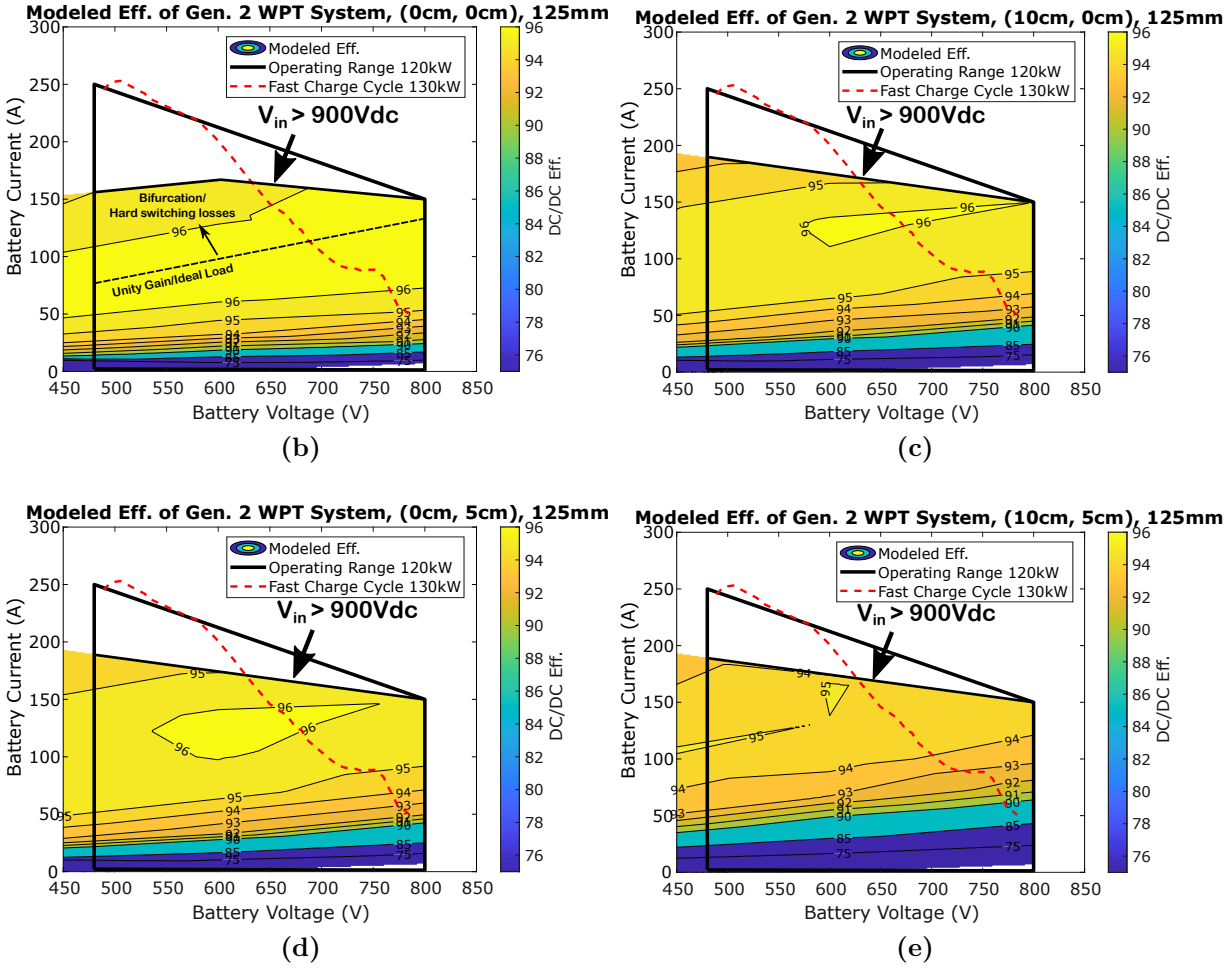

(b) (c) (d) (e)

Figure 6.2: Modeled performance of the Gen. 2 demonstrator: (a) Operating range and 130 kW fast charge cycle equivalent output resistance. Efficiency contours of the Gen. 2 System at 125 mm airgap at different alignments: (b) (0 cm, 0 cm), (c) (10 cm, 0 cm), (d) (0 cm, 5 cm), and (e) (10 cm, 5 cm).

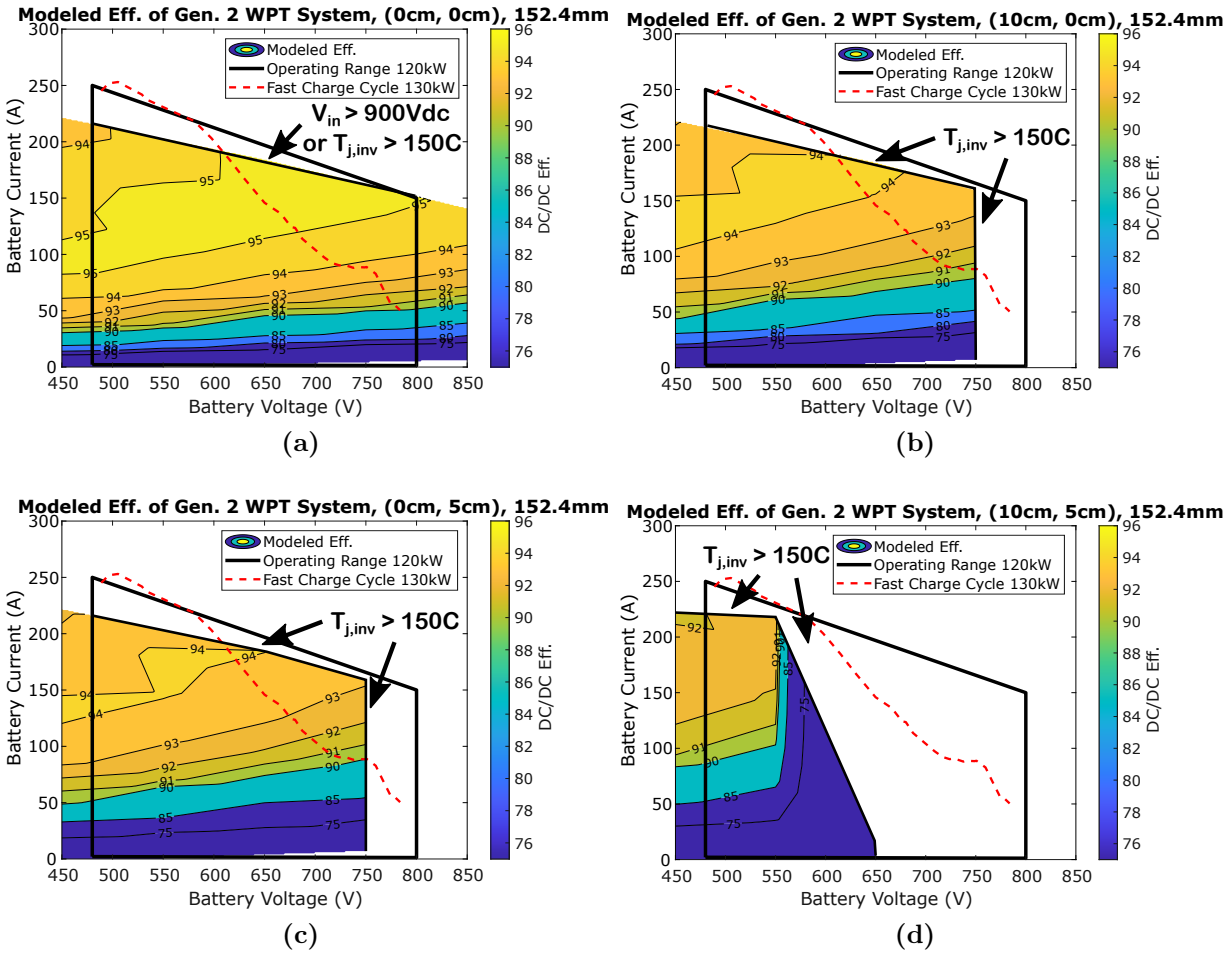

Figure 6.3: Efficiency contours of the Gen. 2 Demonstrator at 152.4 mm airgap at different alignments: (a) (0 cm, 0 cm), (b) (10 cm, 0 cm), (c) (0 cm, 5 cm), and (d) (10 cm, 5 cm).

input voltages and inverter hard-switching at low output impedance, and high input current at high output impedance. In general, for the 900 V maximum DC-link with the 1.2 kV, 325 A(rms) Cree CAS325M12HM2 modules, the input impedance must be above 1.1 Ω and below 5.5 Ω at 120 kW for the inverter to operate safely. At relatively high operating frequencies and power levels, such as in the Gen. 2 demonstrator, operating conditions with impedances outside of this range should be avoided to maintain high efficiency and long maintenance intervals by either derating the system performance or modifying it.

Therefore, a few methods are considered to expand the Gen. 2 demonstrator operating range. The first set of these approaches does not require modifications to the coil design: compensation network adaptation [98, 71, 101, 102]. Later, adaptations to the coil geometry and design are considered to suit different operating conditions, such as designing the GA to be larger than the VA and changing the number of turns in the VA to suit different battery voltages. These adaptations to the coil geometry are aided by the use of the FAM methodology.

6.2.1 Compensation Network Adaptation

The Gen. 2 demonstrator was measured and modeled with series-series compensation. Series-series (SS) compensation has advantages in terms of simplicity and efficiency, but suffers under varying loading from high input current under low coupling and high output resistance, and with hard-switching and high input voltages under low output resistance. Over the fast charging cycle shown in Figure 6.2, the output resistance varies from 2 to 15 Ω. The input impedance of the SS-compensated Gen. 2 system, including the lead inductance, is plotted over this range in Figures 6.5a and 6.5b at alignment at the 125 mm and at (10 cm, 5 cm) at a 152.4 mm airgap. The component values for the Gen. 2 demonstrator used to create these plots are repeated in Table 6.2.

To improve the soft-switching range of the Gen. 2 demonstrator, previous work has shown that series-series compensation can be slightly detuned or the switching frequency can be changed dynamically to result in a more inductive phase [98]. This creates an additional reactive phase at all operating points, which will induce additional losses, but can extend the soft-switching range of the system. This was seen in the Gen. 2 tests, as soft switching

was still possible slightly under unity gain as in the 400 V output tests plots in Figure 5.47 due to the GA inductance being slightly larger than the VA inductance. A slight detuning of the Gen. 2 demonstrator by reducing the VA compensation by 1 nF as in Table 6.2 results in the input impedance of Figures 6.5c and 6.5d. Here, detuning does not significantly improve the phase of the 2 Ω curve at (0 cm, 0 cm) at 125 mm airgap, but does at (10 cm, 5 cm) at 152.4 mm airgap.

Detuning or changing the switching frequency dynamically helps in extending the soft-switching range of the system. However, the problem of high input current and voltages remains. This problem can be solved by adapting the input impedance magnitude to suit the inverter ratings over the operating range. A large variety of other compensation networks are available to accomplish this such as parallel or LCC compensation [71]. For high power applications, the selection of compensation networks are limited in complexity by the additional loss each element introduces. On the VA, the size and weight of additional compensation components is also a factor such that LCC-series (LCC-S) tuning may be preferred over LCC-LCC tuning.

There is a large degree of freedom in the design of LCC-S and LCC-LCC tuning networks to match different inverter ratings and battery voltages [101, 102]. A schematic of an LCC-LCC tuned system is shown in Figure 6.4. For an example of the application of LCC tuning to the Gen. 2 demonstrator, the component values in Table 6.3 were used to produce Figure 6.6. These values use a 1:6 ratio between the main coil inductance L_1 and L_2 and the compensation inductors L_{11} and L_{22}. Standard tuning was used for the parallel compensation capacitors $\omega_r = 1/\sqrt{L_{11}C_{11}} = 1/\sqrt{L_{22}C_{22}}$ and the series compensation capacitors $\omega_r = 1/\sqrt{(L_1 - L_{11})C_{12}} = 1/\sqrt{(L_2 - L_{22})C_{21}}$, where ω_r is the resonant frequency, with slight detuning to adjust the phase of the input impedance to be inductive [101]. The components resistance values were set with a $Q = 300$ for the inductors and the measured resistance values for the 1 µF Celem CSM150/300 capacitor banks used in the Gen. 2 demonstrator.

In Figure 6.6, it is seen that a load-independent inductive phase can be achieved at the resonant frequency for the LCC-S and LCC-LCC tuning, but this frequency varies from around 86.5 kHz to 88 kHz as the self-inductance of the coils varies as a function of airgap. For LCC-S tuning at 125 mm airgap, the high reflected impedance seen at the 2 Ω output is

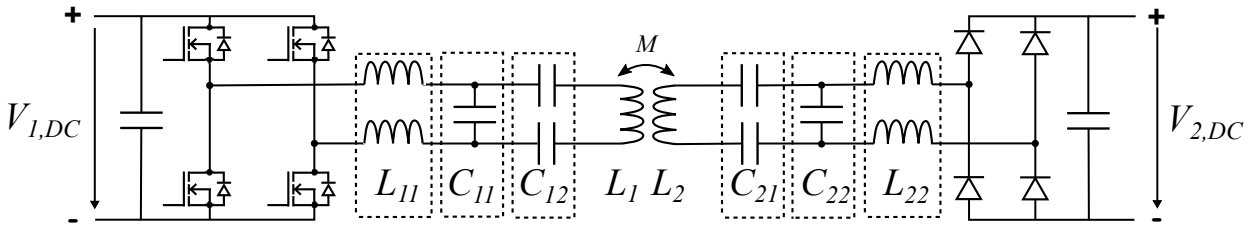

Figure 6.4: Schematic of a typical LCC-LCC tuned WPT system.

Table 6.2: Series-Series Compensation Networks for the Gen. 2 Demonstrator

Component Description	GA	VA
Coil and Leads, 125 mm	40.4µH, 28 mΩ	40.4µH, 28 mΩ
Mut. Ind. (k), 125 mm, Aligned	8.1µH (0.200)	
Coil and Leads 152.4 mm	38.7µH, 28 mΩ	38.7µH, 28 mΩ
Mut. Ind. (k), 152.4 mm, (10 cm, 5 cm)	3.4µH (0.087)	
SS Capacitors	84.1 nF, 9.6 mΩ	84.1 nF, 9.6 mΩ
Detuned SS Capacitors	84.1 nF, 9.6 mΩ	83.1 nF, 9.6 mΩ

Table 6.3: Example LCC Compensation Networks for the Gen. 2 Demonstrator

Component Description	GA	VA
LCC-S Tuning Inductor	L_{11} =6.5 µH, 12 mΩ	
LCC-S Capacitors	C_{11} =500 nF, 1.6 mΩ C_{12} =100 nF, 8 mΩ	85.1 nF, 9.6 mΩ
LCC-LCC Tuning Inductors	L_{11} =6.5 µH, 12 mΩ	L_{22} =6.5µH, 12 mΩ
LCC-LCC Capacitors	C_{11} =500 nF, 1.6 mΩ C_{12} =100 nF, 8 mΩ	C_{22} =505 nF, 1.6 mΩ C_{21} =102 nF, 8 mΩ

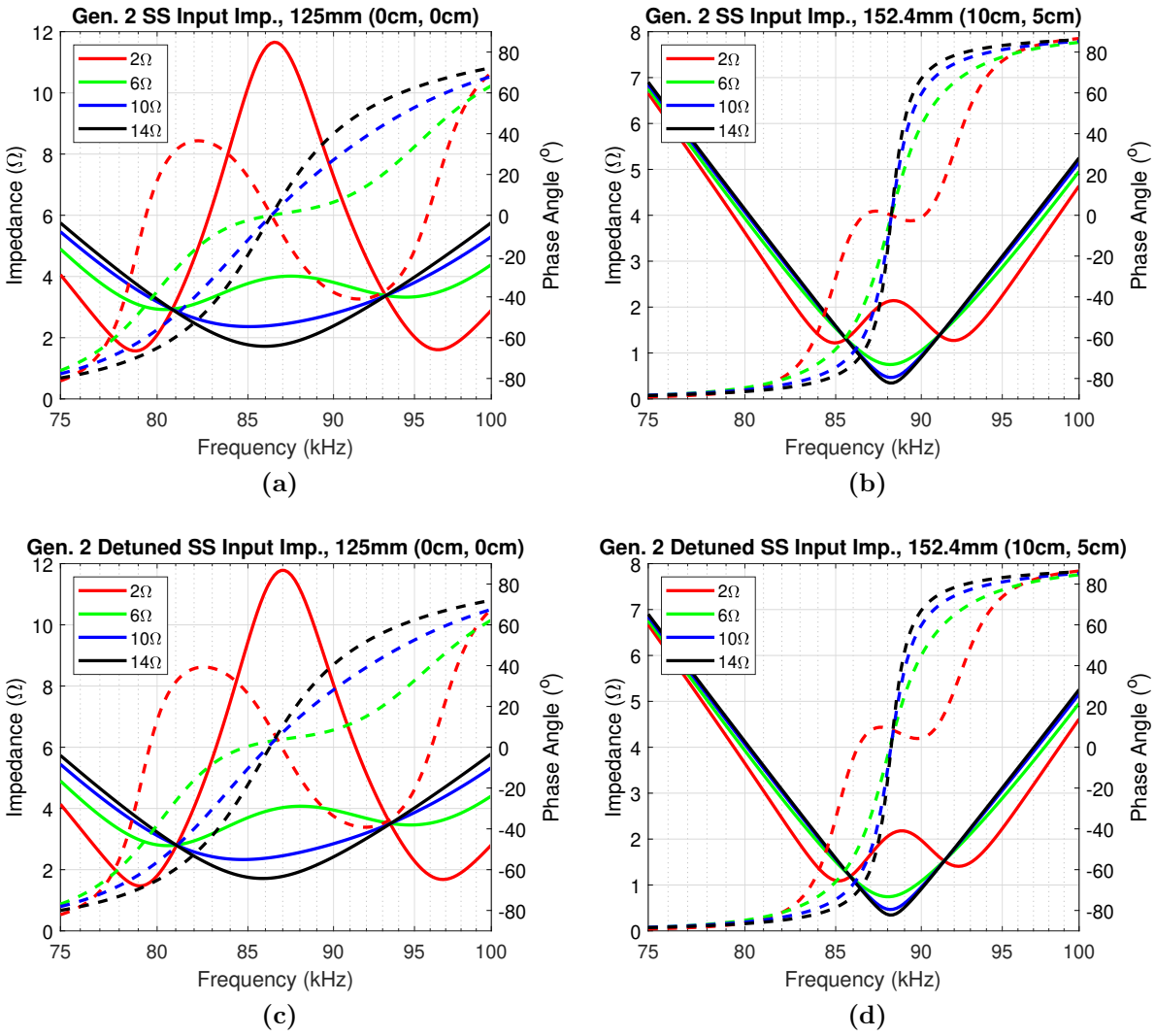

Figure 6.5: The input impedance of the series-series compensated Gen. 2 Demonstrator with different DC output loading. (a) Aligned at 125 mm airgap with normal tuning. (b) (10 cm, 5 cm) at 152.4 mm airgap with normal tuning. (c) Aligned at 125 mm airgap with detuning. (d) (10 cm, 5 cm) at 152.4 mm airgap with detuning.

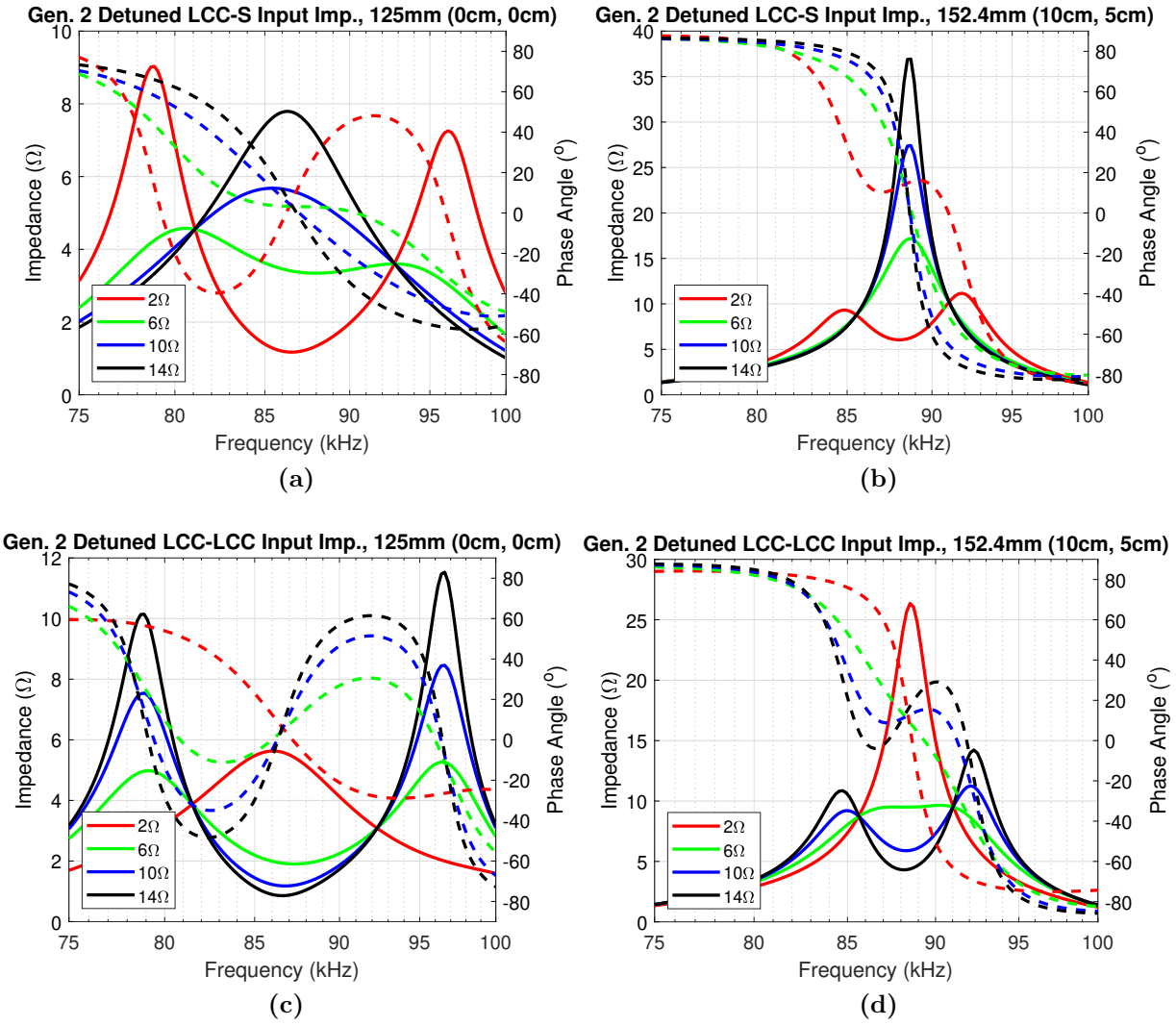

Figure 6.6: Impedance plots of the Gen. 2 Demonstrator compensated with LCC-S and LCC-LCC tunings using the component values in Table 6.2. LCC-S compensated system with a (a) 125 mm airgap at alignment and (b) 152.4 mm airgap with (10 cm, 5 cm) alignment. LCC-LCC compensated system with a (c) 125 mm airgap at alignment and (d) 152.4 mm airgap with (10 cm, 5 cm) alignment.

transformed into a low input impedance which is helpful to reduce the input voltage, but the system will have a high input current at this point, which may reduce the power level due to the temperature limit of the devices. The higher output resistances are likewise transformed to higher input impedances compared to SS tuning. However, at lower k and high output resistances, the input impedances becomes large which may limit the power level due to the voltage limit. LCC-LCC also decreases the impedance at the 2 Ω output, but has low input impedance for higher load resistances, again leading to even higher input current at high output resistance values than with SS compensation. At low coupling, all impedances increase, leading to lower input current and maximum output power because the system will be limited once again by inverter device voltage limits.

In these examples, the adjustment of the phase and input impedance of the Gen. 2 demonstrator was possible with the application of different compensation networks. The detuning of the SS compensation improved the inductive phase of the system for soft-switching. Likewise, the LCC-S and LCC-LCC compensations adjusted the input impedance to more suitable ranges for the inverter, but caused the input impedance to increase greatly with lower coupling to the extent that it is out of the 1.1 Ω to 5.5 Ω range for the 1.2 kV inverter with a less than 900 V DC-link input. Similar compensation networks may be designed to suit different geometries and loads in future work.

6.2.2 Geometry and Inverter Rating Adaptation

Next, adaptations to the Gen. 2 coil geometry and the inverter were considered to show how the geometry of the GA and VA could be changed to suit the operating range of Table 6.1. This was done by designing the GA to be larger than the VA, changing the number of turns in the GA and VA, and considering FAM optimization outputs with higher $B_{str,lim}$ than the Gen. 2 geometry. As seen in the Gen. 2 stray field measurements, even at (10 cm, 5 cm) misalignment at 125 mm the stray field was below the 27 µT ICNIRP limit at a vector sum of 6.80 µT(rms) and 5.20 µT(rms) at 80 cm on the X and Y axes, respectively. These adaptations to the coil geometry were aided by the use of FAM modeling and the previous optimization results. The inverter ratings can also be adapted to meet higher currents and voltages to further eliminate limitations, such as by paralleling 1.7 kV half-bridge modules.

FAM modeling can be used to expand and contract coil geometries by dividing or multiplying their respective wavenumbers by a scalar. To preserve quality and reduce the impact of the limited number of basis functions used in FAM, the finely discretized spatial potential was used in the transformation and then the discrete Fourier transform of the cropped potential was taken to determine the Fourier components to use in FAM. This process is similar to the calculation of rotation, as detailed previously.

Using the FAM methodology, the coupling and inductance were calculated for different sizes and number of turns to tune the system for a series-series compensated application. The size of the VA was fixed to that of the Gen. 2 demonstrator, but the size of the GA was increased equally in the X and Y directions. The $B_{str,lim}$ =100 µT, $\cos x \sin y$ geometry of the Gen. 2 demonstrator did not allow the required misalignment performance without greatly increasing the size of GA, so the $B_{str,lim}$ of the solution was increased until a solution with an impedance greater than 1 Ω and less than 12 Ω over the load and misalignment range was found. The input impedance of 12 Ω approximates the maximum input voltage with 1.7 kV devices at a 1.350 kV DC-link at 120 kW with allowance for deadtime. This choice of maximum DC-link voltage is a slightly lower safety factor of 26% relative to the 33% safety margin used in the 900 V maximum rating for 1.2 kV devices. The inverter must also be able to supply the current near the 1 Ω input impedance at 120 kW or around 350 A(rms). Therefore, four Cree CAS380M17HM3 1.7 kV, 380 A(rms) half-bridge modules were chosen for the inverter with two in parallel per phase leg of the full-bridge inverter.

A solution was found meeting these conditions with a GA sized 1.4 times the size of the VA, or approximately 55 cm × 70 cm, with a 40 cm × 50 cm VA both with the $B_{str,lim}$ =400 µT, $\cos x \sin y$ geometry. The coupling over misalignment at 125 mm and 152.4 mm airgaps are given in Figures 6.7a and 6.7b. The input of the impedance of the system was calculated at the maximum and minimum coupling over a range of different GA and VA turns at the minimum and maximum battery load impedance at 120 kW, approximately 2 Ω at 480 V and 5.33 Ω at 800 V as seen in Figures 6.7c and 6.7d. Due to the change in coupling from around 0.34 to 0.21, the input impedance of the system was less than 1 Ω and greater than 12 Ω across most combinations of GA and VA turns. Soft-switching operation is also preferred, limiting the number of turns on the VA to 8 to avoid

bifurcation and capacitive phase at most loads. With this, 10 and 8 turns were selected for the GA and VA, respectively, as in Figures 6.7e and 6.7f.

With these number of turns, the inductance and capacitor values for series-series compensation are given in Table 6.4. Resistance values are calculated using the previously detailed loss models with 2 AWG litz wire of 42 AWG stranding. The resistances modeled for the GA and VA tanks at the fundamental frequency of 85 kHz are shown in Figure 6.10. An impedance plot of the system at different output resistances can be seen in Figure 6.8. Here, the lowest output resistance of 2 Ω at maximum coupling barely avoids the capacitive phase from bifurcation by operating near the 125 mm resonant point at 83.5 kHz with detuning with an input impedance right at 11 Ω. With high output resistance and low coupling, the input impedance of the system quickly becomes low, leading to low light load efficiency with high GA currents. At maximum misalignment, (10 cm, 5 cm) at a 152.4 mm airgap, the 2 Ω DC load results in a comfortable input impedance around 4 Ω, but the input impedance at higher output resistances and battery voltages becomes very low, around 1.2 Ω for a 6 Ω DC load impedance. The resonant frequency at 152.4 mm also changes to around 85 kHz due to the changes in the GA and VA self-inductance. The efficiency in the operating range in these two alignments for the system with series-compensation is plotted in Figure 6.9 using the loss model parameters in Table 6.5 and the PLECS simulation model detailed in Section 5.7. Switching loss lookup tables under soft-switching conditions were developed for the four CAS380M17HM3 1.7 kV, 380 A(rms) half-bridge modules from the manufacturer's datasheet and PLECS model.

Lastly, FEA simulations at the (0 cm, 0 cm) aligned case at 125 mm airgap and the fully misaligned case at (10 cm, 5 cm) and a 152.4 mm airgap were performed in order to estimate the stray field performance of the system at 80 cm on the X and Y axes as shown in Figure 6.11. The coil currents were determined from the PLECS simulations at 120 kW output power at the 800 V output voltage for the 125 mm (0 cm, 0 cm) case and at 650 V for the 152.4 mm (10 cm, 5 cm) case. The summary of the simulation parameters and outputs are given in Table 6.6. These stray field values were calculated by taking the peak field magnitude over one period and dividing by the square root of two to produce the equivalent RMS value. This is different from the vector sum of the RMS values of each component

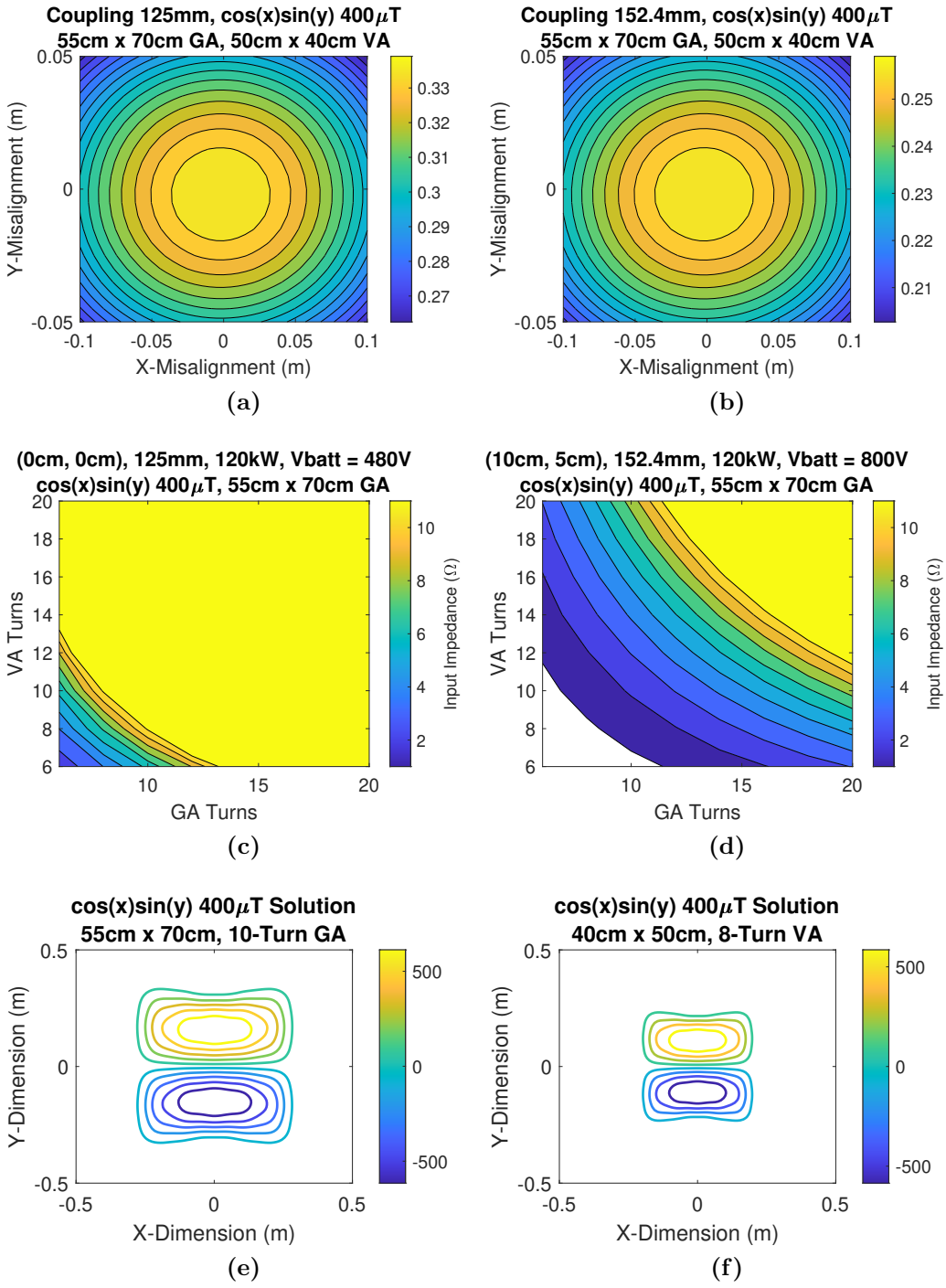

Figure 6.7: Coupling and input impedance of a 55 cm × 70 cm GA with a 40 cm × 50 cm VA with the $B_{str,lim}$ =400 µT, $\cos x \sin y$ geometry. Coupling of the GA and VA over misalignment at a (a) 125 mm and (b) 152.4 mm airgap. The input impedance magnitude of the system with different numbers of GA and VA turns when (c) aligned at a 125 mm airgap with the minimum battery output resistance and (d) fully misaligned at (10 cm, 5 cm) at a 152.4 mm airgap with the maximum battery output resistance. The geometries of the (e) 10-turn GA and (f) 8-turn VA.

Table 6.4: Modeled Resized System Impedance Values

Component Description	55 cm×70 cm GA	40 cm×50 cm 8-T VA
Coils + Leads, 125 mm Airgap	37.0 µH, 13.5 mΩ	14.9 µH, 11.0 mΩ
Mut. Ind. (k), 125 mm (0 cm, 0 cm)	8.0 µH (0.34)	
Coils + Leads, 152.4 mm Airgap	34.6 µH, 13.5 mΩ	14.4 µH, 11.0 mΩ
Mut. Ind. (k), 152.4 mm (10 cm, 5 cm)	4.7 µH (0.21)	
SS Capacitors	101.4 nF, 8.6 mΩ	244.0 nF, 3.5 mΩ

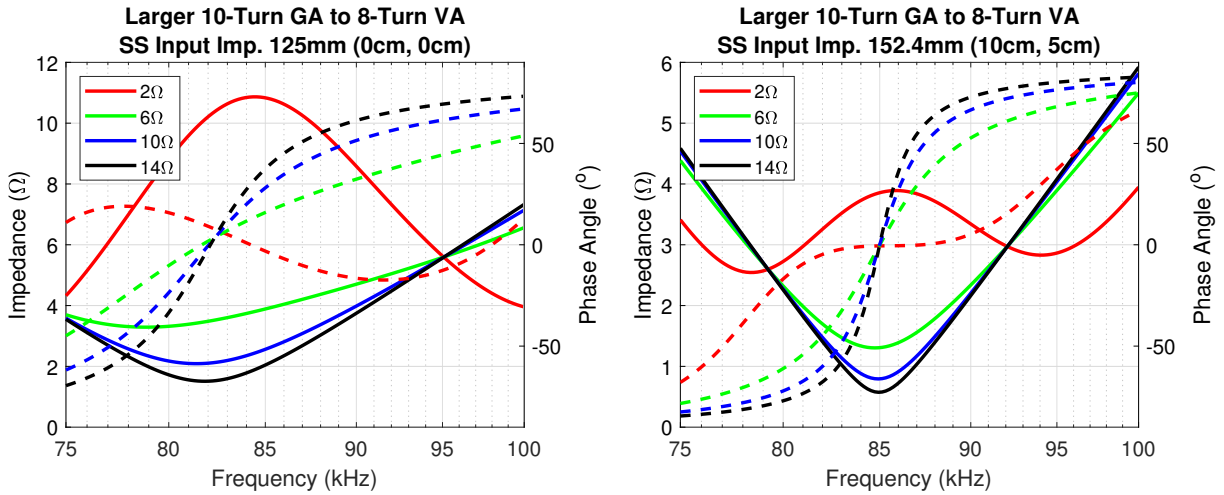

(a) **(b)**

Figure 6.8: Input impedance with varying output loads of the series-series compensated system of Table 6.4 at (a) (0 cm, 0 cm) alignment at a 125 mm airgap and at (b) (10 cm, 5 cm) alignment with a 152.4 mm airgap.

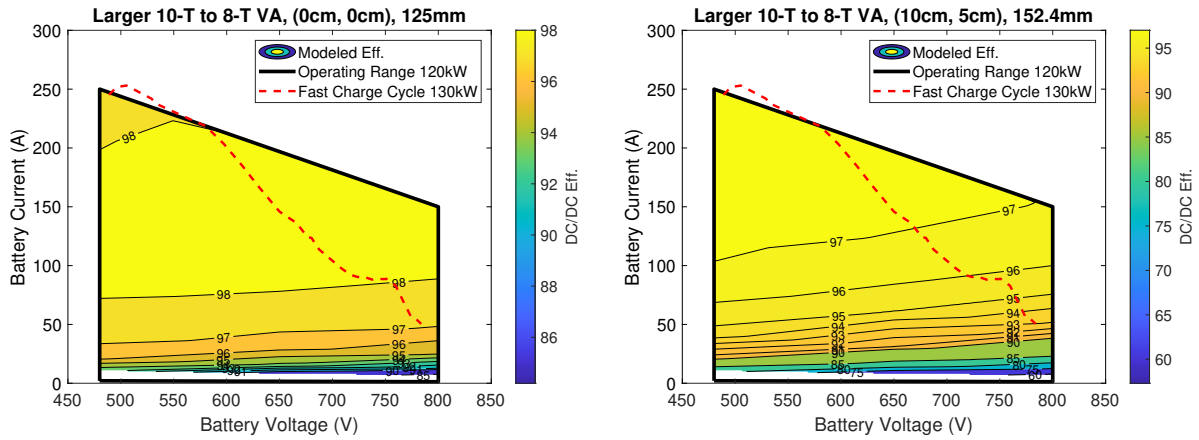

(a) (b)

Figure 6.9: Estimated operating range of the resized system with a larger 10-turn GA and 8-turn VA: (a) Approximate operating range at a 125 mm airgap at alignment with a 83.5 kHz operating frequency. (b) Approximate operating range at a 152.4 mm airgap at (10 cm, 5 cm) alignment with a 85.5 kHz operating frequency.

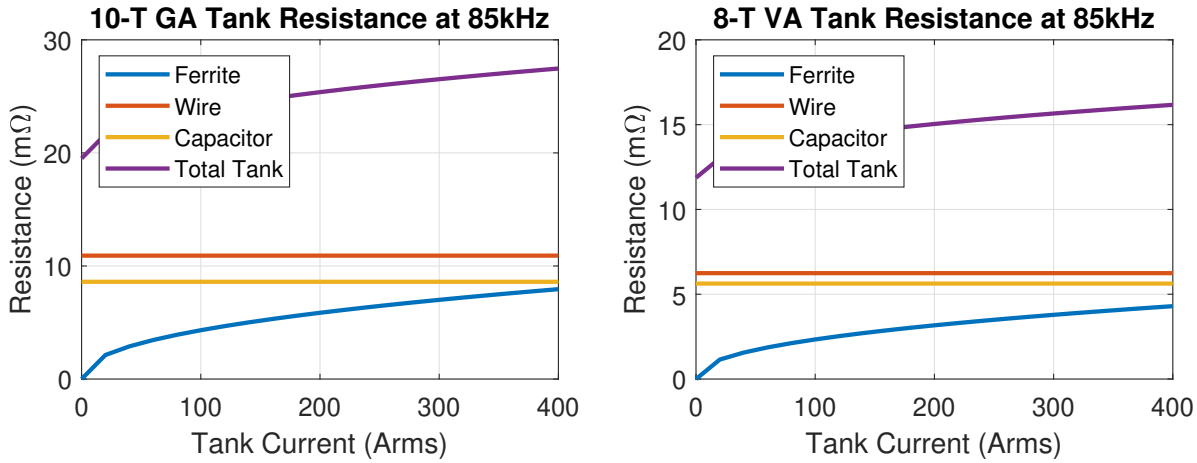

(a) (b)

Figure 6.10: Modeled tank resistance of the Gen. 2 demonstrator at 85 kHz for the (a) larger 10-turn GA and (b) 8-turn VA.

Table 6.5: Model Parameter Values for the 55 cm×70 cm 10-turn GA and 8-turn VA Resized System

Parameters		Value
Ferrite Steinmetz Parameters Ferroxcube 3C95 20 kHz-150 kHz		$\mu_r = 3000$ $C_m = 92.1\text{e-}3$ mW/cm^3 α =1.045; β =2.440 $C_t = 1.332$; $C_{t1} = 0.0079$; $C_{t2} = 4.62\text{e-}5$
Temperature of Ferrite		T_{fer} =19°C
Ferrite Thickness		GA, $t_{fer} = 20$ mm (all) VA, $t_{fer} = 10$ mm (all)
Litz Wire	Outer Diameter Number of Strands Strand Diameter Cabling Operations Wire Length	$d_{out} = 14.2$ mm $n = 10800$ $d_{str} = 0.0635$ mm $N_b = 2$ $N_c = 1$ GA, $L_T = 11.2$ m VA, $L_T = 6.4$ m
GA/VA Lead Resistance (1/2 for GA)		R_{lead} =5 mΩ, 85 kHz 24 mΩ, 255 kHz 55 mΩ, 425 kHz 102 mΩ, 595 kHz 163 mΩ, 765 kHz 235 mΩ, 935 kHz
Inverter Parameters 4 x CAS380M17HM3 Module Gate Drive Board CGD1700HB3P-HM3		R_{DS} =3.74 mΩ C_{oss} =1.70 nF t_{dt} =600 ns V_{GS} =-4/+15 V
Rectifier Device Curve Fit 4 x BSM300D12P2E001 Modules		$V_f = 0.9$ V $R_f = 3$ mΩ
Heatsink (HS) Thermal Resistance Coolant (Liq.) Temperature		(0.014 (HS/Liq.)+ 0.035 (Case/HS Rohm))/2 °C/W 25°C
Copper Wire Resistivity at 20°C		ρ_{Cu} =1.724e-8 Ω-m
Temperature Coefficient, Copper		$C_{Cu,t}$ = +0.393 %/°C
Temperature of Copper		$T_{Cu} = 40$ °C
Gap Between Ferrite and Wire Planes		$z_g = 6.5$ mm

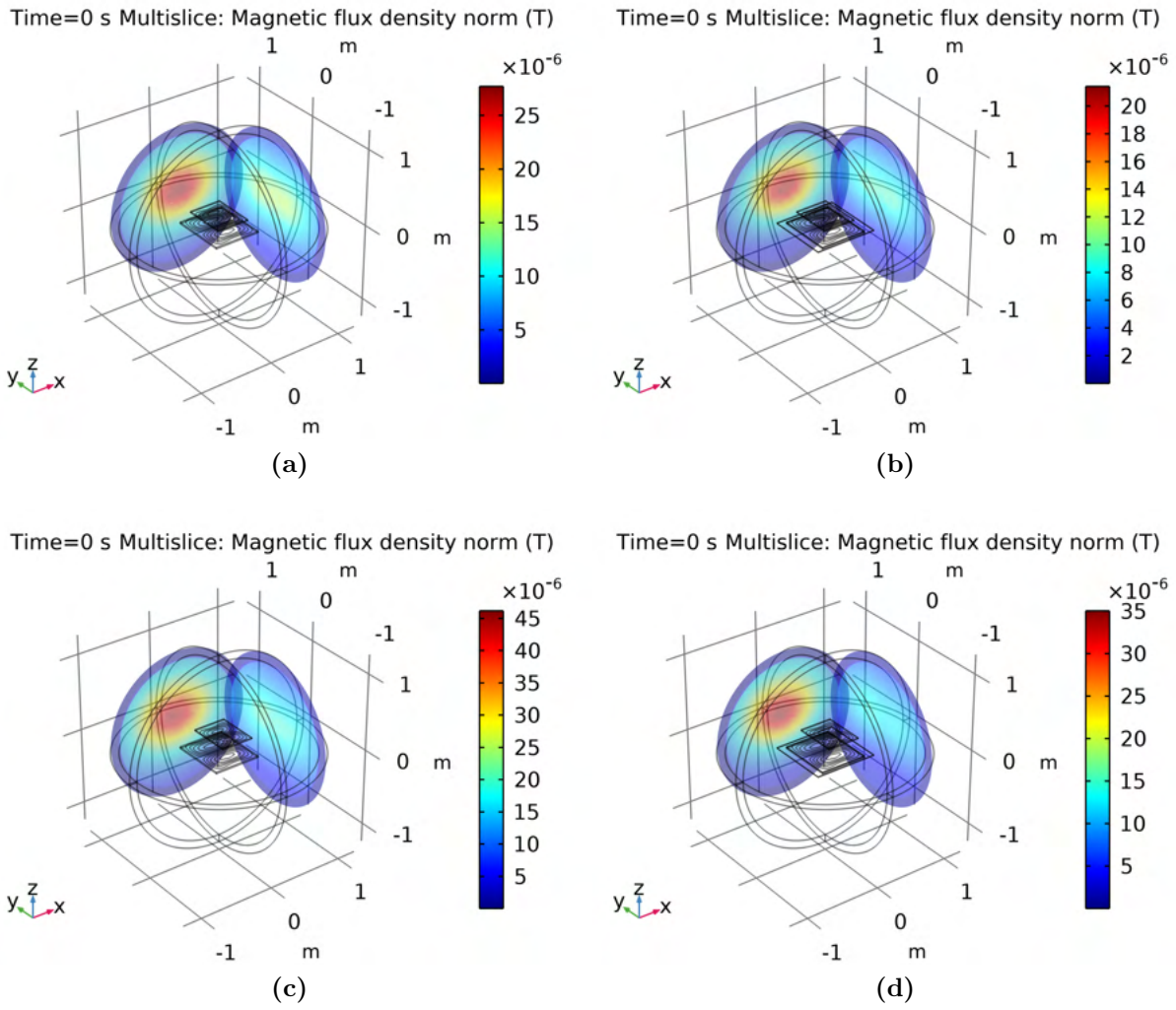

Figure 6.11: FEA simulation of the peak stray field magnitude at 0.8 m at 120 kW at (a) alignment at 125 mm without and (b) with with an additional 80 cm x 80 cm x 5 mm ferrite sheet around the GA and at (c) (10 cm, 5 cm) at 152.4 mm without and (d) with an additional 80 cm x 80 cm x 5 mm ferrite sheet around the GA.

Table 6.6: Operating Points and Simulated Stray Field Magnitude (X, Y) Mid-Airgap at 80 cm at 120 kW with the 55 cm×70 cm 10 Turn GA and 8 Turn VA of the $B_{str,lim}$ =400 µT, $\cos x \sin y$ Geometry

Airgap/Alignment	Output Voltage (DC/DC Eff.)	Coil Currents (RMS) (GA, VA)	Stray Field (RMS) Unshielded/ (With Ferrite Shield)
125 mm (0 cm, 0 cm)	800 V (98.4%)	173 A, 169 A	10.21 µT, 19.35 µT (5.80 µT, 13.36 µT)
152.4 mm (10 cm, 5 cm)	650 V (97.4%)	236 A, 206 A	14.79 µT, 30.67 µT (8.71 µT, 23.20 µT)

because the peaks of the field components in each direction often occur at different phases. The currents of the GA and VA were assumed to be 90 degrees out of phase. As seen, the system meets the 27 µT(rms) limit in the 125 mm (0 cm, 0 cm) case, but not in the 152.4 mm (10 cm, 5 cm) case on the Y axis where the field was 30.67 µT(rms). To stay under the 27 µT(rms) limit using the same ratio of output power to stray field ($kW^{0.5}/\mu T$), the output power at this worst-case alignment would be limited to 93 kW. Adding additional shielding materials, such as ferrite around the GA, could lower the stray field. As reviewed previously, in [40, 103] an extended ferrite sheet was shown to reduce the stray field around bipolar coils. An initial simulation of an extended 80 cm x 80 cm x 5 mm ferrite sheet around the GA reduced the stray field to 8.71 µT(rms) on the X-axis and 23.20 µT(rms) on the Y-axis, which would be compliant with the 27 µT(rms) limit. This would add an additional 6.1 kg of ferrite material to the GA. The full characterization of this effect for this and other geometries is left to future work. An example of the effect of shielding the Gen. 2 geometry, a simple bipolar coil, and a simple rectangular coil with an extended ferrite sheet around the GA or a VA aluminum shield is given in Section 7.2.6 as a starting point.

As seen, FAM modeling can be used to resize and adapt the turn numbers of coil geometries to adjust the coupling and input impedance of the system. Expanding the size of the GA and and using a less shielded geometry for both the GA and VA can increase the coupling and misalignment performance, but still produced a maximum input impedance around 11 Ω. This required the upsizing of the inverter with four 1.7 kV paralleled modules to increase the voltage and current range. With this inverter, the resized system can operate over the operating range with efficiencies over 96% at the higher power levels. However, with the increase in GA size and less shielded geometries, the stray field of the system increased to exceed the 27 µT(rms) limit in the 152.4 mm (10 cm, 5 cm) case with a 80 cm Y-axis stray field magnitude of 30.67 µT(rms). This can be reduced with an extended 80 cm x 80 cm x 5 mm ferrite sheet around the GA to 23.20 µT(rms) on the Y-axis. This result further demonstrates the tradeoff between coupling coefficient and stray field as seen in the FAM optimization results. It is possible to use larger and less shielded geometries to improve the operating range of the system, but at the cost of increased stray field.

6.2.3 Active Rectification or an Onboard DC/DC

In the previous sections, varying coupling and output resistance over the operating range caused the input impedance of the inverter to go out the desirable operating range for the inverter. Instead of changing the compensation, coil geometry, or inverter ratings as done previously, the output impedance of the wireless stage could be actively controlled to match the load to the coupling of the coils. Active rectifiers or onboard DC/DCs have been used to this effect to have wide control over the output phase and the equivalent load of the wireless stage [104]. Both of these options require active devices and control on the vehicle side, but these may already be present in inductive charging systems with bidirectional capability or in EV on-board chargers (OBCs).

Active rectifiers up to 6.78 MHz have been demonstrated [105] implying that effective control of active rectifiers in the 85 kHz fundamental band is possible. Active rectification allows the phase and duty cycle of the rectifier to be dynamically adjusted during operation. Although this can be achieved by detuning the system or adding additional compensation elements, these cause additional losses at all operating points, including where no additional phase or load change is needed. Instead, an active rectifier can be used to adapt the equivalent phase of the load only in the cases where additional inductive phase is required or to adjust the load to avoid bifurcation. Soft-switching of the active rectifier requires a capacitive phase shift between the rectifier input current and voltage. This equivalent capacitive load impedance reflects as inductive phase in the input impedance. This capacitive phase was also seen in the negative power factor measurements, λ_3, of the passive rectifier used in the Gen. 2 system as seen previously in Figure 5.34. The duty cycle of the active rectifier can be reduced to lower the equivalent output resistance of the wireless stage.

On-board DC/DC converters coupled to the output of the wireless stage have also been demonstrated. For example, in [22, 106], a buck-boost stage was added to the output of the rectifier with a nominal efficiency of 98.80%. This allowed a wide range of output impedance control and was used to operate the WPT coils at optimum loading and efficiency at the cost of additional weight and losses in the on-board DC/DC stage. The overall efficiency was defined by the performance of both the WPT and DC/DC stages over the operating

range. With a similar type of implementation for the Gen. 2 system, the WPT stage would be controlled to operate in the region of maximum efficiency over misalignment and airgap as in Figure 6.12 to expand the operating range by controlling the output resistance of the wireless stage. Higher output load resistances may not be practical due to device voltage ratings, such as over 6.75 Ω where the DC-link voltage before the buck stage would be over 900 V. Figure 6.12a assumes a buck DC/DC stage with a DC-link voltage less than 900 V or a boost DC/DC stage with a duty cycle between 0 and 0.75. As the unregulated battery load is close to that of the unity load for the Gen. 2 system, a buck-boost may be needed to operate at the optimal load in both the 125 mm and 152.4 mm airgap cases, but with more cost and weight than that of a buck or boost stage. Instead, either a buck or boost could be chosen depending on known ground clearance and airgap of the target vehicle. At lower airgaps, such as 125 mm, a buck could be used to increase the effective output resistance, while with higher airgaps, such as 152.4 mm and beyond, a boost or activer rectifier could be used to lower the effective output resistance. To approximate the efficiency of the DC/DC converter, the 98% to 99% DC/DC efficiency of the non-isolated 360 kW bidirectional half-bridge traction converter of [107] was used to produce the efficiency contours of Figure 6.12. As specified in the datasheet, this converter is 12 kg and can serve as a buck or a boost. The efficiency of this half-bridge converter is dependent upon duty cycle with nearly 99% efficiency near a duty cycle of 1, near unity gain, and a 98% efficiency near a duty cycle of 0.5 or a gain of 0.5 for the buck and a gain of 2 for the boost. To approximate the published measurements of the light-load performance of the DC/DC stage, a light load efficiency drop was added as in Figure 6.12b.

In these plots, for each battery voltage and power level, the simulated data points were iterated over to select points with the same output power level. For each of these, the duty cycle needed to produce the desired output battery voltage was calculated and the interpolated buck or boost efficiency was multiplied with the WPT DC/DC efficiency to produce a total DC/DC efficiency. All combinations were compared to determine the one with the highest DC/DC efficiency. As shown, with the DC/DC on the output the Gen. 2 system could operate over the entire desired operating range at the maximum and minimum coupling.

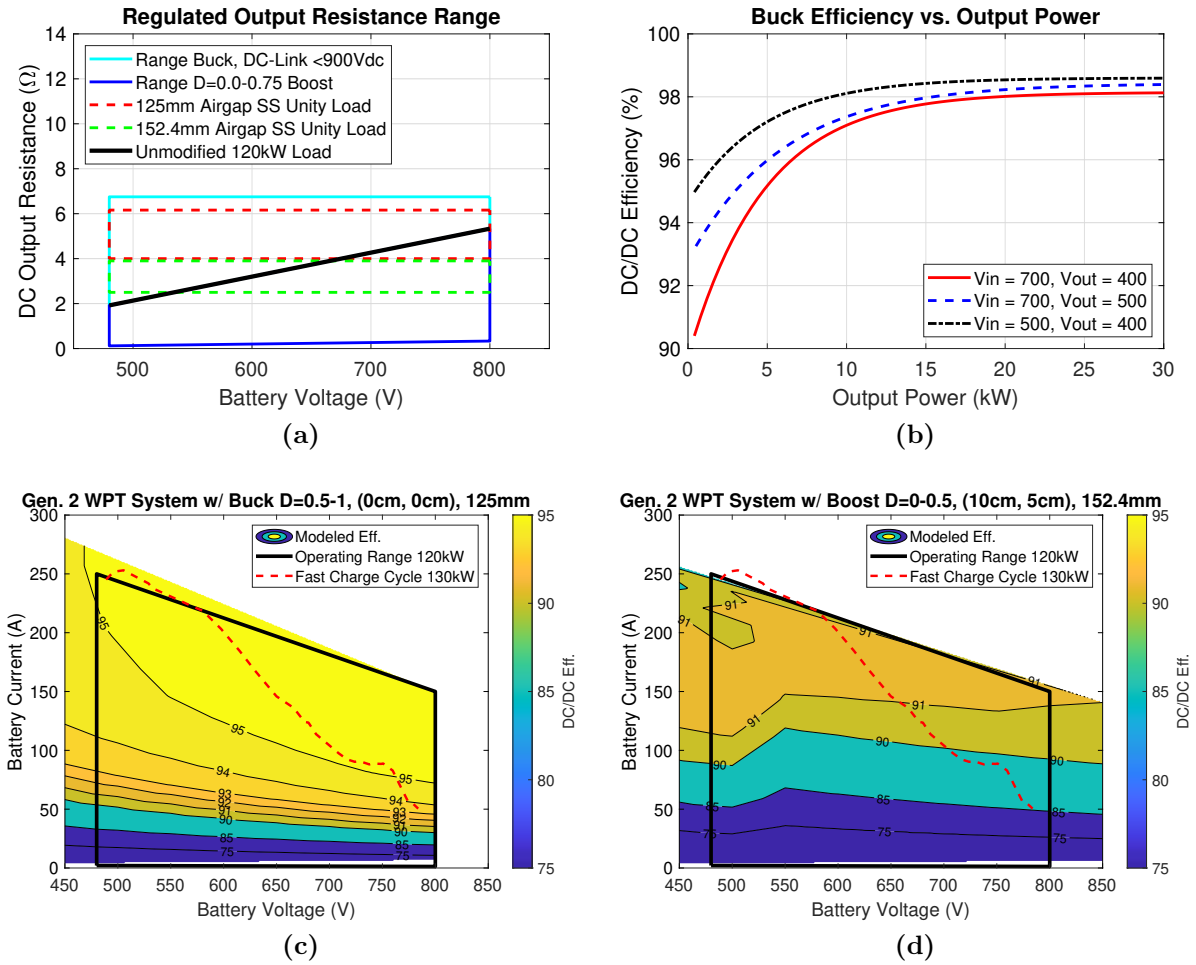

Figure 6.12: Estimated operating range of the Gen. 2 demonstrator with an onboard DC/DC converter (98%-99% efficiency): (a) Possible output resistance range with a buck or boost added between the WPT stage and battery. The buck is limited to a DC-link voltage of 900 V. (b) Estimated efficiency of the DC/DC stage including light-load efficiency at example conversion ratios. (c) Approximate operating range at a 125 mm airgap at alignment with a buck on the output. (d) Approximate operating range at a 152.4 mm airgap at (10 cm, 5 cm) alignment with a boost on the output.

6.3 Interoperability Analysis of the Gen. 2 Geometry

As reviewed in Chapters 1 and 2, the interoperability of different types of coil geometries is important for widespread adoption. In SAE J2954 standard, the interoperability of coil assemblies with various geometries such as the circular/square type, bipolar or Double-D type, and others are required in terms of efficiency, misalignment, and power up to the rated power of the VA [24]. SAE J2954 describes the concept of natural offsets between coil assemblies of different types to align the GA and VA so that they are well coupled over the misalignment range. Therefore, FAM is used to model and analyze the compatibility of the Gen. 2 geometry with geometries derived from the FAM optimization in terms of the coupling coefficient over misalignment at a 125 mm airgap. The geometries are the optimization outputs of the FAM optimization in Figure 5.3. In each case, the geometries are shown with 14 turns, but different number of turns can be chosen. All of these geometries are restricted to the same area of 40 cm by 50 cm in the optimization.

As a baseline, the coupling coefficient of the Gen. 2 geometry, the $\cos x \sin y$, $B_{str,avg}$ =100 µT output, to an identical geometry as in the Gen. 2 tests and to the $\cos x \sin y$, $B_{str,avg}$ =1 mT output is given in Figure 6.13. Here, the maximum coupling coefficient at alignment improves to 0.25 for the $\cos x \sin y$, $B_{str,avg}$ =1 mT output relative to 0.2 and stays high over a wider range of misalignments. This higher coupling comes at the cost of a higher stray field from the $\cos x \sin y$, $B_{str,avg}$ =1 mT geometry, but may still have compliant stray fields at low power levels.

The coupling of the Gen. 2 geometry with two of the $\cos x \cos y$ outputs is shown in Figure 6.14. Here, the coupling is zero at alignment and maximized when the $\cos x \cos y$ geometries are misaligned to be centered over one of the poles of the Gen. 2 bipolar structure. As only one of the Gen. 2 poles is coupled in this alignment, relatively low maximum coupling coefficients of around 0.12 and 0.15 are achieved for $\cos x \cos y$, $B_{str,avg}$ =100 µT and $\cos x \cos y$, $B_{str,avg}$ =1 mT outputs, respectively.

Next, two $\sin x \cos y$ outputs are considered as in Figure 6.15. These geometries are also bipolar, but rotated 90° compared to the Gen. 2 geometry. Without rotation, the coupling of the system is zero at alignment, and increases as the coil is moved so that one of the poles of

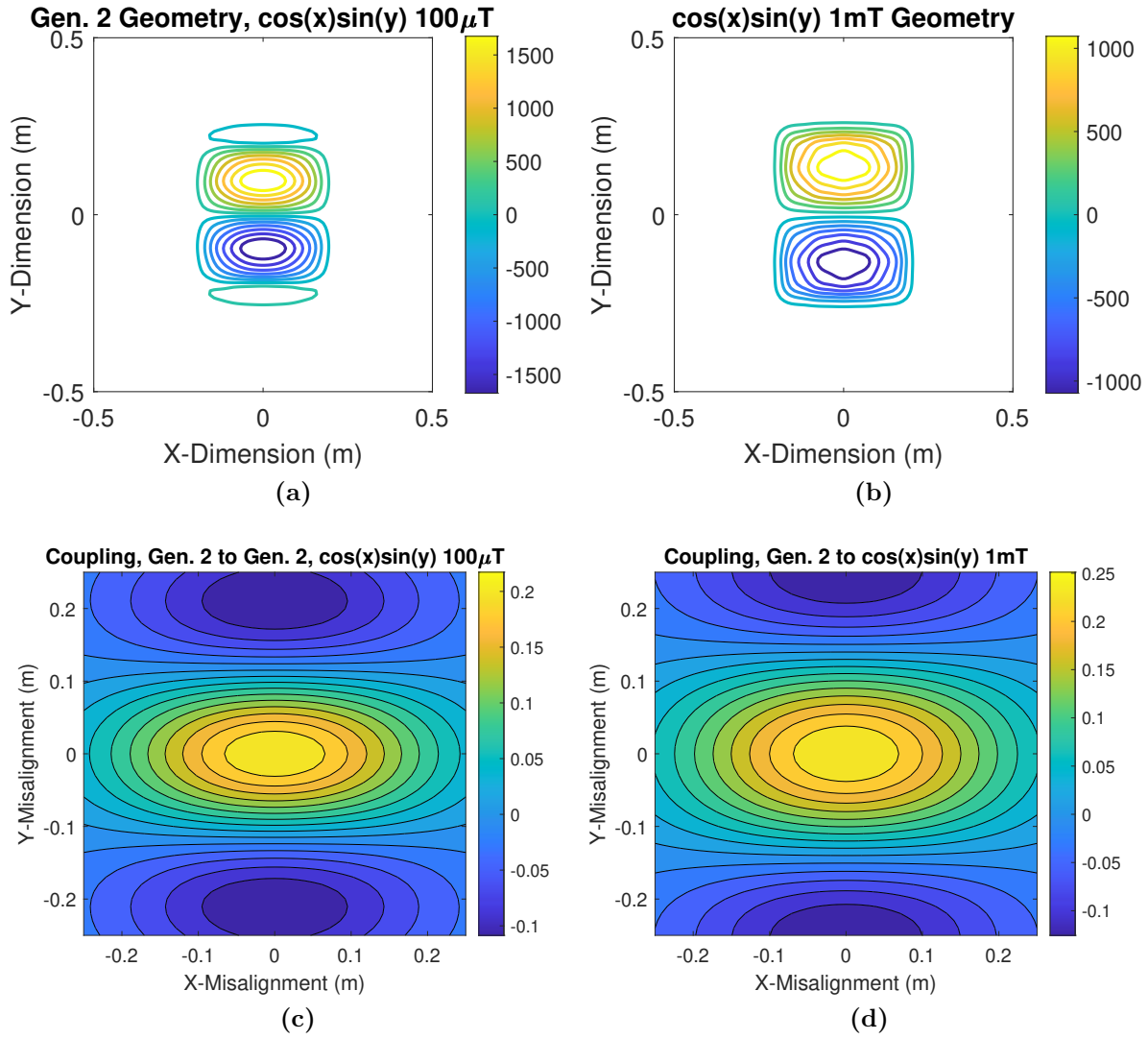

Figure 6.13: Coupling coefficient of the Gen. 2 geometry with $\cos x \sin y$ at a 125 mm airgap. (a) The Gen. 2 geometry, which is the $\cos x \sin y$, $B_{str,avg}$ =100 µT output with 14 turns. (b) The $\cos x \sin y$, $B_{str,avg}$ =1 mT output with 14 turns. Coupling of the Gen. 2 geometry to the (c) Gen. 2 geometry and to the (d) $\cos x \sin y$, $B_{str,avg}$ =1 mT outputs over misalignment.

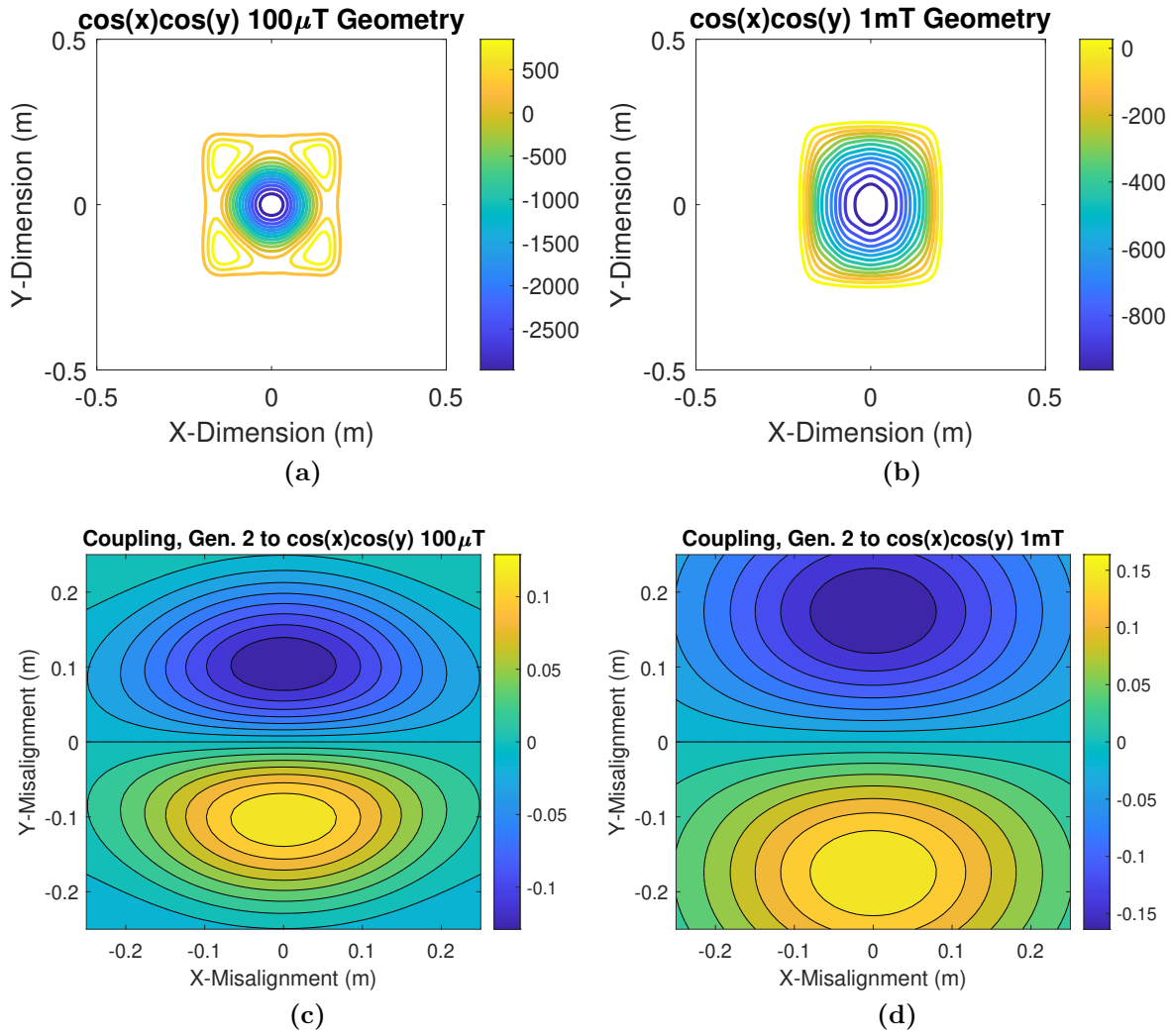

Figure 6.14: Coupling coefficient of the Gen. 2 geometry with $\cos x \cos y$ geometries at a 125 mm airgap. The (a) $\cos x \cos y$, $B_{str,avg}$ =100 µT and (b) $\cos x \cos y$, $B_{str,avg}$ =1 mT optimization outputs with 14 turns. Coupling of the Gen. 2 geometry to the (c) $\cos x \cos y$, $B_{str,avg}$ =100 µT output and to the (d) $\cos x \cos y$, $B_{str,avg}$ =1 mT output over misalignment.

the $\sin x \cos y$ geometries is over the center of one of the Gen. 2 poles. This results in a very low maximum coupling of around 0.05. However, if the $\sin x \cos y$ outputs are rotated by 90°, the coupling increases to be similar to the $\cos x \sin y$ geometries with similar misalignment characteristics.

Lastly, the coupling to two $\sin x \sin y$ geometries are modeled as in Figure 6.16. These geometries are comprised of four small poles with alternating direction. With misalignment in the X-direction, two of these poles align with the two poles of the Gen. 2 bipolar structure to achieve maximum coupling of around 0.08 and 0.1 for the $\sin x \sin y$, $B_{str,avg}$ =100 µT output and the $\sin x \sin y$, $B_{str,avg}$ =1 mT geometries, respectively.

As shown, FAM modeling was used to assess the coupling of different types of coil geometries. The maximum coupling and dropoffs with misalignment in the X and Y directions are shown in Figures 6.17a and 6.17b. The coupling of each of the types to the Gen.= 2 geometry is maximized at different alignments. The maximum overall coupling was achieved when bipolar geometries were used such as the $\sin x \cos y$ and $\cos x \sin y$. High coupling translates to high coil-coil efficiency because less current is needed in the geometries to transfer a certain amount of power. The $\cos x \cos y$ and $\sin x \sin y$ types result in uncoupled poles, but for the $\cos x \cos y$ outputs coupling of around 0.12 and 0.15 is still achieved. This level of coupling suggests that acceptable efficiency may be possible between the Gen. 2 system and coils from the $\cos x \cos y$ outputs or other rectangular or circular geometries.

For expanded misalignment tolerance, a larger 64 cm × 80 cm GA can be used with the smaller 40 cm × 50 cm VA as analyzed in the previous section. The maximum coupling and dropoff with misalignment is summarized in Figures 6.17c and 6.17d. Here, the larger GA produces higher coupling to most of the geometries, though likely at the cost of higher stray field, which is not detailed here. The coupling to the $\sin x \sin y$ $B_{str,avg}$ =100 µT VA is reduced as the larger poles of the GA overlap more opposing VA poles. The coupling to the $\cos x \cos y$, $B_{str,avg}$ =1 mT VA increases as one of the larger GA poles can encompass more of the single VA pole. A similar methodology can be used to investigate the effect of different geometry aspect ratios in future work.

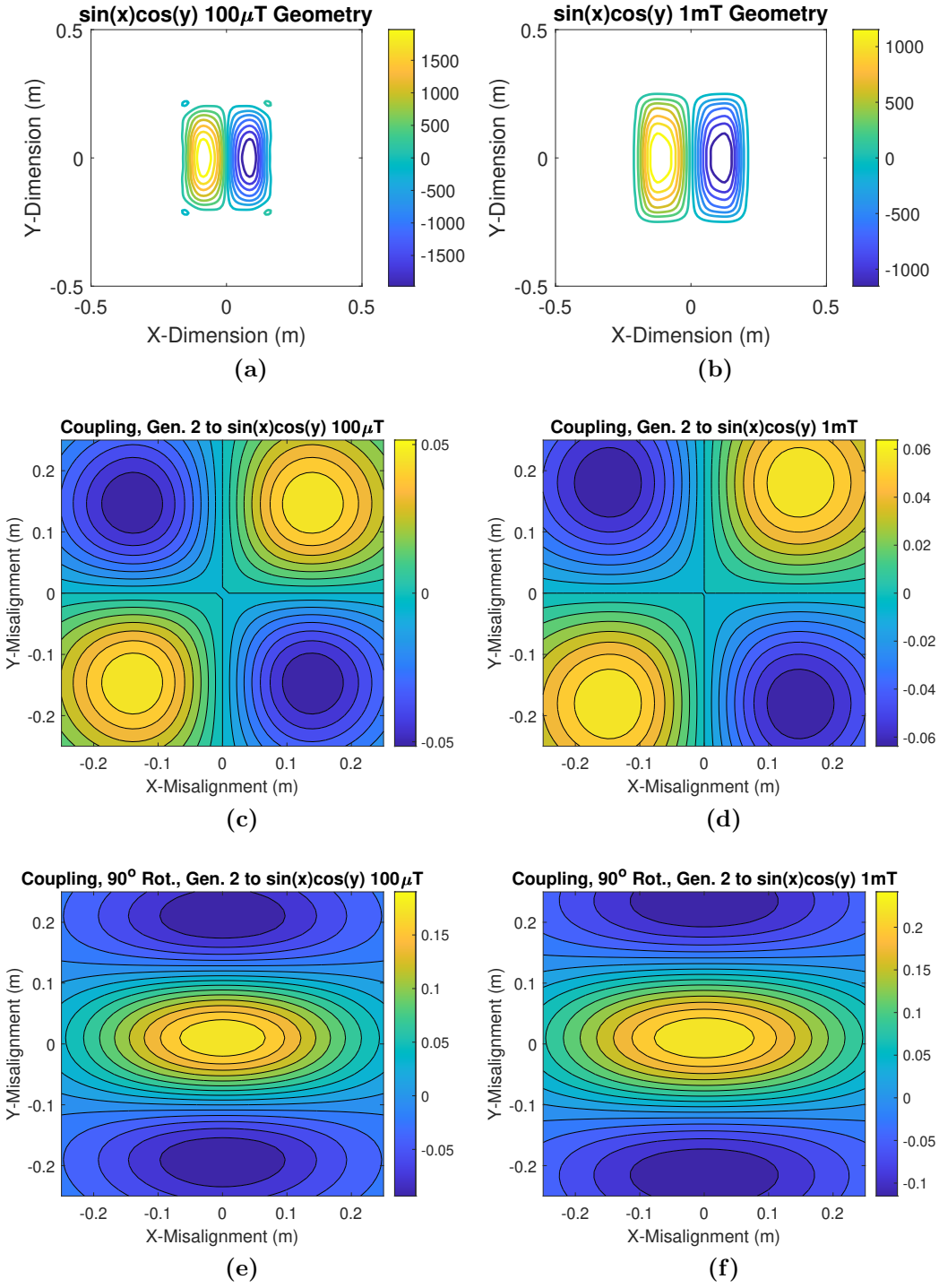

Figure 6.15: Coupling coefficient of the Gen. 2 geometry with $\sin x \cos y$ geometries at a 125 mm airgap. The (a) $\sin x \cos y$, $B_{str,avg}$ =100 µT and (b) $\sin x \cos y$, $B_{str,avg}$ =1 mT outputs with 14 turns. Coupling of the Gen. 2 geometry to the (c) $\sin x \cos y$, $B_{str,avg}$ =100 µT output and to the (d) $\sin x \cos y$, $B_{str,avg}$ =1 mT output over misalignment. Coupling of the Gen. 2 geometry with the 90°-rotated (e) $\sin x \cos y$, $B_{str,avg}$ =100 µT output and to the (f) $\sin x \cos y$, $B_{str,avg}$ =1 mT output over misalignment.

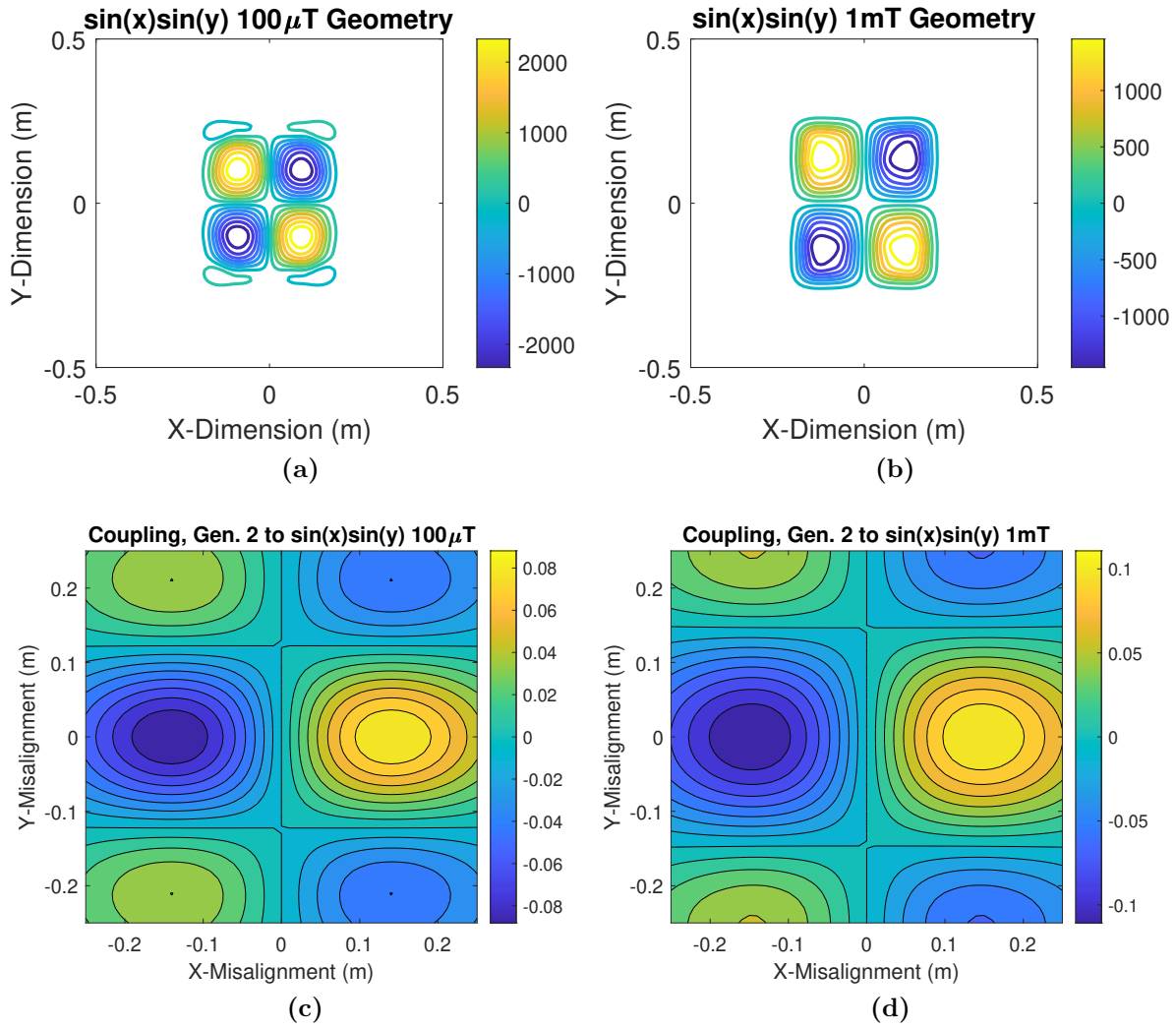

Figure 6.16: Coupling coefficient of the Gen. 2 geometry with $\sin x \sin y$ geometries at a 125 mm airgap. The (a) $\sin x \sin y$, $B_{str,avg}$ =100 µT and (b) $\sin x \sin y$, $B_{str,avg}$ =1 mT optimization outputs with 14 turns. Coupling of the Gen. 2 geometry to the (c) $\sin x \sin y$, $B_{str,avg}$ =100 µT output and to the (d) $\sin x \sin y$, $B_{str,avg}$ =1 mT output over misalignment.

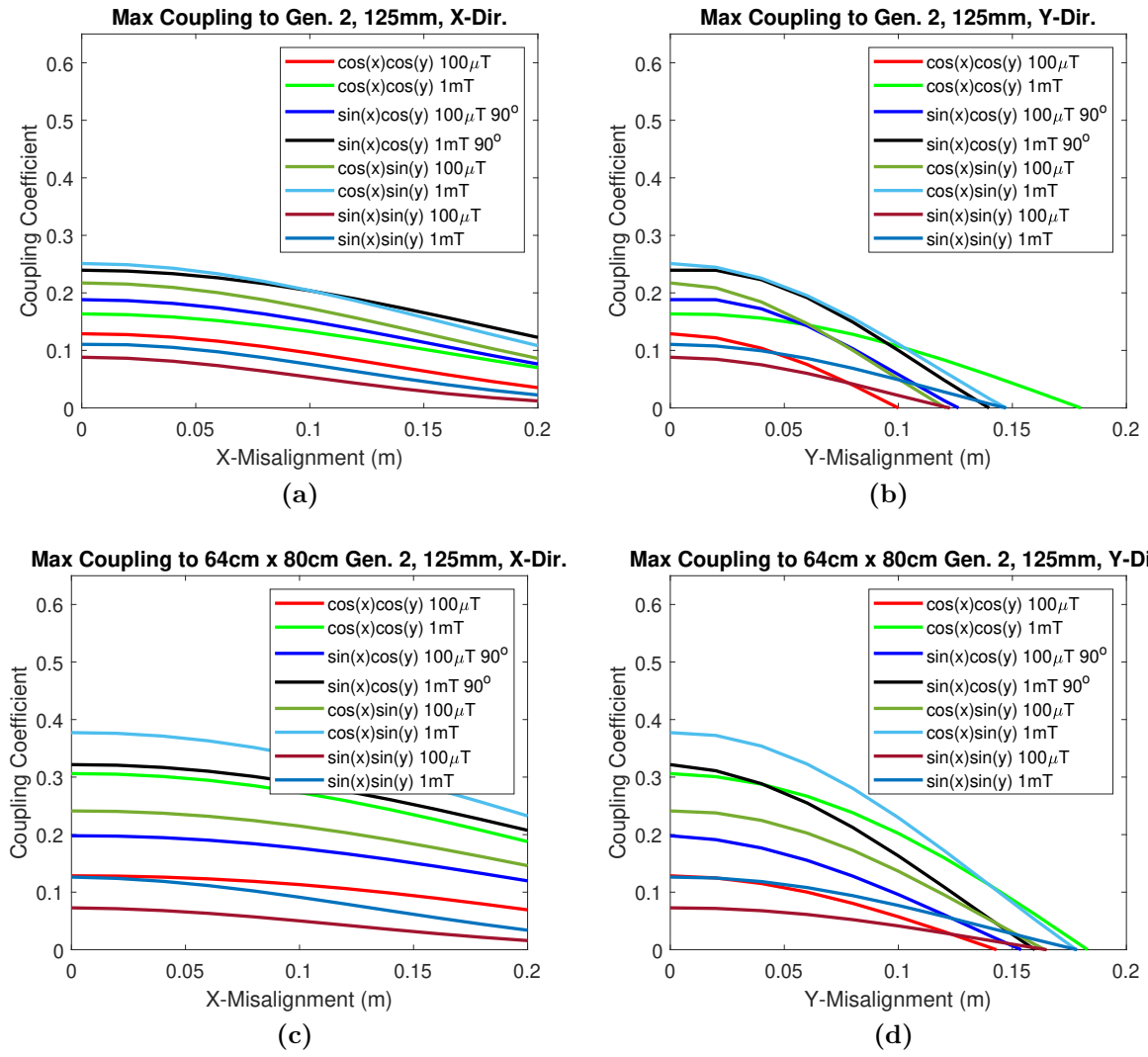

Figure 6.17: Summary of the maximum coupling coefficient of the Gen. 2 geometry with other FAM-generated 40 cm × 50 cm geometries and drop off in the (a) X-direction and the (b) Y-direction. The maximum coupling coefficient of the 64 cm × 80 cm GA with a larger Gen. 2 geometry with the 40 cm × 50 cm VA with the other geometries and drop off in the (c) X-direction and the (d) Y-direction.

6.3.1 Interoperability with a Three-Phase Bipolar Coil

The FAM modeling can be used to import existing coil geometries into Fourier components. This is most conveniently done with spatial surface current, scalar potential, or surface field data of the coil geometry taken at regular intervals and taking the DFT of this to derive the Fourier basis function weights. The input file can be generated using FEA software or by other methods. After the geometry is in the Fourier components, analysis of inductance, coupling, and losses can be performed in FAM as established in previous parts of this work.

To demonstrate this, the interoperability in term of coupling of the Gen. 2 demonstrator and the 50 kW ORNL three-phase bipolar coil of [41] as seen in Figure 6.18 was modeled in FAM and compared to measurements. The ORNL three-phase bipolar coil is a two-layer coil made up of three nearly identical 10-turn bipolar windings of 6 AWG litz at 120° rotations from one another. Each bipolar winding has one pole on the top layer of the coil and the other on the bottom layer. These will be referred to as the X, Y, and Z-windings of the 3Φ coil.

To import the 3Φ coil into Fourier components, an FEA simulation of the surface field of one of the phases was performed as in Figure 6.18c. The surface B_z field of the Z-winding, which was oriented in the models and measurements in the same direction as the Gen. 2 demonstrator, was imported into FAM. The surface B_z field and resulting potential are shown in Figure 6.19. As the FEA simulation placed one winding closer to the plane than the other, some imbalance in the field and potential is seen. The X-winding and Y-winding potentials were derived by rotating this potential in FAM. These potentials were used to model the inductance and coupling of each of the three-phase windings to the Gen. 2 GA as previously done. Measurements were taken using the setup in Figure 6.18b to compare with the model values. The modeled and measured values are summarized in Table 6.7. The measured coupling of each of the phases are compared with modeled values in Figure 6.20. As seen, the largest differences are in the self-inductance of the coils, whereas the mutual inductance and coupling are similar. It is observed that the poles of the 3Φ coil are slightly rotated around 10° compared to the nominal coil axes direction. As seen, the FAM provides similar accuracy as FEA modeling.

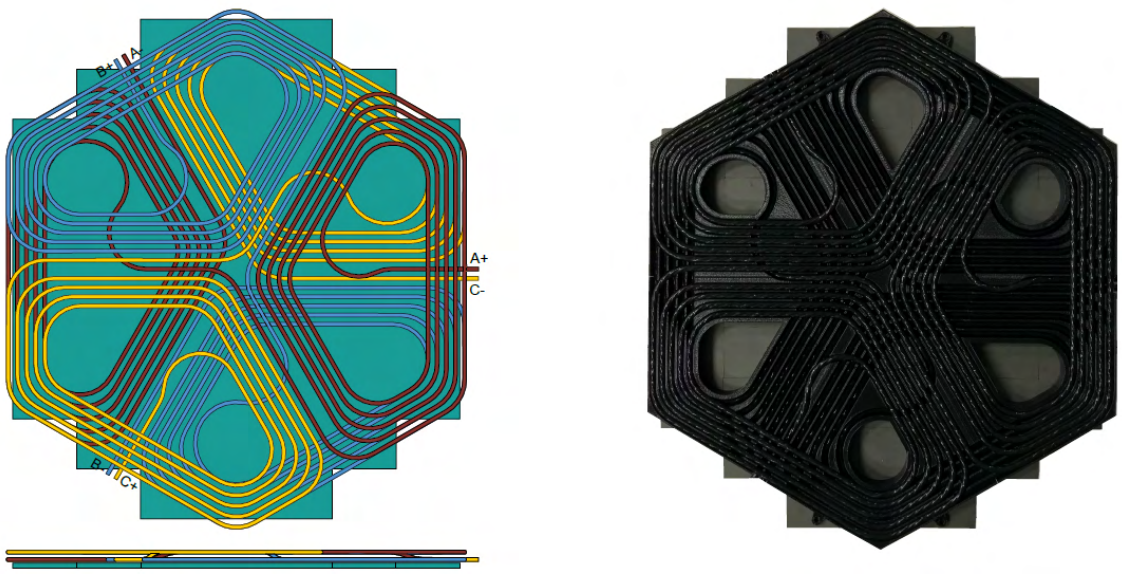

(a)

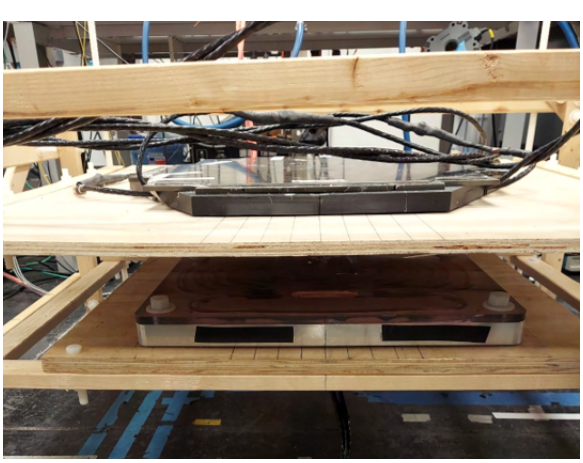

(b)

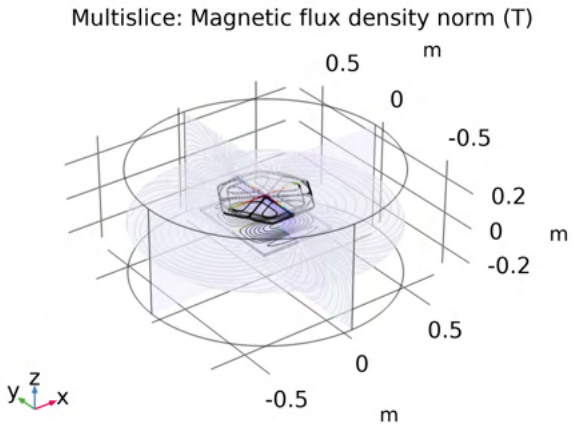

(c)

Figure 6.18: Modeling and measurement of the Gen. 2 coil and 3Φ coil. (a) The ORNL 50 kW 3Φ two-layer coil of [41]. (b) Measurement setup of the Gen. 2 GA and the ORNL 50 kW 3Φ coil. (c) FEA simulation of the Gen. 2 coil and 3Φ coil.

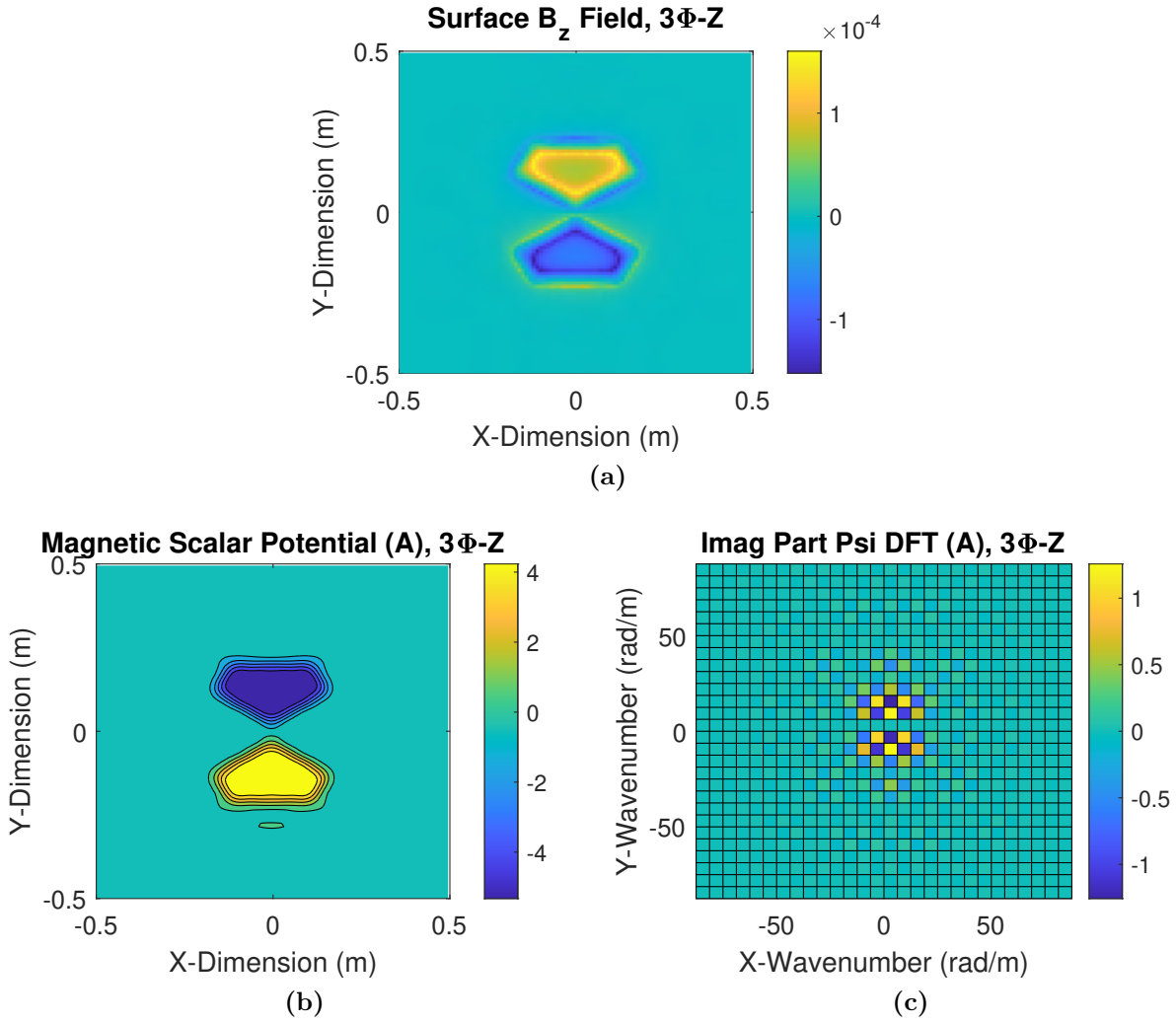

Figure 6.19: Importation of the Z-winding of the 3Φ coil into Fourier components. (a) The surface B_z field of the Z-winding with 1 A. The resulting (b) magnetic scalar potential and (c) discrete Fourier components.

Table 6.7: Gen. 2 and ORNL 50 kW 3Φ Coil Inductance at Alignment

	Measured	FAM	FEA
Gen. 2 GA Self Ind., L_G	39.1 µH	37.8 µH	40.4 µH
3Φ-X Self Ind., L_X	31.4 µH	33.1 µH	32.7 µH
3Φ-Y Self Ind., L_Y	31.3 µH	33.1 µH	32.7 µH
3Φ-Z Self Ind., L_Z	31.1 µH	33.1 µH	32.7 µH
GA to 3Φ-X Mut. Ind., M_{GX} (k)	3.7 µH (0.11)	4.3 µH (0.12)	4.2 µH (0.12)
GA to 3Φ-Y Mut. Ind., M_{GY} (k)	4.6 µH (0.13)	4.3 µH (0.12)	4.2 µH (0.12)
GA to 3Φ-Z Mut. Ind., M_{GZ} (k)	8.0 µH (0.23)	8.2 µH (0.23)	8.1 µH (0.22)

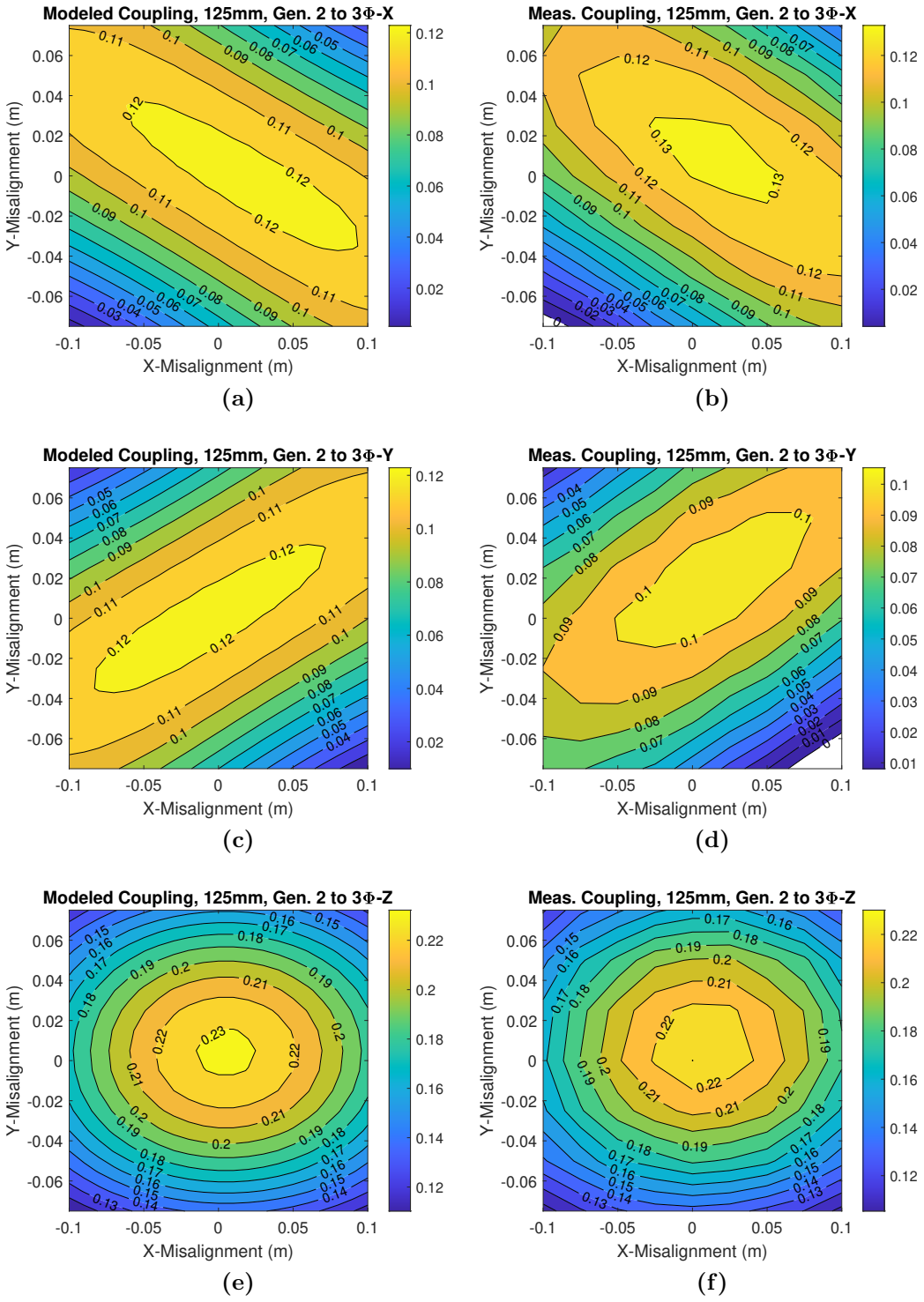

Figure 6.20: Comparison of the FAM-derived and measured coupling over misalignment of the Gen. 2 GA and the ORNL 50 kW 3Φ Coil at 125 mm airgap with the Z-winding aligned with the Gen. 2 GA. (a) Modeled and (b) measured coupling to the X-winding. (c) Modeled and (d) measured coupling to the Y-winding. (e) Modeled and (f) measured coupling to the Z-winding.

The efficiency of the Gen. 2 GA and the ORNL 50 kW 3Φ VA was measured over misalignment at a 125 mm airgap at fixed output voltages in Figure 6.22. A summary of these measurements at constant power over misalignment is also shown in Figure 6.23. The test setup, waveform, and power analyzer screenshot of the aligned 50 kW test is seen in Figure 6.21. For this test, the same Gen. 2 GA and inverter were used with the Rohm rectifier modules of the previous tests in parallel with an additional three-phase rectifier. Each of the three phases of the VA is placed in series with a 97.2 nF capacitor comprised of three Celem CSP 120 of 330 nF-330 nF-250 nF to compensate the self-inductance of each winding. Each of these was connected in an open-winding configuration with a full-bridge rectifier so that each was independently rectified.

As seen, a peak DC/DC efficiency above 95% was measured in the aligned case and over 93% efficiency seen at (10 cm, 5 cm) alignment. In each case, the aligned Z-winding transmitted most of the power, but the X and Y-windings also contributed some power. For example, in the test of Figure 6.21b, the Z-winding contributed 29.5 kW of the 41.4 kW output power whereas the X-winding contributed around 2.6 kW and the Y-winding around 9.3 kW. The effect of the cross-coupling between the VA phases can been seen in the offset phase of the X and Y-winding currents and voltages and distortions seen in Figure 6.21b. The PLECS simulation used modeled values for VA resistances and losses with 6 AWG of 38 AWG stranding litz and 5 mm ferrite and VA winding cross-coupling as detailed in [41]. The modeled tank resistances at 89 kHz are plotted in Figure 6.24 for the parameters in Table 6.8. The PLECS model includes the effect of the long 6 AWG leads needed in the test setup to connect the three VA windings to the series capacitors and the two rectifiers, which was measured to be around 5.6 µH and 60 mΩ. This greatly increased the self-inductance and resistance of the VA tanks compared to the inductance and resistance of the coils alone. The Gen. 2 GA tank and inverter were the same as modeled for the previous tests of the Gen. 2 demonstrator as in Table 5.6.

The modeled efficiency is higher than the measured values at alignment, but matches well at the (10 cm, 0 cm) and (0 cm, 5 cm) alignments. However, at the (10 cm, 5 cm) alignment, the measured efficiency is higher than the modeled values. Future work could also be done to capture the cross-coupling of the ferrite loss, which is a nonlinear loss mechanism, from

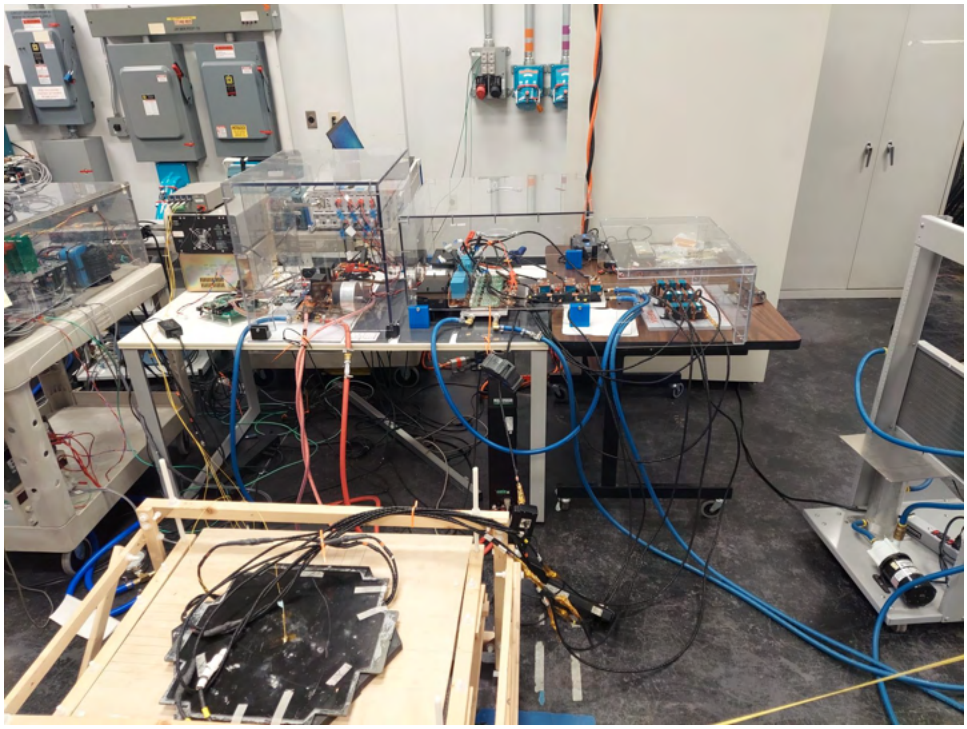

(a)

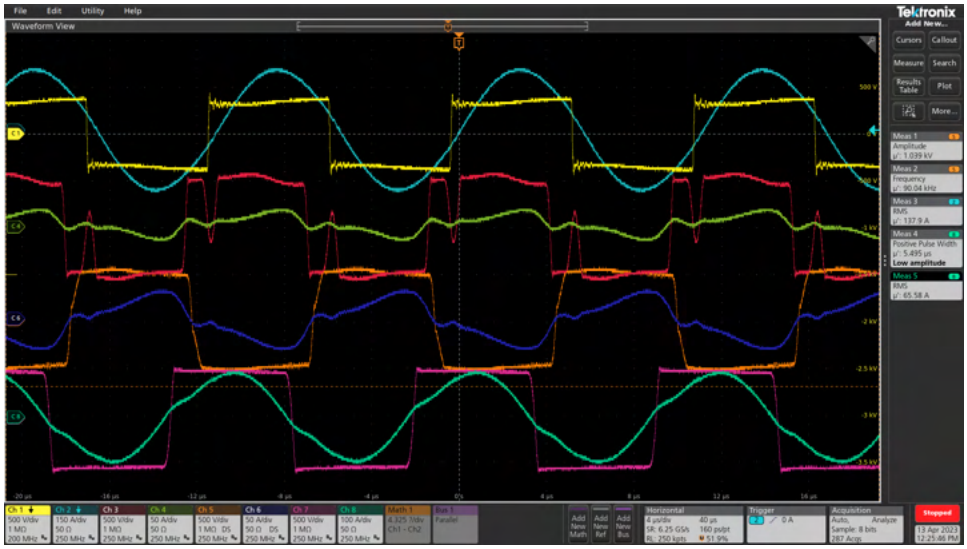

(b)

Figure 6.21: Test of the Gen. 2 coil as a GA with the ORNL 50 kW 3Φ Coil as the VA at 125 mm airgap. (a) Test setup with the inverter, rectifiers, and series capacitors. (b) Waveforms at 41.4 kW output power at (5 cm, 0 cm) alignment: GA inverter CH1 output voltage and CH2 current, VA X-winding CH3 voltage and CH4 current, VA Y-winding CH5 voltage and CH6 current, VA Z-winding CH7 voltage and CH8 current.

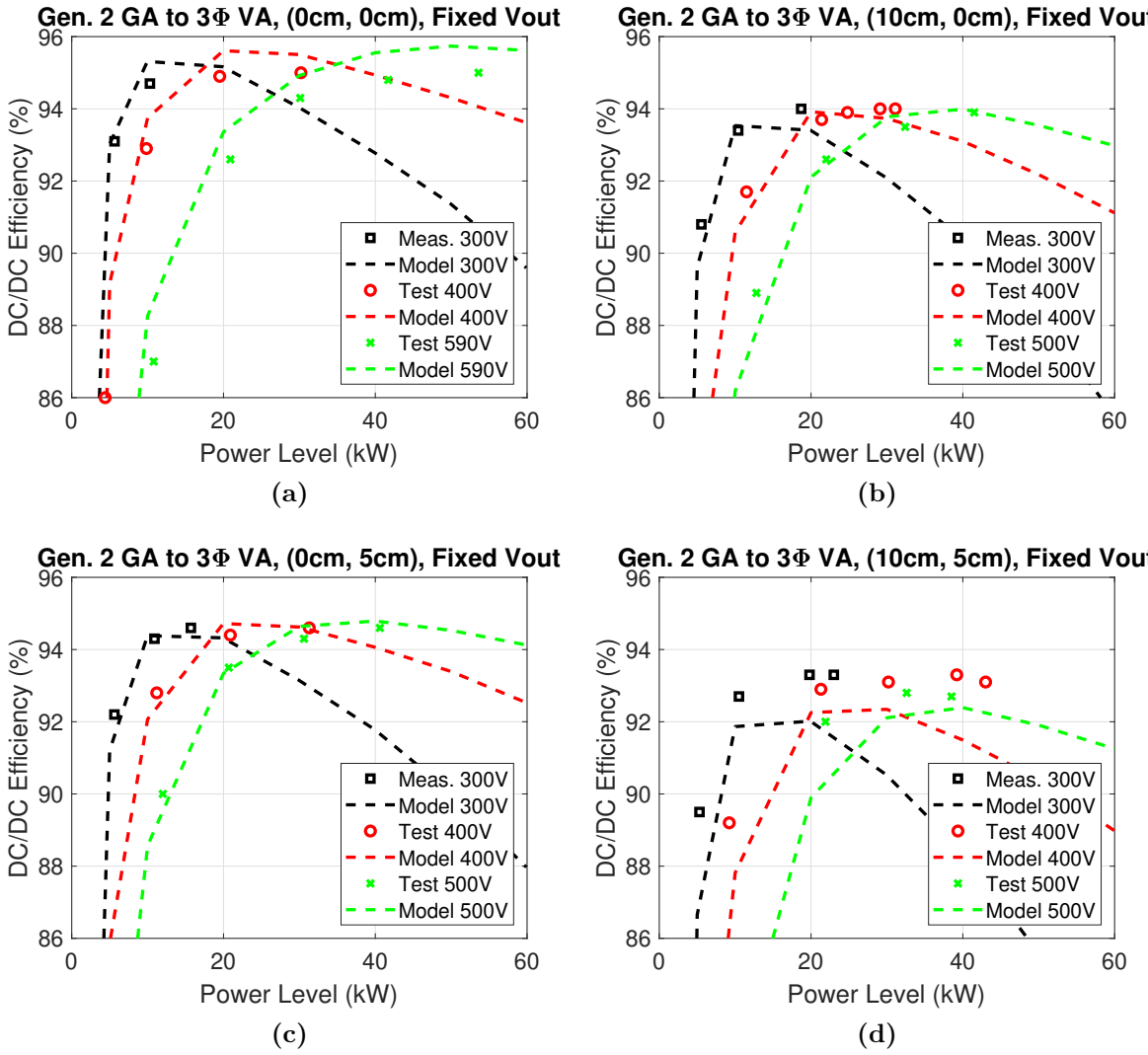

Figure 6.22: Tests of the Gen. 2 GA and 3Φ VA at different alignments compared to modeled values at fixed output voltages and an airgap of 125 mm. Output power vs. DC/DC efficiency at alignments of (a) (0 cm, 0 cm), (b) (10 cm, 0 cm), (c) (0 cm, 5 cm), and (d) (10 cm, 5 cm).

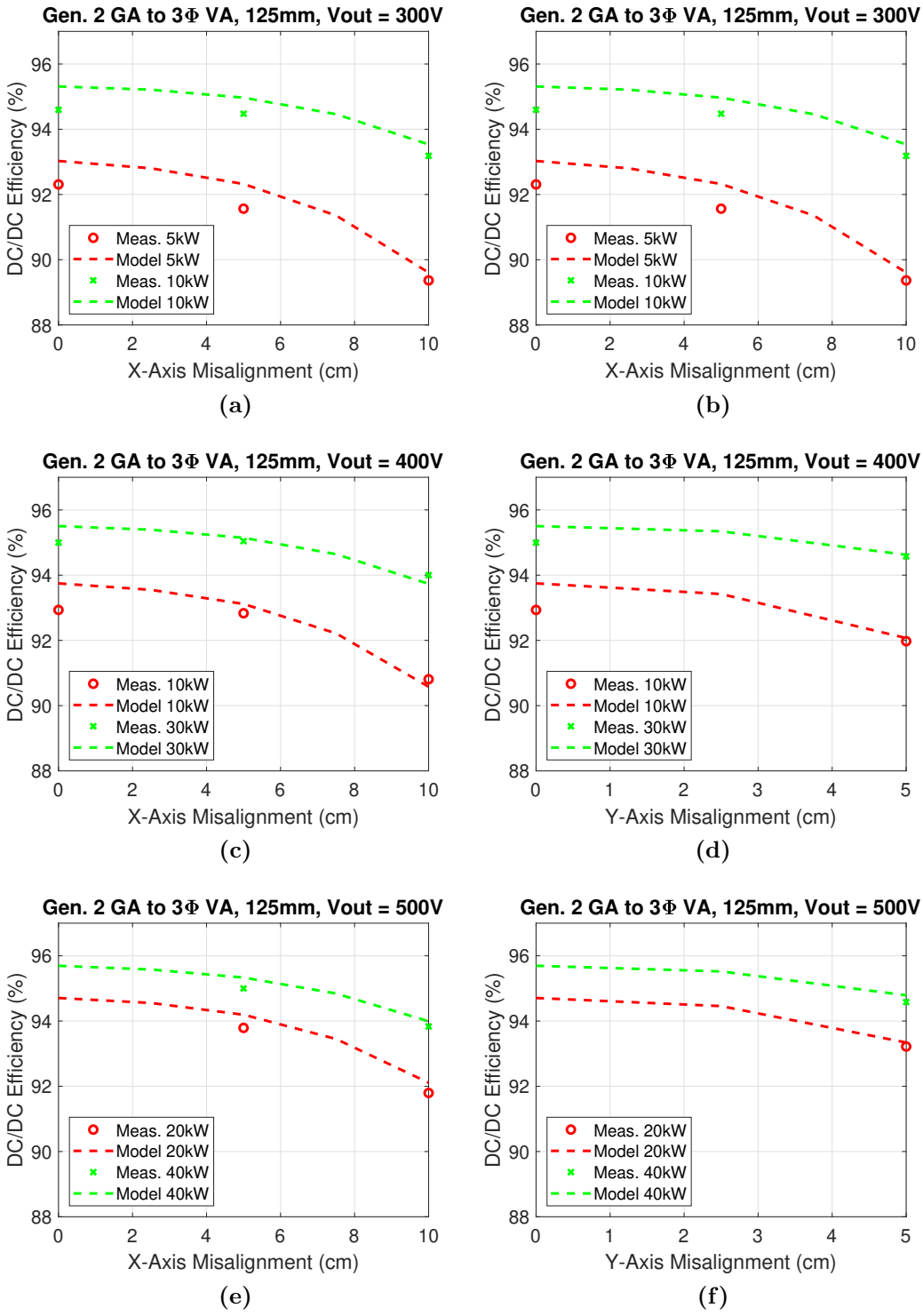

Figure 6.23: Interpolated measurements vs. models of the Gen. 2 GA and the ORNL 3Φ VA at constant power over alignment at fixed output voltages and an airgap of 125 mm. DC/DC efficiency at 300 V output over (a) X-misalignment and (b) Y-misalignment. DC/DC efficiency at 400 V output over (c) X-misalignment and (d) Y-misalignment. DC/DC efficiency at 500 V output over (e) X-misalignment and (f) Y-misalignment.

Table 6.8: Loss Model Parameter Values for the 50 kW 3Φ VA

Parameters		Value
Ferrite Steinmetz Parameters Ferroxcube 3C95 20 kHz-150 kHz		$\mu_r = 3000$ $C_m = 92.1\text{e-}3$ mW/cm^3 α =1.045; β =2.440 $C_t = 1.332$; $C_{t1} = 0.0079$; $C_{t2} = 4.62\text{e-}5$
Temperature of Ferrite		T_{fer} =19°C
Ferrite Thickness		VA, $t_{fer} = 5$ mm (all)
Litz Wire	Outer Diameter Number of Strands Strand Diameter Cabling Operations Wire Length	$d_{out} = 7.5$ mm $n = 2625$ $d_{str} = 0.1016$ mm $N_b = 2$ $N_c = 2$ $L_T = 8.0$ m
VA Lead Inductance and Resistance (Estimate from Measurement)		L_{lead} =5.6 µH, R_{lead} =60 mΩ, 89 kHz 260 mΩ, 267 kHz 608 mΩ, 445 kHz 1.125 Ω, 623 kHz 1.792 Ω, 801 kHz 2.588 Ω, 979 kHz
Rectifier Device Curve Fit BSM300D12P2E001 Module Diode		$V_f = 0.9$ V $R_f = 3$ mΩ
Heatsink (HS) Thermal Resistance Coolant (Liq.) Temperature		0.014 (HS/Liq.)+0.035 (Case/HS Rohm) °C/W 25°C
Copper Wire Resistivity at 20°C		ρ_{Cu} =1.724e-8 Ω-m
Temperature Coefficient, Copper		$C_{Cu,t}$ = +0.393 %/°C
Temperature of Copper		$T_{Cu} = 40$ °C
Gap Between Ferrite and Wire Planes		$z_g = 6.5$ mm

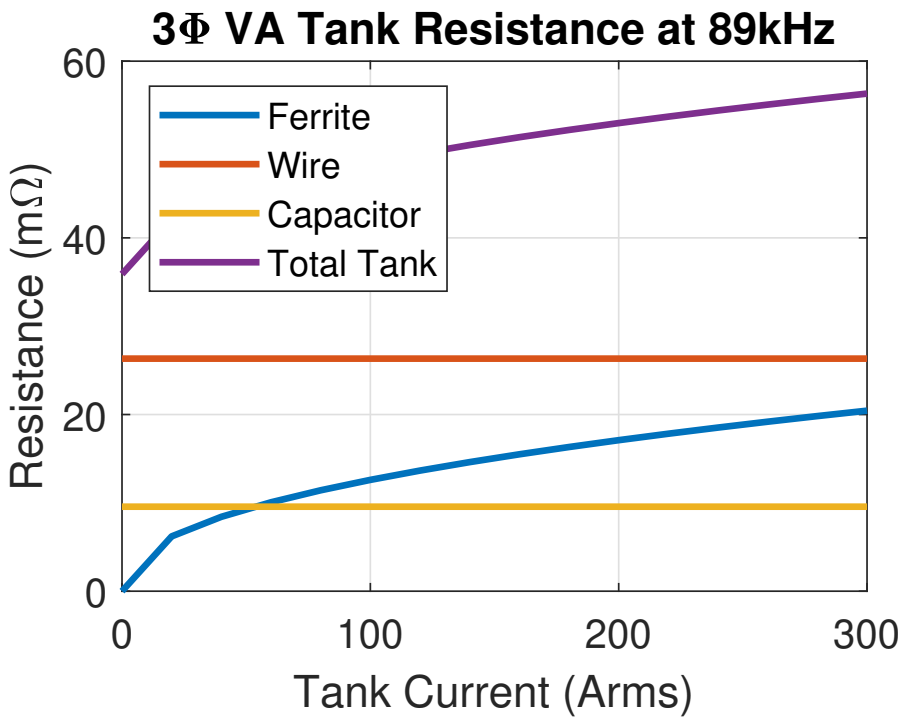

Figure 6.24: Modeled tank resistance of one of the windings of the 50 kW 3Φ VA without the lead resistance.

the three VA windings as well as the effect of additional resonances seen in the waveforms. In future work, integrating all of the phase-leg modules in a single DC-link and reducing the VA lead length of the system would likely further improve the efficiency of this setup. As seen, the models are able to predict the misalignment performance, inductance, and efficiency of the Gen. 2 GA and 50 kW 3Φ VA. This demonstrates the capability of FAM to import and model complex coil geometries and shows the applicability of the FAM modeling approach to the coil assemblies of other works.

6.4 Recommendations for Vehicular Implementation

In the previous sections, the analysis of the Gen. 2 proof-of-concept demonstrator and other related designs were analyzed for the target application of passenger electric vehicle fast charging. The interoperability of the Gen. 2 geometry with a variety of other geometries was analyzed, including initial experiments with a three-phase bipolar VA that produced a peak DC-DC efficiency over 95%. The current Gen. 2 demonstrator was limited over the over the target battery voltage and current range defined in Table 6.1 from 480 V to 800 V battery voltage with a power range up to 120 kW. Therefore, several modifications to the Gen. 2 demonstrator were proposed. Compensation network adaptation with detuned series-series or LCC compensation networks helped to extend soft-switching or the input impedance range, but was still limited by too low or too high input impedance over the range of coupling. Using a larger GA with the same size VA with different number of turns with series-series compensation improves the misalignment performance, but still suffered from low input impedance and high inverter currents with low coupling and higher DC-link voltages requiring the upgrade of the inverter. Finally, the performance of the current Gen. 2 demonstrator with an active rectifier or onboard DC/DC to match the load was analyzed, which requires the additional onboard cost and weight of a high power DC/DC converter.

Only two of the modeled implementation approaches explored enabled system operation over the target operating range: the geometry and inverter adaptation with the larger GA with the resized system and the addition of an onboard DC/DC or active rectifier. The comparison of the two approaches in terms of weight, complexity, stray field performance,

device ratings, and efficiency is given in Table 6.9. As seen, the resized system with a larger GA and upgraded inverter results in better efficiency at the cost of more active material weight, with the majority of the increase in weight on the GA. However, the increased stray field of the resized system with the larger GA and less shielded geometry requires additional shielding materials to meet the stray field limits in the higher airgap and misaligned conditions; otherwise, the power level would need to be limited in worst-case conditions. With the additional 80 cm x 80 cm x 5 mm ferrite sheet, the stray field at 120 kW at a 152.4 mm airgap at (10 cm, 5 cm) alignment is 8.71 µT on the X-axis and 23.20 µT on the Y-axis at 80 cm as in Table 6.6. This meets the ICNIRP 27 µT stray field limit, but not the 15 µT limit recommended for pacemaker compatibility. The power would need to be limited to around 50 kW to meet the 15 µT limit. This would require misalignment detection to determine when derating is necessary. In contrast, the Gen. 2 demonstrator with an onboard DC/DC has acceptable stray fields over the misalignment and airgap range.

The efficiencies of the two options are compared over a 120 kW fast charging cycle in Figure 6.25 and to commercial DC fast chargers in Table 6.10. The efficiency numbers for the DC fast chargers were found on manufacturers datasheets. Some manufacturers state the breakdown of losses of the front-end AC/DC rectifier and the isolated DC/DC stage and cable at the user unit, while others only specify the overall system efficiency. Assuming an onboard DC/DC stage like in [107] on the output of the Gen. 2 WPT system and a 98% front-end AC-DC rectifier, the Gen. 2 system has an efficiency 2-6% lower than the conductive fast charging systems. Some of this difference is caused by the assumed 98% to 99% efficiency of the onboard DC/DC, but most is due to the lower efficiency of around 92-96% of the Gen. 2 system relative to the 98.5% efficiency of the isolated DC/DC and the charging cable in the conductive systems. In comparison, the resized system with a larger GA is similar in efficiency to the conductive systems.

With better efficiency and no need for an onboard DC/DC with the resized system is the better option for vehicular implementation in the operating range defined in Table 6.1. The overall modeled performance capability of this implementation option is summarized in Table 6.11 and the arrangement is illustrated in Figure 6.26. The VA ferrite and litz weight of the resized system is 12.4 kg relative to 8.8 kg for the Gen. 2 system VA, or 40%

Table 6.9: Comparison of the Two Vehicular Implementation Options

Comparison Criteria	Gen. 2 System with Onboard DC/DC	Resized System with 1.7 kV Inverter and Extended Ferrite Shield
Ferrite and Litz Weight GA Coil Assembly	(40 cm×50 cm) Ferrite = 6.0 kg Litz Wire = 2.8 kg Total = 8.8 kg	(55 cm×70 cm) Ferrite = 37.0 kg Ferrite Shield = 6.1 kg Litz Wire = 4.5 kg Total = 47.6 kg
Ferrite and Litz Weight VA Coil Assembly	(40 cm×50 cm) Ferrite = 6.0 kg Litz Wire = 2.8 kg Total = 8.8 kg	(40 cm×50 cm) Ferrite = 9.8 kg Litz Wire = 2.6 kg Total = 12.4 kg
Onboard DC/DC Converter Weight	12 kg	
Capacitor Bank	GA = 12S-1 µF VA = 12S-1 µF Celem CSM150/300 (700V/450A)	GA = 10S-1 µF VA = 4S-1 µF Celem CSM150/300 (700V/450A)
Inverter Devices	2×CAS325M12HM2 1.2 kV, 325 A Modules	4×CAS380M17HM3 1.7 kV, 380 A Modules
DC/DC Eff. (WPT Stage) (0 cm, 0 cm) 125 mm 120 kW, 650 V Battery	95.4% (96.7%)	98.3%
DC/DC Eff. (WPT Stage) (10 cm, 5 cm) 152.4 mm 120 kW, 650 V Battery	91.2% (92.6%)	97.4%
Stray Field Mag. 80 cm (X, Y) (0 cm, 0 cm) 125 mm, 120 kW	1.87 µT, 1.36 µT	5.80 µT, 13.36 µT
Stray Field Mag. 80 cm (X, Y) (10 cm, 5 cm) 152.4 mm, 120 kW	7.77 µT, 6.93 µT	8.71 µT, 23.20 µT
Overall Pros	- Lower stray field - Lower material cost	- Higher efficiency - Fewer onboard components
Overall Cons	- Larger onboard weight and cost - Lower efficiency with misalignment	- Requires additional shielding material - More expensive inverter - Larger and more expensive GA

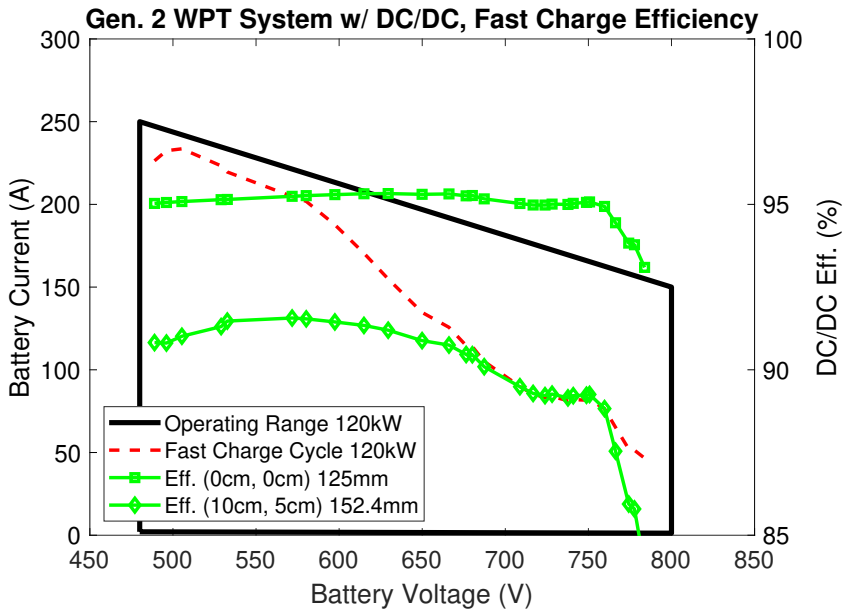

(a)

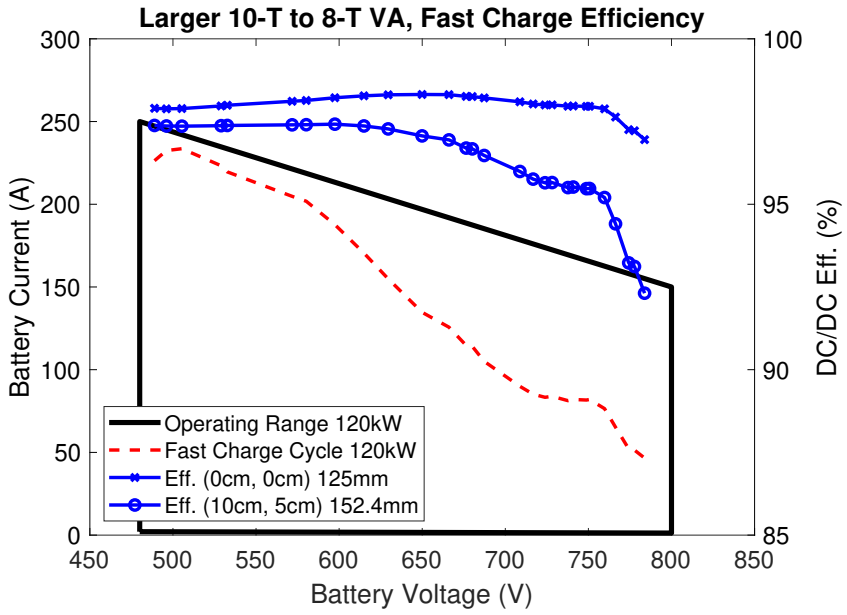

(b)

Figure 6.25: Charge profile efficiency at (0 cm, 0 cm) at 125 mm and (10 cm, 5 cm) at 152.4 mm for the (a) onboard DC/DC option with the Gen. 2 geometry and (b) larger GA with a less shielded geometry resized option.

Table 6.10: Comparison of the Two Modeled WPT Implementation Options with Commercially Available Conductive DC Fast Chargers (As of 2023 Q1)

	System Name	Rated Power	Front-End Eff.	Isolated DC/DC Eff. (WPT Stage)	Total Eff.
Commercial Conductive DC Fast Chargers	Delta City Charger 200 kW [108]	200 kW			96%
	Tritium PK350 [109]	350 kW	98%	98.5%	96.5%
	ABB Terra 184 [110]	180 kW			95%
	Siemens VersiCharge Ultra 175 [111]	178 kW	96%	98.5%	94.6%
	Siemens Sicharge D 300 Flex [112]	300 kW			96%
Modeled WPT Implementation Options	Gen. 2 System with Onboard DC/DC (0 cm, 0 cm) 125 mm 650 V Battery	120 kW	≈98%	95.4% (96.7%)	93.5%
	Gen. 2 System with Onboard DC/DC (10 cm, 5 cm) 152.4 mm 650 V Battery	120 kW	≈98%	91.2% (92.6%)	89.4%
	Resized System with 1.7 kV Inverter (0 cm, 0 cm) 125 mm 650 V Battery	120 kW	≈98%	98.3%	96.3%
	Resized System with 1.7 kV Inverter (10 cm, 5 cm) 152.4 mm 650 V Battery	120 kW	≈98%	97.4%	95.4%

more. However, the weight of the GA ferrite and litz wire of the resized system is 47.6 kg relative to 8.8 kg for the Gen. 2 system GA, or 441% more. With the larger ferrite and wire weight, the overall material costs for the resized system would be greater, but much of the difference is located on the GA side which is desirable for commercialization. The cost of the inverter will also increase with 4, higher-voltage 1.7 kV modules used for the resized system inverter relative to 2, 1.2 kV modules used for the Gen. 2 system. Significantly less onboard compensation capacitors are also needed with 4 for the resized system and 12 for the Gen. 2 system of the same Celem CSM150/300 package, or 66% less. The control for the resized system could also be located on the GA side as there are no active devices in the VA.

Summary

In this chapter, the modeled and measured performance of the 120 kW Gen. 2 demonstrator was mapped to an example EV fast charging application operating range. The system had a high peak efficiency in the range at matched loading at different alignments, but limited performance at some points in the operating range due to hard-switching and high input voltages and current. Methods to improve the performance of the current Gen. 2 demonstrator, as built and tested in this work, over the operating range were discussed including different compensation networks, changes to the geometry, turns, and size of the Gen. 2 coil demonstrator, and the use of an a onboard DC/DC converter or active rectifier. The interoperability of the Gen. 2 geometries to a variety of coil geometries was modeled showing the best coupling to other bipolar coil geometries followed by unipolar or circular or rectangular types. The applicability of FAM to import and model other types of arbitrary coil shapes was also demonstrated in modeling the interoperability of a Gen. 2 GA with a 50 kW three-phase bipolar VA. The modeling of the Gen. 2 GA and 50 kW three-phase bipolar VA was validated by experiments that included impedance, coupling, and efficiency measurements. Finally, the two options of adding a DC/DC converter to the Gen. 2 demonstrator or resizing the geometry and inverter were compared to provide recommendations for the vehicular implementation.

Table 6.11: Operating Range of the Resized System with a 1.7 kV Inverter

Performance Metric	Value
Power Rating	120 kW
Peak DC/DC Efficiency	98.4%, 125 mm (0 cm, 0 cm) 97.4%, 152.4 mm (10 cm, 5 cm)
Battery Voltage Range	480 V - 800 V
Airgap Range	125 mm - 152.4 mm
Inverter DC-Link Voltage Range	≤1350 V
X-Direction Misalignment	+/- 10 cm
Y-Direction Misalignment	+/- 5 cm
GA Dimension	55 cm x 70 cm with 80 cm x 80 cm x 5 mm Ferrite Shield
VA Dimension	40 cm x 50 cm
Maximum Stray Field at 80 cm	≤ 27 µT(rms)

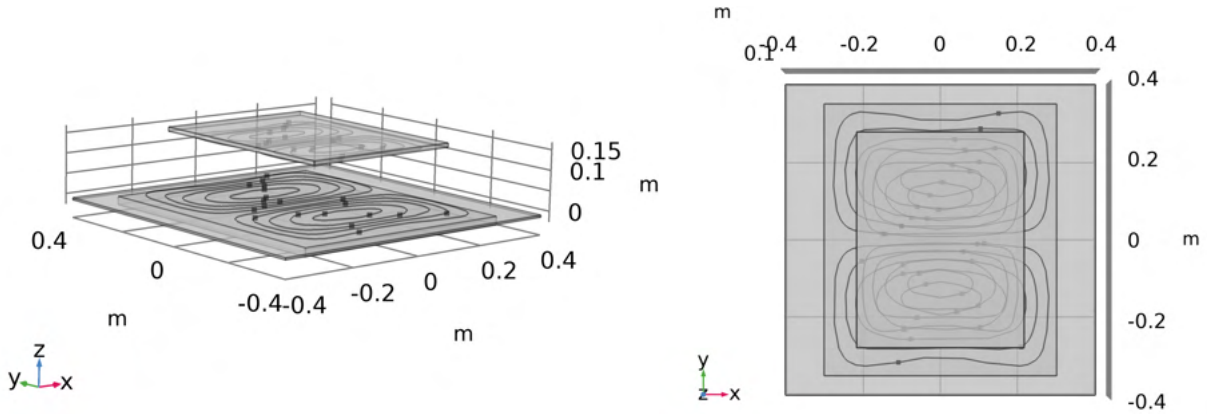

(a) **(b)**

Figure 6.26: Simplified illustration of the Resized System with an Extended Ferrite Sheet: (a) 3D profile at 152.4 mm airgap and (b) XY view.

Chapter 7

Conclusions and Future Work

7.1 Conclusions

In this dissertation, the modeling and validation of a design process for inductive wireless power transfer coils based on the Fourier Analysis Method (FAM) was detailed. Using this method, the fields, losses, and performance of a large variety of generalized coil shapes can be considered yielding flexibility and complexity beyond typical FEA-based design and evaluation methods. These models were used to explore the Pareto front of stray field and current requirements to produce geometries that are both efficient and meet applicable field limits. These geometries enable high-power wireless systems where low stray field and high-efficiency operation are critical. These were used to design and validate a 6.6 kW demonstrator and two 120 kW demonstrators. As part of the design and testing of the 120 kW demonstrators, several mechanical aspects of high-power WPT were also explored, including thermal design and modeling, the effects of encapsulation material residual stress on ferrite loss, and the implementation of indirect liquid cooling in two 120 kW WPT demonstrators. The tradeoff of cost, weight, and loss was also explored as part of the design process. The Gen. 2 120 kW demonstrator resulted in a measured 97.2% DC/DC efficiency at 120 kW output. The magnitude of the fields the center of the airgap at 80 cm at 120 kW output at alignment were very low at 3.4 µT and 3.5 µT on the X and Y axes, respectively. Further testing and modeling of this system for an EV fast charging application

highlighted the impact of widely varying output impedance and coupling on inverter soft-switching and overall system efficiency. To help improve performance over the operating range, the implementation of different compensation networks, different GA and VA sizes and turns, and an onboard DC/DC converter or active rectifier were considered. The FAM was also used to assess the interoperability of different types of geometries over misalignment. Lastly, the modeling and experimental validation of the interoperability of the Gen. 2 120 kW demonstrator and a bipolar multiphase coil was also performed to demonstrate the generality of FAM.

7.1.1 Contributions

In summary, the completed contributions of this work are as follows:

- Framework for the co-optimization of stray field and losses through Fourier Analysis encompassing a broader range of geometries including complex symmetric shapes
- New loss modeling methods built upon the generalized Fourier Analysis Method framework
- Thermal modeling and cooling implementation for high-power WPT coils in the Fourier Analysis Method framework
- Interoperability assessment of various coil geometries and sizes in the Fourier Analysis Method framework

7.2 Future Work

The realistic implementation of a high power inductive charger is complex and may require DC/DC stages to control the load of the wireless stage, additional control and communication, safety interlocks, foreign and live object detection, and vehicle coolant integration as illustrated in Figure 7.1. The system implementation must also consider worst-case scenarios like vandalism and negligence to successfully operate in public places. In this context, there are several avenues for future work on inductive charging as briefly

described in this section. These topics represent other aspects and extensions of this research that were not fully explored in this dissertation.

7.2.1 Further Cost and Weight Optimization

In the implementation of FAM for the 6.6 kW and 120 kW demonstrators, the optimization and selection of the ferrite material thicknesses and the litz wire types were done after the selection of the coil geometry. More work could be done to integrate these elements into the initial geometry selection. Additional cost and weight optimizations could be done to improve upon the aluminum backplate, capacitor bank, and other components of the Gen. 2 demonstrator for cost, weight, and manufacturability. Further consideration of mismatched coil sizes for GA and VA sizes could also be done, as the minimization of the VA size and cost is highly desirable and the initial analysis on the Gen. 2 demonstrator with larger GA sizes showed improved coupling and misalignment performance.

7.2.2 Compensation Component Optimization

In the 120 kW demonstrators, the compensation capacitor bank was conservatively designed and tested with 12 capacitors in series on the GA and VA. During testing, the external temperature of the polypropelene film resonant capacitors was monitored and kept below 45^{o}C per manufacturer recommendation, but higher temperatures with derating are allowed. There are other high-temperature capacitors available with higher rated temperatures. With temperature considerations and the wide range of compensation networks available, different designs of the capacitor banks or other resonant components for the GA and VA sides can also be considered. This is motivated by the different space, cost, weight, and cooling requirements for the GA and VA in most applications.

Integration of the design method with foil-based coils or other self-resonant coils could be done. The complex geometries shown in this work could be conveniently built using well-established manufacturing processes similar to those of PCB fabrication rather than being wound manually with litz wire. This would also eliminate the need for additional capacitor

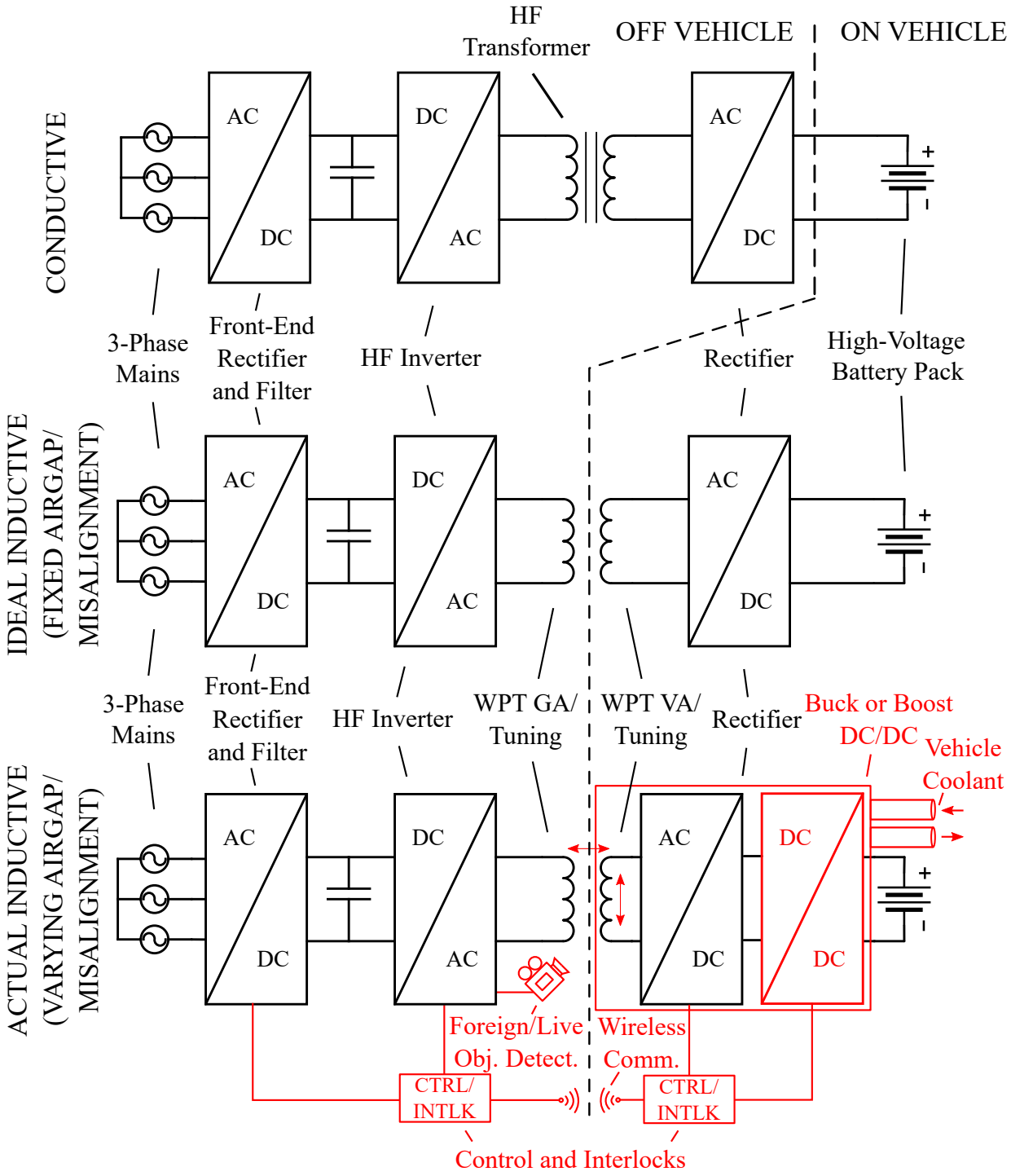

Figure 7.1: Block diagram of a typical conductive fast-charger with an isolated DC/DC converter compared to a simplified and more realistic wireless fast-charging system. Here, several practical considerations for the implementation of a wireless charging system are shown in red including an onboard buck or boost DC/DC, vehicle coolant integration, wireless communication, foreign object detection, and additional control and interlocks.

banks and may further reduce the cost and weight as shown in other works. The thermal analysis of high-power self-resonant coils is another area of focus.

7.2.3 High Temperature Operation and Mechanical Design

Thermal effects were considered in the design of indirect liquid cooling of the Gen. 1 and Gen. 2 120 kW demonstrators. Further improvements to this implementation, such as the encapsulation material, the coil enclosure, and the former, may be made with this in mind. However, other mechanical aspects of the system must be pursued to further maturity. On the GA side, water ingress and tire loads are of concern, but the system is not as constrained by space, weight, or cooling. On the VA side, weight, cost, and cooling capacity become critical as well as surviving vibration, impacts, and a variety of other factors. High temperature capability for VA is necessary, as traction and motor cooling loops with coolant temperatures exceeding 45^{o}C are typical in EVs. Therefore, designing and testing VAs to perform at elevated coolant temperatures is necessary in future research and design.

7.2.4 Tradeoff Analysis of Single Phase and Polyphase Coil Geometries

As demonstrated, there is a tradeoff in the stray field and misalignment performance of coil geometries. The Gen. 2 demonstrator of this work demonstrated experimentally that a high-power system with high efficiency and low stray field is possible, but this came at the cost of reduced misalignment and airgap performance. The Fourier Analysis Method is a useful tool in navigating this Pareto front and the power level breakpoint for single phase geometries: rectangular coils, bipolar coils, or even quadrupole coils may vary as a function of the airgap, stray field requirements, and coil dimension.

As an example, the FAM optimization outputs of Figure 5.3 used in the generation of the Gen. 2 geometry can also be normalized to coil-coil power level and constrained by a constant stray field limit at 80 cm at the middle of the airgap as in Figure 7.2. This plot calculates the maximum mid-airgap stray field at the original stray field extents of $x_{ext} = y_{ext}$ =60 cm or a radius of 30 cm, doubles this value to represent the combined fields of the GA and

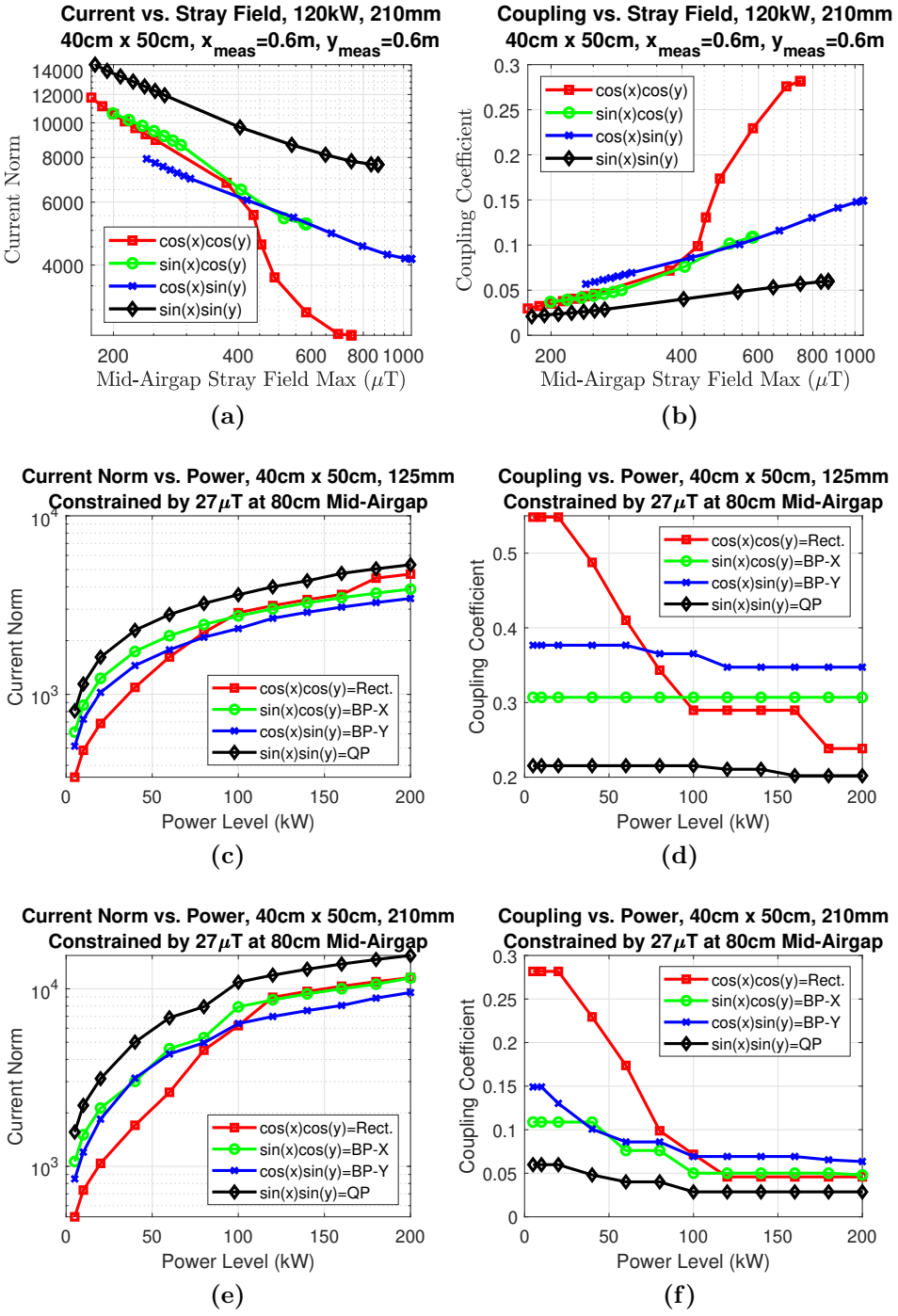

Figure 7.2: Tradeoff analysis of the 40 cm x 50 cm single-phase geometries as a function of power level when constrained by a constant stray field at 80 cm. (a) Current vs. stray field and (b) coupling vs. stray field at mid-airgap at $x_{ext} = y_{ext} = 60$ cm at 120 kW and 210 mm. (c) Current norm and (d) coupling vs. power level at a 125 mm airgap. (e) Current norm and (f) coupling vs. power level at a 210 mm airgap.

VA at the peak value, and divides this by the square root of two to derive the RMS value. The dipole approximation is then used to predict the fields at 80 cm as a ratio of the cube of 30 cm and 80 cm. For each power level and basis function set, the power-normalized stray field at 80 cm is calculated and the output with minimum current under the constant stray field of 27 µT(rms) is selected. This example considers only the aligned condition. The sweep is plotted for both a 125 mm airgap and a 210 mm airgap. For lower power levels, the geometries are less constrained by stray field, and geometries with high coupling such as the rectangular or circular geometries have the highest coupling. As the power level increases, more shielded geometries with less coupling begin to be used for all geometries and bipolar geometries begin to have the highest coupling beyond around 75 kW for the 125 mm airgap or 100 kW for the 210 mm airgap. The power levels will scale downward if the analysis is repeated for lower stray field limits, such as the 15 µT(rms) limit proposed by the American Association of Medical Instrumentation (AAMI) for pacemaker compatibility or the ICNIRP 1998 magnetic field limit of 6.25 µT(rms) still used in some standards [24].

At some point in this sweep of the power level, instead of using single-phase shielded geometries with less coupling, it may be beneficial instead to use polyphase designs such as in [41] with each phase geometry operating at a lower power level and less limited by the stray field. At the 210 mm airgap for the set of parameters in this example, this may occur around 75 kW where the coupling coefficient of the rectangular coils is around 0.1 while coupling of the 25 kW bipolar in the Y-direction (BP-Y) geometry is around 0.125.

The extension of the FAM to polyphase coil geometries was briefly considered in this work, but more can be done. The integration of shielded bipolar coil geometries generated by FAM for multilayer polyphase coils is clearly possible. The spans and extents of each of the phases can be put into similar optimization as done in this work with non-rectangular boundaries such as mirrored circular sectors. Using shielded coil geometries for each phase would likely reduce the stray field of the overall system during polyphase or single-phase operation.

7.2.5 Active Rectification/Bidirectional Power Transfer

It is possible to enable bidirectional power transfer from the VA to the GA with active devices on the VA. This would enable vehicle to home or vehicle to grid operation similar to that which is becoming available in conductive chargers. The operation of the VA devices as an inverter and the compensation must be considered for this application and leads to many possible degrees of freedom. With active devices on the VA and enough control capability, active rectification becomes possible to extend soft-switching along with other capabilities if an on-board DC/DC is applied. Some hard-switching may also be allowable with SiC inverters. For vehicle to grid operation, the grid interface converter can be used similarly to control the voltage and equivalent load of the GA DC-link.

7.2.6 Geometry Co-Optimization with Shielding Materials

The placement and arrangement of aluminum and ferrite extents in coil assemblies have been shown to effect stray field and efficiency. Due to the emphasis on FAM-generated shielded coil geometries and compact coil assemblies, these topics were not introduced in the design of the demonstrators of this work. Future exploration of the interaction of different coil shapes and conductive materials and magnetic shielding materials may be done to improve efficiency, stray field, cost, or weight.

As an example of the impact of different shielding materials on stray field, the geometries of the 120 kW Gen. 2 demonstrator, a bipolar and rectangular coil are used as three examples to briefly assess the effect of shielding materials. These geometries are summarized in Figure 7.3. These three geometries represent the shielded bipolar coil of this work and conventional unshielded bipolar and rectangular coil geometries. Following the approach of [40, 103], the stray field at alignment at a 150 mm airgap is simulated in FEA in the baseline case with a 42 cm × 54 cm ferrite shield, with a 1 m × 1 m × 0.7 mm aluminum VA shield behind the 42 cm × 54 cm ferrite, and a 0.6 m × 0.6 m × 5 mm GA ferrite shield. In each case, the coil-coil power transfer is set to 120 kW with fixed GA and VA current from the mutual inductance of the baseline case, and the stray field is modeled on the X and Y axes in the middle of the airgap at 80 cm. The number of turns of the bipolar and

rectangular coils was chosen to have similar mutual inductance at alignment to the Gen. 2 system, resulting in similar coil current. The quality factor $Q = \omega L/(R_{11} + R_{fer})$, where R_{11} is the total AC resistance of the coil and R_{fer} is the equivalent ferrite resistance normalized to the coil current, was calculated using the FAM loss models of this work with the same 4 AWG litz wire of 42 AWG stranding as the wire and a constant ferrite thickness of 3C95 ferrite of 1 cm. Using the quality factor, the maximum coil-coil efficiency can be calculated as in Section 5.3,

$$\eta = \frac{k^2Q^2}{\left(1 + \sqrt{1 + k^2Q^2}\right)^2} \approx 1 - \frac{2}{kQ}. \tag{7.1}$$

The results of these simulations are summarized in Table 7.1. Here, the bipolar and rectangular coils have a significantly larger stray field, but higher coupling than the Gen. 2 coils. As also observed in [40, 103], the rectangular coil stray field is reduced by the aluminum VA shield but increases with the GA ferrite shield. Conversely, the bipolar coil stray field is not effectively shielded by the aluminum VA shield, but is reduced by the GA ferrite shield. The Gen. 2 coil, which is a bipolar geometry, follows a pattern similar to the simple bipolar coil. The modeled fields of the baseline Gen. 2 system at a 150 mm airgap are slightly above the measured fields at a 125 mm airgap in Table 5.13.

As shown, placing shielding materials around the coil assemblies greatly impacts the stray field depending on the material and type of geometry. However, even with the shielding materials in place, conventional geometries may still exceed the stray field standards such as the 15 µT(rms) or 27 µT(rms) standards mentioned in Section 1.3.2. With the Gen. 2 shielded coil design, the additional stray field reduction from the GA ferrite shield is not needed as the fields are already well below the standards at 3.4 µT and 3.5 µT on the X and Y axes, respectively. However, the additional shielding comes at the cost of coupling and misalignment performance such that the maximum coil to coil efficiency drops to 95.8% at the (10 cm, 7.5 cm) alignment leading to even lower DC/DC efficiency. Therefore, including the reduction of the stray field by additional shielding materials in future work may relax the stray field constraints in the FAM optimization or geometry selection, allowing less shielded geometries with higher coupling, efficiency, and misalignment tolerance under the stray field limits. From an efficiency perspective, the system should meet the field limits and EMI

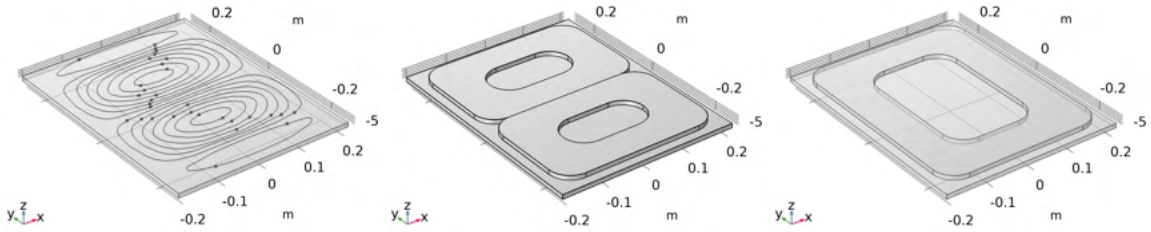

(a) (b) (c)

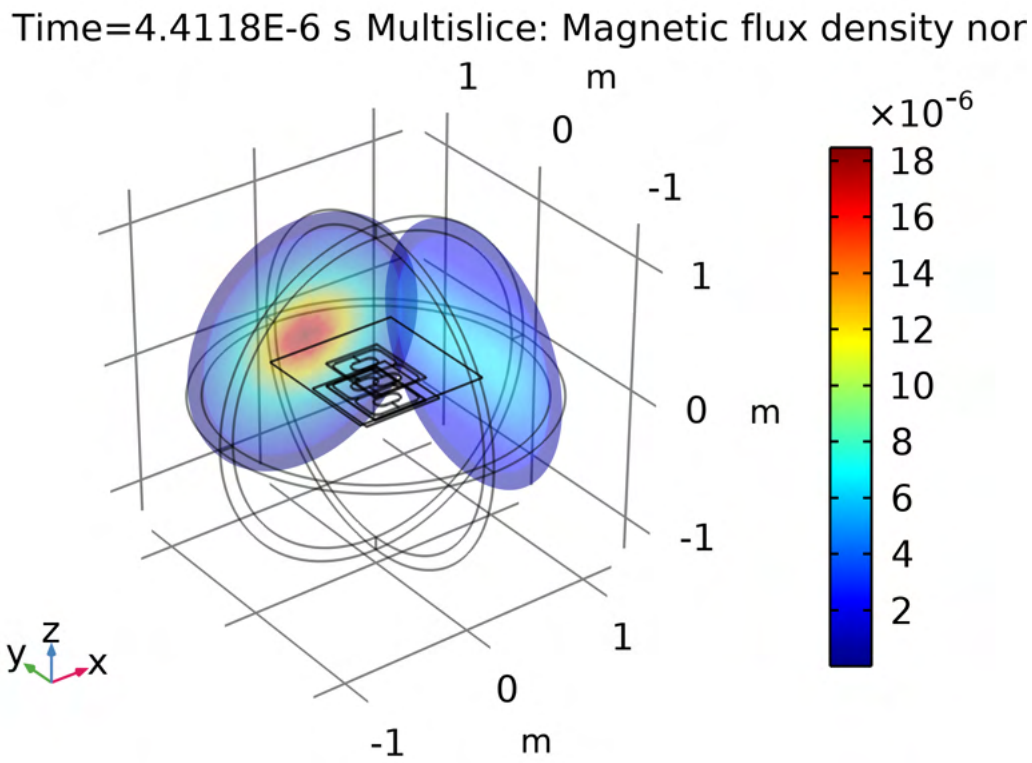

(d)

Figure 7.3: The three geometries used in the stray field comparison with 42 cm × 54 cm ferrite dimensions: (a) The Gen. 2 geometry, which is the $\cos x \sin y$, $B_{str,avg}$ =100 µT output with 14 turns. (b) The conventional bipolar geometry derived with FEA software. (c) The conventional rectangular geometry derived with FEA software. (d) A FEA simulation of the bipolar coil with both the VA aluminum shield and the GA ferrite shield.

Table 7.1: Comparison of Modeled Coupling, Quality Factor, and RMS Stray Field Magnitude (X, Y) Mid-Airgap at 80 cm with a 150 mm Airgap and 85 kHz with Shielding Materials at a 120 kW Coil-Coil Power Level

(0 cm, 0 cm) Alignment			
	Gen. 2 Geometry 14-turn	Bipolar/DD 10-turn	Rectangular 5-turn
Self-Ind. Mut. Ind. (k) Coil Current (RMS) Mod. Resistance (Q) Equivalent k^2Q^2 Eff.	39.4 µH 5.8 µH (0.147) 197.2 A 27.9 mΩ (756) 98.2%	29.9 µH 7.5 µH (0.251) 173.2 A 18.3 mΩ (873) 99.1%	23.8 µH 7.6 µH (0.315) 172.4 A 16.4 mΩ (774) 99.2%
Baseline	3.25 µT, 3.56 µT	6.30 µT, 14.84 µT	32.01 µT, 35.60 µT
Alum. VA Shield 1 m × 1 m × 0.7 mm	3.17 µT, 3.84 µT	6.41 µT, 15.81 µT	13.09 µT, 15.51 µT
Ferrite GA Shield 0.6 m × 0.6 m × 5 mm	2.00 µT, 2.55 µT	4.28 µT, 11.50 µT	34.38 µT, 36.95 µT
(10 cm, 7.5 cm) Alignment			
	Gen. 2 Geometry 14-turn	Bipolar/DD 10-turn	Rectangular 5-turn
Self-Ind. Mut. Ind. (k) Coil Current (RMS) Mod. Resistance (Q) Equivalent k^2Q^2 Eff.	39.3 µH 2.6 µH (0.065) 296.3 A 29.0 mΩ (724) 95.8%	29.8 µH 4.4 µH (0.147) 226.5 A 18.9 mΩ (844) 98.4%	23.9 µH 4.9 µH (0.206) 213.5 A 17.0 mΩ (753) 98.7%
Baseline	9.76 µT, 10.13 µT	14.93 µT, 29.53 µT	53.90 µT, 57.40 µT
Alum. VA Shield 1 m × 1 m × 0.7 mm	10.30 µT, 10.16 µT	14.63 µT, 33.77 µT	40.20 µT, 40.87 µT
Ferrite GA Shield 0.6 m × 0.6 m × 5 mm	6.30 µT, 7.37 µT	10.39 µT, 24.58 µT	54.31 µT, 59.41 µT

limits at the worst-case airgap, alignment, and loading at peak power by a small margin. Otherwise, the geometry may be less coupled than needed with lower overall efficiency. In addition, in the integration of many wireless chargers into vehicles the distance to the edge or front of the vehicle may be greater than 80 cm leading to less need for shielding in the geometry design.

7.2.7 Extensions of the Fourier Analysis Method

This work produced an 120 kW optimized shielded coil with aggressive area-related power density, high aligned efficiency, and very low stray field. However, system performance suffered with mismatched loading conditions, misalignment, and operation at different airgaps as summarized in Chapter 6. This highlights several opportunities to extend the approach of this work:

- The effect of misalignment, different airgaps, and mismatched loading on system performance was clearly seen in the demonstrators developed in this work. Therefore, including the worst-case analysis in the optimization and selection of the coil geometry is needed earlier in the FAM design process. The use of an active rectifier or onboard DC/DC converter should be considered in the selection of the number of turns. For example, if a buck is used on the output, the turns should be chosen to increase the output voltage of the system based on the gain and performance of the buck stage so that the wireless stage can operate at the highest efficiency at optimal loading over more of the operating area and possible output voltages. Compensation networks such as LCC-LCC or LCC-S tuning also need to be considered in an earlier step.

- FAM optimization could be used to design coil geometries with more constant coupling over misalignment. This would likely produce coils with lower peak coupling and efficiency, but the problems related to the change in coupling would decrease. For example, this might be accomplished by modifying the optimization to limit the variation in the field or coupling at a given airgap over the misalignment range.

- The FAM optimization and design of this work was done with matched GA and VA sizes and numbers of turns. In practice, GAs and VAs have very different requirements in

terms of cooling, cost, and weight and the initial size of the GA and VA couplers selected for the FAM optimization and their designs will likely be different. For example, different battery voltage ranges and airgaps may necessitate the design of different VA variants to work with the same universal GA. Integration of the thermal models and loss models of this work could also limit thermal hotspots or magnetic flux concentrations in the optimization.

Overall, this work has shown that Fourier Analysis is a useful analytical tool to optimize and design inductive wireless power transfer coil assemblies, as it has been for other magnetic components. It is a way to generate, optimize, and include a large number of complex, symmetric coil geometries that are otherwise not usually considered with FEA or other analytical design methods. It can also be used to analyze existing geometries as has been shown in previous works. It is the hope of this author that this work, alongside the many others in this research area, will help to improve wireless charging to help it become a convenient and practical way of powering electric vehicles as they continue to be produced and adopted.

List of Publications

Parts of the research presented in this work have been published or may be published in conference proceedings or journals. These and other previous publications and co-authorships not covered in this work are listed below.

Journal Papers

- A. Foote, D. Costinett, R. Kusch, M. Mohammad, and O. Onar, "Fourier analysis and loss modeling for inductive wireless electric vehicle charging with reduced stray field," Resubmitted, *IEEE Transactions on Transportation Electrification*, 2023.

- A. Foote, D. Costinett, R. Kusch, M. Mohammad, and O. Onar, "Fourier analysis and design of a 120kW inductive wireless system," To be submitted, *IEEE Transactions on Power Electronics*, 2023.

Conference Papers

- A. Foote, D. Costinett, R. Kusch, J. Pries, M. Mohammad, and B. Ozpineci, "Fourier analysis method for wireless power transfer coil design," in *2020 IEEE 21st Workshop on Control and Modeling for Power Electronics (COMPEL)*, 9-12 Nov. 2020, pp. 1-8.

- A. Foote, D. Costinett, W. Henken, R. Kusch, M. Mohammad, and O. Onar, "Encapsulation residual stress and ferrite loss in inductive coil assemblies." Accepted to *2023 IEEE Energy Conversion Conference and Expo (ECCE)*.

Patent Applications

- A. Foote, "Generating coil geometries for wireless power transfer system," United States Patent Application No. 17/061,067, Filed October 1st, 2020.
- A. Foote, D. Costinett, "Devices, systems, and methods for wireless vehicle charging," United States Patent Application No. 18/076,052, Filed December 6th, 2022.

Other Publications and Co-Authorships

- A. Foote, B. Ozpineci, M. Chinthavali, and J. M. Li, "Sizing dynamic wireless charging for light-duty electric vehicles in roadway applications," in *2016 IEEE PELS Workshop on Emerging Technologies: Wireless Power Transfer (WoW)*, 4-6 Oct. 2016, pp. 224-230.
- A. Foote and O. C. Onar, "A review of high-power wireless power transfer," in *2017 IEEE Transportation Electrification Conference and Expo (ITEC)*, 22-24 June 2017, pp. 234-240.
- D. Honorio, L. H. S. C. Barreto, A. Foote, B. Ozipineci, and J. O. P. Pinto, "Modular transformer in isolated multiport power converters," in *2017 IEEE Southern Power Electronics Conference (SPEC)*, 4-7 Dec. 2017, pp. 1-5.
- S. Debnath, A. Foote, O. C. Onar, and M. Chinthavali, "Grid impact studies from dynamic wireless charging in smart automated highways," in *2018 IEEE Transportation Electrification Conference and Expo (ITEC)*, 13-15 June 2018, pp. 950-955.
- A. Foote, O. C. Onar, S. Debnath, M. Chinthavali, B. Ozpineci, and D. E. Smith, "Optimal sizing of a dynamic wireless power transfer system for highway applications," in *2018 IEEE Transportation Electrification Conference and Expo (ITEC)*, 13-15 June 2018, pp. 1-6.

- A. Foote, O. C. Onar, S. Debnath, J. Pries, V. P. Galigekere, and B. Ozpineci,"System design of dynamic wireless power transfer for automated highways," in *2019 IEEE Transportation Electrification Conference and Expo (ITEC)*, 19-21 June 2019, pp. 1-5.

- Y. Yan, H. Bai, A. Foote, and W. Wang, "Securing full-power-range zero-voltage switching in both steady-state and transient operations for a dual-active-bridge-based bidirectional electric vehicle charger," *IEEE Transactions on Power Electronics*, vol. 35, no. 7, pp. 7506-7519, 2020.

- Y. Huang, J. Walden, A. Foote, H. Bai, D. Lu, F. Jin, B. Cheng, "Analytical characterization of CM and DM performance of three-phase voltage-source inverters under various PWM patterns," *IEEE Transactions on Power Electronics*, vol. 36, no. 4, pp. 4091-4104, 2021.

Bibliography

[1] IEA, "Global EV outlook 2020/2022," report, International Energy Agency, 2020, 2022. xiv, 1, 2, 3

[2] D. Oreizi, "31 countries and U.S. states with gas car bans." https://www.chargedfuture.com/countries-and-states-with-gas-car-bans/, 2020. 1

[3] A. Tomaszewska, Z. Chu, X. Feng, S. O'Kane, X. Liu, J. Chen, C. Ji, E. Endler, R. Li, L. Liu, *et al.*, "Lithium-ion battery fast charging: A review," *ETransportation*, vol. 1, p. 100011, 2019. 2

[4] D. Howell, S. Boyd, B. Cunningham, S. Gillard, L. Slezak, S. Ahmed, I. Bloom, A. Burnham, K. Hardy, and A. N. Jansen, "Enabling fast charging: A technology gap assessment," report, US Department of Energy,, October 2017. xiv, 2, 3, 4, 27

[5] Transport Research Laboratory, "Feasibility study: Powering electric vehicles on England's major roadways," report, Highways England, 2015. 2

[6] Dalroad, "An introduction to electric vehicle rapid charging standards." https://www.dalroad.com/resources/an-introduction-to-electric-vehicle-rapid-charging-standards/, 2021. 2

[7] Electrify America, "Electrify America." https://www.electrifyamerica.com/, 2021. 2, 4, 8

[8] A. Foote, O. C. Onar, S. Debnath, J. Pries, V. P. Galigekere, and B. Ozpineci, "System design of dynamic wireless power transfer for automated highways," in *2019 IEEE Transportation Electrification Conference and Expo (ITEC)*, pp. 1–5, 2019. 2, 4

[9] CharIN, "CharIN whitepaper: Megawatt charging system (MCS)." https://www.charin.global/technology/mcs/, 2022. 2

[10] H. Tu, H. Feng, S. Srdic, and S. Lukic, "Extreme fast charging of electric vehicles: A technology overview," *IEEE Transactions on Transportation Electrification*, vol. 5, no. 4, pp. 861–878, 2019. 4, 17, 187

[11] P. Beck, "Top circuit protection considerations for DC fast chargers, a new class of high-voltage consumer electronics," *Charged Electric Vehicles Magazine*, April 2021 2019. 4

[12] A. Foote and O. C. Onar, "A review of high-power wireless power transfer," in *2017 IEEE Transportation Electrification Conference and Expo (ITEC)*, pp. 234–240, 2017. 4, 8

[13] C. C. Mi, G. Buja, S. Y. Choi, and C. T. Rim, "Modern advances in wireless power transfer systems for roadway powered electric vehicles," *IEEE Transactions on Industrial Electronics*, vol. 63, no. 10, pp. 6533–6545, 2016. 6, 8

[14] D. Patil, M. K. McDonough, J. M. Miller, B. Fahimi, and P. T. Balsara, "Wireless power transfer for vehicular applications: Overview and challenges," *IEEE Transactions on Transportation Electrification*, vol. 4, no. 1, pp. 3–37, 2018. 6

[15] Momentum Dynamics, "Momentum Wireless Power." https://momentumdynamics.com/, 2019. 6, 7

[16] V. P. Galigekere, J. Pries, O. C. Onar, G. Su, S. Anwar, R. Wiles, L. Seiber, and J. Wilkins, "Design and implementation of an optimized 100 kW stationary wireless charging system for EV battery recharging," in *2018 IEEE Energy Conversion Congress and Exposition (ECCE)*, pp. 3587–3592, 2018. 6, 19, 21, 24, 27

[17] K. Askley, "ORNL demonstrates 120-kilowatt wireless charging for vehicles." https://www.ornl.gov/news/ornl-demonstrates-120-kilowatt-wireless-charging-vehicles, October 2018. 6

[18] J. M. Miller, A. W. Daga, F. J. McMahon, P. C. Schrafel, B. Cohen, and A. W. Calabro, "A closely coupled and scalable high power modular inductive charging system for vehicles," *IEEE Journal of Emerging and Selected Topics in Power Electronics*, pp. 1–1, 2020. 7, 28

[19] Wireless Advanced Vehicle Electrification (WAVE), "A future of electric vehicles with unlimited range." https://waveipt.com/

wave-provides-a-glimpse-into-a-visionary-future-of-electric-vehicles-with-unlimited-range/, 2020. 7

[20] Sustainable Bus, "Wireless charging in the spotlight: IPT Group takes over Primove from Bombardier." https://www.sustainable-bus.com/news/ipt-group-primove-wireless-charging/, April 2021. 7

[21] M. Yilmaz and P. T. Krein, "Review of battery charger topologies, charging power levels, and infrastructure for plug-in electric and hybrid vehicles," *IEEE Transactions on Power Electronics*, vol. 28, no. 5, pp. 2151–2169, 2013. 8

[22] R. Bosshard, *Multi-objective optimization of inductive power transfer systems for EV charging*. Thesis, ETH Zurich, 2015. 8, 18, 19, 24, 26, 73, 110, 171, 206

[23] H. Feng, R. Tavakoli, O. C. Onar, and Z. Pantic, "Advances in high-power wireless charging systems: Overview and design considerations," *IEEE Transactions on Transportation Electrification*, vol. 6, no. 3, pp. 886–919, 2020. 8

[24] Society of Automotive Engineers, "J2954: Wireless power transfer for light-duty plug-in/electric vehicles and alignment methodology," 2022. 8, 9, 10, 11, 12, 23, 119, 209, 239

[25] Society of Automotive Engineers, "J2954/2: Wireless power transfer for heavy-duty electric vehicles," 2022. 8

[26] J. Schneider, R. Carlson, J. Sirota, R. Sutton, E. Taha, M. Kesler, K. Kamichi, I. Teerlinck, H. Abeta, and Y. Minagawa, "Validation of wireless power transfer up to 11kW based on SAE J2954 with bench and vehicle testing," *SAE Technical Paper*, vol. 2019-01-0868, no. 0148-7191, 2019. 9, 28, 30

[27] International Commission on Non-Ionizing Radiation Protection, "Guidelines for limiting exposure to time-varying electric and magnetic fields (1 Hz to 100 kHz)," *Health physics*, vol. 99, no. 6, pp. 818–836, 2010. 9, 12, 163, 183

[28] V. X. Thai, G. C. Jang, S. Y. Jeong, J. H. Park, Y. S. Kim, and C. T. Rim, "Symmetric sensing coil design for the blind-zone free metal object detection of a stationary wireless electric vehicles charger," *IEEE Transactions on Power Electronics*, pp. 1–1, 2019. 11, 14

[29] F. Grazian, W. Shi, J. Dong, P. Duijsen, T. B. Soeiro, and P. Bauer, "Survey on standards and regulations for wireless charging of electric vehicles," in *2019 AEIT International Conference of Electrical and Electronic Technologies for Automotive (AEIT AUTOMOTIVE)*, pp. 1–5, 2019. 13

[30] IEC, "IEC 61980-1: Electric vehicle wireless power transfer (WPT) systems - Part 1: General requirements," July 2015. xiv, 13, 14

[31] IEC, "CISPR 11: Industrial scientific and medical equipment - Radio-frequency disturbance characteristics - Limits and methods of measurement," June 2016. 13

[32] J. W. Kolar and T. Friedli, "The essence of three-phase PFC rectifier systems—Part I," *IEEE Transactions on Power Electronics*, vol. 28, no. 1, pp. 176–198, 2013. 13

[33] J. Dai and D. C. Ludois, "A survey of wireless power transfer and a critical comparison of inductive and capacitive coupling for small gap applications," *IEEE Transactions on Power Electronics*, vol. 30, no. 11, pp. 6017–6029, 2015. 16

[34] S. Bandyopadhyay, J. Dong, L. Ramirez-Elizondo, and P. Bauer, "Determining relation between size of polarized inductive couplers and nominal airgap," in *2018 IEEE 18th International Power Electronics and Motion Control Conference (PEMC)*, pp. 248–255, IEEE, 2018. 16

[35] A. L. Stein, P. A. Kyaw, and C. R. Sullivan, "Figure of merit for resonant wireless power transfer," in *2017 IEEE 18th Workshop on Control and Modeling for Power Electronics (COMPEL)*, pp. 1–7, 2019. 16, 105, 110

[36] J. Yuan, L. Dorn-Gomba, A. D. Callegaro, J. Reimers, and A. Emadi, "A review of bidirectional on-board chargers for electric vehicles," *IEEE Access*, vol. 9, pp. 51501–51518, 2021. 17

[37] M. Budhia, J. T. Boys, G. A. Covic, and C.-Y. Huang, "Development of a single-sided flux magnetic coupler for electric vehicle IPT charging systems," *IEEE Transactions on Industrial Electronics*, vol. 60, no. 1, pp. 318–328, 2013. 18, 21

[38] R. Bosshard, U. Iruretagoyena, and J. W. Kolar, "Comprehensive evaluation of rectangular and double-D coil geometry for 50 kW/85 kHz IPT system," *IEEE Journal of Emerging and Selected Topics in Power Electronics*, vol. 4, no. 4, pp. 1406–1415, 2016. 18, 19, 24, 26, 32

[39] M. G. S. Pearce, G. A. Covic, and J. T. Boys, "Leakage and coupling of square and double D magnetic couplers," in *2016 IEEE 2nd Annual Southern Power Electronics Conference (SPEC)*, pp. 1–6, 2016. 18

[40] M. Mohammad, J. L. Pries, O. C. Onar, V. P. Galigekere, G. J. Su, and J. Wilkins, "Comparison of magnetic field emission from unipolar and bipolar coil-based wireless charging systems," in *2020 IEEE Transportation Electrification Conference and Expo (ITEC)*, pp. 1201–1207, 2020. 18, 205, 240, 241

[41] J. Pries, V. P. N. Galigekere, O. C. Onar, and G.-J. Su, "A 50-kW three-phase wireless power transfer system using bipolar windings and series resonant networks for rotating magnetic fields," *IEEE Transactions on Power Electronics*, vol. 35, no. 5, pp. 4500–4517, 2020. 18, 19, 21, 24, 27, 28, 216, 217, 220, 239

[42] M. Mohammad, J. Pries, O. Onar, V. P. Galigekere, G. Su, S. Anwar, J. Wilkins, U. D. Kavimandan, and D. Patil, "Design of an EMF suppressing magnetic shield for a 100-kW DD-coil wireless charging system for electric vehicles," in *2019 IEEE Applied Power Electronics Conference and Exposition (APEC)*, pp. 1521–1527, 2019. 18, 19, 21, 22, 23, 24

[43] B. Goeldi, J. Tritschler, and S. Reichert, "Measurement results of a 22 kW bidirectional inductive charger," in *Proceedings of PCIM Europe 2015; International Exhibition and Conference for Power Electronics, Intelligent Motion, Renewable Energy and Energy Management*, pp. 1–8, 2015. 19, 21

[44] A. Ridge, K. K. Ahamad, R. McMahon, and J. Miles, "Development of a 50 kW wireless power transfer system," in *2019 IEEE PELS Workshop on Emerging Technologies: Wireless Power Transfer (WoW)*, pp. 406–409, 2019. 19, 24, 26

[45] P. A. J. Lawton, F. J. Lin, and G. A. Covic, "Magnetic design considerations for high-power wireless charging systems," *IEEE Transactions on Power Electronics*, vol. 37, no. 8, pp. 9972–9982, 2022. 19, 130, 132

[46] M. Lu and K. D. T. Ngo, "Circuit models and fast optimization of litz shield for inductive-power-transfer coils," *IEEE Transactions on Power Electronics*, vol. 34, no. 5, pp. 4678–4688, 2019. 20, 22

[47] T. Campi, S. Cruciani, F. Maradei, and M. Feliziani, "Active coil system for magnetic field reduction in an automotive wireless power transfer system," in *2019 IEEE International Symposium on Electromagnetic Compatibility, Signal and Power Integrity (EMC+SIPI)*, pp. 189–192, 2019. 20, 22, 32

[48] M. Mohammad, E. Wodajo, S. Choi, and M. Elbuluk, "Modeling and design of passive shield to limit EMF emission and to minimize shield loss in unipolar wireless charging system for EV," *IEEE Transactions on Power Electronics*, pp. 1–1, 2019. 20, 22

[49] M. Mohammad, M. S. Haque, and S. Choi, "A litz-wire based passive shield design to limit EMF emission from wireless charging system," in *2018 IEEE Energy Conversion Congress and Exposition (ECCE)*, pp. 97–104, 2018. 20

[50] B. Zhang, R. B. Carlson, V. P. Galigekere, O. C. Onar, and J. L. Pries, "Electromagnetic shielding design for 200 kW stationary wireless charging of light-duty EV," in *2020 IEEE Energy Conversion Congress and Exposition (ECCE)*, pp. 5185–5192, 2020. 23

[51] M. K. Kazimierczuk, *High-frequency magnetic components*. John Wiley and Sons, 2009. xi, 23, 25, 52, 53

[52] C. R. Sullivan, "Cost-constrained selection of strand diameter and number in a litz-wire transformer winding," *IEEE Transactions on Power Electronics*, vol. 16, no. 2, pp. 281–288, 2001. 24, 104

[53] M. Mohammad, S. Choi, Z. Islam, S. Kwak, and J. Baek, "Core design and optimization for better misalignment tolerance and higher range of wireless charging of PHEV," *IEEE Transactions on Transportation Electrification*, vol. 3, no. 2, pp. 445–453, 2017. 24, 105

[54] M. G. S. Pearce, G. A. Covic, and J. T. Boys, "Robust ferrite-less double D topology for roadway IPT applications," *IEEE Transactions on Power Electronics*, vol. 34, no. 7, pp. 6062–6075, 2019. 24

[55] D. E. Gaona-Erazo, S. S. Ghosh, and T. Long, "Feasibility study of nanocrystalline-ribbon cores for polarized inductive power transfer pads," *IEEE Transactions on Power Electronics*, pp. 1–1, 2019. 26

[56] D. E. Gaona-Erazo, C. Jiang, and T. Long, "Highly efficient 11.1 kW wireless power transfer utilizing nanocrystalline ribbon cores," *IEEE Transactions on Power Electronics*, pp. 1–1, 2021. 26

[57] S. Kim, M. Amirpour, G. Covic, and S. Bickerton, "Thermal characterisation of a double-D pad," in *2019 IEEE PELS Workshop on Emerging Technologies: Wireless Power Transfer (WoW)*, pp. 1–5, 2019. 26

[58] R. Wojda, V. P. Galigekere, J. Pries, and O. Onar, "Thermal analysis of wireless power transfer coils for dynamic wireless electric vehicle charging," in *2020 IEEE Transportation Electrification Conference & Expo (ITEC)*, pp. 835–838, 2020. 26, 27

[59] C. Liang, G. Yang, F. Yuan, X. Huang, Y. Sun, J. Li, and K. Song, "Modeling and analysis of thermal characteristics of magnetic coupler for wireless electric vehicle charging system," *IEEE Access*, vol. 8, pp. 173177–173185, 2020. 26

[60] R. Bosshard and J. W. Kolar, "Inductive power transfer for electric vehicle charging: Technical challenges and tradeoffs," *IEEE Power Electronics Magazine*, vol. 3, no. 3, pp. 22–30, 2016. 27

[61] S. C. Mohapatra and D. Loikits, "Advances in liquid coolant technologies for electronics cooling," in *Semiconductor Thermal Measurement and Management Twenty First Annual IEEE Symposium, 2005*, pp. 354–360, 2005. 27

[62] F. Specht, "Water cooling for induction systems: Inside and out," *Heat Treating Progress*, October 2009. 27

[63] Z. Zi-Chao, S. Qiang, and B. Ahmed, "Innovative design of the cooling topologies for electric vehicle motors," *IOP Conference Series: Materials Science and Engineering*, vol. 533, 2019. 27

[64] P. A. Kyaw, M. Delhommais, J. Qiu, C. R. Sullivan, J.-L. Schanen, and C. Rigaud, "Thermal modeling of inductor and transformer windings including litz wire," *IEEE Transactions on Power Electronics*, vol. 35, no. 1, pp. 867–881, 2020. 27, 112

[65] T. Shijo, K. Ogawa, M. Suzuki, Y. Kanekiyo, K. Ogura, S. Obayashi, and M. Ishida, "Radiated disturbance measurements in SAC and on OATS for wireless power transfer system," in *2019 International Symposium on Electromagnetic Compatibility - EMC EUROPE*, pp. 461–464, 2019. 28, 30

[66] T. Shijo, K. Ogawa, M. Suzuki, Y. Kanekiyo, M. Ishida, and S. Obayashi, "EMI reduction technology in 85 kHz band 44 kW wireless power transfer system for rapid contactless charging of electric bus," in *2016 IEEE Energy Conversion Congress and Exposition (ECCE)*, pp. 1–6, 2016. 28

[67] M. Suzuki, K. Ogawa, T. Shijo, Y. Kanekivo, K. Inoue, K. Ogura, S. Obayashi, and M. Ishida, "Conducted emission in an 85 kHz, 50 kW WPT system with opposite-phase transfer and spread spectrum," in *2019 IEEE PELS Workshop on Emerging Technologies: Wireless Power Transfer (WoW)*, pp. 1–4, 2019. 28, 29

[68] S. Chiuk, K. Hongseok, D. H. Jung, Y. Kibum, C. Yeonje, K. Sunkyu, K. Younghwan, and K. Joungho, "Three-phase magnetic field design for low EMI and EMF automated resonant wireless power transfer charger for UAV," in *2015 IEEE Wireless Power Transfer Conference (WPTC)*, pp. 1–4, 2015. 28

[69] C. Song, H. Kim, Y. Kim, D. Kim, S. Jeong, Y. Cho, S. Lee, S. Ahn, and J. Kim, "EMI reduction methods in wireless power transfer system for drone electrical charger using tightly coupled three-phase resonant magnetic field," *IEEE Transactions on Industrial Electronics*, vol. 65, no. 9, pp. 6839–6849, 2018. 28, 29

[70] M. Suzuki, K. Ogawa, F. Moritsuka, T. Shijo, H. Ishihara, Y. Kanekiyo, K. Ogura, S. Obayashi, and M. Ishida, "Design method for low radiated emission of 85 kHz band 44 kW rapid charger for electric bus," in *2017 IEEE Applied Power Electronics Conference and Exposition (APEC)*, pp. 3695–3701, 2017. 28, 29

[71] W. Zhang and C. C. Mi, "Compensation topologies of high-power wireless power transfer systems," *IEEE Transactions on Vehicular Technology*, vol. 65, no. 6, pp. 4768–4778, 2016. 29, 192, 193

[72] S. Li, W. Li, J. Deng, T. D. Nguyen, and C. C. Mi, "A double-sided LCC compensation network and its tuning method for wireless power transfer," *IEEE Transactions on Vehicular Technology*, vol. 64, no. 6, pp. 2261–2273, 2015. 29

[73] T. Campi, S. Cruciani, F. Maradei, and M. Feliziani, "Conducted emission of wireless power transfer charging system in electric vehicle," in *2017 IEEE International Symposium on Electromagnetic Compatibility and Signal/Power Integrity (EMC+SIPI)*, pp. 619–622, 2017. 29

[74] H. Uno, K. Ogawa, T. Shijo, Y. Kanekiyo, K. Ogura, S. Obayashi, and M. Ishida, "EMI reduction techniques from 100 kW wireless charging systems for heavy-duty vehicles," in *2020 International Symposium on Antennas and Propagation (ISAP)*, pp. 729–730, 2020. 29, 30

[75] D. Ahmadi, K. Zou, C. Li, Y. Huang, and J. Wang, "A universal selective harmonic elimination method for high-power inverters," *IEEE Transactions on Power Electronics*, vol. 26, no. 10, pp. 2743–2752, 2011. 29, 30

[76] K. Inoue, K. Kusaka, and J.-I. Itoh, "Reduction in radiation noise level for inductive power transfer systems using spread spectrum techniques," *IEEE Transactions on Power Electronics*, vol. 33, no. 4, pp. 3076–3085, 2018. 29

[77] R. Bosshard and J. W. Kolar, "Multi-objective optimization of 50kW/85kHz IPT system for public transport," *IEEE Journal of Emerging and Selected Topics in Power Electronics*, vol. 4, no. 4, pp. 1370–1382, 2016. 32

[78] M. Poole, P. Weiss, H. S. Lopez, M. Ng, and S. Crozier, "Minimax current density coil design," *Journal of Physics D: Applied Physics*, vol. 43, no. 9, 2010. 33

[79] G. N. Peeren, *Stream function approach for determining optimal surface currents*. Thesis, Eindhoven University of Technology, 2003. 33

[80] M. Landreman, "An improved current potential method for fast computation of stellarator coil shapes," *Nuclear Fusion*, vol. 57, no. 4, 2017. 33

[81] J. R. Melcher, *Continuum electromechanics*, vol. 2. MIT Press Cambridge, 1981. 33, 36

[82] B. L. J. Gysen, K. J. Meessen, J. J. H. Paulides, and E. A. Lomonova, "General formulation of the electromagnetic field distribution in machines and devices using Fourier analysis," *IEEE Transactions on Magnetics*, vol. 46, no. 1, pp. 39–52, 2010. 33

[83] Z. Luo and X. Wei, "Analysis of square and circular planar spiral coils in wireless power transfer system for electric vehicles," *IEEE Transactions on Industrial Electronics*, vol. 65, no. 1, pp. 331–341, 2018. 33

[84] J. P. C. Smeets, T. T. Overboom, J. W. Jansen, and E. A. Lomonova, "Three-dimensional magnetic field modeling for coupling calculation between air-cored

rectangular coils," *IEEE Transactions on Magnetics*, vol. 47, no. 10, pp. 2935–2938, 2011. 33

[85] J. P. C. Smeets, T. T. Overboom, J. W. Jansen, and E. A. Lomonova, "Three-dimensional analytical modeling technique of electromagnetic fields of air-cored coils surrounded by different ferromagnetic boundaries," *IEEE Transactions on Magnetics*, vol. 49, no. 12, pp. 5698–5708, 2013. 33

[86] A. Foote, D. Costinett, R. Kusch, J. Pries, M. Mohammad, and B. Ozpineci, "Fourier analysis method for wireless power transfer coil design," in *2020 IEEE 21st Workshop on Control and Modeling for Power Electronics (COMPEL)*, pp. 1–8, 2020. 33

[87] C. Feeney, J. Zhang, and M. Duffy, "AC winding loss of phase-shifted coupled windings," *IEEE Transactions on Power Electronics*, vol. 31, no. 2, pp. 1472–1478, 2016. 51

[88] J. Mühlethaler, *Modeling and multi-objective optimization of inductive power components*. Thesis, ETH Zurich/ Power Electronic Systems Laboratory, 2012. 52, 53

[89] M. Lu and K. D. T. Ngo, "Analytical calculation of proximity-effect resistance for planar coil with litz wire and ferrite plate in inductive power transfer," *IEEE Transactions on Industry Applications*, pp. 1–1, 2019. 53

[90] Illinois Capacitor, "Illinois capacitor." https://www.illinoiscapacitor.com/, 2020. 61, 63, 69, 72

[91] J. H. I. Leinhard and J. H. V. Leinhard, *A Heat Transfer Textbook*. Phlogiston Press, 2019. xi, 111, 113, 117, 165

[92] M. C. Kulan, S. Sahin, and N. J. Baker, "An overview of modern thermo-conductive materials for heat extraction in electrical machines," *IEEE Access*, vol. 8, pp. 212114–212129, 2020. 121

[93] K. Larson, "Can you estimate modulus from durometer hardness for silicones," *Dow Corning Corporation*, pp. 1–6, 2016. 121

[94] V. Tsakaloudi, D. Holz, and V. Zaspalis, "The effect of externally applied uniaxial compressive stress on the magnetic properties of power MnZn-ferrites," *Journal of Materials Science*, vol. 48, no. 10, pp. 3825–3833, 2013. 121, 123, 127

[95] I. M. Daniel, O. Ishai, I. M. Daniel, and I. Daniel, *Engineering mechanics of composite materials*. Oxford University Press New York, 2006. 123

[96] K. Venkatachalam, C. R. Sullivan, T. Abdallah, and H. Tacca, "Accurate prediction of ferrite core loss with nonsinusoidal waveforms using only Steinmetz parameters," in *2002 IEEE Workshop on Computers in Power Electronics*, pp. 36–41, 2002. 144

[97] E. A. Jones, *Review and characterization of gallium nitride power devices*. Masters Thesis, University of Tennessee, 2016. 150

[98] K. Aditya and S. S. Williamson, "Design guidelines to avoid bifurcation in a series–series compensated inductive power transfer system," *IEEE Transactions on Industrial Electronics*, vol. 66, no. 5, pp. 3973–3982, 2019. 171, 192

[99] L. Xue, V. Galigekere, G. J. Su, R. Zeng, M. Mohammad, E. Gurpinar, S. Chowdhury, and O. Onar, "Design and analysis of a 200 kW dynamic wireless charging system for electric vehicles," in *2022 IEEE Applied Power Electronics Conference and Exposition (APEC)*, pp. 1096–1103, 2022. 171

[100] M. Hackmann, "P3 charging index report 07/22 – comparison of the fast charging capability of various electric vehicles," *P3 Group*, 2022. xix, 189

[101] M. Mohammad, O. C. Onar, G.-J. Su, J. Pries, V. P. Galigekere, S. Anwar, E. Asa, J. Wilkins, R. Wiles, C. P. White, and L. E. Seiber, "Bidirectional LCC–LCC-compensated 20-kW wireless power transfer system for medium-duty vehicle charging," *IEEE Transactions on Transportation Electrification*, vol. 7, no. 3, pp. 1205–1218, 2021. 192, 193

[102] V. P. Galigekere, O. Onar, J. Pries, S. Zou, Z. Wang, and M. Chinthavali, "Sensitivity analysis of primary-side LCC and secondary-side series compensated wireless charging

system," in *2018 IEEE Transportation Electrification Conference and Expo (ITEC)*, pp. 885–891, 2018. 192, 193

[103] M. Mohammad, O. C. Onar, V. P. Galigekere, G. J. Su, and J. Wilkins, "Magnetic shield design for the Double-D coil-based wireless charging system," *IEEE Transactions on Power Electronics*, vol. 37, no. 12, pp. 15740–15752, 2022. 205, 240, 241

[104] A. Berger, M. Agostinelli, S. Vesti, J. A. Oliver, J. A. Cobos, and M. Huemer, "A wireless charging system applying phase-shift and amplitude control to maximize efficiency and extractable power," *IEEE Transactions on Power Electronics*, vol. 30, no. 11, pp. 6338–6348, 2015. 206

[105] P. Pham, S. Cochran, D. J. Costinett, and L. M. Tolbert, "Active rectifier design and synchronization control for 6.78 MHz wireless power transfer," in *2020 IEEE Energy Conversion Congress and Exposition (ECCE)*, pp. 5501–5508, 2022. 206

[106] R. Bosshard and J. W. Kolar, "All-SiC 9.5 kW/dm^3 on-board power electronics for 50 kW/85 kHz automotive IPT system," *IEEE Journal of Emerging and Selected Topics in Power Electronics*, vol. 5, no. 1, pp. 419–431, 2017. 206

[107] Fraunhofer Institute for Integrated Systems and Device Technology, "Full SiC traction 600 A DC-DC converter for electric, hybrid, and fuel cell vehicles." https://www.iisb.fraunhofer.de/content/dam/iisb2014/en/Documents/Media-PDF/Flyer_IISB-6M_v3.pdf. 207, 227

[108] Delta Electronics Incorporated, "DC Charger / City Charger 200 kW." https://www.deltaww.com/en-us/products/EV-Charging/UFC-200. 230

[109] Tritium, "PK350/350kW Specifications." https://tritiumcharging.com/wp-content/uploads/2023/02/TRI105.DTA_.002_Veefil-PK350-Specifications.pdf. 230

[110] ABB, "Terra 94/124/184 UL product guide." https://library.e.abb.com/public/e1bbf68ba97f4ae6a210083421a7ae23/Terra-94-124-184_UL_Product-Guide_G.pdf. 230

[111] Siemens, "VersiCharge Ultra 175 DC Charger." https://www.siemens.com/us/en/products/energy/topics/transportation-electrification/versicharge-ultra-dc-fast-chargers.html. 230

[112] Siemens, "SICHARGE D - The future of fast charging: High-power, flexible, modular, and scalable." https://www.siemens.com/global/en/products/energy/medium-voltage/solutions/emobility/sicharge-d.html. 230

Appendices

A Mechanical Design of the 6.6 kW Demonstrator

A.1 Coil Enclosure and Former

This appendix details the construction and parts of the 6.6 kW demonstrator of Chapter 4. In Figures 4, 5, and 6, drawings of the coils and capacitor banks are given. In Figure 7 and Table 2, the breakdown of the cost, weight, and volume and a list of the parts used in the demonstrator are given.

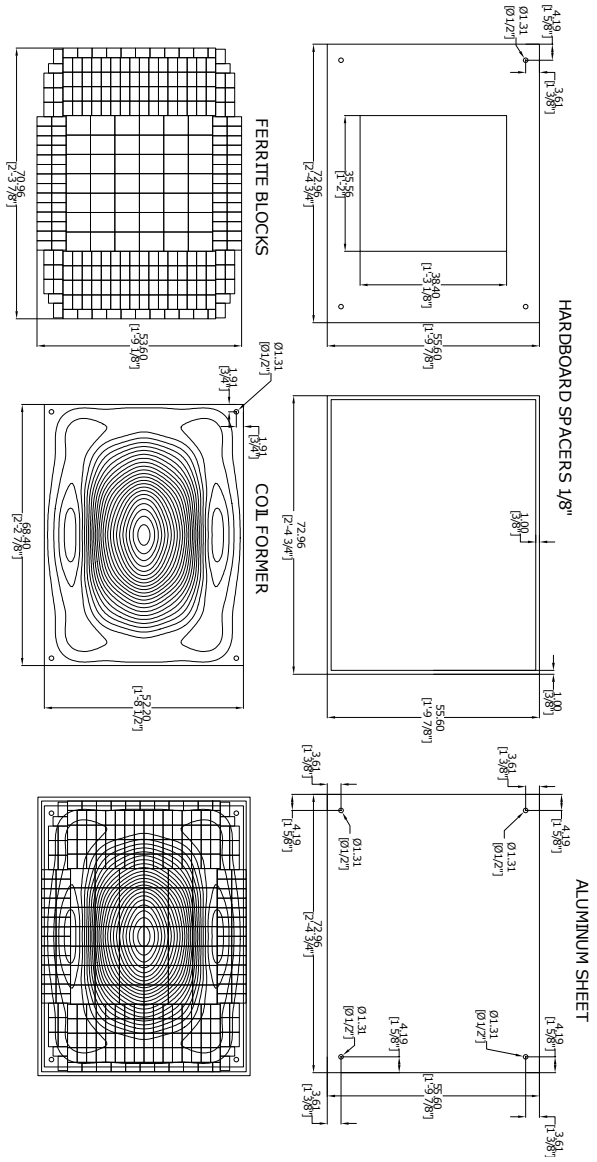

Figure 4: Mechanical Detail of 6.6 kW Demonstrator Coils

A.2 Compensation Capacitor

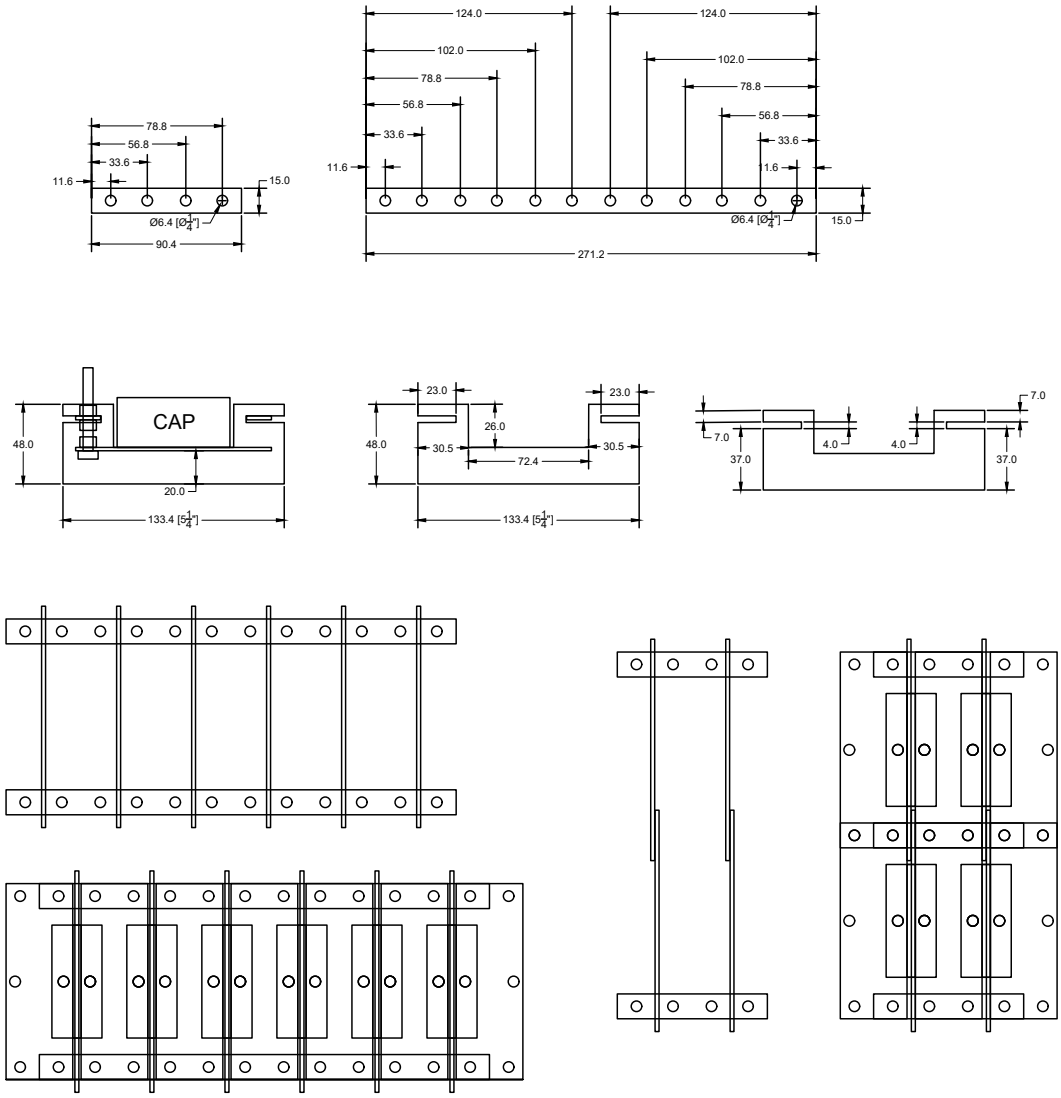

Figure 5: Mechanical Detail of Insulation Fins and Spacers for Capacitor Banks

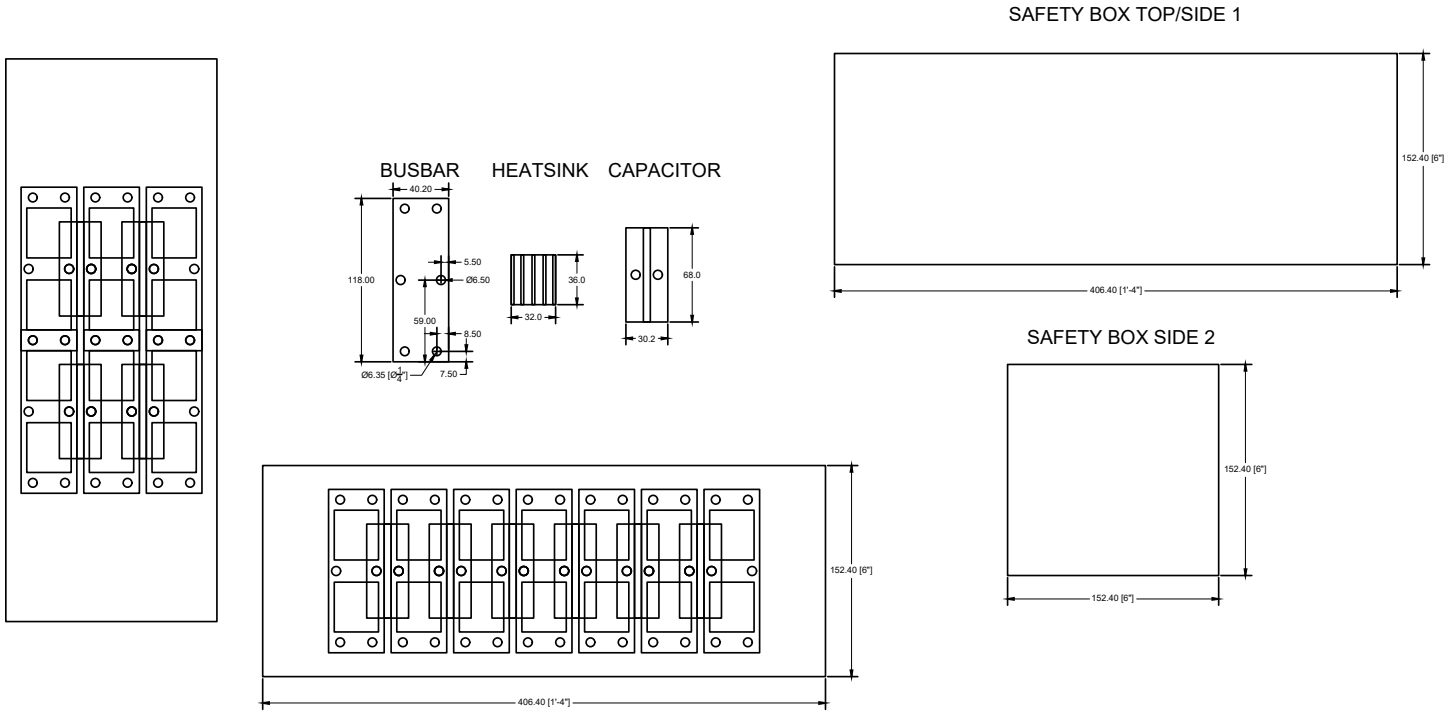

Figure 6: Mechanical Detail of Capacitor Banks

A.3 Part Identification and Costs

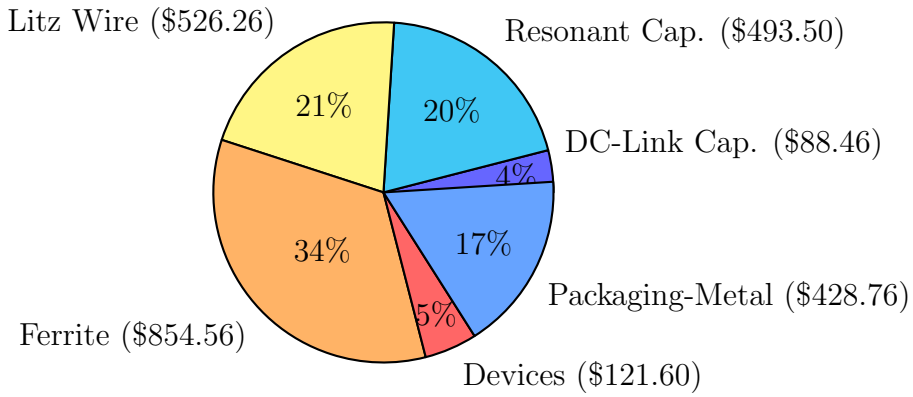

(a)

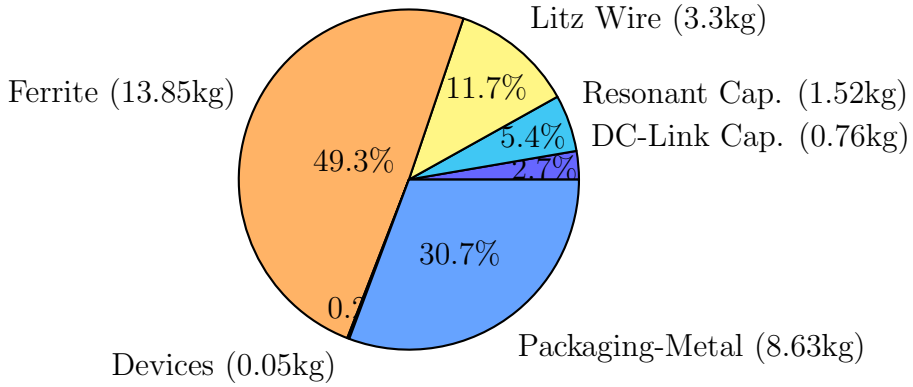

(b)

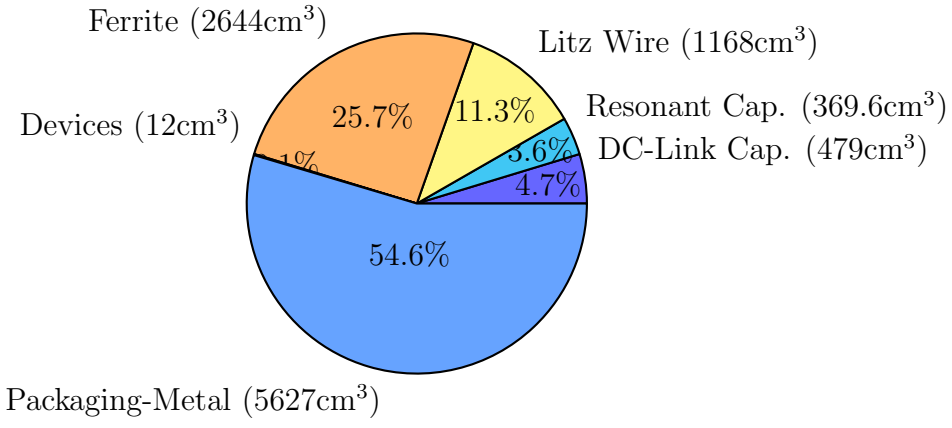

(c)

Figure 7: 6.6 kW demonstrator cost, weight and volume breakdown: (a) Pie Chart of Cost; (b) Pie Chart of Weight; (c) Pie Chart of Volume.

Table 2: Part Count and BOM of 6.6 kW Demonstrator System with the 86.5 kHz Operating Frequency

Part Description	Manufacturer Part Number	Quantity	Unit Cost	Ext. Cost	Unit Weight (g)	Ext. Weight (kg)	Unit Volume (cm^3)	Ext. Volume (cm^3)
Ferrite Blocks 5mm	Ferroxcube PLT64/50/5-3C95	84	$4.34	$364.56	78	6.55	16	1344
Ferrite Blocks 2.7mm	Ferroxcube PLT38/25/2.7-3C95	500	$0.98	$490.00	14.6	7.3	2.6	1300
10 AWG Litz Wire	New England Wire 10 AWG 5x5/44/40 Single Polyurethane-Nylon, Gray ETFE	59.6m	$8.83/m	$526.26	55.6/m	3.3	19.6/m	1168
High-Density Resonant Film Capacitor	Illinois Capacitor 503HC1102K2SM6	6	$82.25	$493.50	253	1.52	61.6	369.6
SiC MOSFET 1.2kV 40mΩ , 60A	ON Semiconductor NVHL040N120SC1	4	$15.37	$61.48	6	0.024	1.5	6
SiC Schottky Diode 1.2kV, 38A	STMicroelectronics STPSC40H12CWL	4	$15.03	$60.12	6	0.024	1.5	6
Electrolytic DC-Link Cap. 450V, 560µF	United Chemi-Con E36D401HPN561	4	$16.73	$66.92	138	0.552	76	304
Film DC-Link Cap. 900V, 50µF	Vishay MKP1848C65090JY5	2	$10.77	$21.54	104	0.21	87.5	175
6061 Aluminum Sheet 0.127cm × 55.6cm × 73cm		2	$16.58	$33.15	1392	2.8	515.5	1031
110 Copper Busbars 0.159cm × 4cm × 12cm		8	$3.95	$31.56	68.4	0.55	7.6	61
Coil Former P.C. 0.635cm × 52.2cm × 68.4cm		2	$182.00	$364.00	2667	5.3	2267	4535
Total		618		$2538.35		28.1		10300

B 6.6kW Demonstrator Scaled Field Measurements

This appendix details the stray field measurements of the 6.6 kW demonstrator of Chapter 4. The fields were measured on the X and Y axes at the 50.5 kHz, 86.5 kHz, and 121.5 kHz axes as shown in the following plots.

B.1 Field Measurements at 50.5 kHz

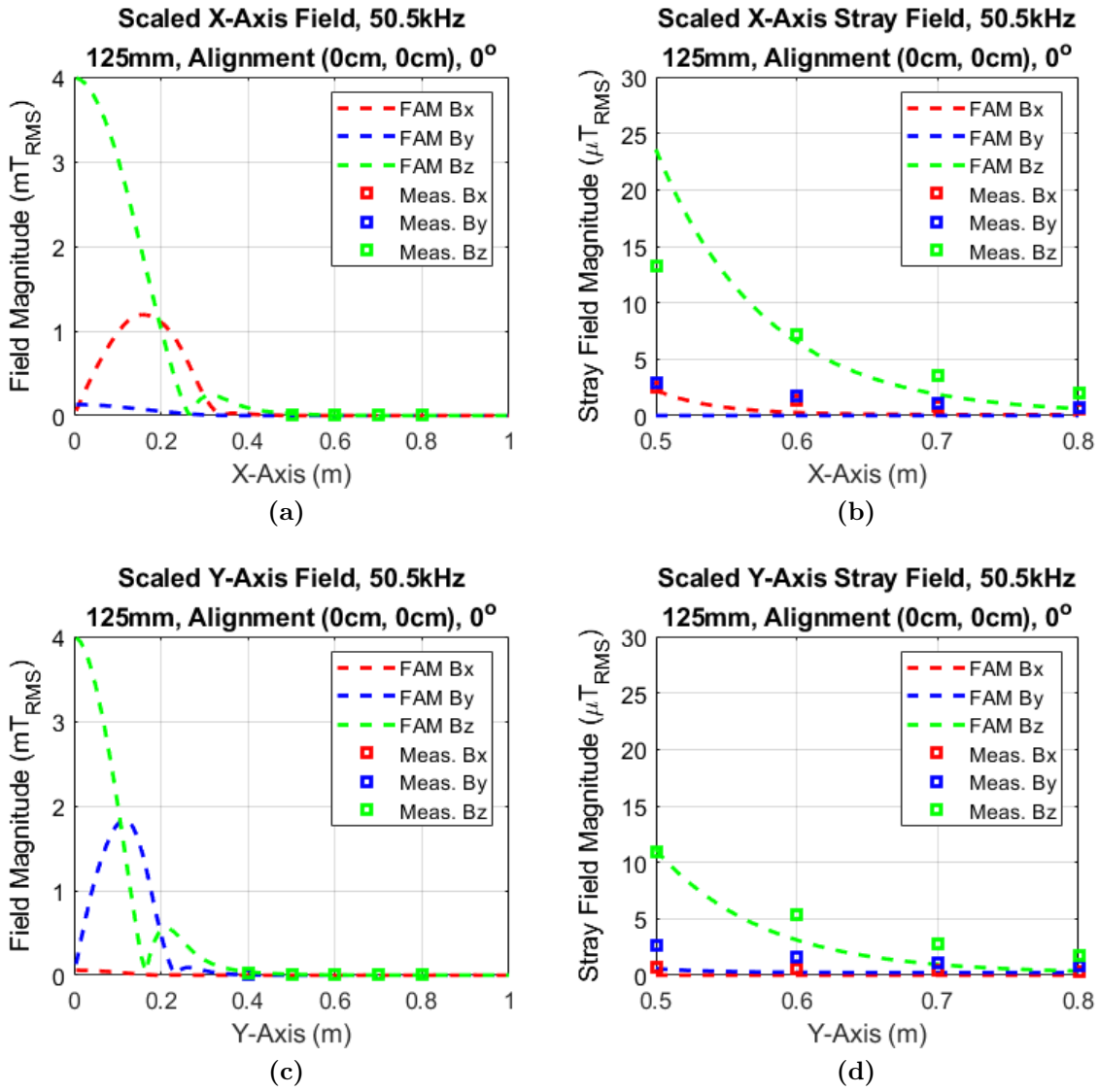

Figure 8: Scaled measured and modeled field at 50.5 kHz, 125 mm, and 6.6 kW. (a) Fields on the X-axis (b) stray fields on X-axis. (c) Fields on the Y-axis (d) stray fields on Y-axis.

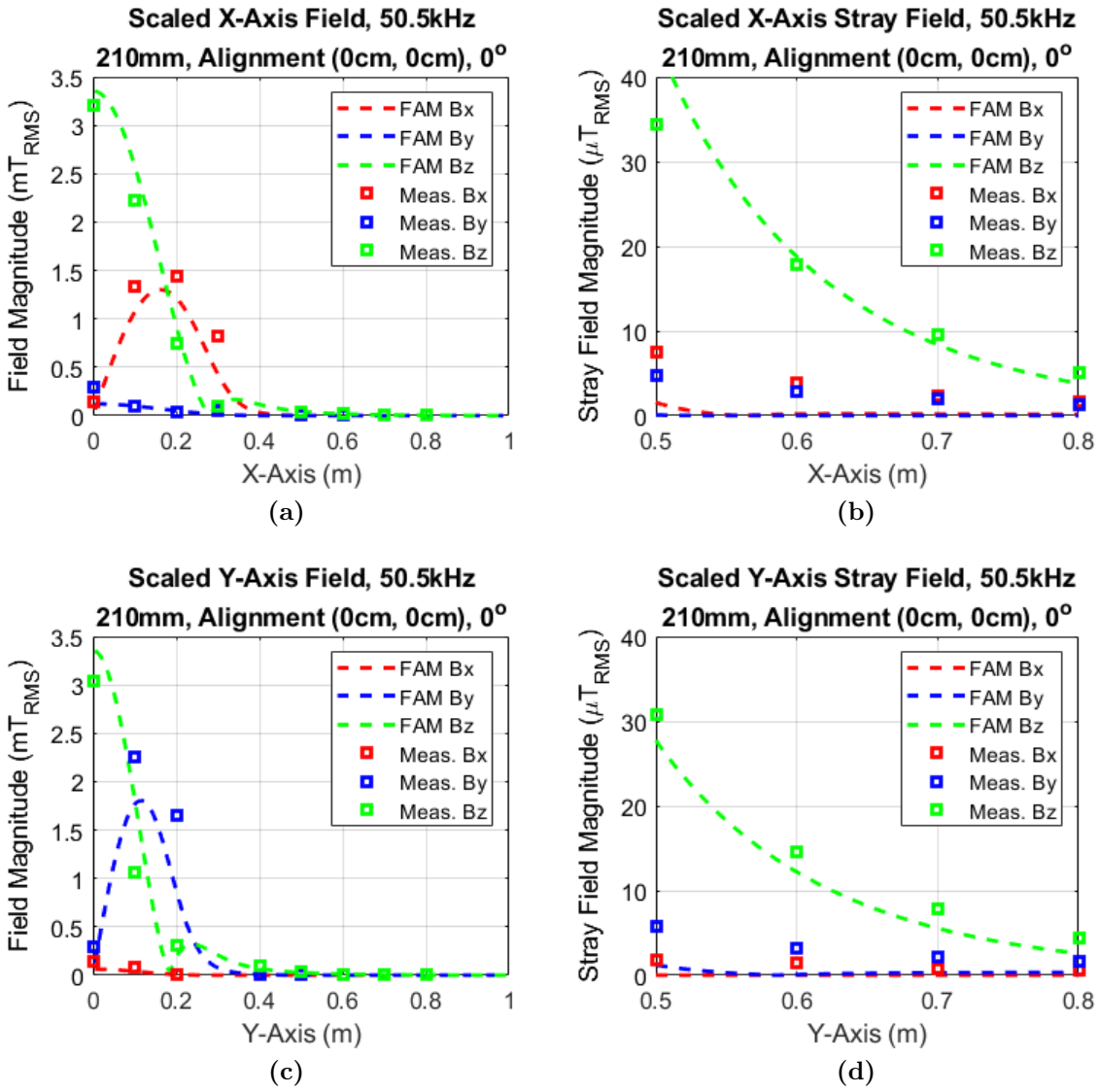

Figure 9: Scaled measured and modeled field at 50.5 kHz, 210 mm, and 6.6 kW. (a) Fields on the X-axis (b) stray fields on X-axis. (c) Fields on the Y-axis (d) stray fields on Y-axis.

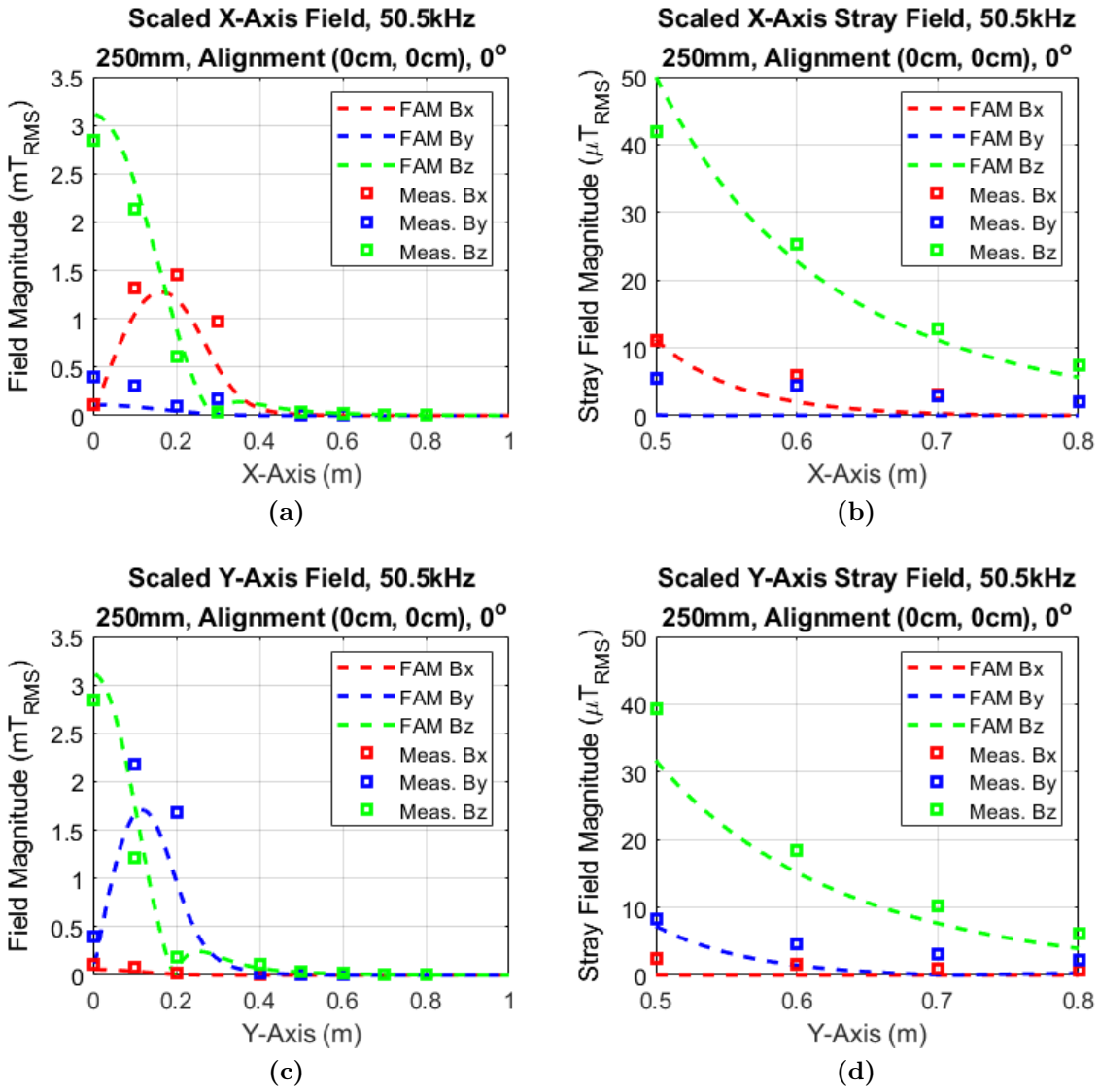

Figure 10: Scaled measured and modeled field at 50.5 kHz, 250 mm, and 6.6 kW. (a) Fields on the X-axis (b) stray fields on X-axis. (c) Fields on the Y-axis (d) stray fields on Y-axis.

B.2 Field Measurements at 86.5kHz

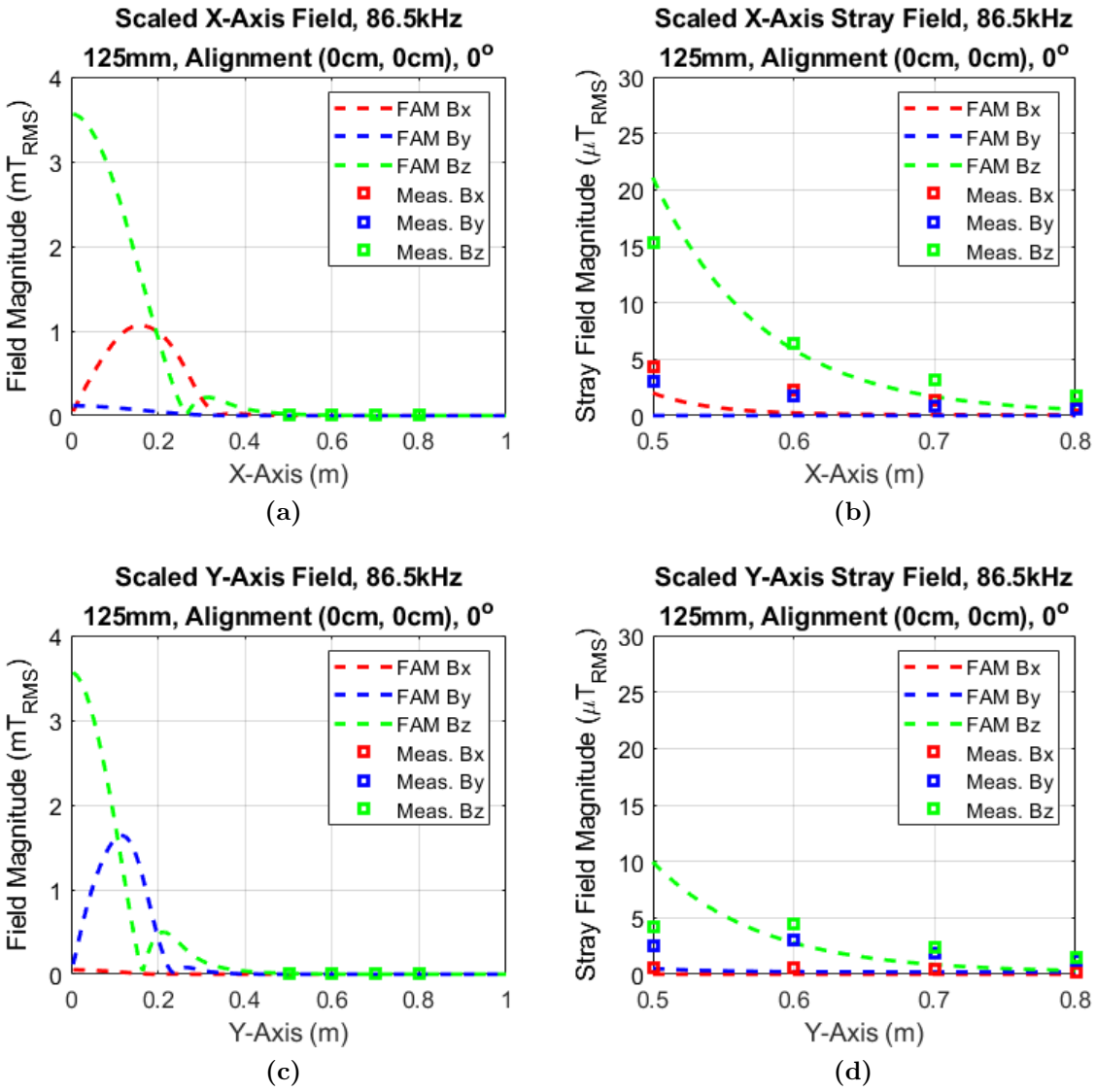

Figure 11: Scaled measured and modeled field at 86.5 kHz, 125 mm, and 6.6 kW. (a) Fields on the X-axis (b) stray fields on X-axis. (c) Fields on the Y-axis (d) stray fields on Y-axis.

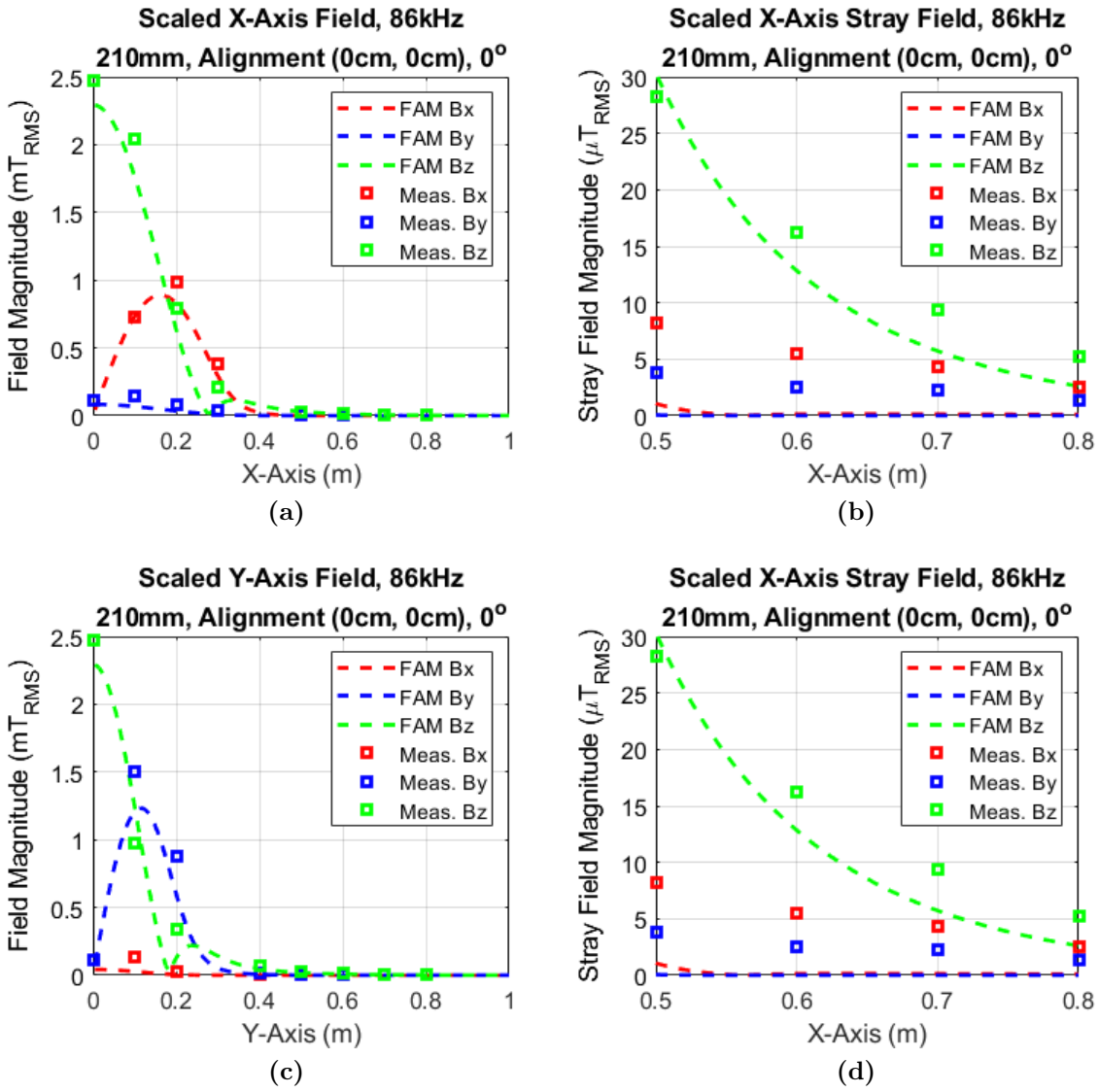

Figure 12: Scaled measured and modeled field at 86.5 kHz, 210 mm, and 6.6 kW. (a) Fields on the X-axis (b) stray fields on X-axis. (c) Fields on the Y-axis (d) stray fields on Y-axis.

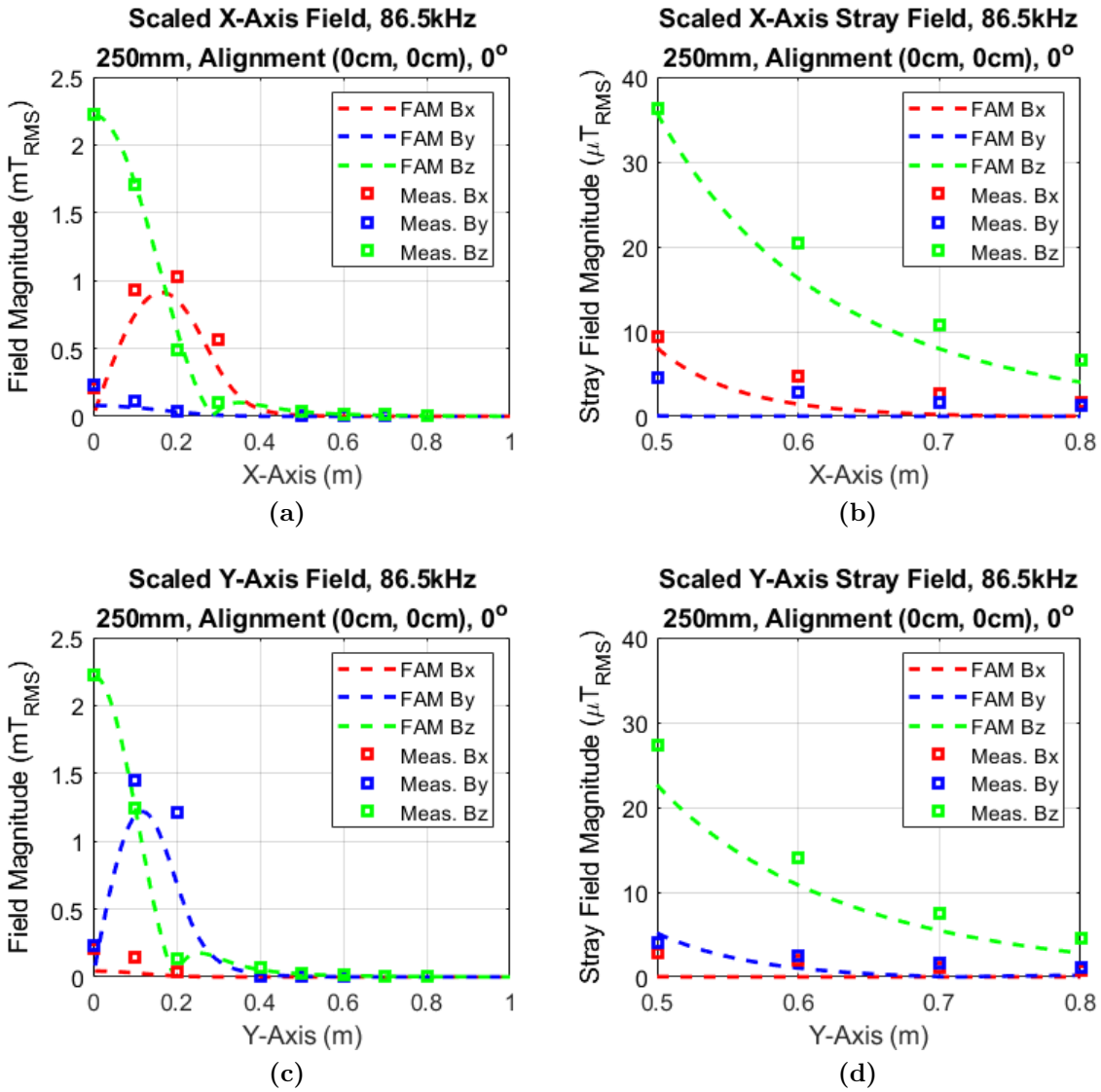

Figure 13: Scaled measured and modeled field at 86.5 kHz, 250 mm, and 6.6 kW. (a) Fields on the X-axis (b) stray fields on X-axis. (c) Fields on the Y-axis (d) stray fields on Y-axis.

B.3 Field Measurements at 121.5kHz

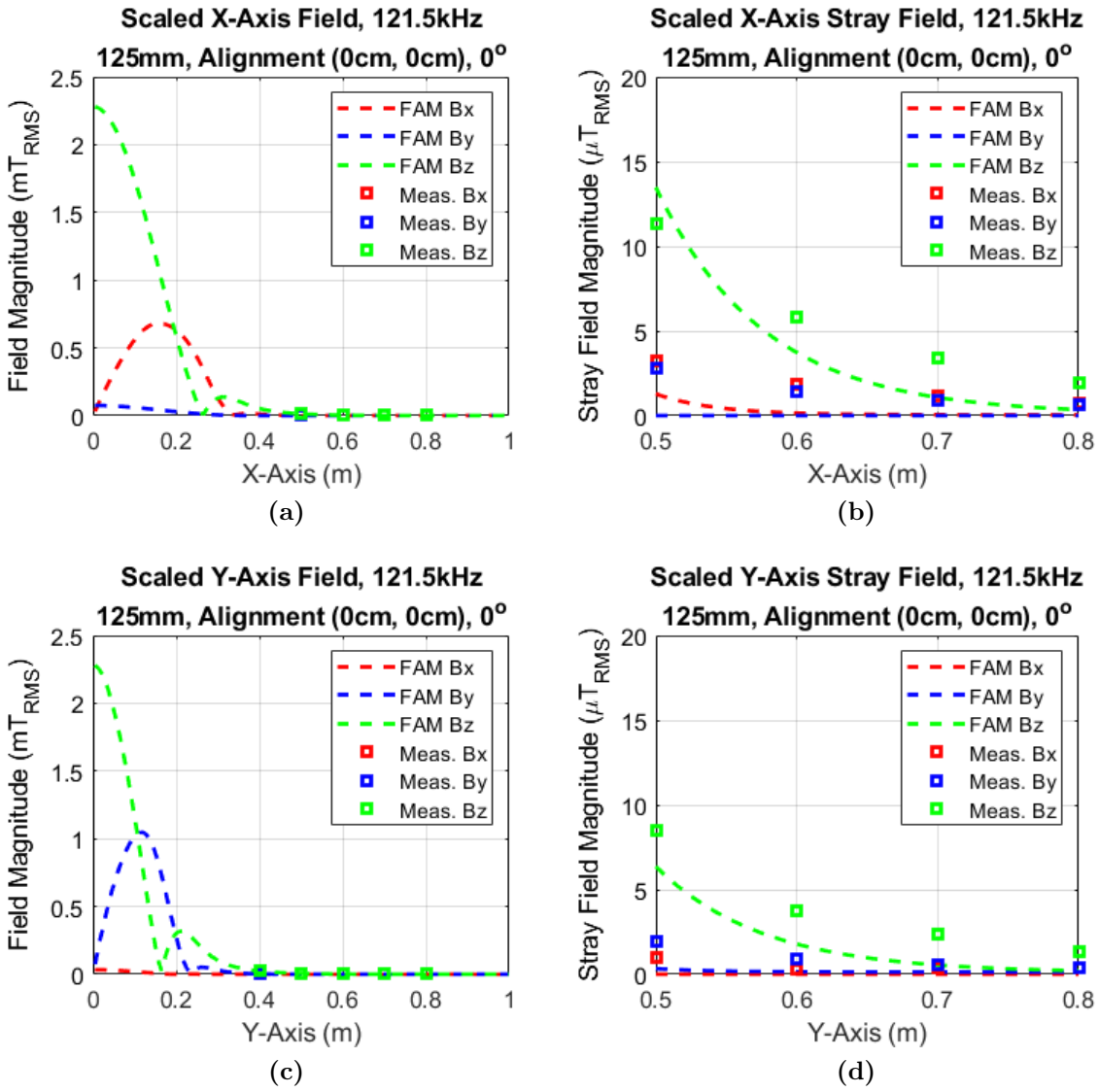

Figure 14: Scaled measured and modeled field at 121.5 kHz, 125 mm, and 6.6 kW. (a) Fields on the X-axis (b) stray fields on X-axis. (c) Fields on the Y-axis (d) stray fields on Y-axis.

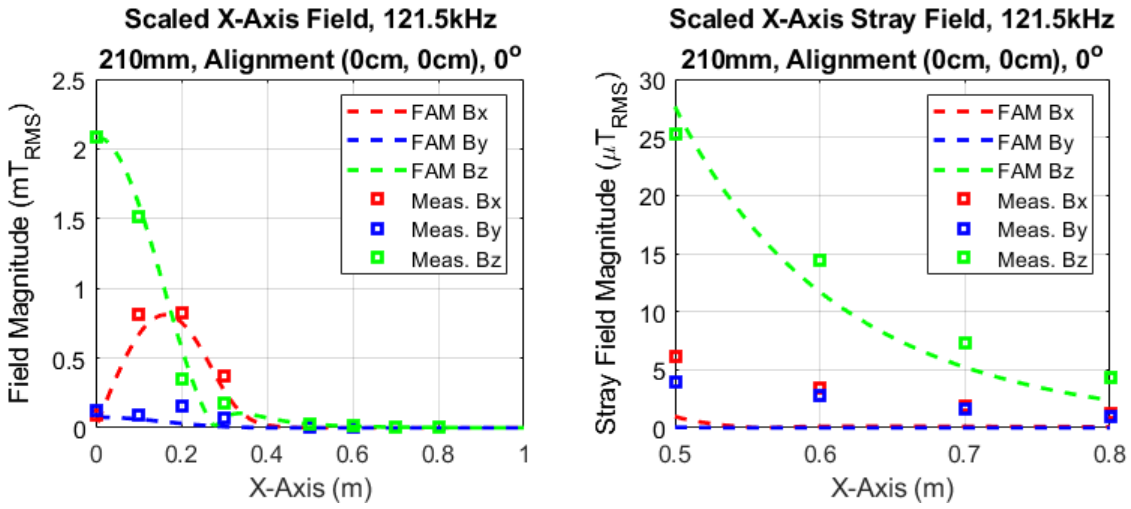

Figure 15: Scaled field measurements and model outputs at 121.5 kHz, 210 mm, and 6.6 kW. (a) Fields on the X-axis (b) stray fields on X-axis. (c) Fields on the Y-axis (d) stray fields on Y-axis.

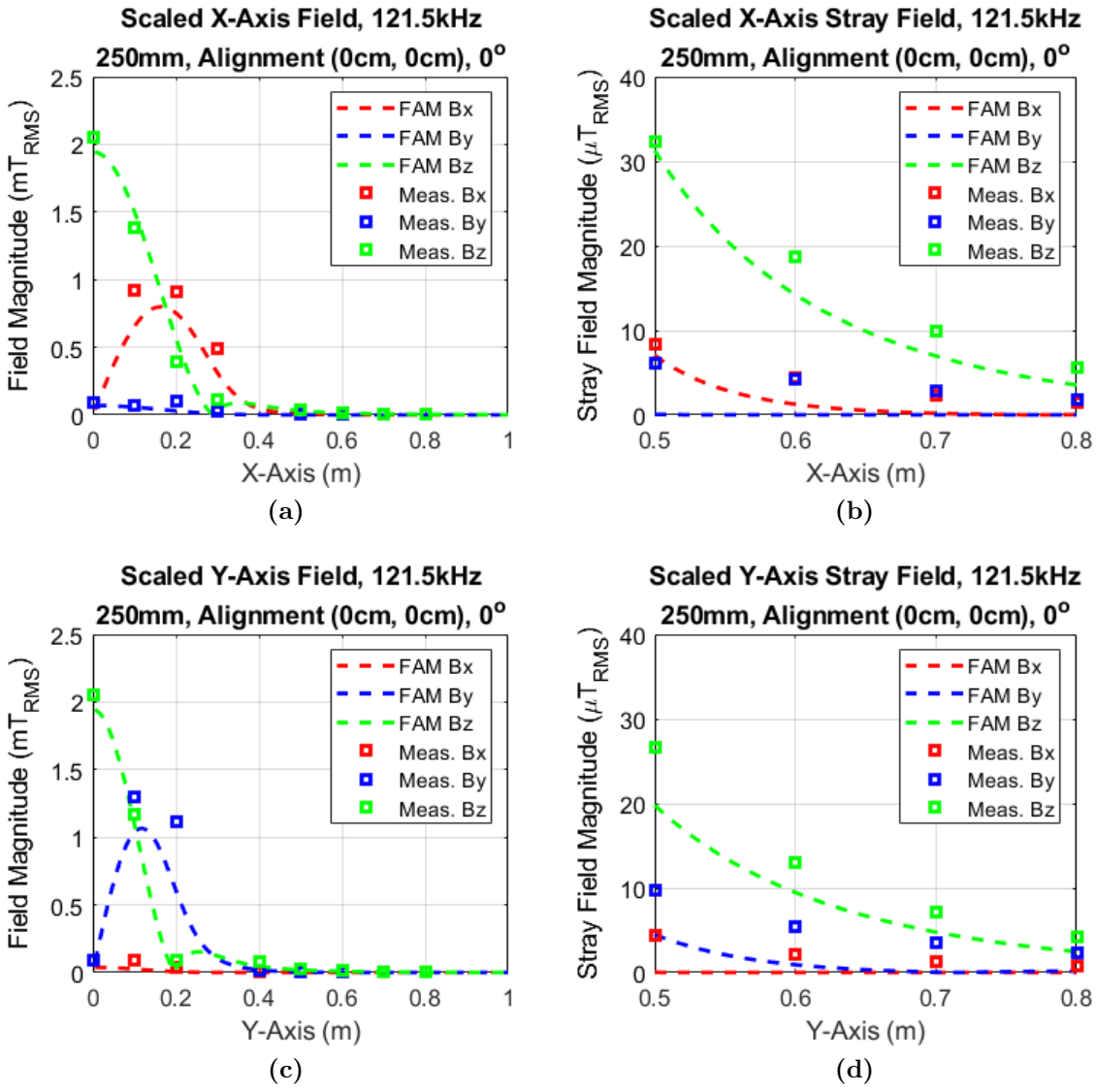

Figure 16: Scaled field measurements and model outputs at 121.5 kHz, 250 mm, and 6.6 kW. (a) Fields on the X-axis (b) stray fields on X-axis. (c) Fields on the Y-axis (d) stray fields on Y-axis.

C 120kW Demonstrator Design Details

C.1 Small-Scale Compression Test Coil

In Section 5.4, the effect of residual stress on ferrite loss was detailed. A small scale coil assembly was used to isolate this effect. Dimensional drawings of this assembly are given in Figure 17.

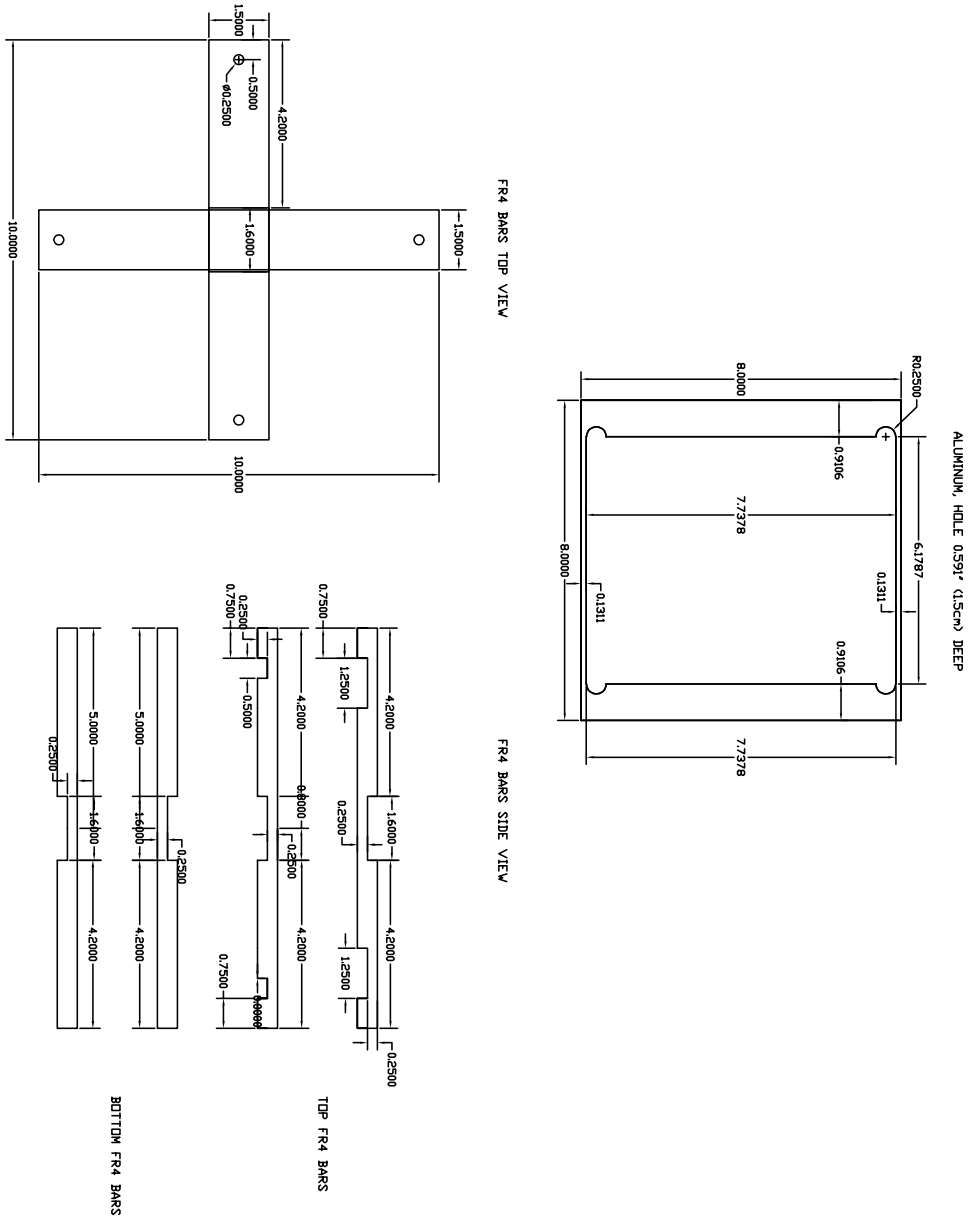

Figure 17: Dimensional drawings of the small-scale coil used to confirm the effect of compressive stress on ferrite hysteresis loss.

C.2 Part Identification and Costs

In Chapter 5, the design of two 120 kW WPT demonstrators is detailed. The cost and weight breakdown of the Gen. 2 demonstrator is given in Figure 18. A list of parts used in the demonstrator is given in Table 3.

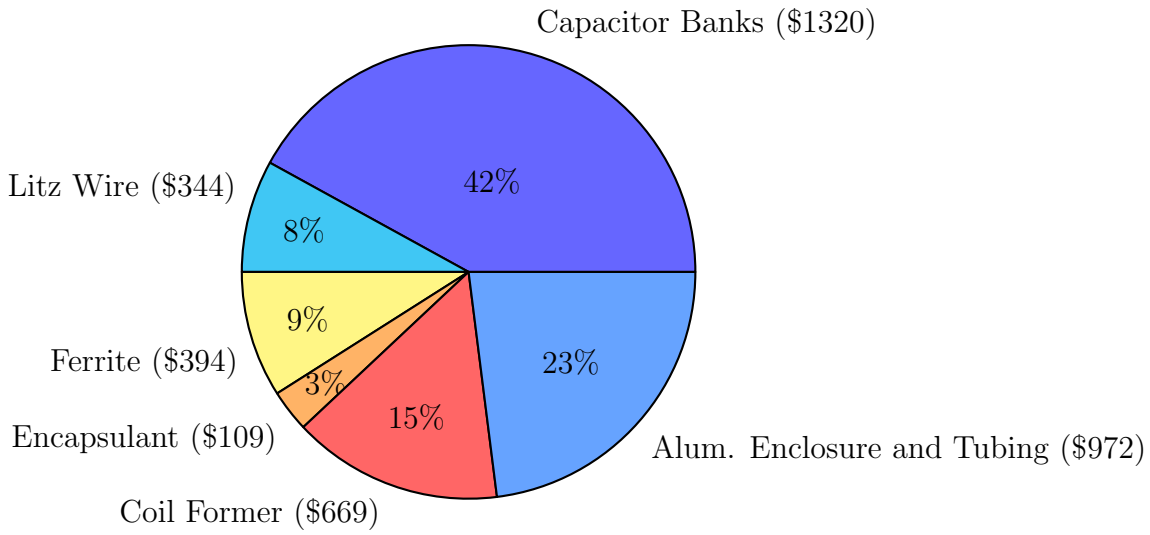

(a)

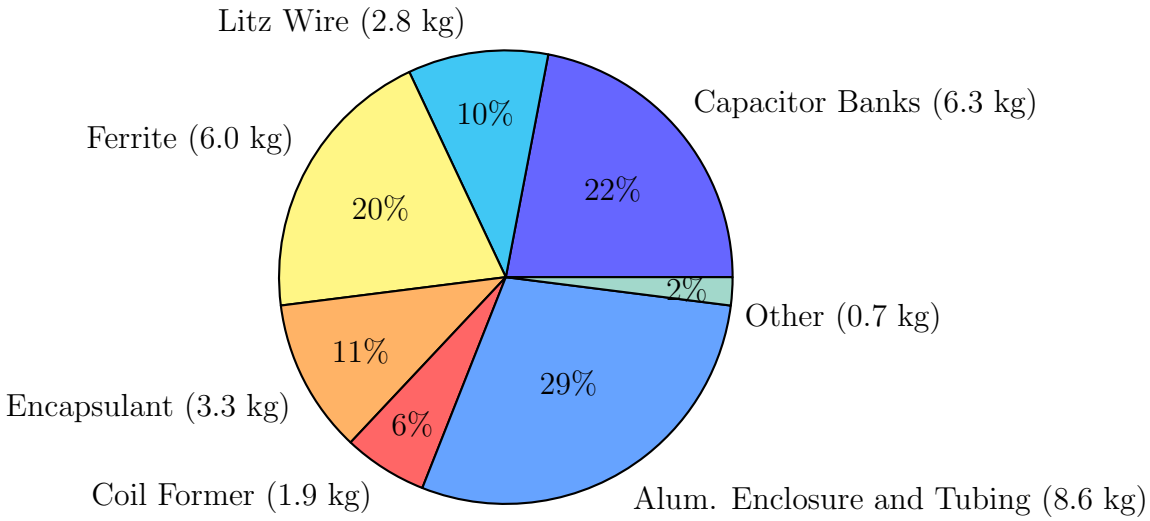

(b)

Figure 18: Repeated from Chapter 5.6. Breakdown of the (a) cost and (b) weight of one of the Gen. 2 demonstrator assemblies.

Table 3: Part Count and Bill of Material of one Gen. 2 Coil Assembly. (*Estimate, contract manufacturer.)

Part Description	Manufacturer Part Number	Quantity	Unit Cost	Ext. Cost	Unit Weight (g)	Ext. Weight (kg)
Ferrite Blocks 5mm	Ferroxcube PLT64/50/5-3C95	77	$5.12	$394	78	6.0
Silicone Elastomer Encapsulant	Parker Lord Cooltherm SC320	1.1L	$3741/10gal	$109	3100g/L	3.3
4 AWG Litz Wire and Terminations	New England Wire 4 AWG 6750/42 MW77-C, Black ETFE	11.9m	$28.90/m	$344	239.2/m	2.8
Coil Former P.C. 42cm×54cm×0.95cm	Custom CNC	1		$669*		1.9
Aluminum Enclosure 42cm×54cm×2.5cm	Custom CNC	1		$972*		7.7
Copper Tubing	5/16" O.D., 0.049" Wall Thickness	4m		$45		0.9
Nylon Fasteners and Sealant		24				0.5
High-Density Resonant Film Capacitor	Celem CSM 150/300	12	$110	$1320	253	3.0
316 Stainless Steel Fasteners		84				0.2
Copper Busbars 3.0cm×6.6cm×1.5mm	Custom Waterjet	14	$12.91*	$181*	123	1.7
G10 Compression Plates	Custom CNC	2	$154*	$307*	617	1.2
Silicone Thermal Pad	TG-AH486 100mm×40mm×1.5mm	2	$15.97	$32	108.9	0.2
Total		220		$4373		29.3

D Modeled and Tested Efficiency of the Gen. 2 System

The Gen. 2 120 kW demonstrator of Chapter 5 was tested over a variety of conditions over misalignment and with constant output resistance and constant output voltage. These Figures detail the measured and modeled values over these conditions for the 125 mm airgap. Some modeled values for the 152.4 mm airgap are also given in Figures 25 and 26.

D.1 Constant Output Resistance Tests

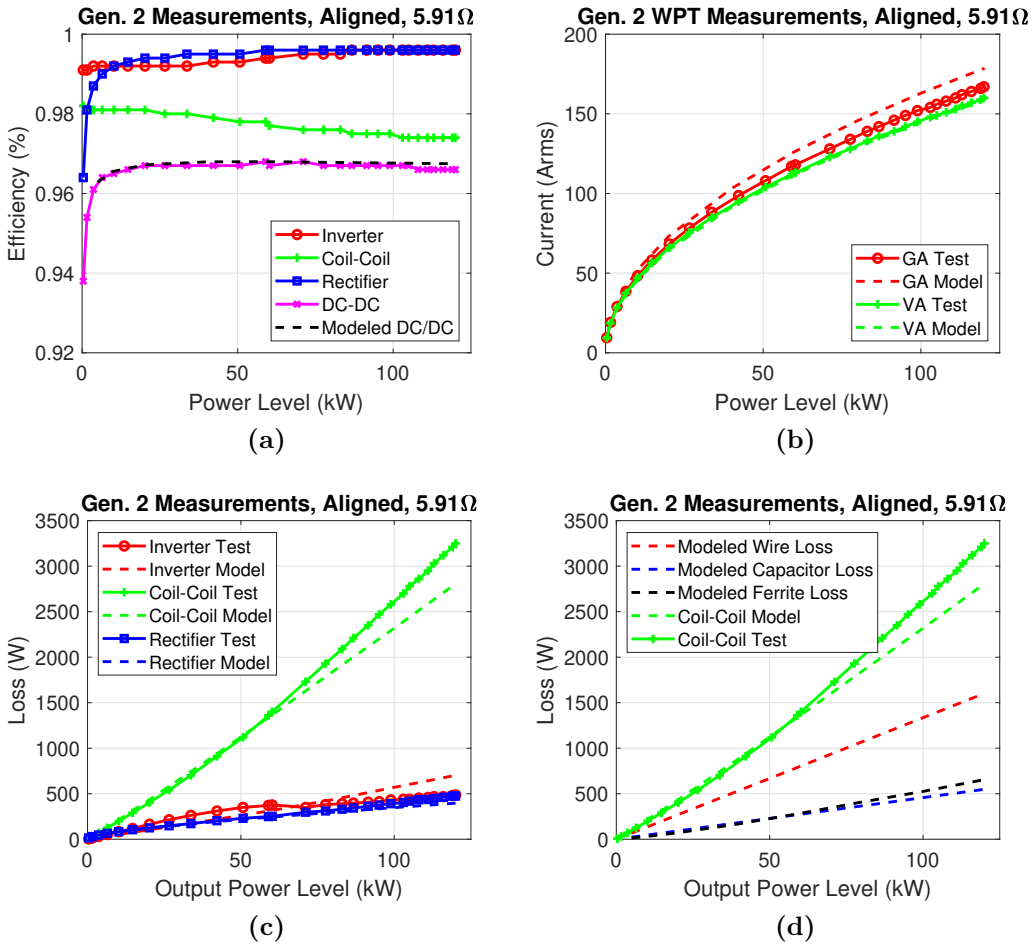

Figure 19: Repeated from Chapter 5. Test of the Gen. 2 demonstrator at alignment near unity gain (grid offset of (-7 mm, -5 mm)) and 125 mm. (a) Efficiency breakdown vs. output power. (b) Measured vs. modeled GA and VA current. (c) Measured vs. modeled system losses. (d) Breakdown of the modeled coil-coil losses vs. measured.

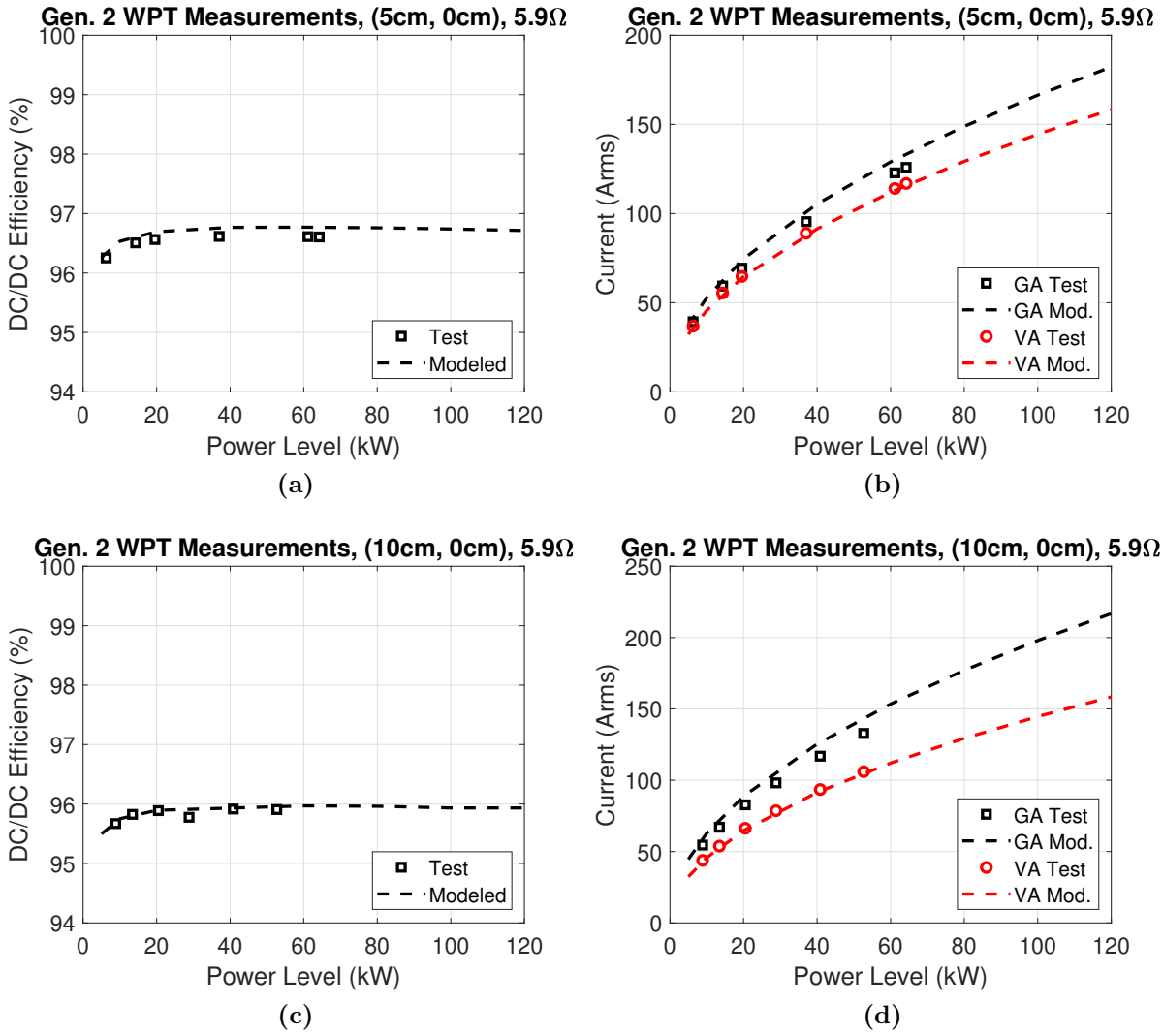

Figure 20: Tests of the Gen. 2 demonstrator at different alignments compared to modeled values near unity gain (grid offset of (-7 mm, -5 mm)) and an airgap of 125 mm. (a) DC/DC efficiency and (b) GA and VA current at (5 cm, 0 cm). (c) DC/DC efficiency and (d) GA and VA current at (10 cm, 0 cm).

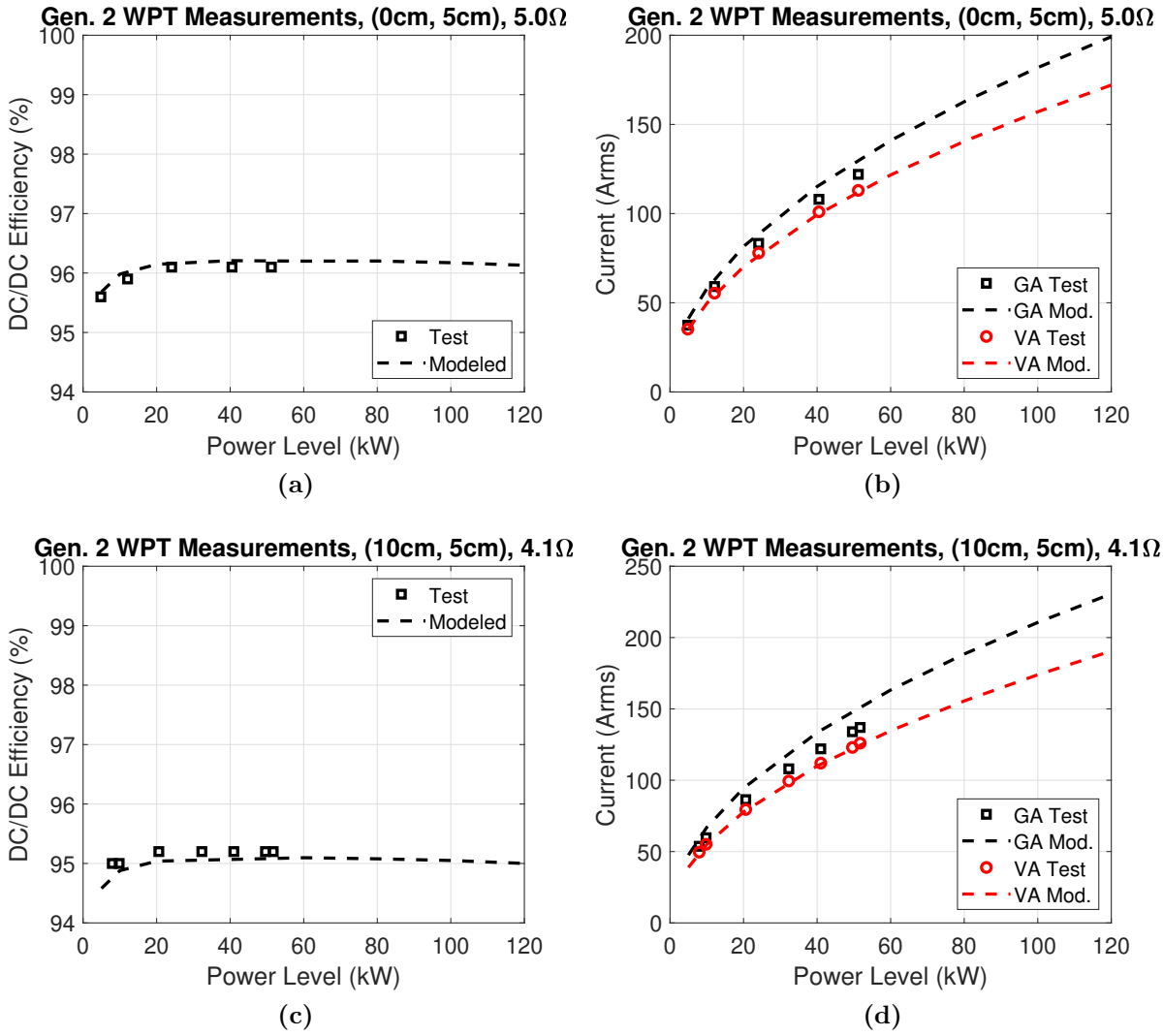

Figure 21: Tests of the Gen. 2 demonstrator at different alignments compared to modeled values near unity gain (grid offset of (-7 mm, -5 mm)) and an airgap of 125 mm. (a) DC/DC efficiency and (b) GA and VA current at (0 cm, 5 cm). (c) DC/DC efficiency and (d) GA and VA current at (10 cm, 5 cm).

D.2 Constant Output Voltage Tests

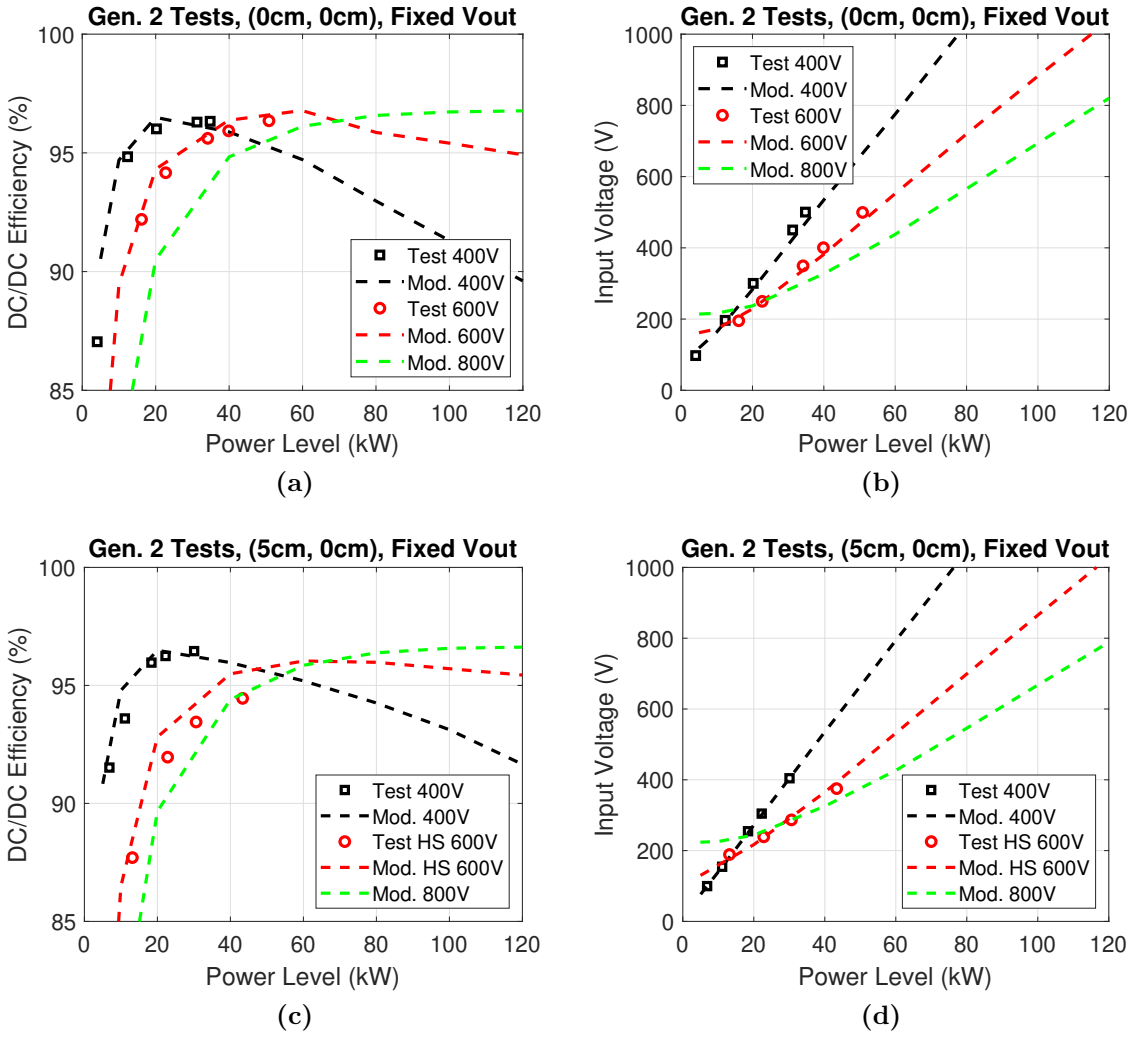

Figure 22: Repeated from Chapter 5. Tests of the Gen. 2 demonstrator at different alignments compared to modeled values at fixed output voltages (grid offset of (-7 mm, -5 mm)) and an airgap of 125 mm. (a) DC/DC efficiency and (b) output power vs. input voltage at (0 cm, 0 cm). (c) DC/DC efficiency and (d) output power vs. input voltage at (5 cm, 0 cm).

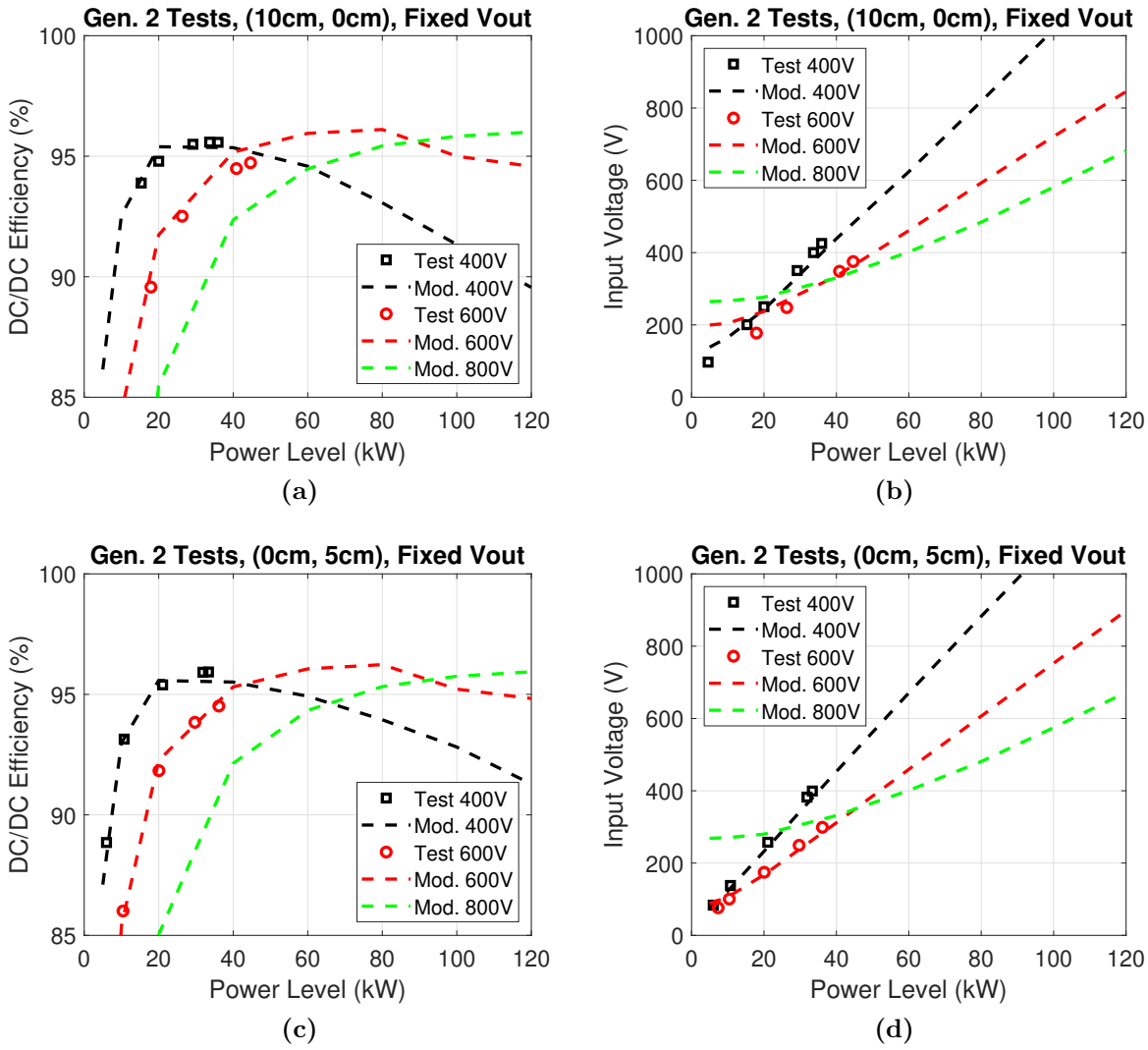

Figure 23: Tests of the Gen. 2 demonstrator at different alignments compared to modeled values at fixed output voltages (grid offset of (-7 mm, -5 mm)) and an airgap of 125 mm. (a) DC/DC efficiency and (b) output power vs. input voltage at (10 cm, 0 cm). (c) DC/DC efficiency and (d) output power vs. input voltage at (0 cm, 5 cm).

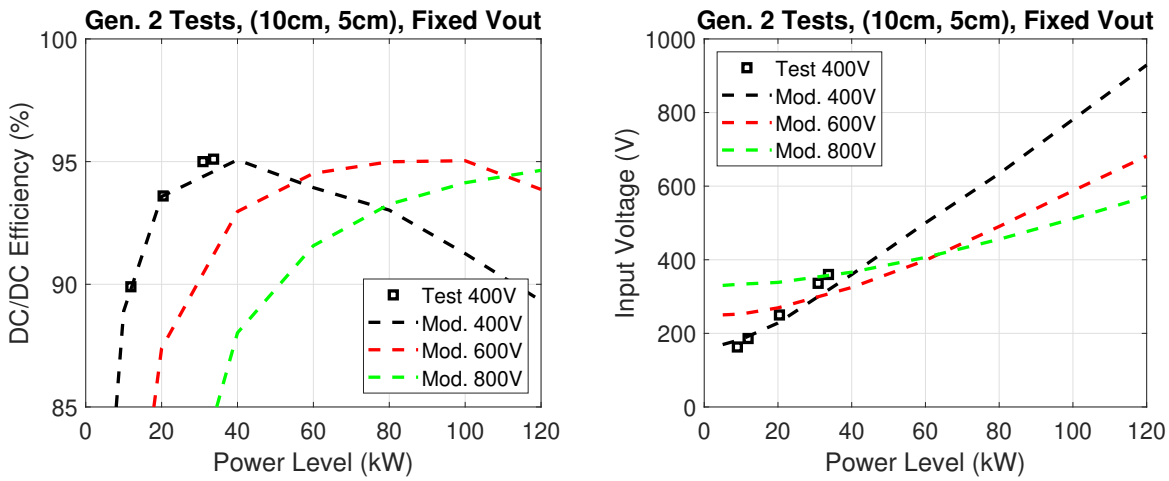

Figure 24: Tests of the Gen. 2 demonstrator at different alignments compared to modeled values at fixed output voltages (grid offset of (-7 mm, -5 mm)) and an airgap of 125 mm. (a) DC/DC efficiency and (b) output power vs. input voltage at (10 cm, 5 cm).

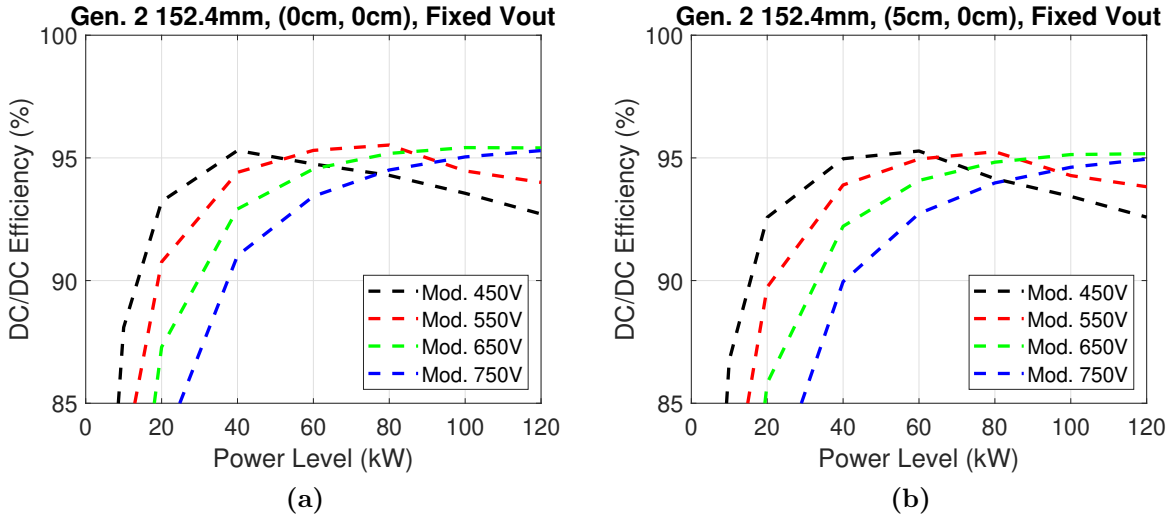

Figure 25: Modeled Gen. 2 demonstrator performance near alignment at fixed output voltages and an airgap of 152.4 mm. (a) DC/DC efficiency at (0 cm, 0 cm) and (b) (5 cm, 0 cm).

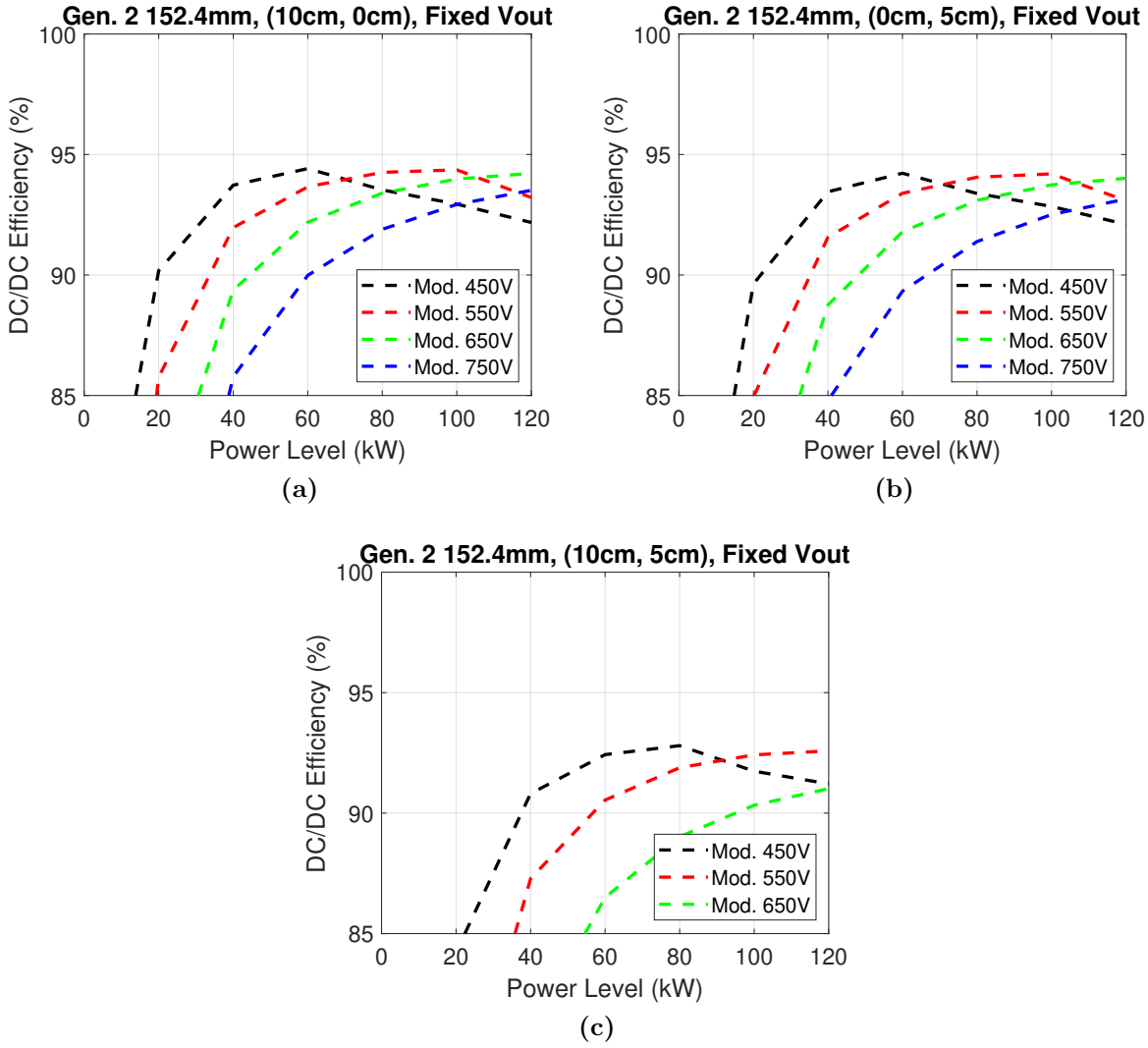

Figure 26: Modeled Gen. 2 demonstrator performance at different alignments at fixed output voltages and an airgap of 152.4 mm. (a) DC/DC efficiency at (10 cm, 0 cm), (b) (0 cm, 5 cm), and (c) (10 cm, 5 cm).

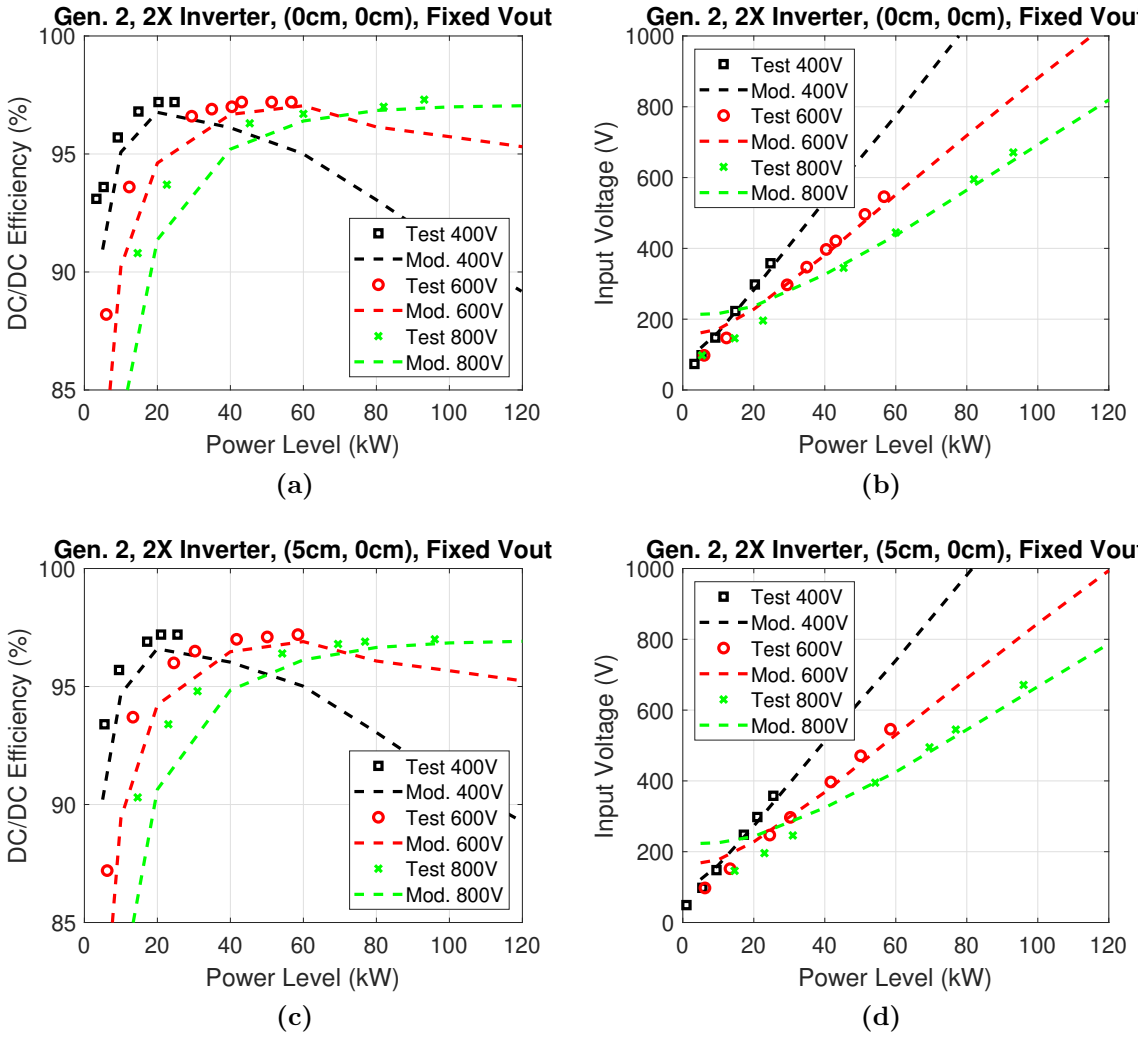

Figure 27: Repeated from Chapter 5. Tests of the Gen. 2 demonstrator with the 2X Inverter at different alignments compared to modeled values at fixed output voltages (grid offset of (-7 mm, -5 mm)) and an airgap of 125 mm. (a) DC/DC efficiency and (b) output power vs. input voltage at (0 cm, 0 cm). (c) DC/DC efficiency and (d) output power vs. input voltage at (5 cm, 0 cm).

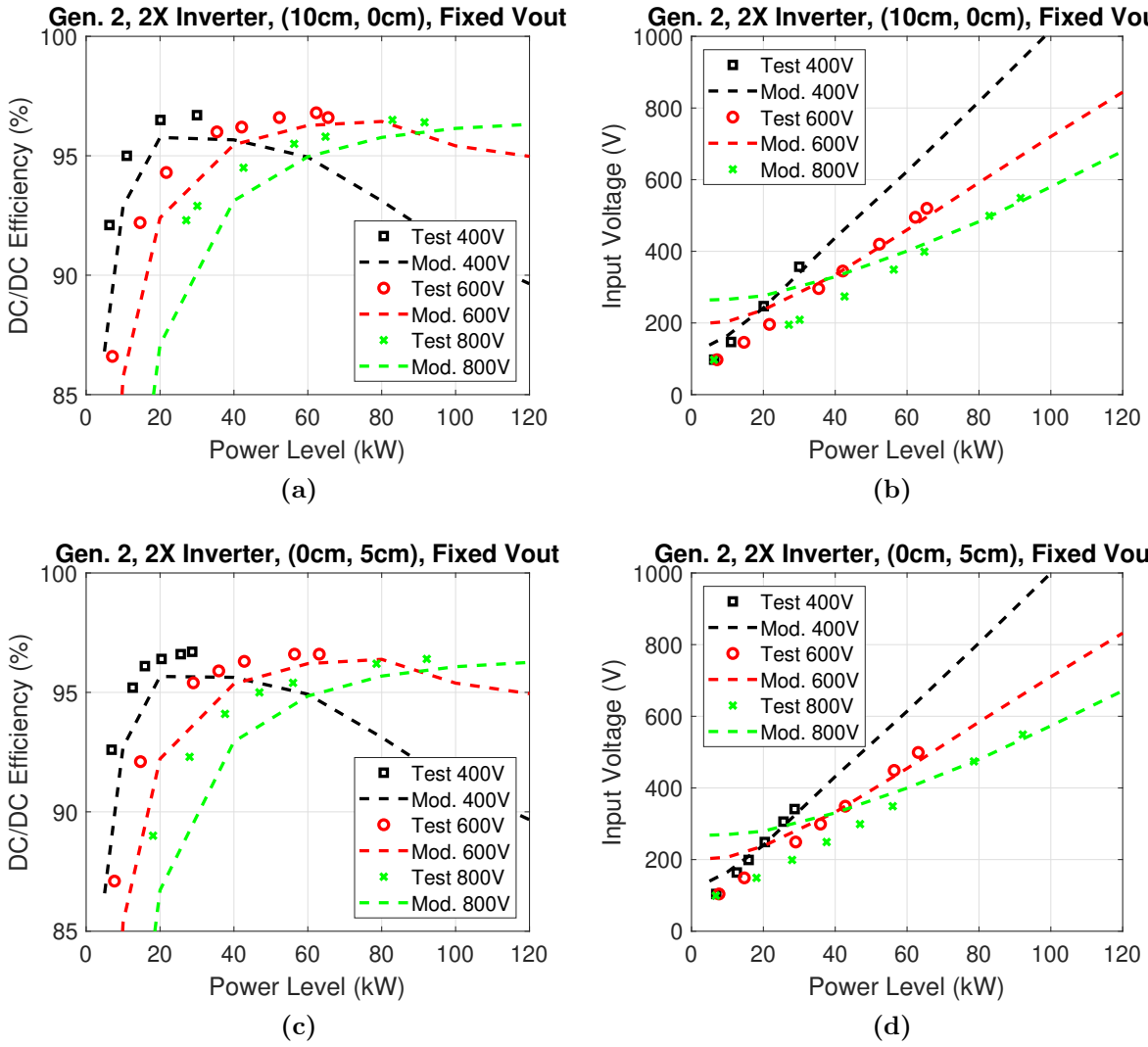

Figure 28: Tests of the Gen. 2 demonstrator with the 2X Inverter at different alignments compared to modeled values at fixed output voltages (grid offset of (-7 mm, -5 mm)) and an airgap of 125 mm. (a) DC/DC efficiency and (b) output power vs. input voltage at (10 cm, 0 cm). (c) DC/DC efficiency and (d) output power vs. input voltage at (0 cm, 5 cm).

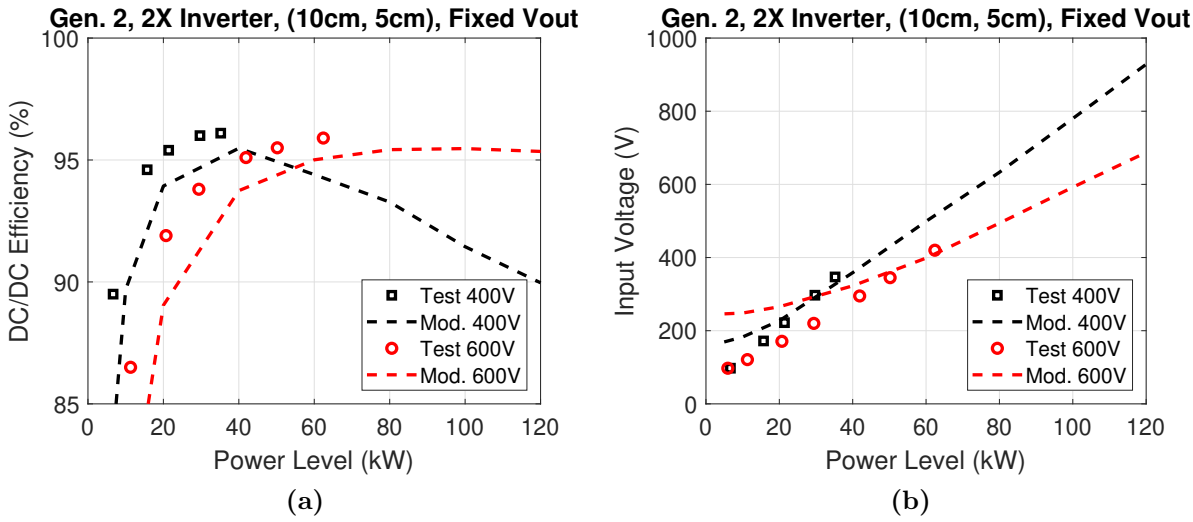

Figure 29: Tests of the Gen. 2 demonstrator with the 2X Inverter at different alignments compared to modeled values at fixed output voltages (grid offset of (-7 mm, -5 mm)) and an airgap of 125 mm. (a) DC/DC efficiency and (b) output power vs. input voltage at (10 cm, 5 cm).

Vita

Andrew Foote received his BS in Electrical Engineering from Auburn University in Auburn, Alabama in 2016. He started his PhD in 2016 in the Energy Science and Engineering PhD program in the Bredesen Center for Interdisciplinary Research. As a graduate research assistant, he worked at Oak Ridge National Laboratory in the Power Electronics and Electric Machinery Research Center from June 2016 to January 2020 focusing on the system-level implementation and modeling of Dynamic Wireless Power Transfer on roadways within the Department of Energy SMART Mobility Project. He received his Master of Science in Electrical Engineering from the University of Tennessee, Knoxville in 2019. In 2020, he joined Volkswagen Group of America at Innovation Hub Knoxville as part of the first cohort of PhD Fellows. At the time of this document, his research with Volkswagen includes the optimization and design of high-power inductive wireless power transfer, magnetic components, resonant tank elements, cooling, and power electronics.